이학박사 학위논문

Pressure-induced changes in carbon speciation and atomic structures of carbon-bearing silicate glasses and crystals in Earth's mantle up to 14 GPa: Insights from multi-nuclear solid-state NMR and Raman spectroscopy

지구 맨틀의 최대 14 GPa까지에서 탄소를 포함하는 비정질 및 결정질 규산염 물질의 압력에 따른 탄소 화학종 및 원자 구조 변화: 고상 핵자기공명 분석 및 라만 분광분석 연구

A dissertation in partial fulfillment of the requirements
for the degree of Doctor of Philosophy

2019년 2월

서울대학교 대학원
지구환경과학부

김 은 정

Abstract

Pressure-induced changes in carbon speciation and atomic structures of carbon-bearing silicate glasses and crystals in Earth's mantle up to 14 GPa: Insights from multi-nuclear solid-state NMR and Raman spectroscopy

Eun Jeong Kim
School of Earth and Environmental Sciences
The Graduate School
Seoul National University

Mantle is the largest carbon reservoir in the Earth and the speciation of carbon in the Earth's interior plays an important role in the geophysical and geochemical properties of silicate melts and overall distribution of carbon in the mantle. Due to its importance, previous researchers have reported the speciation and the solubility of carbon in silicate melts at high pressure up to 4 GPa. Yet the speciation of carbon in silicate melts and the effect of carbon species on silicate melts and crystals at high pressure above 4 GPa up to 14 GPa is not fully understood due to the difficulties in synthesizing samples and the lack of suitable probes to detect carbon species.

This dissertation is for a systematic exploration of pressure-induced speciation of carbon in silicate glasses and crystals at high pressure up to 14 GPa using multi-nuclear (^{13}C, ^{27}Al, ^{29}Si, ^{17}O, and ^{7}Li) solid-state nuclear

magnetic resonance (NMR) and Raman spectroscopy. The main objective of this thesis is probing and quantifying the carbon species in silicate melts and crystals at high pressure. The pressure-induced structural changes of alkali silicate melts at high pressure is also studied.

The systematic protocols to characterize carbon-bearing fluid inclusions and other carbon-bearing species in enstatite synthesized with ^{13}C-enriched amorphous carbon were established using high-resolution ^{13}C solid-state NMR and Raman spectroscopy. The Raman spectra revealed the presence of various molecular species in fluid inclusion, such as CO_2, CO, CH_4, H_2O, and H_2, and their heterogeneous distribution in carbon-bearing fluid inclusion. ^{13}C MAS NMR spectra showed the presence of CO_2, CO, and CO_3^{2-} in enstatite. As the carbonate species is not observed in fluid inclusions by Raman spectroscopy, the relationship between ^{13}C abundance and peak intensity in the ^{13}C magic angle spinning (MAS) NMR was established to identify the phase of carbonate species in the carbon-bearing enstatite. The estimated carbonate species is ~28–45 ppm, which is much higher than the solubility of carbon species in enstatite (0.05–4.7 ppm). The current methods to characterize carbon-bearing species in enstatite using Raman and NMR spectroscopy can be used to provide quantitative analysis of carbon species in silicate crystals.

The structural changes of carbon and its effect on the silicate network in binary sodium silicate and ternary sodium aluminosilicate melts at high pressure up to 8 GPa were investigated using multi-nuclear solid-state NMR. In binary sodium silicate melts, only carbonate species are observed, and the formation of bridging carbonates is observed above 6 GPa. In contrast, the presence of CO_2, CO, and CO_3^{2-} is observed in ternary sodium

aluminosilicate melts at high pressure up to 6 GPa, and the fraction of carbonate species gradually increases with increasing pressure. Among four carbonate species, the fraction of $Al(CO_3)Si$ increases the most with increasing pressure which may be related to the topological disorder of Al in ^{27}Al 3QMAS NMR spectra for carbon-bearing sodium aluminosilicate melts. Based on the peak intensity in ^{13}C MAS NMR spectra and the spin-lattice relaxation time of CO_2 in carbon-bearing sodium aluminosilicate melts, the total carbon contents gradually increase from ~1 wt% at 1.5 GPa to ~4 wt% at 6 GPa. The current results on the speciation of carbon in silicate melts above 4 GPa give insights into the carbon species and its contents in carbon-bearing silicate melts in the upper mantle.

To identify the structural changes of carbon-free silicate melts at high pressure and the effect of cation mixing in those melts, multi-nuclear solid-state NMR study on the Na-Li silicate glasses quenched from melts at high pressure up to 8 GPa was performed. ^{29}Si MAS NMR spectra of Na-Li silicate glasses show a relatively constant ratio of highly coordinated Si at high pressure regardless of lithium content (X_{Li}). ^{7}Li MAS NMR spectra of Na-Li silicate glasses show continuous changes of peak position and widths with varying X_{Li} and pressure. Based on the spin-spin relaxation of ^{7}Li in Na-Li silicate glasses at high pressure, the cation disorder of Na and Li changes from random distribution to more chemically ordered structure with increasing pressure in X_{Li} = 0.50 and 0.75. This indicates the pressure-induced chemical order in mixed alkali cations in silicate melts at high pressure.

The structural changes of carbon species in silicate melts at high pressure up to 14 GPa were investigated using Raman spectroscopy and

solid-state NMR. In carbon-bearing sodium aluminosilicate glasses, the fraction of bridging carbonates increases with increasing pressure up to 9.2 GPa, which is generally consistent with previous theoretical calculations. Raman spectra of carbon-bearing sodium aluminosilicate crystals formed at 14 GPa showed the presence of nano-diamonds in the sample and ^{13}C MAS NMR spectra showed the presence of carbonate minerals and nano-diamonds. In carbon-bearing sodium silicate melts at high pressure up to 14 GPa, the fraction of bridging carbonates [$Si(CO_3)Si$] increases up to ~60 % with increasing pressure up to 14 GPa. The increase of bridging carbonates with pressure may provide insight into the structural proxy of polymerization of carbon-bearing silicate melts at high pressure and immiscibility of carbonatite and silicate melts in the mantle.

Keywords: carbon species, silicate melts, high pressure, solid-state nuclear magnetic resonance, Raman spectroscopy

Student Number: 2012-30094

Table of Contents

List of Figures

spinning side bands for background signal at 130 ppm. The spinning sideband of the spectrum for carbon-bearing enstatite at 14 kHz overlaps with a small peak at ~ -9 ppm.

Figure 2.3. (A) Single point energy of $C(OH)_4$ cluster with varying C–O bond length. A model $C(OH)_4$ cluster is also shown in the inset. (B) NMR chemical shift of $C(OH)_4$ cluster with varying C–O bond length.

Figure 2.4. (Top) ^{13}C MAS NMR spectrum for the mixtures of ADM-SiO_2 with varying ADM/SiO_2 ratio [X_{ADM} = 1/4 (25 wt%, 2750 ppm of ^{13}C), 1/8 (12.5 wt%, 1375 ppm of ^{13}C), 1/16 (6.25 wt%, 688 ppm of ^{13}C), 1/50 (2.0 wt%, 220 ppm of ^{13}C), 1/233 (0.43 wt%, 47 ppm of ^{13}C), 1/310 (0.32 wt%, 35 ppm of ^{13}C)]. (Bottom) Variation of peak intensity in the ADM-SiO_2 mixture as a function of ^{13}C abundance (in ppm) calculated from nominal X_{ADM} ratio and peak area of carbon species in ^{13}C MAS NMR spectra. Diamonds and circles refer to the amounts of ^{13}C estimated from nominal X_{ADM} ratio with and without proton decoupling, respectively. Their peak areas were retrieved from ^{13}C MAS NMR results for ADM-SiO_2 mixtures. Rectangles refer to the amounts of ^{13}C species in carbon-bearing enstatite estimated from ^{13}C MAS NMR spectra for carbon-bearing enstatite.

Figure 2.A1. ^{13}C MAS NMR spectrum for carbon-bearing enstatite under proton decoupling with an applied Lorentzian broadening factor of 40.

Figure 2.A2. (A) ^{1}H MAS NMR spectra for compressed amorphous carbon, amorphous carbon, and rotor-stator background. Asterisks denote spinning sidebands. (B) Expanded ^{1}H MAS NMR spectra for the samples as labeled.

Figure 2.A3. ^{13}C MAS NMR spectra for ADM-SiO_2 mixtures with varying X_{ADM} ratio with decoupling power of 33 kHz.

Figure 2.A4. ^{13}C NMR spectra for 1 M $Na_2{}^{13}CO_3(aq)$, 1 M

Spinning sidebands are marked with an asterisk. The numbers labeled on the right side of the spectra refer to the amount of input CO_2 in the system. See section 2.2 for the measurement of background signal

Figure 3.6. Saturation-recovery of CO_2 in the carbon-bearing albite melts at 1.5 GPa and 6 GPa. Diamonds and circles refer to the normalized peak intensity of carbon-bearing albite glasses at 1.5 and 6 GPa, respectively, with varying delay time. Solid lines and dashed lines refer to calculated peak intensity, following the spin-lattice relaxation time equation. Error bars represent a 10% error.

Figure 3.7. Carbon contents in the albite melts with increasing pressure. Black, blue, red, and violet closed circles refer to total carbon content and the amount of CO_2, CO_3^{2-}, and CO species in albite glasses calculated from ^{13}C MAS NMR spectra, respectively. Open triangles and rectangles refer to data from Stolper et al. (1987) and Brooker et al. (1999), respectively.

Figure 3.8. (Top) Simulation results for ^{13}C MAS NMR spectra for carbonates in carbon-bearing albite melts with varying pressure at 1.5 and 6 GPa. Green, red, blue, purple, and black lines correspond to $^{[4]}Si(CO_3)^{[4]}Si$, $^{[4]}Si(CO_3)^{[4]}Al$, $^{[4]}Al(CO_3)^{[4]}Al$, free carbonates ($Na\cdots CO_3^{2-}$), and total simulation results, respectively. (Bottom) Variations in the CO_3^{2-} ion population with pressure in carbon-bearing albite melts. Blue, red, and green circles refer to $^{[4]}Al(CO_3)^{[4]}Al$, $^{[4]}Si(CO_3)^{[4]}Al$, and $^{[4]}Si(CO_3)^{[4]}Si$, respectively. Violet triangles denote free CO_3^{2-} ions near the non-bridging oxygen in network polyhedra, charge-balancing with the Na^+ ions. Open symbols refer to data from Brooker et al. (1999).

Figure 3.S1. ^{27}Al MAS NMR spectra for carbon-bearing albite glasses at 1.5

represent the peak intensity of ^{7}Li NMR spectra at 1 atm, 6 GPa, and 8 GPa, respectively. (B) ^{7}Li T_2 curves at X_{Li} = 0.25, 0.50, and 0.75 as functions of pressure up to 8 GPa.

Figure 4.5. (A) ^{17}O 3QMAS NMR spectra of NLS3 glasses with varying X_{Li} and at different pressures up to 6 GPa. Contour lines are drawn at 5% increments from 13 to 93% of the relative intensity, with added lines at 5%, 7%, and 10% to show low-intensity peaks better. (B) Total isotropic projection of the ^{17}O 3QMAS NMR spectra of NLS3 glasses at different pressures and X_{Li} values.

Figure 4.6. (Top) Simulation for the total isotropic projection of the ^{17}O 3QMAS NMR spectra of NLS3 glasses at different X_{Li} and pressures. (Bottom) The estimated oxygen fraction in NLS3 glasses as a function of pressure and X_{Li}.

Figure 4.S1. (Top) Simulation results of the ^{29}Si MAS NMR spectra of NLS3 glasses with varying X_{Li} and at different pressure up to 8 GPa. The thin green, red, blue, and black lines correspond to Q^2, Q^3, Q^4, and total simulation results, respectively. (Bottom) Variations in the Q^n fraction with respect to pressure in the NLS3 glasses. The triangles, rectangles, and circles refer to X_{Li} = 0.25, 0.50, and 0.75, respectively. The green, red, and blue colors correspond to Q^2, Q^3, and Q^4, respectively.

Figure 4.S2. ^{7}Li MAS NMR spectra of NLS3 glasses with X_{Li} = 0.25 at 14.1 T.

Figure 4.S3. ^{17}O MAS NMR spectra of NLS3 glasses with varying pressure and X_{Li} at 9.4 T.

Figure 4.S4. Raman spectra of NLS3 glasses with varying X_{Li} and at different pressures up to 6 GPa.

Figure 4.S5. Full-width at half-maximum (FWHM) in ^{7}Li MAS NMR spectra

List of Tables

Chapter 1. Introduction

1.1. Introduction

Geological processes originated from the Earth's interior, such as volcanic eruptions and earthquakes, are related to the macroscopic properties of crystalline and amorphous silicates at high pressure, which depend on their microscopic structures. For example, the changes in coordination number of network-former cations and oxygen, and topological and chemical disorder of silicate melts at high pressure affects the viscosity of silicate melts at high pressure (Lee, 2005, 2010). The presence of volatile species, such as CO_2, in silicate melts and crystals changes the viscosity and chemical composition of silicate melts, and the overall carbon flux between the Earth's surface and interior (Ni and Keppler, 2013 and references therein). Therefore, it is important to understand the atomistic structure of earth materials at high pressure to understand macroscopic properties of silicate crystals and melts and diverse geological processes.

The pressure-induced structural changes of silicate melts with or without the presence of volatile species is one of the importance processes in the Earth's interior. CO_2 is one of the most abundance volatiles in the magma (Hazen et al., 2012), and the presence of carbon species in the diverse earth environments affects the geochemical and geophysical processes. For example, burial of organic carbon in oceanic sediments and its subduction into the mantle by the subducting oceanic crust can change the fraction of O_2 in the atmosphere (Duncan and Dasgupta, 2017; Ruhl et al., 2009), and oxidation of reduced carbon species in the mantle would affect the oxygen fugacity in the mantle (Nicholis and Rutherford, 2009;

Pawley et al., 1992; Stagno et al., 2013). The decomposition of carbonates within the subduction zone provides CO_2 in the mantle, resulting in the volatile-induced formation of silicate melts and recycling of CO_2 to the atmosphere by the volcanic eruption (Blundy et al., 2010; Galvez et al., 2016; Mann and Schmidt, 2015). The volatile-induced formation of silicate melts is one of the several causes to form a low velocity zone at the boundary of upper mantle-transition zone (~410 km depth) (Revenaugh and Sipkin, 1994; Song et al., 2004).

The structural changes of silicate melts at high pressure without volatile species is also important as their structural changes at high pressure give insights into the anomalous changes in the macroscopic properties of the corresponding liquids. For example, diffusivity of oxygen in silicate melts at high pressure showed the non-linear behavior with increasing pressure and this non-linearity is closely related to the fraction of $^{[5]}$Al and $^{[5]}$Si at high pressure (Poe et al., 1997). The changes of viscosity in silicate melts at high pressure is related to the decrease of non-bridging oxygen (NBO) in the silicate melts at high pressure (e.g., Lee, 2004, 2010; Lee et al., 2003). In addition, the diffusivity of cations in silicate melts are closely related to the cation disorder in silicate melts (Ali et al., 1995; Gee and Eckert, 1996), resulting in the distribution of cations during the magma ocean (Lee et al., 2008a; Park and Lee, 2012, 2016).

Revealing the effect of pressure on the speciation of carbon, the distribution of mixed-cations in silicate melts, and the relevant structural changes of silicate melts at high pressure is important to understand the thermodynamic and transport properties of silicate melts at high pressure. For example, the addition of carbon as CO_2 in alkali aluminosilicate melts

affects the viscosity of silicate melts at constant pressure (Brearley and Montana, 1989; White and Montana, 1990), and the presence of carbonate species in silicate melts may cause the drastic decrease of viscosity in carbon-bearing silicate melts at high pressure (Kono et al., 2014). As the fraction of carbon species in silicate melts varies with increasing pressure (Brooker et al., 2001a), probing the speciation of carbon in carbon-bearing silicate melts at high pressure can provide insights into the changes in thermodynamic and transport properties of silicate melts, and shed light on the geochemical and geophysical processes in the Earth.

Because of its importance, the solubility and the speciation of carbon in silicate melts at high pressure has been extensively studied at high pressure up to 4 GPa (e.g., Eggler and Kadik, 1979; Eggler and Rosenhauer, 1978; Fine and Stolper, 1985; Kohn et al., 1991; Morizet et al., 2010; Mysen et al., 1975; Nowak et al., 2004). Previous studies revealed that the solubility of carbon increases with increasing the NBO/T ratio, proportion of SiO_2 ratio, the fraction of Ca, Mg contents, and the pressure (e.g., Blank and Brooker, 1994; Fine and Stolper, 1985; King and Holloway, 2002; Kohn et al., 1991; Morizet et al., 2010; Mysen et al., 2009; Nowak et al., 2004; Stolper et al., 1987). However, due to the difficulties in synthesizing the sample above 4 GPa and the lack of suitable probes to detect carbon species in silicate melts at high pressure above 4 GPa, experimental data on the carbon species and its contents in silicate melts at high pressure above 4 GPa has been limited. Therefore, in this study, I aim to elucidate the speciation of carbon in binary sodium silicate and ternary sodium aluminosilicate melts at high pressure up to 14 GPa.

This thesis consists of six chapters including Introduction (this

chapter) and appendix. In chapter 2, protocols to probe carbon-bearing species and CO_2 inclusion in the reaction product of amorphous carbon-$MgSiO_3$ enstatite at 1.5 GPa was studied using ^{13}C solid-state NMR and Raman spectroscopy (Kim et al., 2016). In this study, information on the collective vibration of molecules of different isotopes in Raman spectra and element-specific information on the carbon species in silicate crystals in ^{13}C NMR give complementary information on the carbon species in crystalline silicates, such as spatial distribution of carbon species and the total carbon contents. In addition, the calibration of carbon contents and ^{13}C NMR spectra is reported. In chapter 3, the effect of pressure on the short-range structure and speciation of carbon in alkali silicate and aluminosilicate glasses and melts at high pressure up to 8 GPa was explored using multi-nuclear solid-state NMR (Kim et al., 2018). The first experimental data of the speciation of carbon in carbon-bearing silicate glasses at high pressure is reported. The protocol to measure the carbon contents in carbon-bearing silicate glasses at high pressure is provided taking into consideration the pressure-induced changes in spin-lattice relaxation time of carbon species at high pressure. In chapter 4, the effect of pressure on the cation disorder and the relevant structural changes of silicate network in Na-Li silicate melts was studied with varying pressure and the ratio of Li/(Na+Li) (Kim et al., in preparation). The cation disorder of Li is estimated by the ^{7}Li spin-spin relaxation time at high pressure up to 8 GPa. In chapter 5, the speciation of carbon in binary sodium silicate glasses and ternary sodium aluminosilicate melts and crystals at high pressure up to 14 GPa was studied using Raman spectroscopy and multi-nuclear solid-state NMR (Kim and Lee, in preparation). The presence of hexagonal diamonds was observed inside of

the sodium aluminosilicate crystals. As the Na_2CO_3 is used as a carbon reservoir, the transformation of carbonate into hexagonal diamonds indicates the changes in oxygen fugacity in the aluminosilicate crystals and glasses. The effect of carbon species in the structural changes of silicate melts at 14 GPa will shed light on understanding the formation of silicate melts and the presence of low velocity zone in upper mantle-transition zone boundaries. Finally, an abstract for a publication in Korean journal, publication lists, and presentation lists in domestic and international conferences are presented in the appendix.

1.2. Estimation of carbon budget in the mantle

Total carbon contents in the Earth is estimated as 2.1–9.3 × 10^{24} g (Dasgupta and Hirschmann, 2010; Kelemen and Manning, 2015). While the carbon content in the Earth's surface including biosphere, hydrosphere, atmosphere, and soil is 4.1 × 10^{19} g of C (~0.004%–0.002% of total carbon contents), the amounts of carbon in the crust and mantle are 1.4 × 10^{22} g and ~0.8–12.5 × 10^{23} g, respectively (Dasgupta and Hirschmann, 2010). As the carbon content in the crust and the mantle is 3–5 orders of magnitude higher than that in the Earth's surface, the sudden increase in the influx of carbon from the mantle and/or crust would cause severe changes in the environments of the Earth's surface. Due to its important, previous studies have focused on both the carbon budget and flux between the Earth's surface and the mantle (e.g., Dasgupta and Hirschmann, 2010; Foley and Fischer, 2017; Kelemen and Manning, 2015; Ruhl and Kürschner, 2011; Sverjensky et al., 2014).

The total carbon contents in the Earth is estimated from the carbon

contents in the meteorites and the partitioning coefficient of carbon between liquid metals and silicate liquids (Dasgupta, 2013). The average carbon contents in the carbonaceous meteorites are 2.7–4.4 wt% (Anders and Grevesse, 1989; Lodders, 2003; Lodders, 2010). The carbon contents in the bulk Earth is estimated as ~730 ppm (Marty, 2012; McDonough, 2003). The relatively low concentration of carbon in the current Earth compared with meteorites is due to the volatility of CO_2 and CH_4, which can be eliminated from the Earth during the early stage of Earth formation. It is estimated that the core contains 0.4–3.5 wt% of carbon, and the mantle contains ~14.5–50 ppm of carbon (Dasgupta, 2013; McDonough, 2003). Based on the fraction of carbon in each reservoir, the estimated total carbon contents in the Earth are ~3.5×10^{27} g of carbon in the core (with ~0.4 wt% of carbon in the core), and ~0.4×10^{26} g of carbon in the mantle (with ~50 ppm of carbon in the mantle) (Dasgupta, 2013). Together with this rough estimation of total carbon contents in the Earth, experimental data have collected the carbon contents from basaltic rocks and volcanic gases.

Estimation of carbon budget in the mantle needs an assumption that partitioning of CO_2 is similar to that of noble gas, such as He, as the CO_2 content in the magma varies with the partial melting of the crystalline silicate mantle, crystal fractionation in the magma, and the degassing of gaseous CO_2 from the magma (Dasgupta and Hirschmann, 2010; Kelemen and Manning, 2015). In addition, as the degassing process of CO_2 is very efficient, the detection of CO_2 contents from the fluid inclusion in the basaltic rocks may only indicates the lower bound of CO_2 concentration in the primary magma (Wallace, 2005). The carbon budget in the mantle is estimated from basalts and simultaneously emitted fluids (e.g., Bureau et

al., 1998; Dixon, 1997), mantle-derived fluids such as trapped fluid inclusions in basalts (e.g., Aubaud et al., 2006), hydrothermal vent fluids (e.g., Sansone et al., 1998), and the ratio of CO_2 over incompatible elements, such as CO_2/He (e.g., Zhang and Zindler, 1993), CO_2/Nb (Cartigny et al., 2008; Saal et al., 2002), CO_2/Ar (Cartigny et al., 2001; Tingle and Aines, 1988), and CO_2/Cl (Saal et al., 2002).

The distribution of carbon in the mantle, estimated from the mid-ocean-ridge-basalts (MORB) source, is heterogeneous. For example, the measured CO_2 from depleted MORB mantle is 20–30 ppm (Hirschmann and Dasgupta, 2009; Saal et al., 2002) while that from enriched MORB is 300–1300 ppm (Aubaud et al., 2006; Bureau et al., 1998; Dixon, 1997). Therefore, the estimation of total carbon contents in the mantle varies with the mixing ratio of the depleted and enriched mantle sources. Assuming that the carbon content in the whole mantle are only from depleted mantle, the estimated carbon content is 0.8–1.2 × 10^{23} g (Dasgupta and Hirschmann, 2010). The carbon budget can be estimated as much as 2.7–12.5 × 10^{23} g when the carbon content in the whole mantle is composed of 40% from depleted mantle and 60% from the enriched mantle (Dasgupta and Hirschmann, 2010).

1.3. Carbon flux between Earth's surface and the mantle

Carbon flux between Earth's surface and the mantle is estimated from ingassing and outgassing of carbon species in the ocean, subduction zone, oceanic island, mid-ocean ridge, and continental lift zone (e.g., Aubaud et al., 2006; Bureau et al., 1998; Dasgupta, 2018; Dasgupta and Hirschmann, 2010; Foley and Fischer, 2017; Kagoshima et al., 2015; Lee et al., 2016; Luth,

2003; Saal et al., 2002). Ingassing of carbon from the Earth's surface to the mantle includes the precipitation of $CaCO_3$ as sediments in the ocean and the transport of carbon through the oceanic crust, overlying sediments, and underlying mantle lithosphere. The estimated amount of $CaCO_3$ precipitated in the ocean is 2.0×10^{14} g of C/y and that of carbon species transported through the subduction zone is $4.0–6.6 \times 10^{13}$ g of C/y (Dasgupta and Hirschmann, 2010; Kelemen and Manning, 2015). The major carbon species carried by the oceanic crust and mantle lithosphere are CO_2 in fluid inclusions and/or carbonate minerals within the crust, those carried by the overlying sediments are reduced carbon species, such as remains of organic carbons and precipitated carbonate minerals, and those carried by the mantle lithosphere beneath the oceanic crust are ophicarbonates which are composed of serpentine and carbonates (e.g., Dasgupta and Hirschmann, 2010; Duncan and Dasgupta, 2017; Kagoshima et al., 2015; Kelemen and Manning, 2015).

Outgassing process occurs when the carbon-bearing oceanic crust goes into the mantle and the crust experiences the increase of temperature and pressure, resulting in the decomposition of carbonate minerals into CO_2 and the formation of silicate melts by the interaction between silicate minerals and volatile species, such as CO_2 and H_2O (Grotzinger et al., 2010). Those gaseous CO_2 formed between the mantle wedge and the subducting slab can move along the boundary between mantle wedge and the subducting slab, incorporate into the mantle wedge, and return to the atmosphere by volcanic eruption while remnant carbonate minerals and reduced carbon species can be transported into the deeper mantle by the subducting slab. The estimated fraction of recycling CO_2 to the atmosphere

through subduction zone varies from ~1% to 80% depending on the flux models (Bebout, 1995; Dasgupta and Hirschmann, 2010; Gorman et al., 2006; Johnston et al., 2011; Kelemen and Manning, 2015).

Outgassing of carbon from the mantle to the Earth's surface, such as atmosphere and hydrosphere, is estimated as 2.2–12.7 × 10^{13} g of C/y, including outgassing from oceanic island basalts (0.8–4.2 × 10^{13} g of C/y), mid-ocean ridge basalts (0.12–3.0 × 10^{13} g of C/y), arc volcanoes (1.8–3.7 × 10^{13} g of C/y), and diffusion outgassing through oceanic crust (0.4–1.2 × 10^{13} g of C/y) (Dasgupta and Hirschmann, 2010; Kelemen and Manning, 2015). Recent studies on the continental rift zones suggested that the carbon outgassing through the continental rift zone is also significant, as much as 1.9 × 10^{13} g of C/y (Foley and Fischer, 2017; Lee et al., 2016).

The outgassing process inevitably involves changes in speciation of carbon into silicate melts with varying pressure and temperature and the carbon carrying capacity of silicate melts is important to estimate the amount of carbon emitted through the subduction zone. For example, the solubility of CO_2 and carbonates into silicate melts is much higher than that of graphite or hydrocarbon species at the same pressure and temperature conditions (e.g., Keppler et al., 2003; Mysen et al., 2011; Shcheka et al., 2006). Therefore, neutral to reduced carbon species are much easier to remain in the subducting crust and be carried into the deep mantle while CO_2 and carbonates are moved with silicate melts formed above the subducting crust (e.g., Duncan and Dasgupta, 2017).

While the current carbon flux between Earth's surface and the mantle is balanced to move more carbon species into the mantle, sudden changes in volcanic activities can change the carbon flux between two carbon

reservoirs. For example, the carbon isotope data of long-change n-alkanes from waxes of land plants showed the sudden decrease of $\delta^{13}C$ value (~ -8.5 ‰) within 10,000–20,000 years at the end of Triassic (Ruhl et al., 2011). The sudden changes of isotope value are thought to be related to the mass injection of CO_2 from volcanic eruption in the Central Atlantic Magmatic Province (Ruhl et al., 2011), which erupted a volume of ~2-3 × 10^6 km^3 of basaltic magma (Balckburn et al., 2013). The estimated carbon contents emitted by the eruption is 8000–9000 Gt of carbon (Ruhl et al., 2011). Together with the density of basaltic melts, the estimated fraction of carbon in the basaltic magma erupted in the Central Atlantic Magmatic Province is 0.13–0.2 wt%. While the fraction of dissolved CO_2 carried by the basaltic magma is relatively low compared with carbon carrying capacity of basaltic melts (~ several wt% of carbon in basaltic melts) (Ni and Keppler, 2013 and references therein), this implies that the flux of total magma and the total eruption time is important for estimating the total carbon contents outgassed by the volcanic eruption, resulting in the huge changes in carbon isotope values. Therefore, the flux of carbon species between Earth's surface and the mantle should be considered as a crucial factor for controlling the distribution of carbon in the Earth's surface and the mantle.

1.4. The speciation of carbon in silicate crystals and glasses at high pressure

Previous pioneering researchers have reported the speciation of carbon in silicate crystals and glasses at high pressure using Raman spectroscopy (e.g., Duncan and Dasgupta, 2017; Morizet et al., 2009; Mposkos and Kostopoulos, 2001; Mysen, 2013, 2017; Pawley et al., 1992; Rosso and Bodnar, 1995; Sandler et al., 2003; Seitz et al., 1996), FT-IR

spectroscopy (e.g., Behrens et al., 2004; Brooker et al., 2001a, b; Fine and Stolper, 1985; Kadik et al., 2004; King and Holloway, 2002; Morizet et al., 2002; Mysen, 2018; Mysen et al., 1975; Pan et al., 1991; Stanley et al., 2012; Stolper et al., 1987), ^{13}C solid-state NMR (e.g., Brooker et al., 1999; Kohn et al., 1991; Morizet et al., 2002; Morizet et al., 2017; Papenguth et al., 1989; Sen et al., 2013; Xue et al., 2018), in-situ Brillouin scattering spectroscopy (Murakami and Bass, 2011), and molecular dynamic simulations (Guillot and Sator, 2011; Moussallam et al., 2016; Sarda and Guillot, 2005; Vuilleumier et al., 2015). The carbon species detected varies with the spectroscopy methods. For example, FT-IR spectroscopy provides information on molecular CO_2 and carbonate species which are detected at ~2349 cm^{-1} and 1415 cm^{-1}, respectively (Brooker et al., 2001b; Ni and Keppler, 2013) and the degeneration of antisymmetric stretching vibration of carbonates induces a split of carbonate peaks in IR spectra, showing the distortion of carbonate with varying composition (Brooker et al., 2001b; Ni and Keppler, 2013). Raman spectroscopy, on the other hand, provides information on the CO_2, carbonate species, CH_4, and sp^2 and sp^3 bonding in graphite and diamonds at ~1337 cm^{-1}, ~1100 cm^{-1}, ~2916 cm^{-1}, ~1360 cm^{-1} and 1560 cm^{-1}, respectively (Ferrari, 2007; Ni and Keppler, 2013; Seitz et al., 1996). The CO_2 in Raman spectroscopy showed Fermi resonance doublet, showing the symmetric bending of ν_1 and $2\nu_2$ of $^{12}CO_2$ at ~1385 cm^{-1} and ~1285 cm^{-1}, respectively (Rosso and Bodnar, 1995). The frequency difference of ν_1 and $2\nu_2$ of CO_2 is used to measure the internal pressure of CO_2 in fluid inclusion, giving the pressure and temperature condition of trapping of the fluid inclusion (Kim et al., 2016; Rosso and Bodnar, 1995; Seitz et al., 1996). In addition, isotropic composition of CO_2 and CH_4 can be identified by the

peak position in Raman spectra: $^{13}CO_2$ at ~1360 and 1260 cm^{-1}, and $^{12}CH_4$ at 2918 cm^{-1}, $^{13}CH_4$ at 2916 cm^{-1}, respectively (e.g., Dang-Nhu et al., 1979; Kim et al., 2016; Seitz et al., 1996). The changes of chemical bonding of neural carbon species from sp^2 to sp^3 bonding can also be identified by the Raman spectroscopy (Ferrari and Robertson, 2001; Hanfland et al., 1989; Knight and White, 1989; Kuzmany et al., 2004; Lopez-Rios et al., 1996; Reich and Thomsen, 2004; Vidano and Fischbach, 1978). ^{13}C NMR spectroscopy is only active for ^{13}C nuclide in the sample and provides the quantitative information around carbon species. The peaks for CO_2, carbonate species, CH_4, and sp^2 and sp^3 bonding in graphite and diamonds are ~125 ppm, ~160–171 ppm, ~-5 ppm, ~110–140 ppm and ~65 ppm, respectively (Kohn et al., 1991; Mysen, 2013; Ni and Keppler, 2013). The area of the NMR peaks are directly proportional to the abundance of carbon species in the bulk sample (Sandler et al., 2003) and the detection limit is estimated as several tens of ppm of ^{13}C carbon species (Kim et al., 2016).

Carbon in the mantle mostly exists as accessory mineral phases, such as graphite, diamond, and carbonate minerals, between grain boundaries of silicate minerals (Hazen and Schiffries, 2013; Keppler et al., 2003; Luth, 2003; Shcheka et al., 2006). Once those mineral phases of carbon dissolved into silicate melts, the speciation of carbon varies strongly with the composition of silicate melts and oxygen fugacity of the mantle and is independent on the total carbon content (Behrens and Gaillard, 2006; Ni and Keppler, 2013). In oxidized condition, the dominant carbon species in highly polymerized silicate melts, such as rhyolitic melts, is molecular CO_2 weakly bound to the bridging oxygen (BO) in the silicate network, while only dissolved carbonate species is observed in depolymerized melts, such as basaltic and

peridotitic melts (e.g., Blank and Brooker, 1994; Brooker et al., 1999; Morizet et al., 2002). In reduced condition, the dominant carbon species in silicate melts are CO and CH_4 (Mysen, 2013; Mysen and Richet, 2005b), and the solubility of those reduced carbon species generally 2–4 times lower than that of oxidized species (Mysen et al., 2011).

The speciation of carbon in silicate melts is closely related to the solubility of carbon in the silicate melts. The formation of carbonates is favored in mafic and ultramafic melts (depolymerized melts) as the following equation:

$$CO_2 + O^{2-} = CO_3^{2-}$$

where O^{2-} stands for a non-bridging oxygen (NBO) atom in the silicate network and the solubility of carbon in silicate melts generally increases with increasing the fraction of NBO (Mysen, 2012; Ni and Keppler, 2013). The relative abundance of CO_2/CO_3^{2-} in silicate melts does not depend significantly on pressure up to 0.8 GPa (Behrens and Gaillard, 2006; Blank and Brooker, 1994; Nowak et al., 2003), and the CO_2/CO_3^{2-} ratio decreases with the further increase of pressure up to 3.5 GPa (e.g., Brooker et al., 1999). However, the experimental data on the speciation of carbon above 4 GPa has not been reported due to the difficulties in synthesizing sample above 4 GPa and the lack of suitable probe to detect carbon species at high pressure. Recent molecular dynamic simulations on the carbon species in rhyolitic melts at high pressure up to 15 GPa predicted that the fraction of $CO_2/(CO_2+CO_3^{2-})$ in rhyolitic melt at 15 GPa would be ~27% (Guillot and Sator, 2011).

The carbonate species in silicate melts can be divided into three: free carbonates charge-balancing with network modifying cations, such as Na^+,

non-bridging carbonates which are linked to one non-bridging oxygen, such as $Si(CO_3^{2-})\cdots Na^+$ or $Al(CO_3^{2-})\cdots Na^+$, and bridging carbonates which are linked to two non-bridging oxygen, such as $Al(CO_3)Si$ (e.g., Brooker et al., 2001b; Kohn et al., 1991; Tossell, 1995). While the dissolved CO_2 seems similar to that of non-bridging carbonates, the dissolved CO_2 has weak interaction with BO and non-bridging carbonates are linked to NBO. Sometimes, the dissolved CO_2 which has very short CO_2–BO distance (< 1.4 Å) is classified as CO_3^{2-} although it is linked to BO (e.g., Figure 21 in Ni and Keppler, 2013). Therefore, it is important to check the atomic structures of carbon species that the authors used. Identification of non-bridging carbonates from bridging carbonates has not been made in experimental spectroscopies and carbonates are usually categorized into free carbonates and bridging carbonates in ^{13}C NMR (Brooker et al., 2001b; Brooker et al., 1999; Xue et al., 2018).

1.5. Pressure-induced structural changes of silicate melts at high pressure

The structure of silicate melts is very different from that of crystalline silicate. For example, crystalline anorthite ($CaAl_2Si_2O_8$) is a fully polymerized silicate, which has NBO/T ratio of 0, while $CaAl_2Si_2O_8$ glasses quenched from melt at 1 atm shows significant amount of NBO by forming $^{[5]}Al$ in the system (Stebbins and Xu, 1997). The structural changes of silicate melts from crystalline silicate result in the increase of heat capacity and the entropy of the system, the decrease of viscosity of melts, and changes of diffusion of network modifying cations in the melts (Stebbins, 1995; Stebbins, 2016; Stebbins and Xu, 1997).

The structure of silicate melts varies with composition, temperature,

and pressure. Among those variables, the pressure-induced structural changes of silicate melts are important to understand non-linear changes of viscosity and diffusivity of silicate melts at high pressure (Brearley and Montana, 1989; Poe et al., 1997; Suzuki, 2018; White and Montana, 1990). As glasses preserve the structure of silicate melts near the glass transition temperature (T_g), the structure of silicate melts at high pressure is often deduced from that of silicate glasses quenched from melts at high pressure (Mysen and Richet, 2005a; Stebbins, 2016). The densification of silicate melts at high pressure follows three steps. First, the topological rearrangement of glass network, such as changes in T-O-T angle (where T = Si and/or Al) and changes in T-O bond lengths, occurs below the threshold pressure at which the highly coordinated framework units are formed (Lee, 2010 and references therein). The increase of topological disorder is observed as the broadening of peak widths in silicate glasses at high pressure without the changes in coordination number (e.g., Allwardt et al., 2004; Kim et al., 2018; Lee et al., 2004). Above the threshold pressure, the formation of highly coordinated network-former and a decrease of NBO fraction control the overall densification of silicate melts, and the network modifying cations often changes its role from network modifier to charge balancing cations around highly coordinated cations (Allwardt et al., 2004; Lee, 2010; Lee et al., 2004; Lee et al., 2003; Wolf and McMillan, 1995; Xue et al., 1991). At higher pressure, oxygens with three Si frameworks are formed by the twisting of silicate network rings (Lee, 2010; Lee et al., 2008b) and this induces the further densification of silicate melts at high pressure.

The structural changes of silicate melts at high pressure are related to the transport properties of silicate melts at high pressure. The diffusivity of

Si^{4+} and O^{2-} increases with increasing the fraction of highly coordinated Al and Si in the silicate glasses (Poe et al., 1997), implying the lowering of viscosity due to the easier O^{2-} transfer between NBO at high pressure. The fraction of NBO with the same SiO_2 ratio at high pressure varies with the mixing of cations, implying the cation-composition dependence on the viscosity (Lee et al., 2008a). Therefore, understanding the structural changes of silicate melts at high pressure would give insights into the macroscopic properties of magma, such as viscosity and diffusivity (e.g., Allwardt et al., 2003; Bottinga and Richet, 1995; Lee, 2011; Poe et al., 1997; Suzuki et al., 2011; Xue et al., 1991).

1.6. Introduction to multi-anvil press

This part includes the study published in Journal of Mineralogical Society of Korea in 2018. A figure shown here is from Kim and Lee (2018).

The high-pressure experimental apparatuses are divided into two categories: apparatuses generating hydrostatic pressure and those generating shear stress. Among those high-pressure apparatuses, apparatuses generating hydrostatic pressure include piston cylinder, multi-anvil press, and diamond anvil cell (DAC). Multi-anvil press can generate the hydrostatic pressure ranging from 5 to 25 GPa using tungsten carbide cubes and the temperature up to 2300 °C, which can generate the pressure and temperature conditions of upper mantle to the boundary of transition zone and lower mantle. Whereas the sample volume of piston cylinder is 125–180 mm^3 and that of DAC is ~0.001 mm^3, respectively, the volume of the sample chamber in multi-anvil press varies 2–140 mm^3, which is useful to synthesize the ex-situ high pressure samples. The high-pressure glass

samples were synthesized by fusing the sample at the target pressure and then by quenching the sample with a turn off of electric power. The initial quench rate was estimated to > 500 °C/s. The high-pressure glass samples were synthesized by fusing the sample at the target pressure and then by quenching the sample with a turn off of electric power. The initial quench rate was estimated to > 500 °C/s.

Multi-anvil press was invented by Bridgman in 1940s with tetrahedral shape press which can generate the pressure up to 10 GPa (Liebermann, 2011). Cubic anvil press was invented in 1950s for reducing the experimental failure on pressuring the tetrahedral cell (Liebermann, 2011) and then multi-anvil press was developed in 1970s by Kawai (Kawai and Endo, 1970), applying six-split first-stage anvils and eight-split second-stage anvils into a uniaxial press and generating hydrostatic pressure on samples through octahedral pressure-medium and the twelve-wings of pyrophyllite sticks (Figure 1.1). As the junction of pyrophyllites does affect the stability of high-pressure experiments (Schwarz, 2010), Walker module was developed in 1990 by simplifying pressure-medium structure, adding pyrophyllite wing to the octahedral structure (Walker et al., 1990).

The pressure limit that can be generated by a multi-anvil press is determined by the limit of shear deformation of the materials of the second-stage anvil. The most common materials used for second-stage anvil is tungsten carbide (WC) which can generate the pressure up to 30 GPa (Leinenweber et al., 2012; Yoneda et al., 1984). Sintered diamonds are recently used as second-stage anvil materials because they can generate the pressure up to 120 GPa (Ito, 2007; Shatskiy et al., 2011; Yamazaki et al., 2018). Recent study reported the addition of two third-stage anvils with a 1-

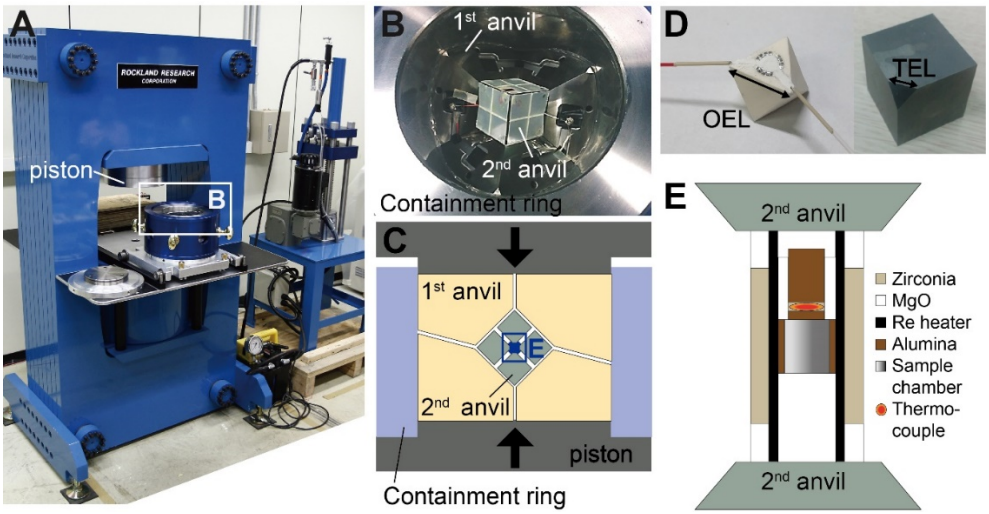

Figure 1.1. (a) A photograph of 1100-ton multi-anvil press equipped in author's laboratory, Seoul National University. (b) A plan view of the multi-anvil press (open square with label "b") in Fig. 1.1a. A containment ring, three first-stage anvils (1st anvil) and assembled second-stage anvils (2nd anvil) are shown. (c) A section drawing of the multi-anvil press. Grey, violet, yellow, and green areas represent pistons, a containment ring, first-stage anvils, and second-stage anvils, respectively. The black arrows show the direction of force applied to pistons. (d) Photographs of an octahedral pressure medium and a second-stage anvil. OEL is referred to the octahedral edge lengths the pressure medium and TEL is an abbreviation of truncated edge lengths of the second-stage anvil. (e) A schematic diagram of an assembly set with straight heater (open square with label "e") in Fig. 1.1c. This figure is from Kim and Lee (2018).

mm diameter in a uniaxial direction parallel to the outermost uniaxial press and achieved around 100 GPa of pressure by this method (Kunimoto et al., 2008).

As the multi-anvil press generate the pressure by using oil inside of the press, the calibration of oil pressure and the actual pressure generated on the sample is necessary. This oil load-pressure calibration process includes pressure loss between the containment ring and the first-stage anvils, pressure loss between first-stage anvils and second-stage anvils, press loss due to the frictional force between extruded pressure medium and the second anvils (Ito, 2007; Leinenweber et al., 2012). The load-pressure calibration varies with the truncated edge lengths of second-stage anvils (TEL) over the octahedral edge lengths of pressure medium (OEL), the volume of sample chamber, and the differences due to the temperature. The pressure-load calibration curve for 1100-ton multi-anvil press in Seoul National University is reported in Kim and Lee (2018).

References

Ali, F., Chadwick, A.V., Greaves, G.N., Jermy, M.C., Ngai, K.L. and Smith, M.E. (1995) Examination of the mixed-alkali effect in (Li,Na) disilicate glasses by nuclear magnetic resonance and conductivity measurements. *Solid State Nuclear Magnetic Resonance* **5**, 133-143.

Allwardt, J.R., Lee, S.K. and Stebbins, J.F. (2003) Bonding preferences of non-bridging O atoms: Evidence from ^{17}O MAS and 3QMAS NMR on calcium aluminate and low-silica Ca-aluminosilicate glasses. *American Mineralogist* **88**, 949-954.

Allwardt, J.R., Schmidt, B.C. and Stebbins, J.F. (2004) Structural mechanisms of compression and decompression in high-pressure $K_2Si_4O_9$ glasses: an investigation utilizing Raman and NMR spectroscopy of glasses and crystalline materials. *Chemical geology* **213**, 137-151.

Aubaud, C., Pineau, F., Hékinian, R. and Javoy, M. (2006) Carbon and hydrogen isotope constraints on degassing of CO_2 and H_2O in submarine lavas from the Pitcairn hotspot (South Pacific). *Geophysical Research Letters* **33**.

Bebout, G.E. (1995) The impact of subduction-zone metamorphism on mantle-ocean chemical cycling. *Chemical Geology* **126**, 191-218.

Behrens, H. and Gaillard, F. (2006) Geochemical Aspects of Melts: Volatiles and Redox Behavior. *Elements* **2**, 275-280.

Behrens, H., Ohlhorst, S., Holtz, F. and Champenois, M. (2004) CO_2 solubility in dacitic melts equilibrated with H_2O-CO_2 fluids: Implications for modeling the solubility of CO_2 in silicic melts. *Geochimica et Cosmochemica Acta* **68**, 4687-4703.

Blank, J.G. and Brooker, R.A. (1994) Experimental studies of carbon dioxide in silicate melts: Solubility, speciation, and stable carbon isotope behavior, In *Volatiles in Magmas*, (Eds. Carroll, M.R., Holloway, J.R.).

Blundy, J., Cashman, K.V., Rust, A. and Witham, F. (2010) A case for CO_2-rich arc magmas. *Earth Planet. Sci. Lett.* **290**, 289-301.

Bottinga, Y. and Richet, P. (1995) Silicate melts: The "anomalous" pressure dependence of the viscosity. *Geochimica et Cosmochimica Acta* **59**, 2725-2731.

Brearley, M. and Montana, A. (1989) The effect of CO_2 on the viscosity of silicate liquids at high pressure. *Geochimica et Cosmochimica Acta* **53**, 2609-2616.

Brooker, R.A., Kohn, S.C., Holloway, J.R. and McMillan, P.F. (2001a) Structural controls on the solubility of CO_2 in silicate melts Part I: bulk solubility data. *Chemical Geology* **174**, 225-239.

Brooker, R.A., Kohn, S.C., Holloway, J.R. and McMillan, P.F. (2001b) Structural controls on the solubility of CO_2 in silicate melts Part II: IR characteristics of carbonate groups in silicate glasses. *Chemical Geology* **174**, 241-254.

Brooker, R.A., Kohn, S.C., Holloway, J.R., McMillan, P.F. and Carroll, M.R. (1999) Solubility, speciation and dissolution mechanisms for CO_2 in melts on the $NaAlO_2$-SiO_2 join. *Geochimica et Cosmochimica Acta* **63**, 3549-3565.

Bureau, H., Pineau, F., Métrich, N., Semet, M. and Javoy, M. (1998) A melt and fluid inclusion study of the gas phase at Piton de la Fournaise volcano (Réunion Island). *Chemical geology* **147**, 115-130.

Cartigny, P., Jendrzejewski, N., Pineau, F., Petit, E. and Javoy, M. (2001) Volatile (C, N, Ar) variability in MORB and the respective roles of mantle source heterogeneity and degassing: the case of the Southwest Indian Ridge. *Earth and Planetary Science Letters* **194**, 241-257.

Cartigny, P., Pineau, F., Aubaud, C. and Javoy, M. (2008) Towards a consistent mantle carbon flux estimate: Insights from volatile

systematics (H_2O/Ce, δD, CO_2/Nb) in the North Atlantic mantle (14° N and 34° N). *Earth and Planetary Science Letters* **265**, 672-685.

Dang-Nhu, M., Pine, A.S. and Robiette, A.G. (1979) Spectral intensities in the ν_3 bands of $^{12}CH_4$ and $^{13}CH_4$. *Journal of Molecular Spectroscopy* **77**, 57-68.

Dasgupta, R. (2018) Volatile-bearing partial melts beneath oceans and continents–Where, how much, and of what compositions? *American Journal of Science* **318**, 141-165.

Dasgupta, R. and Hirschmann, M.M. (2010) The deep carbon cycle and melting in Earth's interior. *Earth and Planetary Science Letters* **298**, 1-13.

Dixon, J.E. (1997) Degassing of alkalic basalts. *American Mineralogist* **82**, 368-378.

Duncan, M.S. and Dasgupta, R. (2017) Rise of Earth's atmospheric oxygen controlled by efficient subduction of organic carbon. *Nature Geoscience* **10**, 387-392.

Eggler, D.H. and Kadik, A.A. (1979) System $NaAlSi_3O_8$-H_2O-CO_2 to 20 kbar pressure 1. Compositional and thermodynamic relations of liquids and vapors coexisting with albite. *American Mineralogist* **64**, 1036-1048.

Eggler, D.H. and Rosenhauer, M. (1978) Carbon-dioxide in silicate melts 2. Solubilites of CO_2 and H_2O in $CaMgSi_2O_6$ (diopside) liquids and vapors at pressure to 40 kb. *American Journal of Science* **278**, 64-94.

Ferrari, A.C. (2007) Raman spectroscopy of graphene and graphite: Disorder, electron–phonon coupling, doping and nonadiabatic effects. *Solid State Communications* **143**, 47-57.

Ferrari, A.C. and Robertson, J. (2001) Origin of the 1150 cm^{-1} Raman mode in nanocrystalline diamond. *Physical Review B* **63**, 121405.

Fine, G. and Stolper, E. (1985) The speciation of carbon-dioxide in soium aluminosilicate glasses. *Contributions to Mineralogy and Petrology* **91**, 105-121.

Foley, S.F. and Fischer, T.P. (2017) An essential role for continental rifts and lithosphere in the deep carbon cycle. *Nature Geoscience* **10**, 897-902.

Galvez, M.E., Connolly, J.A. and Manning, C.E. (2016) Implications for metal and volatile cycles from the pH of subduction zone fluids. *Nature* **539**, 420-424.

Gee, B. and Eckert, H. (1996) Cation distribution in mixed-alkali silicate glasses. NMR studies by ^{23}Na-{^{7}Li} and ^{23}Na-{^{6}Li} spin echo double resonance. *The Journal of Physical Chemistry* **100**, 3705-3712.

Gorman, P.J., Kerrick, D. and Connolly, J. (2006) Modeling open system metamorphic decarbonation of subducting slabs. *Geochemistry, Geophysics, Geosystems* **7**.

Grotzinger, J., Jordan, T.H. and Press, F. (2010) Understanding earth. Macmillan.

Guillot, B. and Sator, N. (2011) Carbon dioxide in silicate melts: A molecular dynamics simulation study. *Geochimica et Cosmochimica Acta* **75**, 1829-1857.

Hanfland, M., Beister, H. and Syassen, K. (1989) Graphite under pressure: Equation of state and first-order Raman modes. *Physical Review B* **39**, 12598-12603.

Hazen, R.M., Hemley, R.J. and Mangum, A.J. (2012) Carbon in Earth's interior: Storage, cycling, and life. *Eos, Transactions American Geophysical Union* **93**, 17-18.

Hazen, R.M. and Schiffries, C.M. (2013) Why deep carbon?, In *Carbon in Earth*, (Eds. Hazen, R.M., Jones, A.P., Baross, J.A.). Mineralogical Society of America, Virginia, U.S.A.

Hirschmann, M.M. and Dasgupta, R. (2009) The H/C ratios of Earth's near-surface and deep reservoirs, and consequences for deep Earth volatile cycles. *Chemical Geology* **262**, 4-16.

Ito, E. (2007) Theory and Practice – Multianvil Cells and High-Pressure Experimental Methods, In *Treatise on Geophysics*, (Eds. Schubert, G., Romanowicz, B., Dziewonski, A.), pp. 197-230.

Johnston, F.K., Turchyn, A.V. and Edmonds, M. (2011) Decarbonation efficiency in subduction zones: Implications for warm Cretaceous climates. *Earth and Planetary Science Letters* **303**, 143-152.

Kadik, A., Pineau, F., Litvin, Y., Jendrzejewski, N., Martinez, I. and Javoy, M. (2004) Formation of carbon and hydrogen species in magmas at low oxygen fugacity. *J. Petrol.* **45**, 1297-1310.

Kagoshima, T., Sano, Y., Takahata, N., Maruoka, T., Fischer, T.P. and Hattori, K. (2015) Sulphur geodynamic cycle. *Scientific Reports* **5**, 8330.

Kawai, N. and Endo, S. (1970) The generation of ultrahigh hydrostatic pressures by a split sphere apparatus. *Review of Scientific Instruments* **41**, 1178-1181.

Kelemen, P.B. and Manning, C.E. (2015) Reevaluating carbon fluxes in subduction zones, what goes donw, mostly comes up. *Proceedings of the National Academy of Sciences* **112**, E3997-E4006.

Keppler, H., Wiedenbeck, M. and Shcheka, S.S. (2003) Carbon solubility in olivine and the mode of carbon storage in the Earth's mantle. *Nature* **424**, 414-416.

Kim, E.J., Fei, Y. and Lee, S.K. (2016) Probing carbon-bearing species and CO_2 inclusions in amorphous carbon-$MgSiO_3$ enstatite reaction products at 1.5 GPa: Insights from ^{13}C high-resolution solid-state NMR. *American Mineralogist* **101**, 1113-1124.

Kim, E.J., Fei, Y. and Lee, S.K. (2018) Effect of pressure on the short-range structure and speciation of carbon in alkali silicate and aluminosilicate glasses and melts at high pressure up to 8 GPa: ^{13}C, ^{27}Al, ^{17}O and ^{29}Si solid-state NMR study. *Geochimica et Cosmochimica Acta* **224**, 327-343.

Kim, E.J. and Lee, S.K. (2018) Pressure-load calibration of multi-anvil press and the thermal gradient within the sample chamber. *Journal of Mineralogical Society of Korea* **31**, 161-172.

King, P.L. and Holloway, J.R. (2002) CO_2 solubility and speciation in intermediate (andesitic) melts: the role of H_2O and composition. *Geochimica et Cosmochimica Acta* **66**, 1627-1640.

Knight, D.S. and White, W.B. (1989) Characterization of diamond films by Raman spectroscopy. *Journal of Materials Research* **4**, 385-393.

Kohn, S.C., Brooker, R.A. and Dupree, R. (1991) ^{13}C MAS NMR - A method for studying CO_2 speciation in glasses. *Geochimica et Cosmochimica Acta* **55**, 3879-3884.

Kono, Y., Kenney-Benson, C., Hummer, D., Ohfuji, H., Park, C., Shen, G., Wang, Y., Kavner, A. and Manning, C.E. (2014) Ultralow viscosity of carbonate melts at high pressures. *Nature Communication* **5**.

Kunimoto, T., Irifune, T. and Sumiya, H. (2008) Pressure generation in a 6-8-2 type multi-anvil system: a performance test for third-stage anvils with various diamonds. *High Pressure Research* **28**, 237-244.

Kuzmany, H., Pfeiffer, R., Salk, N. and Günther, B. (2004) The mystery of the 1140 cm^{-1} Raman line in nanocrystalline diamond films. *Carbon* **42**, 911-917.

Lee, H., Muirhead, J.D., Fischer, T.P., Ebinger, C.J., Kattenhorn, S.A., Sharp, Z.D. and Kianji, G. (2016) Massive and prolonged deep carbon emissions associated with continental rifting. *Nature Geoscience* **9**, 145-149.

Lee, S.K. (2004) Structure of silicate glasses and melts at high pressure: Quantum chemical calculations and solid-state NMR. *The journal of Physical Chemistry B* **108**, 5889-5900.

Lee, S.K. (2005) Microscopic origins of macroscopic properties of silicate melts and glasses at ambient and high pressure: Implications for melt generation and dynamics. *Geochimica et Cosmochimica Acta* **69**, 3695-3710.

Lee, S.K. (2010) Effect of pressure on structure of oxide glasses at high pressure: Insights from solid-state NMR of quadrupolar nuclides. *Solid State Nuclear Magnetic Resonance* **38**, 45-57.

Lee, S.K. (2011) Simplicity in melt densification in multicomponent magmatic reservoris in Earth's interior revealed by multinuclear magnetic resonance. *Proceedings of the National Academy of Sciences of the United States of America* **108**, 6847-6852.

Lee, S.K., Cody, G.D., Fei, Y.W. and Mysen, B.O. (2004) Nature of polymerization and properties of silicate melts and glasses at high pressure. *Geochimica et Cosmochimica Acta* **68**, 4189-4200.

Lee, S.K., Cody, G.D., Fei, Y.W. and Mysen, B.O. (2008a) Oxygen-17 nuclear magnetic resonance study of the structure of mixed cation calcium-sodium silicate glasses at high pressure: Implications for molecular link to element partitioning between silicate liquids and crystals. *Journal of Physical Chemistry B* **112**, 11756-11761.

Lee, S.K., Fei, Y.W., Cody, G.D. and Mysen, B.O. (2003) Order and disorder in sodium silicate glasses and melts at 10 GPa. *Geophysical Research Letters* **30**.

Lee, S.K., et al. (2008b) X-ray Raman scattering study of $MgSiO_3$ glass at high pressure: Implication for triclustered $MgSiO_3$ melt in Earth's mantle. *Proceedings of the National Academy of Sciences* **105**, 7925-7929.

Leinenweber, K.D., Tyburczy, J.A., Sharp, T.G., Soignard, E., Diedrich, T., Petuskey, W.B., Wang, Y. and Mosenfelder, J.L. (2012) Cell assemblies for reproducible multi-anvil experiments (the COMPRES assemblies). *American Mineralogist* **97**, 353-368.

Liebermann, R.C. (2011) Multi-anvil, high pressure apparatus: a half-century of development and progress. *High Pressure Research* **31**, 493-532.

Lopez-Rios, T., Sandre, E., Leclercq, S. and Sauvain, E. (1996) Polyacetylene in diamond filmds evidenced by surface enhanced Raman scattering. *Phys. Rev. Lett.* **76**, 4935-4938.

Luth, R.W. (2003) Mantle volatiles--Distribution and consequences, In *Treatise on Geochemistry*, (Eds. Heinrich, D.H., Karl, K.T.). Pergamon, Oxford, pp. 319-361.

Mann, U. and Schmidt, M.W. (2015) Melting of pelitic sediments at subarc depths: 1. Flux vs. fluid-absent melting and a parameterization of melt productivity. *Chemical Geology* **404**, 150-167.

Morizet, Y., Brooker, R.A. and Kohn, S.C. (2002) CO_2 in haplo-phonolite melt: solubility, speciation and carbonate complexation. *Geochimica et Cosmochimica Acta* **66**, 1809-1820.

Morizet, Y., Florian, P., Paris, M. and Gaillard, F. (2017) ^{17}O NMR evidence of free ionic clusters $M^{n+}CO_3^{2-}$ in silicate glasses: Precursors for carbonate-silicate liquids immiscibility. *American Mineralogist* **102**, 1561-1564.

Morizet, Y., Paris, M., Gaillard, F. and Scaillet, B. (2009) Raman quantification factor calibration for CO-CO_2 gas mixture in synthetic fluid inclusions: Application to oxygen fugacity calculation in magmatic systems. *Chemical Geology* **264**, 58-70.

Morizet, Y., Paris, M., Gaillard, F. and Scaillet, B. (2010) C-O-H fluid solubility in haplobasalt under reducing conditions: An experimental study. *Chemical Geology* **279**, 1-16.

Moussallam, Y., et al. (2016) The molecular structure of melts along the carbonatite–kimberlite–basalt compositional joint: CO_2 and polymerisation. *Earth and Planetary Science Letters* **434**, 129-140.

Mposkos, E.D. and Kostopoulos, D.K. (2001) Diamond, former coesite and supersilicic garnet in metasedimentary rocks from the Greek Rhodope: a new ultrahigh-pressure metamorphic province established. *Earth and Planetary Science Letters* **192**, 497-506.

Murakami, M. and Bass, J.D. (2011) Evidence of denser MgSiO3 glass above 133 gigapascal (GPa) and implications for remnants of ultradense silicate melt from a deep magma ocean. *Proceedings of the National Academy of Sciences* **108**, 17284-17289.

Mysen, B. (2013) Structure–property relationships of COHN-saturated silicate melt coexisting with COHN fluid: A review of in-situ, high-temperature, high-pressure experiments. *Chemical Geology* **346**, 113-124.

Mysen, B. (2017) Experimental, in-situ carbon solution mechanisms and isotope fractionation in and between (C–O–H)-saturated silicate melt and silicate-saturated (C–O–H) fluid to upper mantle temperatures and pressures. *Earth and Planetary Science Letters* **459**, 352-361.

Mysen, B. (2018) Mass transfer in the Earth's interior: fluid-melt interaction in aluminosilicate–C–O–H–N systems at high pressure and temperature under oxidizing conditions. *Progress in Earth and Planetary Science* **5**.

Mysen, B.O. (2012) Silicate-COH melt and fluid structure, their physicochemical properties, and partitioning of nominally refractory oxides between melts and fluids. *Lithos* **148**, 228-246.

Mysen, B.O., Arculus, R.J. and Eggler, D.H. (1975) Solubility of carbon-dioxide in melts of andesite, tholeiite, and olivine nephelinite composition to 30 kbar pressure. *Contributions to Mineralogy and Petrology* **53**, 227-239.

Mysen, B.O., Fogel, M.L., Morrill, P.L. and Cody, G.D. (2009) Solution behavior of reduced C-O-H volatiles in silicate melts at high pressure and temperature. *Geochimica et Cosmochimica Acta* **73**, 1696-1710.

Mysen, B.O., Kumamoto, K., Cody, G.D. and Fogel, M.L. (2011) Solubility and solution mechanisms of C–O–H volatiles in silicate melt with variable redox conditions and melt composition at upper mantle temperatures and pressures. *Geochimica et Cosmochimica Acta* **75**, 6183-6199.

Mysen, B.O. and Richet, P. (2005a) Silicate Glasses and Melts, Properties and Structure. Elsevier, Amsterdam.

Mysen, B.O. and Richet, P. (2005b) Volatiles I. The system C-O-H-S, In *Silicate Glasses and Melts*. Elsevier.

Ni, H.W. and Keppler, H. (2013) Carbon in silicate melts, In *Reviews in Mineralogy and Geochemistry*, (Eds. Hazen, R.M., Jones, A.P., Baross, J.A.). Mineralogical Society of America, Virginia, pp. 251-287.

Nicholis, M.G. and Rutherford, M.J. (2009) Graphite oxidation in the Apollo 17 orange glass magma: Implications for the generation of a lunar volcanic gas phase. *Geochimica et Cosmochimica Acta* **73**, 5905-5917.

Nowak, M., Porbatzki, D., Spickenbom, K. and Diedrich, O. (2003) Carbon dioxide speciation in silicate melts: a restart. *Earth and Planetary Science Letters* **207**, 131-139.

Nowak, M., Schreen, D. and Spickenbom, K. (2004) Argon and CO_2 on the race track in silicate melts: A tool for the development of a CO,

speciation and diffusion model. *Geochimica et Cosmochimica Acta* **68**, 5127-5138.

Pan, V., Holloway, J.R. and Hervig, R.L. (1991) The pressure and temperature dependence of carbon dioxide solubility in tholeiitic basalt melts. *Geochimica et Cosmochimica Acta* **55**, 1587-1595.

Papenguth, H.W., Kirkpatrick, R.J., Montez, B. and Sandberg, P.A. (1989) ^{13}C MAS NMR spectroscopy of inorganic and biogenic carbonates. *American Mineralogist* **74**, 1152-1158.

Park, S.Y. and Lee, S.K. (2012) Structure and disorder in basaltic glasses and melts: Insights from high-resolution solid-state NMR study of glasses in diopside–Ca-tschermakite join and diopside–anorthite eutectic composition. *Geochimica et Cosmochimica Acta* **80**, 125-142.

Park, S.Y. and Lee, S.K. (2016) Effects of difference in ionic radii on chemical ordering in mixed-cation silicate glasses: Insights from solid-state ^{17}O and ^{7}Li NMR of Li-Ba silicate glasses. *Journal of the American Ceramic Society*.

Pawley, A.R., Holloway, J.R. and McMillan, P.F. (1992) The effect of oxygen fugacity on the solubility of carbon oxygen fluids in basaltic melt. *Earth and Planetary Science Letters* **110**, 213-225.

Poe, B.T., McMillan, P.F., Rubie, D.C., Chakraborty, S., Yarger, J. and Diefenbacher, J. (1997) Silicon and oxygen self-diffusivities in silicate liquids measured to 15 gigapascals and 2800 kelvin. *Science* **276**, 1245-1248.

Reich, S. and Thomsen, C. (2004) Raman spectroscopy of graphite. *Philosophical Transactions of the Royal Society of London. Series A: Mathematical, Physical and Engineering Sciences* **362**, 2271-2288.

Revenaugh, J. and Sipkin, S.A. (1994) Seismic evidence for silicate melts atop the 410-km mantle discontinuity. *Nature* **369**, 474-476.

Rosso, K.M. and Bodnar, R.J. (1995) Microthermometric and Raman spectroscopic detection limits of CO_2 in fluid inclusions and the Raman spectroscopic characterization of CO_2. *Geochimica et Cosmochimica Acta* **59**, 3961-3975.

Ruhl, M. and Kürschner, W.M. (2011) Multiple phases of carbon cycle disturbance from large igneous province formation at the Triassic-Jurassic transition. *Geology* **39**, 431-434.

Ruhl, M., Kürschner, W.M. and Krystyn, L. (2009) Triassic–Jurassic organic carbon isotope stratigraphy of key sections in the western Tethys realm (Austria). *Earth and Planetary Science Letters* **281**, 169-187.

Saal, A.E., Hauri, E.H., Langmuir, C.H. and Perfit, M.R. (2002) Vapour undersaturation in primitive mid-ocean-ridge basalt and the volatile content of Earth's upper mantle. *Nature* **419**, 451-455.

Sandler, J., Shaffer, M.S.P., Windle, A.H., Halsall, M.P., Montes-Morán, M.A., Cooper, C.A. and Young, R.J. (2003) Variations in the Raman peak shift as a function of hydrostatic pressure for various carbon nanostructures: A simple geometric effect. *Physical Review B* **67**, 035417.

Sansone, F.J., Mottl, M.J., Olson, E.J., Wheat, C.G. and Lilley, M.D. (1998) CO_2-depleted fluids from mid-ocean ridge-flank hydrothermal springs. *Geochimica et Cosmochimica Acta* **62**, 2247-2252.

Sarda, P. and Guillot, B. (2005) Breaking of Henry's law for noble gas and CO_2 solubility in silicate melt under pressure. *Nature* **436**, 95-98.

Schwarz, M.R. (2010) Multianvil calibration and education: A four probe method to measure the entire force-versus-pressure curve in a single run - performed as an interdisciplinary lab-course for students. *Journal of Physics: Conference Series* **215**, 012193.

Seitz, J.C., Pasteris, J.D. and Chou, I. (1996) Raman spectrscopic characterization of gas mixtures. II quantitative composition and

pressure determination of the CO_2-CH_4 system. *American Journal of Science* **296**, 577-600.

Sen, S., Widgeon, S.J., Navrotsky, A., Mera, G., Tavakoli, A., Ionescu, E. and Riedel, R. (2013) Carbon substitution for oxygen in silicates in planetary interiors. *Proceedings of the National Academy of Sciences* **110**, 15904-15907.

Shatskiy, A., Katsura, T., Litasov, K.D., Shcherbakova, A.V., Borzdov, Y.M., Yamazaki, D., Yoneda, A., Ohtani, E. and Ito, E. (2011) High pressure generation using scaled-up Kawai-cell. *Physics of the Earth and Planetary Interiors* **189**, 92-108.

Shcheka, S.S., Wiedenbeck, M., Frost, D.J. and Keppler, H. (2006) Carbon solubility in mantle minerals. *Earth and Planetary Science Letters* **245**, 730-742.

Song, T.-R.A., Helmberger, D.V. and Grand, S.P. (2004) Low-velocity zone atop the 410-km seismic discontinuity in the northwestern United States. *Nature* **427**, 530-533.

Stagno, V., Ojwang, D.O., McCammon, C.A. and Frost, D.J. (2013) The oxidation state of the mantle and the extraction of carbon from Earth's interior. *Nature* **493**, 84-88.

Stanley, B.D., Schaub, D.R. and Hirschmann, M.M. (2012) CO_2 solubility in primitive martian basalts similar to Yamato 980459, the effect of composition on CO_2 solubility of basalts, and the evolution of the martian atmosphere. *American Mineralogist* **97**, 1841-1848.

Stebbins, J.F. (1995) Dynamics and structure of silicate and oxide melts: Nuclear magnetic resonance studies, In *Structure, Dynamics, and Properties of Silicate Melts*, (Eds. Stebbins, J.F., McMillan, P.F., Dingwell, D.B.). Mineralogical Society of America, Wasington, DC, pp. 191-246.

Stebbins, J.F. (2016) Glass structure, melt structure, and dynamics: Some concepts for petrology. *American Mineralogist* **101**, 753-768.

Stebbins, J.F. and Xu, Z. (1997) NMR evidence for excess non-bridging oxygen in an aluminosilicate glass. *Nature* **390**, 60.

Stolper, E., Fine, G., Johnson, T. and Newman, S. (1987) Solubility of carbon dioxide in albitic melt. *American Mineralogist* **72**, 1071-1085.

Suzuki, A. (2018) Effect of carbon dioxide on the viscosity of a melt of jadeite composition at high pressure. *Journal of Mineralogical and Petrological Sciences*.

Suzuki, A., Ohtani, E., Terasaki, H., Nishida, K., Hayashi, H., Sakamaki, T., Shibazaki, Y. and Kikegawa, T. (2011) Pressure and temperature dependence of the viscosity of a $NaAlSi_2O_6$ melt. *Physics and Chemistry of Minerals* **38**, 59-64.

Sverjensky, D.A., Stagno, V. and Huang, F. (2014) Important role for organic carbon in subduction-zone fluids in the deep carbon cycle. *Nature Geoscience* **7**, 909-913.

Tingle, T.N. and Aines, R.D. (1988) Beta track autoradiography and infrared spectroscopy bearing on the solubility of CO_2 in albite melt at 2 GPa and 1450 C.

Tossell, J.A. (1995) Calculation of the C-13 NMR shieldings of the CO_2 complexes of aluminosilicates. *Geochimica et Cosmochimica Acta* **59**, 1299-1305.

Vidano, R. and Fischbach, D.B. (1978) New lines in the Raman spectra of carbons and graphite. *Journal of the American Ceramic Society* **61**, 13-17.

Vuilleumier, R., Seitsonen, A.P., Sator, N. and Guillot, B. (2015) Carbon dioxide in silicate melts at upper mantle conditions: Insights from atomistic simulations. *Chemical Geology* **418**, 77-88.

Walker, D., Carpenter, M.A. and Hitch, C.M. (1990) Some simplifications to multianvil devices for high pressure experiments. *American Mineralogist* **75**, 1020-1028.

Wallace, P.J. (2005) Volatiles in subduction zone magmas: concentrations and fluxes based on melt inclusion and volcanic gas data. *Journal of Volcanology and Geothermal Research* **140**, 217-240.

White, B.S. and Montana, A. (1990) The effect of H_2O and CO_2 on the viscosity of sanidine liquid at high pressures. *J. Geophys. Res.-Solid Earth* **95**, 15683-15693.

Wolf, G. and McMillan, P. (1995) Pressure effects on silicate melt structure and properties. *Reviews in Mineralogy and Geochemistry* **32**, 505-561.

Xue, X., Kanzaki, M., Floury, P., Tobase, T. and Eguchi, J. (2018) Carbonate speciation in depolymerized and polymerized (alumino)silicate glasses: Constraints from 13 C MAS and static NMR measurements and ab initio calculations. *Chemical Geology* **479**, 151-165.

Xue, X.Y., Stebbins, J.F., Kanzaki, M., McMillan, P.F. and Poe, B. (1991) Pressure-induced silicon coordination and tetrahedral structural-changes in alkali oxide-silica melts up to 12 GPa - NMR, Raman, and infrared-spectroscopy. *American Mineralogist* **76**, 8-26.

Yamazaki, D., et al. (2018) High-pressure generation in the Kawai-type multianvil apparatus equipped with tungsten-carbide anvils and sintered-diamond anvils, and X-ray observation on $CaSnO_3$ and $(Mg,Fe)SiO_3$. *Comptes Rendus Geoscience*.

Yoneda, A., Yamamoto, S., Kato, M., Sawamoto, H. and Kumazawa, M. (1984) The use of composite metal gaskets to improve pressure generation in multiple anvil devices. *High Temperature-High Pressures* **16**, 637-656.

Zhang, Y. and Zindler, A. (1993) Distribution and evolution of carbon and nitrogen in Earth. *Earth and Planetary Science Letters* **117**, 331-345.

Chapter 2. Probing carbon-bearing species and CO_2 inclusion in amorphous carbon-$MgSiO_3$ enstatite reaction products at 1.5 GPa: Insights from ^{13}C high-resolution solid-state NMR

Eun Jeong Kim, Yingwei Fei, and Sung Keun Lee

Published in *American Mineralogist*, 2016, v. 101, 1113-1124

Some parts of this study include my previous thesis of Master of Science (M. Sc.), and therefore the part overlapped with M. Sc. was not included here. This study was published in American Mineralogist in 2016.

Abstract

Understanding the carbon speciation in earth materials is important to unravel the geochemical evolution of the earth's atmosphere, composition of partial melts, and overall distribution of carbon in the deep mantle. In an effort to provide the systematic protocols to characterize carbon-bearing fluid inclusions and other carbon-bearing species using high-resolution ^{13}C solid-state NMR, one of the element specific probe of local structure around carbon, we explore the atomic configurations around the carbon species formed during the reaction between ^{13}C-enriched amorphous carbon and $MgSiO_3$ enstatite synthesized at 1.5 GPa and 1400 °C using ^{13}C MAS NMR spectroscopy and Raman spectroscopy. The Raman spectra for the fluid inclusion show the presence of multiple molecular species (e.g., CO_2, CO, CH_4, H_2O, and H_2) and reveal heterogeneous

distribution of these species within the inclusion. ^{13}C MAS NMR results show that the sharp peak at 125.2 ppm is dominant. While the peak could be assigned to either molecular CO_2 in the fluid phase or four-coordinated carbon ($^{[4]}C$), the peak is likely due to fluid CO_2, as revealed by Raman analyses of μm-size fluid inclusions in the sample. The peaks at 161.2, 170.9, and 173.3 ppm in the ^{13}C NMR spectrum correspond to the carbonate ions (CO_3^{2-}) and additional small peak at 184.5 ppm can be attributed to carbon monoxide. Based on the established relationship between ^{13}C abundance and peak intensity in the ^{13}C MAS NMR, the estimated ^{13}C amounts of CO_2, CO_3^{2-}, and CO species are much larger than those estimated from carbon solubility in the crystals, thus, indicating that those carbon species are from external phases. The ^{13}C NMR spectrum for amorphous carbon showed a peak shift from ~ 130 ppm to ~ 95 ppm after compression, thereby suggesting that the amorphous carbon underwent permanent pressure-induced densification, characterized by the transition from sp^2 to sp^3 hybridization and/or pressure-induced changes in sp^2 carbon topology. While direct probing of carbon species in the crystalline lattice using NMR is challenging, the current results and method can be utilized to provide quantitative analysis of carbon-species in the fluid-inclusions in silicates, which is essential for understanding the deep carbon cycle and volcanic processes.

2.1. Introduction

Understanding the carbon speciation in earth materials is important to unravel the geochemical evolution of the earth's atmosphere, composition of partial melts, and overall distribution of carbon in the deep

mantle (Blank and Brooker, 1994; Green, 1972; Keppler et al., 2003; Richet and Bottinga, 1984; Shcheka et al., 2006; Zhang and Zindler, 1993). The properties of carbon-bearing crystalline silicates and their precursor liquids are also influenced by the amount of CO_2 present in these phases (Eggler and Kadik, 1979; Eggler and Rosenhauer, 1978). As the carbon-retention capacity of silicate melts and crystals depends heavily on pressure, decompression processes accompanied by eruption and upwelling of earth materials lead to the formation of exsolved CO_2 inclusions (Blundy et al., 2010; Eggler and Kadik, 1979; Lloyd et al., 2014; Parfitt and Wilson, 2008; Sides et al., 2014; Wallace, 2005).

H_2O and CO_2 are the most abundant volatile components in the Earth's interior. Additional species such as CH_4, H_2, and CO can be formed depending on total bulk chemistry of inclusion, f_{O2} condition, as well as temperature and pressure (e.g., Morizet et al., 2010; Mysen and Richet, 2005; Pawley et al., 1992). While the CO_2 inclusions are not included in an estimate of carbon solubility into silicate crystals and melts, they can contribute to the total bulk carbon contents of magma chambers, thereby affecting their buoyancy and rising speed (Blundy et al., 2010; Burton et al., 2013; Dixon and Clague, 2001; Gerlach et al., 2002; Kaminski and Jaupart, 1997; Lloyd et al., 2014; Parfitt and Wilson, 2008; Rust and Cashman, 2011; Sugioka and Bursik, 1995). For example, the exsolved CO_2 in Kilauea magma was estimated to be ~ 0.61 wt%, which is approximately 87% of the total CO_2 emitted from the volcanic eruption, while that of dissolved (and thus structurally-bound) CO_2 is ~ 0.09 wt% (Gerlach et al., 2002), indicating that the exsolved CO_2 in the glasses is among the important carbon reservoirs.

Together with CO_2 inclusions in the glasses, carbon species in crystalline silicates has been proposed as an additional carbon reservoir in the deep Earth (Green, 1972). Spectroscopic studies of vibrational density of states of species in fluid inclusion have provided useful information on the temperature-pressure conditions of the formation of the inclusion (Rosso and Bodnar, 1995; Seitz et al., 1996). In addition to the dissolved molecular CO_2 inclusions in the silicate crystals, neutral carbon may dissolve into the interstitial site in the crystal and/or dissolve into cation vacancies (Freund, 1981). Additionally, direct substitution of Si^{4+} with C^{4+} or with O^{2-} has also been suggested (Fyfe, 1970; Sen et al., 2013). However, revealing the mechanistic details of carbon incorporation into the crystalline silicates is challenging (Keppler et al., 2003; Shcheka et al., 2006).

Extensive previous studies using spectroscopic techniques such as Raman spectroscopy, Fourier-transform infrared spectroscopy (FTIR), as well as nuclear magnetic resonance spectroscopy (NMR) have revealed the speciation of carbon in silicate glasses (Blank et al., 1993; Brooker et al., 1999; Fine and Stolper, 1985; Kadik et al., 2004; Kohn et al., 1991; Morizet et al., 2002; Morizet et al., 2009, 2010; Mysen, 2013; Mysen et al., 1975; Pawley et al., 1992; Richet and Bottinga, 1984; Stolper et al., 1987). While the Raman and FTIR techniques provide information on the collective vibration, solid-state NMR yields detailed, element-specific, and quantitative information on the environment of nuclides of interest in the diverse crystalline and non-crystalline earth materials (e.g., Cody and Alexander, 2005; Cody et al., 2011; Feng et al., 2006; Kirkpatrick and Brow, 1995; Kirkpatrick et al., 1986; Lee, 2010; Papenguth et al., 1989; Phillips et al., 2000; Stebbins, 1995; Stebbins and Xue, 2014; Tangeman et al., 2001). Particularly, ^{13}C solid-state

NMR has been used to determine the carbon speciation in synthetic silicate glasses with varying pressure and composition [e.g., Na-binary silicate glasses, Mg-binary silicate glasses, and CaO-MgO-Al_2O_3-SiO_2 (CMAS) silicate glasses, etc.] (Brooker et al., 1999; Jones et al., 2005; Kohn et al., 1991; Kwak et al., 2010; Morizet et al., 2002; Morizet et al., 2010). In contrast, the speciation of carbon in crystalline silicates has not been fully explored with the ^{13}C solid-state NMR techniques because carbon solubility into the crystals is often much lower than that into glasses and melts and NMR is one of the insensitive spectroscopic techniques. Additionally, the natural abundance of ^{13}C is only 1.1%, and the ^{13}C isotope enrichment is necessary. To the best of our knowledge, there is only a single ^{13}C NMR study of the carbon species in crystalline oxides (anatase TiO_2) where the sharp peak at 126 ppm was observed. On the basis of the usual peak position of orthocarbonate species in organic solids (121.0 ppm) (Pretsch et al., 2009), the peak was assigned to four-coordinated carbon ($^{[4]}C$) (Rockafellow et al., 2009). However, the 126 ppm peak could also be due to the exsolved CO_2 species in the oxides (Herzfeld and Berger, 1980; Kohn et al., 1991). Despite the difficulty, ^{13}C NMR can provide unique structural information around carbon species that is not accessible with other spectroscopic probes. For instance, the spinning sidebands patterns can be used to indicate whether CO_2 is structurally-incorporated or exsolved in silicate networks: CO_2 molecule in the inclusion may not show spinning sidebands while structurally-bound CO_2 can lead to the formation of spinning sideband patterns due to its large ^{13}C chemical shift anisotropy (Herzfeld and Berger, 1980; Kohn et al., 1991).

Because the solubility of carbon into crystalline lattice is rather low (~

0.1–5 ppm) and the amount carbon in fluid inclusion is also limited, direct probing of carbon species using NMR is challenging. While it is also currently difficult to detect the carbon signal, it would be useful to establish experimental protocols to further distinguish whether the observed NMR peaks are due to carbon species in the crystalline network or from the external phases (e.g., fluid inclusion, grain boundary etc.). Although solid-state NMR is not among the most sensitive spectroscopic techniques, we have made recent progress in probing (and detecting) dilute amount of nuclear spins in the earth materials under the extreme conditions (high pressure) using NMR (Lee, 2010, 2011; Lee et al., 2004; Lee et al., 2012). Furthermore, progress has been made to detect dilute nuclear spins in 2-dimensionally confined, 5 nm amorphous *thin* film (Lee and Ahn, 2014; Lee et al., 2009; Lee et al., 2010). These recent experimental achievements shed light on an opportunity to explore the dilute spins (such as ^{13}C in the inclusion and in the crystal) using high-resolution solid-state NMR. As few attempts to detect carbon species in the fluid inclusion or crystalline silicates have been reported, experimental verification of these species with practical detection limit for ^{13}C has been anticipated.

$MgSiO_3$ is the most abundant mineral composition in the mantle, which is likely to be the earth's largest carbon reservoir (Jambon, 1994; Shcheka et al., 2006). Enstatite is one of the $MgSiO_3$ phases stable in the crust and upper mantle. Here, we explore the atomic configuration around the carbon species formed during the reaction between ^{13}C amorphous carbon and enstatite synthesized at 1.5 GPa and 1400 °C using ^{13}C MAS NMR spectroscopy in order to test the utility of NMR technique to probe the carbon-bearing species in the reaction product and fluid inclusions. The

study also aims to provide the systematic protocols to characterize carbon-bearing fluid inclusion using high-resolution ^{13}C solid-state NMR. We also report the pressure-induced structural changes in the amorphous carbon that was used as a ^{13}C-enriched carbon reservoir in the high-pressure experiments. While the potential result can be helpful to provide comprehensive atomistic insights into the deep carbon cycle in the Earth's mantle, we also discuss the advantages and limitations of the NMR based strategy to detect 0.1–10 ppm of dissolved ^{13}C in crystalline silicates.

2.2. Experimental & computational methods

2.2.1. Sample preparation

The carbon-bearing enstatite samples for the spectroscopic analyses were synthesized by mixing $MgSiO_3$ (initially synthesized at 1.5 GPa) and ^{13}C-enriched amorphous carbon at 1.5 GPa. The starting $MgSiO_3$ enstatite was synthesized from a mixture of powdered SiO_2 and MgO in a Pt capsule using piston-cylinder apparatus with a 0.5" assembly at the Geophysical Laboratory, Carnegie Institution of Washington. The synthesis experiment was performed at 1400 °C and 1.5 GPa for 48 h. Subsequently, the enstatite was mixed with 2.4 wt% of ^{13}C-enriched (~ 99.7% enriched) amorphous carbon and H_2O, and then loaded in a Pt capsule. H_2O was added to promote the overall reaction and control the oxygen fugacity of the system [estimated oxygen fugacity was similar to that of C-CO (CCO) buffer (with estimated f_{O2} value of ~ -7.5), (Zhang and Duan, 2010). See section 2.3.1 for details]. We then ran the experiments at 1.5 GPa and 1400 °C for 48 h to produce carbon-bearing enstatite. We have synthesized two distinct batches of samples under the same P-T conditions to check reproducibility of the

carbon speciation in the synthesized samples. The formation of gas phases was observed when the capsule was opened after the experiments. This could be due to excess gas phases such as H_2O, CO_2 or CH_4 (Mysen et al., 2009; Zhang and Duan, 2010). The resulting products included clear carbon-bearing enstatite and black aggregated amorphous carbon (used as initial carbon source). The latter, referred as compressed amorphous carbon, was handpicked and separated from the enstatite. The decrepitation experiment was performed to identify the stability of the observed carbon species and CO_2 inclusion in the sample: the synthesized $MgSiO_3$ grain [~ 80 μm (w) × 100 μm (h)] with CO_2 inclusions were heated at 750 °C for 10 min in a tube furnace as previous experimental studies often showed that the fluid inclusion in the crystal is not stable above 750 °C (Bodnar et al., 1989).

2.2.2. Raman spectroscopy

The Raman spectra for the carbon-bearing enstatite were collected on a micro Raman spectrometer at Seoul National University. Thin-sections for Raman analysis were made by fixing the enstatite particles in an epoxy resin. The enstatite crystals were polished using 1500 mesh diamond powder (8–10 μm) for 3 h and subsequently using 1 μm diamond paste for 1 h. The spectra were collected under the following conditions: laser wavelength of 488 nm, exposure time of 10 s, and number of accumulations being 60 with grating groove density of 1800/500 L/mm. The spectral resolution is ~ 0.55–0.85 cm^{-1}/pixel and the spectrometer slit width is 250 μm. Typical spectral width is ~ 840 cm^{-1} (centered at 1400 cm^{-1}) and ~ 780 cm^{-1} (centered at 2250 cm^{-1}), respectively. Beam diameter of 3.1 μm (using 50× microscope objectives), laser power of 32.8 mW, and beam scattering of

1 mrad were used. An estimated reproducibility in recorded peak positions of the current spectra is less than ± 0.5 cm^{-1}.

2.2.3. NMR spectroscopy

The ^{13}C MAS NMR spectra were collected on a Varian 400 MHz solid-state NMR spectrometer (9.4 T, Seoul National University) at a Larmor frequency of 100.582 MHz for ^{13}C using a 3.2 mm zirconia rotor in a Varian double-resonance probe. It may require longer relaxation delays to obtain the fully relaxed spectrum for the carbon-bearing enstatite. We therefore performed ^{13}C MAS NMR experiments with varying relaxation delay times. The results showed negligible effect on the different relaxations of carbon peaks. Therefore, the recycle delay of 5 s was used to reduce the total NMR collection time. The magic-angle sample spinning speed of 14 kHz was employed. The current signal-to-noise ratio in the spectra was achieved by averaging nearly 86400 scans (~ 5 days). The spectra were referenced to solid-state adamantane (ADM, $C_{10}H_{16}$), whose resonance of left peak was located at 38.56 ppm relative to the more common reference, tetramethylsilane (TMS). Approximately 20 mg of carbon-bearing $MgSiO_3$, 1.7 mg of ^{13}C-enriched uncompressed amorphous carbon, and 3.2 mg of ^{13}C-enriched compressed amorphous carbon were used in the ^{13}C MAS NMR experiments. The background signals were collected under identical measurement conditions using an empty zirconia rotor. The background spectrum was subsequently subtracted from the ^{13}C MAS NMR spectrum for each sample to yield the NMR spectrum free from any background carbon signals.

^{13}C NMR spin-counting experiment was performed using mixtures of ADM and SiO_2 (Sigma-Aldrich product no. 204358). We collected ^{13}C MAS NMR spectra for the mixtures with varying ADM/SiO_2 ratio [X_{ADM} = 1/4 (25 wt%, 2750 ppm of ^{13}C), 1/8 (12.5 wt%, 1375 ppm of ^{13}C), 1/16 (6.25 wt%, 688 ppm of ^{13}C), 1/50 (2.0 wt%, 220 ppm of ^{13}C), 1/233 (0.43 wt%, 47 ppm of ^{13}C), 1/310 (0.32 wt%, 35 ppm of ^{13}C)]. The mixtures were ground in an agate mortar for 1 h. It is somewhat difficult to constrain the composition of the mixtures with low ADM concentration (e.g., the data for X_{ADM}=1/50, 1/233, and 1/310). This is due to uneven mixing between ADM and SiO_2 in the mortar stemming from the difference in surface adhesiveness of the ADM and SiO_2 particles. Therefore, in order to minimize the ADM loss upon mixing in the agate mortar (i.e., to yield better calibration curve), a designed amount of ADM was located at the center of the rotor and SiO_2 powder was placed both on top and bottom of the rotor. The NMR collection conditions for the mixtures were identical to those for carbon-bearing enstatite.

As elemental analysis does not provide robust measurement of the carbon content in SiO_2-ADM mixture used in the study primarily due to difference in volatilization between ADM and SiO_2, the quantitative carbon content of the mixture with low carbon concentration was constrained using the calibration curve (between NMR peak intensity and carbon content) based on the mixture with higher concentration (see section 2.4.3 below). The NMR experiment under proton decoupling was also performed to improve the quality of ^{13}C abundance and peak intensity calibration curve. Proton decoupling power was optimized using ADM standard. The spectra for the mixtures were collected at a decoupling power $\omega_1/2\pi$ of 33 kHz.

2.2.4. Quantum chemical calculations

Quantum chemical calculations of NMR chemical shift of $C(OH)_4$ clusters were performed using Gaussian 03 in order to get insights into the ^{13}C NMR chemical shielding for $^{[4]}C$ with varying C-O bond lengths (Frisch et al., 2004). A model $C(OH)_4$ cluster was optimized by varying the C-O bond lengths while maintaining the tetrahedral symmetry constraints at the Becke, three-parameters, Lee-Yang-Parr (B3LYP) level of theory with a 6-311+G(2d) basis set. The NMR chemical shielding calculations of the C atoms in $C(OH)_4$ cluster were calculated using the gauge-including atomic orbital (GIAO) method at the B3LYP level of theory with the 6-311G+(2d) and 6-31G(d) basis sets (Lee and Lee, 2009). The ^{13}C NMR chemical shift of the $C(OH)_4$ cluster was estimated by subtracting NMR chemical shielding of TMS (external reference used in the experiment) that was also calculated at the identical energy level of theory and basis sets.

2.3. Results

2.3.1. Probing of CO_2 in fluid inclusions in carbon-bearing enstatite: Insights from Raman spectroscopy

Figure 2.1 shows the optical micrograph image of the sample (Figure 2.1a, grain size of approximately 80 μm (w) × 100 μm (h)] and Raman spectrum for the observed fluid inclusion [4 μm (w) × 10 μm (h)] (Figure 2.1b, c, d). The Raman spectra for the fluid inclusion (Figure 2.1b) show the presence of multiple molecular species (e.g., CO_2, CO, CH_4, H_2O, and H_2) and reveal heterogeneous distribution of these species within the inclusion. The peaks at 1280 and 1380 cm^{-1} correspond to the symmetric stretching vibration (ν_1) and the overtone of the symmetric bending ($2\nu_2$) vibrations in

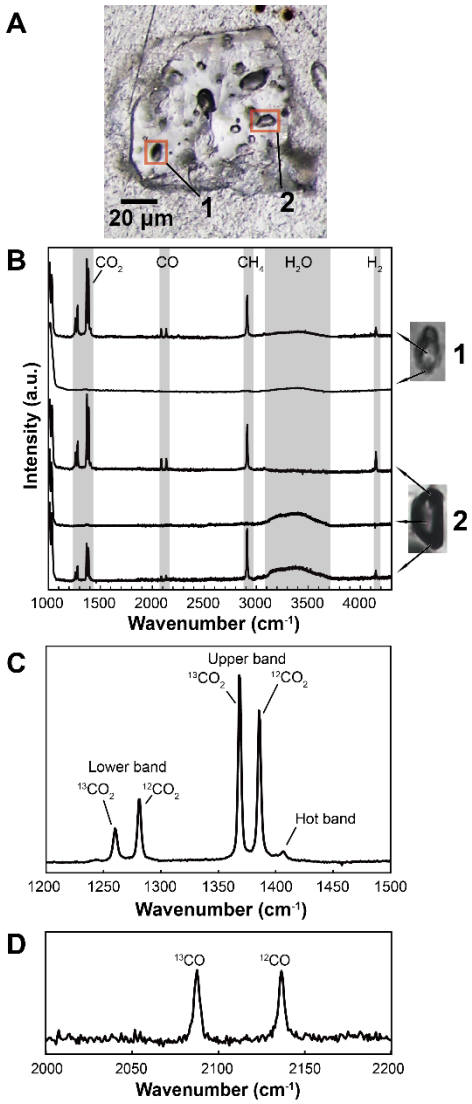

Figure 2.1. (A) A stereoscopic micrograph image of one of the grains of carbon-bearing enstatite. The size of the grain is 80 µm (w) × 100 µm (h) and the fluid inclusions are 4 µm (w) × 10 µm (h) (indicated with red rectangles). (B) Raman spectra for carbon-bearing enstatite in the frequency range of 1000–4300 cm^{-1} and (C) that in the range of 1200–1500 cm^{-1} and (D) 2000–2200 cm^{-1}.

CO_2 (Morizet et al., 2009), and those at 2100 cm^{-1} and 3000–3800 cm^{-1} are due to CO and H_2O (Morizet et al., 2009; Mysen et al., 2011), respectively. The peaks at 2912 and 4150 cm^{-1} originate from CH_4 and H_2, respectively (Mysen et al., 2009).

Figure 2.1c and d shows further details of characteristic of vibrational modes of CO_2 and CO, respectively. The two peaks at 1360 cm^{-1} and 1385 cm^{-1} in Figure 2.1c are characteristic of the overtone of the symmetric bending ($2\nu_2$) vibrations of $^{13}CO_2$ and $^{12}CO_2$ in the fluid inclusions while the two peaks at 1260 cm^{-1} and 1285 cm^{-1} correspond to the symmetric stretching (ν_1) vibrations of $^{13}CO_2$ and $^{12}CO_2$, respectively (Ni and Keppler, 2013). The peak at 1405 cm^{-1} represents the hot band vibration of the low-lying vibration of ν_2 at 667.38 cm^{-1} (Rosso and Bodnar, 1995). Figure 2.1d indicates the presence of minor but detectable ^{13}CO and ^{12}CO species in the fluid inclusion at 2090 cm^{-1} and 2140 cm^{-1}, respectively (Morizet et al., 2009). These Raman features for CO and CO_2 were not observed within the inclusion-free enstatite crystals. The coexistence of these fluid species can correspond to f_{O2} ranging from -7.14 to -10.88 (calculated using the GFluid code), similar to those with C-CO buffer (f_{O2} = ~ -7.5) (Zhang and Duan, 2010).

The internal pressure in the fluid inclusion have been estimated from the frequency difference in upper band and lower band of CO_2 (i.e., ν_1-$2\nu_2$) (Garrabos et al., 1989; Kobayashi et al., 2012; Rosso and Bodnar, 1995; Seitz et al., 1996; Wright and Wang, 1973). Alternatively, the peak position of ν_1 vibration of CH_4 at room temperature has also been utilized to obtain internal pressure (Lin et al., 2007; Seitz et al., 1996). As we have not collected the Raman spectrum for the inclusion with varying temperature, taking into

consideration sources of uncertainty and potential complications in the previous calibration curve, the difference in CO_2 bands (104.2–104.7 cm^{-1}) may not be directly used to provide robust pressure conditions in the current study. In order to estimate the internal pressure of the fluid inclusion from the CH_4 peak positions in the Raman spectrum, the exact composition of the inclusion needs to be known. As the chemical composition of the inclusion is currently not clear, a quantitative estimation of the internal pressure is not straightforward. Roughly, the current peak position of CH_4 (2911.5–2912.2 cm^{-1}) corresponds to the internal pressure of ~ 100–200 bar (e.g. if X_{CH4} = ~ 0.1 in CH_4–CO_2 mixture). Further detailed study with in-situ high-temperature Raman analyses is necessary for robust estimation of internal pressure.

While Raman spectroscopy may not be fully quantitative, previous extensive Raman studies of fluid inclusions in silicate glasses highlighted that quantitative estimation of carbon species concentration is indeed possible, once their respective peak intensity was calibrated with the Raman efficiency for each molecule established from the standard samples with controlled concentrations (Burke, 2001; Morizet et al., 2009). The method is not applied for the samples studied here due mainly to difficulties in establishing the Raman efficiency of the species with the spectrometer used in the current study (mostly due to lack of heating stage, standard samples with known concentrations of molecular species, and heterogeneous distribution of carbon-bearing species in the inclusion). Nevertheless, this earlier approach, combined with NMR, is potentially useful to provide quantitative information of fluid composition and species concentration.

2.3.2. Probing of carbon species and inclusion in carbon-bearing enstatite: ^{13}C MAS NMR results

Figure 2 in Kim et al. (2016) shows the ^{13}C MAS NMR spectrum for carbon-bearing enstatite. Because the ^{13}C MAS NMR spectrum of the empty rotor shows the presence of a detectable amount of carbon background signal from the rotor and stator ranging from 100–170 ppm (Figure 2 bottom, Kim et al., 2016), the background signal was subtracted from the collected spectrum (Figure 2 middle, Kim et al., 2016). The top spectrum in Figure 2 in Kim et al. (2016) shows the background-subtracted ^{13}C MAS NMR spectrum for the sample. The background-subtracted spectrum shows multiple sharp peaks at 184.5, 173.3, 170.9, 161.2, and 125.2 ppm, which can be attributed to the distinct carbon species in enstatite. The sharp peak at 125.2 ppm is prevalent. Based on the NMR chemical shift of the peak, it could be attributed to either molecular CO_2 in fluid phase, structurally bound CO_2 in silicate network, or $^{[4]}C$ (Herzfeld and Berger, 1980; Kohn et al., 1991; Rockafellow et al., 2009). While the origin of the peak at 125.2 ppm in carbon-bearing enstatite will be discussed, the peak is mostly due to molecular CO_2 on the basis of its narrow peak width with negligible spinning sideband intensity and insights from the quantum chemical calculations (see discussion sections 2.4.1 and 2.4.2 below for further details). This assignment is also consistent with the aforementioned Raman results (Figure 2.1).

The 161.2, 170.9, and 173.3 ppm peaks correspond to the carbonate ions (CO_3^{2-}) on the basis of previous studies of carbonate species in the silicate glasses (e.g., Brooker et al., 1999; Kohn et al., 1991; Mysen et al., 2011). Additionally, chemical shifts for carbonate minerals (e.g., calcite,

magnesite, vaterite, dolomite, lithium carbonate, sodium carbonates, and cerussite) also range from 166–171 ppm (Papenguth et al., 1989). Previous quantum simulations of ^{13}C NMR chemical shift in aluminosilicate glasses showed that the distortion of CO_3^{2-} cluster led to a decrease in the ^{13}C NMR chemical shift (Tossell, 1995), as also suggested from an earlier NMR study (Brooker et al., 1999). The simulations also indicated that highly distorted carbonate ions with C-O bond length of 1.265 Å, which was shorter than the average bond lengths of the carbonate minerals (1.285 Å), have smaller NMR chemical shift (Tossell, 1995). The additional small peak at 184.5 ppm observed in the spectrum (Figure 2, Kim et al., 2016) can be attributed to carbon monoxide (Kohn et al., 1991; Tossell, 1995). Figure 3 in Kim et al. (2016) also shows the ^{13}C MAS NMR spectra for carbon-bearing enstatite synthesized at 1.5 GPa and 1400 °C, and that annealed at 750 °C for 10 min. Upon annealing, the ^{13}C MAS NMR spectrum for the annealed carbon-bearing enstatite did not show the presence of carbon species (Figure 3 bottom, Kim et al., 2016). This suggests that the carbon species in enstatite are not stable upon annealing at 750 °C.

On the basis of the relationship between peak area and ^{13}C abundance (see discussion 2.4.3), we should note that the amount of ^{13}CO and $^{13}CO_3^{2-}$ are much larger than the reported solubility of carbon (including ^{12}C and ^{13}C) into enstatite (~ 0.05–4.7 ppm) (Keppler et al., 2003; Shcheka et al., 2006) (see appendix 2.A1 for the previously estimated solubility of carbon species in crystalline silicates at high pressure). Therefore, the observed carbonates and CO species in the spectra are not likely due to carbon species in enstatite crystalline network, rather these stem from external reaction products formed during sample synthesis.

The Raman spectra show the presence of CH_4 in the fluid inclusion (Figure 2.1b). Because the potential peak position for CH_4 species somewhat overlaps with the spinning side bands of the probe background signal (at 14 kHz), ^{13}C MAS NMR spectra for the sample were collected with varying spinning speed (11 and 14 kHz). A small feature at ~ -9 ppm is observed in ^{13}C MAS NMR spectra at 11 kHz (Figure 2.2). Previous study of carbon-bearing Na_2O-$4SiO_2$ glass synthesized at 1.5 GPa and 1400°C reported a sharp peak due to CH_4 species at -5.4 ppm in the ^{13}C MAS NMR (Mysen et al., 2011). Figure 2.A1 in appendix 2.A2 shows ^{13}C MAS NMR spectrum for carbon-bearing enstatite under proton decoupling where any expected decrease in the peak width for the peak ~ -9 ppm is not shown, indicating that the carbon species responsible for -9 ppm peak does not have clear proximity toward hydrogen. ^{1}H MAS NMR spectrum for carbon-bearing enstatite shows the presence of CH_4 species at ~ 0.3 ppm (not shown here) (Pretsch et al., 2009). The result, therefore, indicates that the feature at ~ -9 ppm in ^{13}C MAS NMR spectra is mostly due to the probe background signal and the observed CH_4 in the Raman spectrum is likely due to the ^{12}C infiltrated from the graphite heater (Brooker et al., 1998; Cerfontain et al., 1987).

2.3.3. Pressure-induced structural changes of amorphous carbon: Insights from ^{13}C MAS NMR

Because we used ^{13}C-enriched amorphous carbon as a carbon reservoir, the current NMR experiment for amorphous carbon can also provide insights into the effect of pressure on the structure of amorphous carbon. Figure 5a in Kim et al. (2016) shows the background-subtracted ^{13}C

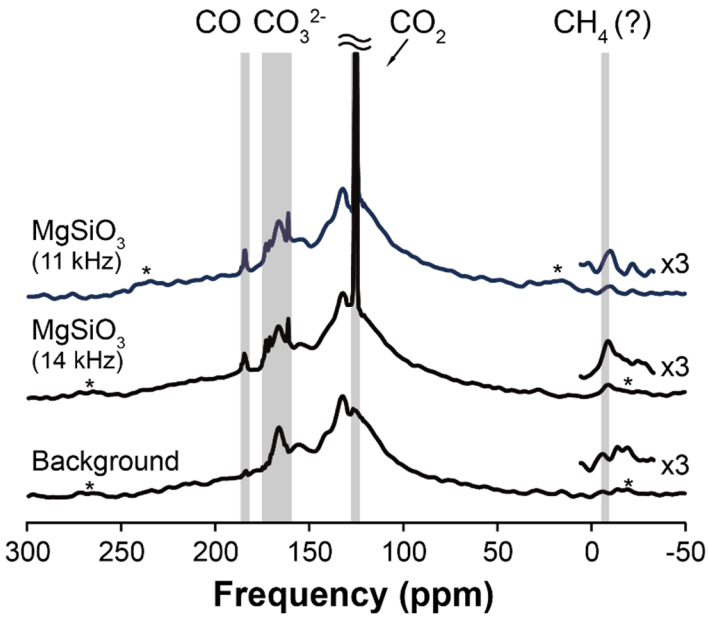

Figure 2.2. ^{13}C NMR spectra for carbon-bearing enstatite and stator and rotor backgrounds at 11 kHz of spinning speed (top), that at 14 kHz of spinning speed (middle), and rotor and stator background at 14 kHz (bottom). The asterisks and dotted arcs denote expected positions of spinning side bands for background signal at 130 ppm. The spinning sideband of the spectrum for carbon-bearing enstatite at 14 kHz overlaps with a small peak at ~ -9 ppm.

MAS NMR spectra for the compressed and uncompressed ^{13}C-enriched amorphous carbon. The ^{13}C NMR spectrum for amorphous carbon shows a broad peak at ~ 130 ppm. After compression at 1.5 GPa and 1400 °C for 48 h, the spectrum for the compressed amorphous carbon shows a broad peak at ~ 95 ppm. The observed pressure-induced changes in the peak position of amorphous carbon in the ^{13}C NMR spectra (Figure 5, Kim et al., 2016) may stem from multiple distinct structural changes upon compression, which includes bonding transition from sp^2 to sp^3 states. This could also be due to incorporation of hydrogen into carbon stemming from H_2O added during synthesis and the pressure-induced changes in network topology without changes in bonding states.

As the peak position for the typical carbon species with sp^2 and sp^3 bonding are ~ 138 ppm and ~ 68 ppm, respectively (Alam et al., 2002; Cho et al., 2008), this observation may indicate that the uncompressed amorphous carbon contains more sp^2 hybridized carbon species, while the compressed amorphous carbon at 1.5 GPa has more sp^3 hybridized carbon; amorphous carbon undergoes permanent pressure-induced densification, characterized by the transition from sp^2 to sp^3 hybridization. Alternatively, the previous studies have also shown that chemical shift and peak positions for sp^2 carbon varies with varying carbon network topology. Table 2.1 shows the ^{13}C NMR chemical shifts (and peak positions) of various carbon species in amorphous and crystalline carbon phases and allotropes. These phases have distinct network topology, yet consisting only of carbons with sp^2 bonding orbitals. While NMR chemical shift for sp^3-like carbon varies from 62 to 67.5 ppm (Alam et al., 2003; Pan et al., 1991), those for sp^2-like carbons also range from 102.3 to 149.7 ppm and are dependent on network topology; for

Table 2.1. ^{13}C NMR chemical shift for various crystalline and amorphous carbon materials.

Sample	Carbon species	Peak position (ppm)	FWHM (ppm)	B_0 (T)	Spin rate (kHz)	Ref.†
Amorphous carbon (rf sputtering)	sp^2-like carbon	130	200	2.35	4.4	(1)
	sp^3-like carbon	62	~ 26.8			
Amorphous carbon (PLD)	sp^2-like carbon	137.8	41.3	9.4	15	(2)
	sp^3-like carbon	67.5	49.8			
Carbon nanotubes	single-walled nanotubes with 2.4 at% Rh/Pd	124		9.4	11.7	(3)
	single-walled nanotubes (pure)	118.8		4.7		(4)
	single-walled nanotubes (with adsorbed CO)	123.8				
	double-walled nanotubes	116.3				
	multi-walled nanotubes (15 ± 5 walls)	106.1				
	multi-walled nanotubes (60 ± 10 walls)	102.3				
Graphene	graphene	123		8.46	9.4	(5)
Fullerene black + C_{60}	C_{60}	142.6	0.7	7.05	5	(6)
	C_{70}	129.9, 144.7, 146.9, 149.7			6.6	
	polyynic carbon chain	~ 70				
Carbon black	aromatic C=C	126		6.35	5.3	(7)
	C=O	167				
	aliphatic C-C	20				

† (1) Pan et al. (1991); (2) Alam et al. (2003); (3) Tang et al. (2000); (4) Abou-Hamad et al. (2011); (5) Si and Samulski (2008); (6) Kanowski et al. (1997); (7) Jäger et al. (1999)

example, the chemical shift of carbon in carbon nanotubes decreases with increasing the number of walls (Abou-Hamad et al., 2011). The peak positions of aromatic C=C bonds in graphene and carbon black is 123–126 ppm (Jäger et al., 1999; Si and Samulski, 2008). The chemical shift for fullerene C_{60} is 142.6 ppm and that for fullerene C_{70} shows multiple sharp peaks at 129.9 ppm, 144.7 ppm, 146.9 ppm and 149.7 ppm; all those crystallographically distinct carbon sites have varying symmetry and topology (Kanowski et al., 1997; Taylor et al., 1990).

Therefore, while the observed peak shift in the ^{13}C MAS NMR spectrum for the amorphous carbon (Figure 5, Kim et al., 2016) can certainly be due to changes in sp^2 to sp^3 hybridization that was also previously reported at higher pressure upon *cold* compression (Lin et al., 2011), it could also stem from the pressure-induced changes in carbon topology while maintaining sp^2 bonding state as shown in Table 2.1. Further experimental and theoretical confirmations are necessary. Finally, while the observed shift may be due to the effect of residual hydrogen, taking into consideration negligible hydrogen content in the compressed amorphous carbon as evidenced by the ^1H NMR spectra, the pressure-induced peak shift is not affected by the proton in the sample (see appendix 2.A3).

We note that the NMR signal is comparable to that of background signal; Figure 5b and c in Kim et al. (2016) show the ^{13}C MAS NMR spectra for ^{13}C-enriched uncompressed and compressed amorphous carbon and those for rotor and stator backgrounds. The observed difference in signal-to-noise ratio between the two spectra (uncompressed vs. compressed) are due to the absolute intensity differences in the two samples because of possible difference in spin-lattice relaxation times and/or the potential paramagnetic

interaction between unpaired electron and ^{13}C nuclides in the amorphous carbons: roughly, the calibration curve between ^{13}C NMR peak intensity and ^{13}C concentration based on the spin-counting experiment (see section 2.4.3 below), the peak intensity of compressed amorphous carbon corresponds to only ~ 20% of ^{13}C in the sample. It is currently difficult to distinguish the effect of paramagnetic interaction from the contribution from the spin-lattice relaxation times (T_1) mostly because of difficulty in estimating T_1 time for the compressed carbon.

In order to yield the background-subtracted spectra, the intensity of the background signal was adjusted (~ 80%) by matching the sharp peak intensity at ~ 170 ppm. A decrease in the background intensity of the ^{13}C MAS NMR spectra for the compressed and uncompressed amorphous carbon is likely due to the presence of the unpaired electrons in both samples [as expected from the presence of sp^2 bonding (Cho et al., 2008)]. While the current result is the first-of-its-kind observation of the pressure-induced permanent structural changes in amorphous carbon using ^{13}C MAS NMR, the effect of paramagnetic interaction (between unpaired electron and ^{13}C nuclides) remains to be fully established.

2.4. Discussion

2.4.1. Origin of peak at 125.2 ppm in carbon-bearing enstatite

The current ^{13}C NMR spectrum shows a strong and sharp resonance peak at 125.2 ppm. The FWHM of the peak is approximately 0.6 ppm with an applied Gaussian broadening factor of 0.01. While the ^{13}C NMR studies of carbon phases in the crystalline silicates have not been performed hitherto, previous studies on the ^{13}C MAS NMR for carbon-bearing anatase

TiO_2 proposed that the extremely sharp peak at 126 ppm can be attributed to $^{[4]}C$ in crystalline TiO_2 (Rockafellow et al., 2009). Alternately, in the previous ^{13}C NMR study of the carbon species in the sodium aluminosilicate glasses, the peak at ~125 ppm with the spinning sidebands was assigned to the dissolved molecular CO_2 in the glass network (Kohn et al., 1991). The dissolved CO_2 molecules bound to the crystalline/non-crystalline silicate networks would be subject to the low degree of freedom. This leads to a relatively large ^{13}C NMR chemical shift anisotropy of ~ 260–270 ppm (Herzfeld and Berger, 1980), resulting in the visible spinning sidebands (Kohn et al., 1991). In contrast, the CO_2 molecules in micro-fluid inclusions, which were not strongly bound to the networks, may not show spinning sidebands (Herzfeld and Berger, 1980; Kohn et al., 1991). If the CO_2 is bound to the enstatite network, the spinning sidebands of the CO_2 peak should appear at approximately 265 ppm and -15 ppm in the current ^{13}C MAS NMR spectrum. However, the spinning sidebands for the CO_2 peak were not observed in the current study. Therefore, the observed peak at 125.2 ppm in the current ^{13}C MAS NMR spectrum is likely to result from the fluid-phase CO_2 molecule in the inclusion as also indicated by the presence of CO_2 band in the Raman spectrum (Figure 2.1). While an experimental artificial signal (central spike) may overlap with the peak at 125.2 ppm in the previous pioneering study (Kohn et al., 1991), the current ^{13}C NMR experiments were performed with the varying carrier frequency. The result confirms that the peak at 125.2 ppm is not due to the additional artifact signal. We also synthesized the sample twice using the identical experimental conditions in the piston cylinder to substantiate the reproducibility: the ^{13}C MAS NMR spectra for both samples also showed a

sharp peak at 125.2 ppm.

2.4.2. ^{13}C NMR chemical shift for orthocarbonate species ($^{[4]}$C): Insights from quantum chemical calculations

A previous study suggested that the peak at ~ 120 ppm can be assigned to $^{[4]}$C (Rockafellow et al., 2009). The peak position also corresponds to suggested peak position for molecular CO_2 (e.g., Brooker et al., 1999; Kohn et al., 1991; Morizet et al., 2010; Mysen et al., 2011). In order to confirm these earlier peak assignments, theoretical confirmation is required. Here, we calculated the chemical shift of $^{[4]}$C [$C(OH)_4$ cluster] using quantum chemical calculations. The theoretical calculation of NMR chemical shielding tensor for the model $C(OH)_4$ cluster shows the effect of the C-O bond length of $^{[4]}$C cluster on the ^{13}C chemical shift (Figure 2.3). The calculated ^{13}C NMR chemical shift is also dependent on the energy level of theory and the basis sets used. Here the calculations were performed at the B3LYP level of theory with a 6-311+G(2d) basis set that reproduced experimental ^{13}C chemical shifts for the known molecules relatively well (Kim and Lee, 2011; Lee and Lee, 2009). For example, the calculated NMR chemical shift for the CO_2 molecule is 125.7 ppm at the B3LYP level of theory with a 6-311+G(2d) basis set (Kim and Lee, 2011). The chemical shift is consistent with the result from experimental ^{13}C liquid-state static NMR spectrum of CO_2 gas molecule (Ettinger et al., 1960). The calculated NMR chemical shift also varies with basis sets used. For instance, the shift of CO_2 molecule calculated at the B3LYP/6-31G(d) is 108.807 ppm (Kim and Lee, 2011).

Figure 2.3 shows that the effect of the C-O bond length on a single

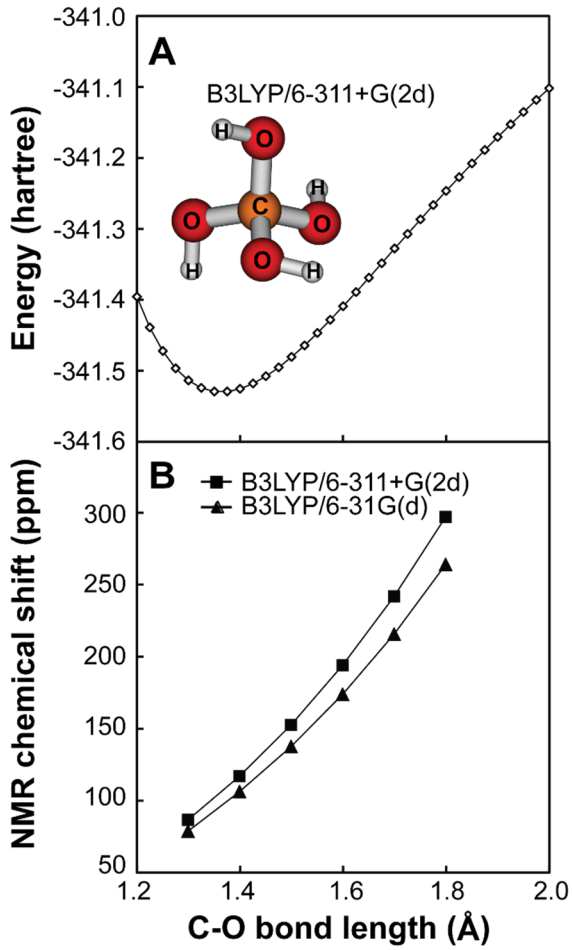

Figure 2.3. (A) Single point energy of $C(OH)_4$ cluster with varying C–O bond length. A model $C(OH)_4$ cluster is also shown in the inset. (B) NMR chemical shift of $C(OH)_4$ cluster with varying C–O bond length.

point energy and NMR chemical shift. The quantum chemical calculations of $C(OH)_4$ cluster with an equilibrium C-O bond length of 1.388 Å [calculated at the B3LYP/6-311+G(2d)] show that the chemical shift is 117.451 ppm. The calculated NMR chemical shift of $C(OH)_4$ cluster gradually increases with increasing the C-O bond length. The ^{13}C chemical shift increases from 121.2 ppm at 1.40 Å to 196.9 ppm at 1.60 Å. In the previous report, we also showed that the $^{[4]}C$ peak with a C-O bond length of 1.60 Å (if C substitutes Si in the chain silicate network) leads to a chemical shift of 254.6 ppm (Kim and Lee, 2011).

If the C-O bond length of the $^{[4]}C$ cluster in the enstatite were ~ 1.388 Å, the peak position of the $^{[4]}C$ species would be ~ 117.451 ppm. Therefore, taking into consideration the similarity between the chemical shifts for CO_2 and $^{[4]}C$, it is difficult to assign the peak based only on the ^{13}C chemical shift. In the current study, as we observed CO_2-rich fluid inclusions confirmed by Raman spectroscopy (Figure 2.1), the peak at 125.2 ppm in the current ^{13}C MAS NMR spectrum is likely to be the free CO_2 molecule in enstatite.

2.4.3. External *vs*. structurally-incorporated carbon species in the carbon-bearing enstatite: Insights from quantitative ^{13}C spin counting experiment using ADM-SiO_2 mixture

Calibration curve between ^{13}C abundance and ^{13}C MAS NMR peak intensity. In order to evaluate whether the observed ^{13}C NMR peaks stem from the structurally-incorporated carbons in the enstatite or those in external phases, it is necessary to estimate the solubility of carbon in enstatite and to perform quantitative measurement of the amount of carbon species in carbon-bearing enstatite in ^{13}C MAS NMR spectra (Figure 2, Kim

et al., 2016), and finally to compare the estimated amount of carbon in enstatite with the solubility of carbon in enstatite. A clear linear relationship between peak intensity and concentration was established for X_{ADM}=1/4, 1/8 and 1/16. We then extrapolated the trend line obtained from the samples with these higher ADM concentration to the samples with lower ADM concentration. The NMR intensity data for the samples with the lower ADM concentration were then adjusted to match the extrapolated line. This allows us to estimate the carbon concentration in the carbon-poor sample. The estimated carbon contents from the calibration curve are 2.0 wt% (220 ppm of ^{13}C) for X_{ADM}=1/50 sample; 0.43 wt% (47 ppm of ^{13}C) for X_{ADM}=1/233 sample; and 0.32 wt% (35 ppm of ^{13}C) for X_{ADM}=1/310 sample, respectively. We note again that the carbon content of the mixture with low carbon concentration was estimated using its peak intensity and established calibration curve for the mixtures with higher carbon concentration, while this may not be fully desirable. This is mainly because of the aforementioned difficulty in homogeneous mixing between a small amount of ADM and SiO_2 and partly due to their differences in volatilization during elemental analysis (see section 2.2.3. for details). Nevertheless, NMR peak intensity does correspond to robust carbon content and thus allows for rigorous estimation of amount of carbon in the mixtures.

Figure 2.4 top shows ^{13}C MAS NMR spectra for ADM-SiO_2 mixtures with varying X_{ADM}. The peak area in each spectrum decreases with decreasing X_{ADM}. Figure 2.A3 in appendix 2.A4 shows the ^{13}C MAS NMR spectra for ADM-SiO_2 mixtures with varying X_{ADM} ratio under proton decoupling. The spectra show that proton decoupling indeed improves signal-to-noise ratio while the peak intensity is conserved. We also note that

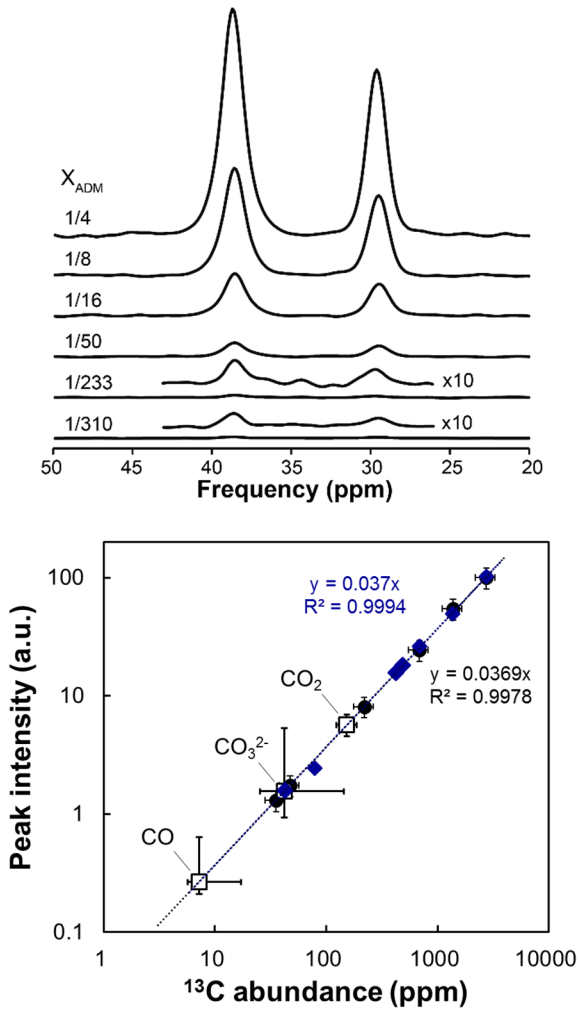

Figure 2.4. (Top) ^{13}C MAS NMR spectrum for the mixtures of ADM-SiO_2 with varying ADM/SiO_2 ratio [X_{ADM} = 1/4 (25 wt%, 2750 ppm of ^{13}C), 1/8 (12.5 wt%, 1375 ppm of ^{13}C), 1/16 (6.25 wt%, 688 ppm of ^{13}C), 1/50 (2.0 wt%, 220 ppm of ^{13}C), 1/233 (0.43 wt%, 47 ppm of ^{13}C), 1/310 (0.32 wt%, 35 ppm of ^{13}C)]. (Bottom) Variation of peak intensity in the ADM-SiO_2 mixture as a function of ^{13}C abundance (in ppm) calculated from

nominal X_{ADM} ratio and peak area of carbon species in ^{13}C MAS NMR spectra. Diamonds and circles refer to the amounts of ^{13}C estimated from nominal X_{ADM} ratio with and without proton decoupling, respectively. Their peak areas were retrieved from ^{13}C MAS NMR results for ADM-SiO_2 mixtures. Rectangles refer to the amounts of ^{13}C species in carbon-bearing enstatite estimated from ^{13}C MAS NMR spectra for carbon-bearing enstatite.

the carbon species (including CO_2, CO_3^{2-}) that do not have hydrogen bonded to carbon may not undergo enhancement in signal-to-noise ratio further. Figure 2.4 bottom shows the relationship between the ^{13}C MAS NMR peak intensity and the estimated ^{13}C abundance in ADM-SiO_2 mixtures. The linear correlation between the ^{13}C abundance (X) in the ADM-SiO_2 mixture and the normalized peak intensity (Y, normalized with respect to that of X_{ADM}=1/4.) in ^{13}C MAS NMR spectra can be established: Y=0.0369X.

Effect of spin-lattice relaxation time. While we used the ADM-SiO_2 mixtures as an analog for the carbon species in the compressed silicates, the spin-lattice relaxation times for ADM and carbon species in the compressed enstatite are different: the T_1 for the latter is longer than that of the former. Because of the differences in spin-lattice relaxation times, the actual carbon concentration (particularly that of carbonate species) in the sample can be higher from those estimated here: T_1 of ADM is ~ 1 s (Resing, 1969) and thus the current recycle delay of 5 s provides quantitative insight into the carbon content in the sample. As for the other carbon species, due to low spin density, the T_1 for the CO_2 has not been estimated. Nevertheless, the previous studies have shown that spin-lattice relaxation time of gas phase

CO_2 varies from ~ 0.2 sec at an internal pressure of 10.3 bar, 16.34 sec at 137.89 bar, and to ~ 22 sec at an internal pressure of 413.68 bar (Etesse et al., 1992). While the T_1 for CO_2 varies with the density, the ^{13}C MAS NMR experiment with 5 s and 40 s delay times does not lead to a noticeable difference in signal intensity. Therefore, the current results with 5 s relaxation delay provide moderately robust estimation of CO_2 content in the glasses. As for the CO_3^{2-} species, the estimated T_1 values for Na_2CO_3 and $CaCO_3$ are ~ 1729 and 6418 s, respectively. That for $MgCO_3$ magnesite is ~ 78 s (Moore et al., 2015). Thus, the calibration curve based on ADM may not provide robust and quantitative estimation of the carbonate content in the current sample, particularly. The predicted $^{13}CO_3^{2-}$ content is likely to be smaller than the actual content.

Estimated carbon contents. The estimated minimum ^{13}C abundance from ^{13}C MAS NMR spectra for ADM-SiO_2 mixture is ~ 35 ppm of ^{13}C from the calibration curve based on ^{13}C MAS NMR experiments. Based on the established calibration curve, we believe that the detection limit is ~ 5–10 ppm for ^{13}C species with the employed instrumentation and the experimental conditions in the current study (~ 5 days of signal averaging at 9.4 T static field with a rf field strength of 66.7 kHz in the 3.2 mm rotor with full sample volume of ~ 19 mm^3). Whereas the spin-lattice relaxation times, particularly carbonates species in the enstatite-amorphous carbon reaction products need to be estimated, because of the limited sample volume, it is currently challenging to measure T_1. Nevertheless, based on the calibration curve, the estimated ^{13}C amounts of CO_2, CO_3^{2-}, and CO species are ~ 142–166 ppm, ~ 28–45 ppm (once calibrated with T_1 effect, the concentration should be higher than the current value), and ~ 6–7 ppm, respectively. The

previously reported solubility of carbon species in enstatite is 0.05–4.7 ppm (Keppler et al., 2003; Shcheka et al., 2006); therefore, the estimated carbon contents from the NMR spectra indicate that those carbon species are from external phases.

External crystalline carbonate phases. Characteristic vibrational frequencies for calcite and magnesite are expected to be at 1088 cm^{-1} and 1095 cm^{-1}, respectively. We note that there is also an expected peak shift toward higher frequency with increasing pressure. C-O asymmetric stretching vibration for bicarbonate species would show up at 1630 cm^{-1}, if exists (Davis and Oliver, 1972; Wen and Brooker, 1995). The Raman spectra for the fluid inclusion in the carbon-bearing enstatite do not show the peak due to carbonate species. Therefore, the carbonate peak observed in the ^{13}C NMR is not from the inclusion. In order to check the potential presence of carbonate phases in the grains, we also performed SEM analysis of the grains. The preliminary analysis does not show any evidence for the carbonate phases although we cannot discard the possibility of its potential presence (See appendix 2.A5 and 2.A6).

2.4.4. Sources of ^{12}C contamination

In this study, ^{13}C-enriched amorphous carbon (~ 99.7%) was used to synthesize the carbon-bearing enstatite and the sample was sealed in a Pt tube (a closed system); therefore, the presence of ^{12}C was not expected. The Raman spectra for fluid-inclusion in enstatite, however, showed the presence of ^{12}C species, which was not present inside the capsule during the sample preparation and welding. The presence of ^{12}C thus indicates a potential contamination by infiltration of carbon from the graphite furnace

during the compression and heating in the piston cylinder (Balta et al., 2011; Brooker et al., 1998; Brooker et al., 1999; Ni and Keppler, 2013). Note that double Pt capsules were used to minimize the changes in f_{O2} in several previous synthesis of carbon-bearing silicates in the previous studies (Balta et al., 2011; Brooker et al., 1998; Ni and Keppler, 2013 and references therein). The ^{12}C infiltrated from the graphite furnace may lead to the spatial heterogeneity in f_{O2}: oxygen fugacity near the boundary of the Pt capsule may be low, resulting in the formation of ^{13}CO species [*via* $^{13}CO_2$ + ^{12}C (from graphite furnace) = ^{13}CO + ^{12}CO] (Brooker et al., 1998; Cerfontain et al., 1987). Despite the observed presence of ^{12}C in the carbon-bearing enstatite (Figure 2.1), the ^{13}C MAS NMR spectrum obtained from the sample shows only the ^{13}C contribution in enstatite, taking into consideration the fact that the ^{13}C is the only active isotope.

2.5. Implications

Here, we have reported the ^{13}C MAS NMR spectrum for carbon-bearing enstatite. The ^{13}C MAS NMR spectrum for the carbon-bearing enstatite shows multiple peaks from different carbon environments: CO, CO_3^{2-}, and molecular CO_2. The Raman spectra for the observed fluid inclusion in the carbon-bearing enstatite show multiple molecular species (e.g., CO_2, CO, CH_4, H_2O, and H_2). The quantum chemical calculations of the $C(OH)_4$ cluster show that ^{13}C chemical shift of the cluster has strong C-O bond length dependence; with increasing C-O bond length from 1.40 Å to 1.60 Å, ^{13}C chemical shift increases from 121.2 ppm to 196.9 ppm.

While the Raman spectrum of the observed fluid inclusions in the carbon-bearing enstatite can provide information on the collective vibration

of molecules of different isotopes (e.g., peaks of $^{13}CO_2$ and $^{12}CO_2$, and ^{13}CO and ^{12}CO), the ^{13}C NMR spectrum can provide complementary and element-specific information on the nature of carbon species in crystalline silicates, distinguishing the molecular CO_2 in fluid phase and structurally bound CO_2 in silicate network. Taking into consideration the similarity between the chemical shifts of CO_2 and $^{[4]}C$, it is not straightforward to assign the peak solely based on the ^{13}C NMR peak positions. Yet, we expect that the method could potentially probe the minor fraction of $^{[4]}C$ whose peak width is expected to be much larger than that of molecular CO_2 due to its pronounced nuclear spin anisotropy. The current results suggest that the ^{13}C MAS NMR technique, combined with Raman spectroscopy can be used as a tool for the detection of carbon species and inclusions in crystalline silicates.

Whereas the ^{13}C MAS NMR technique was utilized to probe carbon speciation in silicates at relatively low pressure (1.5 GPa in the current study), the method can also be utilized to analyze carbon species in carbon-bearing silicate minerals at much higher pressure and additional carbon reservoirs in earth's interior, such as metal carbides and carbonate minerals (Catalli and Williams, 2005; Hazen et al., 2013; Mikhail et al., 2011; Mookherjee, 2011; Mookherjee et al., 2011; Oganov et al., 2013; Rohrbach and Schmidt, 2011; Santillán et al., 2005; Seto et al., 2008). As for the latter, presence of crystalline silicon carbonate phase where silicon behaves as a metal cation in carbonates at 18–26 GPa was also reported (Santoro et al., 2011). While the detailed structural characterization of these phases remains to be seen, future ^{13}C solid-state NMR studies of these phases may reveal the detailed bonding nature of these complexes under compression.

The solubility of carbon into $(Mg,Fe)_2SiO_4$ olivine increases from 0.09

ppm to 12.75 ppm as pressure increases from 1.5 GPa to 11 GPa and that into $MgSiO_3$ bridgmanite at ~ 26 GPa is less than 0.05 ppm (Shcheka et al., 2006). Due to relatively low carbon solubility, it is currently challenging to detect carbon species in these phases using the experimental conditions employed here. While the NMR data indeed provide complementary and unique insights into the speciation of carbon-bearing phases to vibrational spectroscopy, we fully acknowledged the fact that the current data also address the limitation of the NMR studies on quantitative estimation of ~ ppm scales of carbon dissolved in a crystalline lattice: ^{13}C may not reveal the carbon species at concentration below 5–10 ppm using the current experimental protocols at the current stage. NMR experiments at high magnetic field with fast spinning probes lead to significant gain in signal intensity and may provide insights into the carbon solubility mechanism into the crystalline phases in Earth's mantle.

Appendix

2.A1. Solubility of carbon into crystalline silicates at high pressure up to 25 GPa

The solubility and detailed structure around carbon species in crystalline silicates are often difficult to probe. This is partly because the solubility of the carbon species is relatively low, on the order of 0.01 to 10 ppm (Keppler et al., 2003; Shcheka et al., 2006), and suitable probes are limited. Furthermore, the solubility measurement is often complicated by several extrinsic factors including presence of excess carbon in the grain boundary; the resulting carbon solubility in silicate crystals varied from the order of 0.01 ppm to 2500 ppm (Freund et al., 1980; Keppler et al., 2003; Mathez et al., 1984; Shcheka et al., 2006; Tingle and Aines, 1988; Tsong and Knipping, 1986; Tsong et al., 1985) .

Despite the challenge, previous efforts have provided some insights into carbon species in various silicate crystals at pressures up to 26 GPa (Keppler et al., 2003; Shcheka et al., 2006). The carbon solubility in the silicates does not show a great variation depending on the types and composition of the crystals. The estimated total carbon content in the Mg-silicates apparently increases with increasing pressure, but the formation of Mg-perovskite phase leads to a reduction in the carbon solubility in silicate (Keppler et al., 2003; Shcheka et al., 2006). Table 2.A1 summarizes the estimated carbon solubility in the various silicate polymorphs in a pressure range of 1–26 GPa (Keppler et al., 2003; Shcheka et al., 2006). The solubility of carbon in enstatite at 1.5 GPa varies from 0.05 ppm to 4.7 ppm, which may reside from the carbon contents in the grain boundaries.

2.A2. The presence of $^{13}CH_4$ in carbon-bearing enstatite by using proton decoupling

Figure 2.A1 shows ^{13}C MAS NMR spectrum for carbon-bearing enstatite with decoupling power of 33 kHz and spinning speed at 11 kHz. Any decrease in the peak width for the peak ~ -9 ppm in Fig. 3 in Kim et al. (2016) has not been observed. The result may indicate that the small feature at ~ -9 ppm is from background signal.

2.A3. Effect of residual H in the pressure-induced carbon peak shifts in the amorphous carbon

Protonation into carbon could also affect the observed change in peak position of amorphous carbon under compression. We collected ^{1}H MAS NMR spectra for the compressed and uncompressed amorphous carbon in order to identify whether there would be any ^{1}H reservoir and potential protonation of the sample. The spectra were collected on a Varian NMR system (9.4 T) at a Larmor frequency of 400.01 MHz (3.2 mm double-resonance Varian probe). Single-pulse acquisition with a pulse length of 1.6 μs (radio frequency tip angle of about 30° for solids) was used with a recycle delay of 5 s and spinning speeds of 14 kHz. The potential results would allow us to confirm whether the observed changes in the peak shift is due to residual proton from the H_2O added during the sample synthesis. Figure 2.A2 shows the ^{1}H MAS NMR spectra for ^{13}C-enriched uncompressed and compressed amorphous carbon and those for rotor and stator backgrounds. ^{1}H MAS NMR spectra for rotor and stator background show a broad peak at ~ 7 ppm. The shoulder at ~ -1 ppm is observed for uncompressed

amorphous carbon. The assignment of the feature is not trivial, yet previous ^{1}H NMR study for the amorphous carbon under milling showed a broad feature near ~ -1 ppm, assigned to hydrogenated amorphous carbon (Shindo et al., 2011). No noticeable proton peak is observed for compressed amorphous carbon, suggesting the absence of proton reservoir in compressed amorphous carbon. The result confirms that the proton signal from rotor and stator background is far much greater than those from the amorphous carbon and there is no noticeable proton reservoir for the compressed carbon. Taking into consideration negligible H content in the compressed amorphous carbon, it is expected that ^{1}H-^{13}C cross-polarization NMR does not probe the H-C interaction within the amorphous carbon. Indeed, our preliminary ^{1}H-^{13}C cross-polarization NMR spectra for the sample and rotor showed that most of the signals are from the rotor and stator. The current results again confirm the pressure-induced peak shift were not affected by the proton in the sample.

2.A4. Detection limit on ^{13}C MAS NMR under proton decoupling

Figure 2.A3 shows the ^{13}C MAS NMR spectra for ADM-SiO_2 mixtures with varying X_{ADM} ratio with decoupling power of 33 kHz. The spectra show that proton decoupling indeed improves signal-to-noise ratio and ^{13}C MAS NMR spectrum for the sample with X_{ADM} =1/259, ~ 43 ppm can be obtained. See Figure 2.7 for the calibration results based on the decoupling experiments.

2.A5. The characteristics of the ^{13}C peak width of various carbonate species

Figure 2.A4 shows the ^{13}C static NMR spectra of 1 M Na_2CO_3(*aq*) and 1 M ($Na_2{}^{13}CO_3$+$NaHCO_3$)(*aq*), and ^{13}C MAS NMR spectra of calcite and natrite to explore the characteristics of their peak shape in the ^{13}C NMR spectra. The spinning speed for calcite and natrite is 14.7 kHz. The FWHM of calcite and natrite peak in ^{13}C MAS NMR spectra are 0.48 and 0.42 ppm with an employed Lorentzian broadening factor of 10, respectively. The FWHM of 1 M $Na_2{}^{13}CO_3$(*aq*) and 1 M ($Na_2{}^{13}CO_3$+$NaHCO_3$)(*aq*) in ^{13}C MAS NMR spectra are 0.48 and 0.48 ppm with an employed Lorentzian broadening factor of 10, respectively. The FWHM of carbonates peaks in the carbon-bearing enstatite at 161.2, 170.9, and 173.3 ppm are 0.29, 0.37, and 0.35 ppm with a Lorentzian broadening factor of 10, respectively. Therefore, it is difficult to identify their phases (either solid or liquid) based only on their peak widths due to the similarity in FWHM of carbonate minerals and carbonate ions in aqueous solution. Although spectra for aqueous solution collected without spinning at the magic angle, we note that ^{13}C liquid-state NMR under MAS may not reduce the FWHM of the carbonate species in aqueous solution.

2.A6. Estimation of the detection limit of carbonate phase in the enstatite-calcite mixture using conventional XRD

In order to test the detectability of carbonate species in the silicate matrix, we collected XRD patterns from enstatite-calcite mixture with varying concentration of carbonate phase (on Rigaku MiniFlex600, using Cu*Ka* X-rays, voltage of 40 kV, current of 15 mA, a 2θ range of 10°–60°, a

step width of 0.01°, and scan rate of 0.4 s/point). Figure 2.A5 shows the XRD patterns of enstatite-calcite mixture with varying $X_{calcite}$ from 0 to 1/32. The calcite (104) peak (red line at 29.4°) intensity can be seen up to $X_{calcite}$=1/256 (~ 0.39 wt%) sample, which is the detection limit with the employed instrument and conditions used in the study. The estimated carbonate concentration is much smaller than the current detection limit of XRD.

Table 2.A1. Solubility of carbon species in crystalline silicates with varying composition, pressure, and temperature, as reported in previous studies.

Composition	Pressure (GPa)	Temperature (°C)	Duration (h)	Solubility (wt ppm)	Ref.*
Enstatite ($MgSiO_3$)	1.5	900–1100	96–168	0.05(1)–0.19(4)	(1)
	1.5	900	96	3.0–4.7	(2)
	6	1100	5	0.38(3)–0.44(3)	(1)
	16	1400	10	0.69(6)–0.80(6)	
Olivine [$(Mg,Fe)_2SiO_4$]	1	1200	34	Not detected	(1)
	1.5	900–1100	144–168	<0.09–0.38(9)	
	1.5	1200	68	0.14(2)–0.25(2)	
	2	1200	71	0.34(4)	
	3.5	1200	71	0.29(4)–0.54(6)	
	7	1200	10	3.27(29)–3.90(68)	
	11	1200	10	11.57(34)–12.75(53)	
Diopside ($CaMgSi_2O_6$)	1.5	900–1100	96–168	<0.01–0.16(2)	(1)
	1.5	900	168	0.4–0.5	(2)
	6	1100	8	1.45(7)–1.60(6)	(1)
Pyrope ($Mg_3Al_2Si_3O_{12}$)	6	1300	10	0.85(5)–0.87(5)	(1)
	6	1300	10	1.9–2.1	(2)
	9	1300	10	0.83(6)–1.27(7)	(1)
	10	1300	6	0.82(4)–0.96(5)	
Spinel ($MgAl_2O_4$)	1.5	1100	168	<0.02	(1)
	1.5	1100	168	Not detected	
Wadsleyite [$(Mg,Fe)_2SiO_4$]	16	1400	10	<0.04–0.04(1)	(1)
	17	1400	4	<0.05	
Ringwoodite [$(Mg,Fe)_2SiO_4$]	21	1200	10	0.04(1)	
	23	1200	4	<0.07–0.10(2)	
Ilmenite ($MgSiO_3$)	25	1400	10	<0.08	(1)
Bridgmanite (Perovskite) ($MgSiO_3$)	25	1400	10	<0.07	(1)
	26	1400	3	<0.05	

* (1) Shcheka et al. (2006); (2) Keppler et al. (2003)

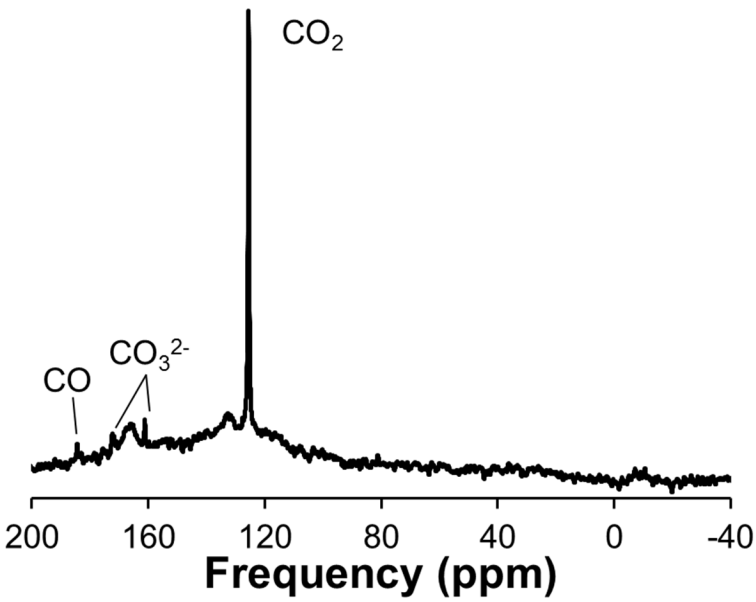

Figure 2.A1. ^{13}C MAS NMR spectrum for carbon-bearing enstatite under proton decoupling with an applied Lorentzian broadening factor of 40.

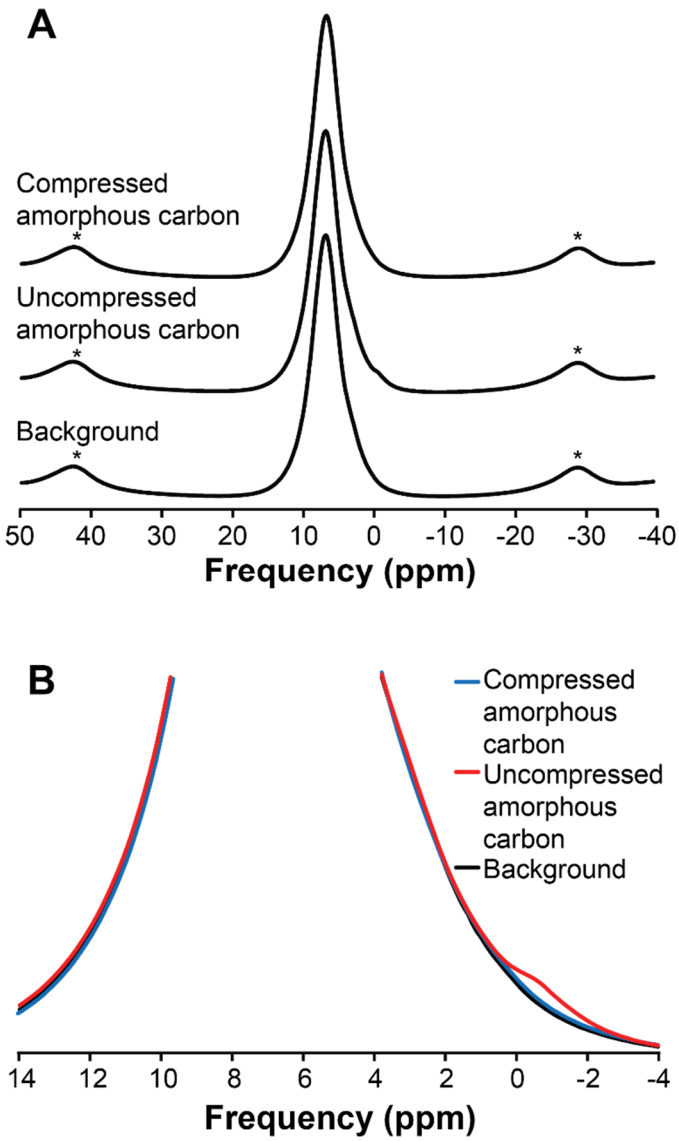

Figure 2.A2. (A) ^{1}H MAS NMR spectra for compressed amorphous carbon, amorphous carbon, and rotor-stator background. Asterisks denote spinning sidebands. (B) Expanded ^{1}H MAS NMR spectra for the samples as labeled.

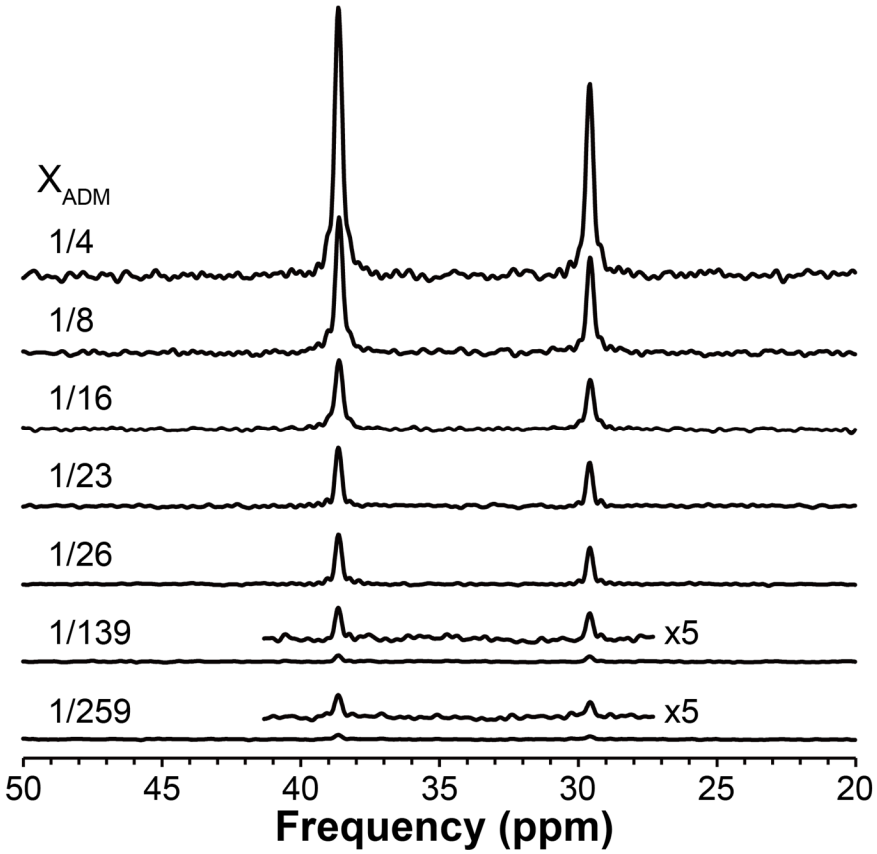

Figure 2.A3. ^{13}C MAS NMR spectra for ADM-SiO_2 mixtures with varying X_{ADM} ratio with decoupling power of 33 kHz.

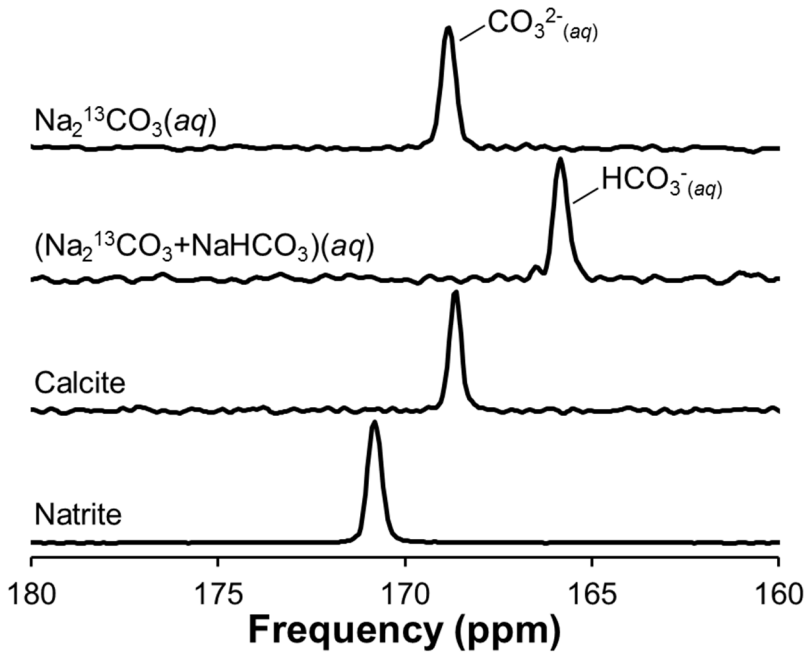

Figure 2.A4. ^{13}C NMR spectra for 1 M $Na_2{}^{13}CO_3$ (*aq*), 1 M ($Na_2{}^{13}CO_3$+$NaHCO_3$) (*aq*), calcite, and natrite with an employed Lorentzian broadening factor of 10.

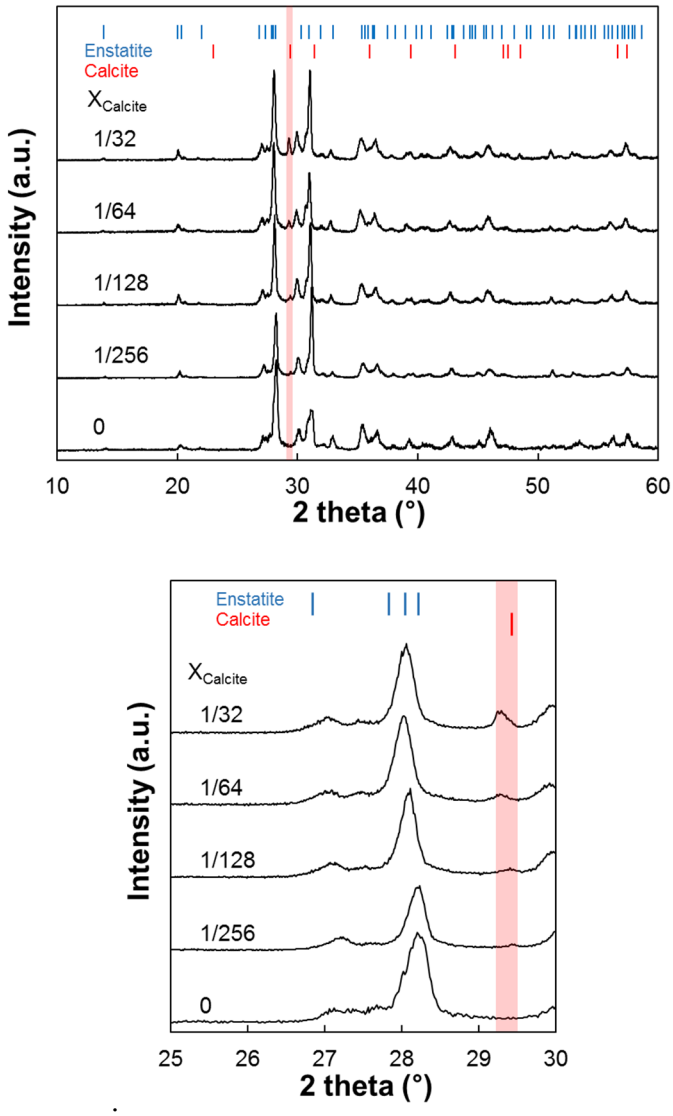

Figure 2.A5. XRD patterns of enstatite-calcite mixture with varying $X_{calcite}$ from 0 to 1/32. Blue and red lines on the top of the figure refer to XRD patterns of enstatite and calcite, respectively. A red area shows the decrease of calcite intensity with decreasing $X_{calcite}$ in the sample.

References

Abou-Hamad, E., et al. (2011) Structural properties of carbon nanotubes derived from ^{13}C NMR. *Physical Review B* **84**, 165417.

Alam, T.M., Friedmann, T.A. and Jurewicz, J.G. (2002) Solid state ^{13}C MAS NMR investigations of amorphous carbon thin films structural changes during annealing, In *Thin Films: Preparation, Characterization, Applications*, (Ed. M. P. Soriaga, J.S., L. A. Bottomley and Y.-G. Kim). Kluwer, New York, pp. 277-289.

Alam, T.M., Friedmann, T.A., Schultz, P.A. and Sebastiani, D. (2003) Low temperature annealing in tetrahedral amorphous carbon thin films observed by ^{13}C NMR spectroscopy. *Physical Review B* **67**.

Balta, J.B., Asimow, P.D. and Mosenfelder, J.L. (2011) Hydrous, low-carbon melting of garnet peridotite. *J. Petrol.* **52**, 2079-2105.

Blank, J.G. and Brooker, R.A. (1994) Experimental studies of carbon dioxide in silicate melts: Solubility, speciation, and stable carbon isotope behavior, In *Reviews in Mineralogy and Geochemistry*, (Eds. Carroll, M.R., Holloway, J.R.). Mineralogical Society of America, Washington, pp. 157-186.

Blank, J.G., Stolper, E.M. and Carroll, M.R. (1993) Solubilities of caron-dioxide and water in rhyolitic melt at 850 °C and 750 bars. *Earth and Planetary Science Letters* **119**, 27-36.

Blundy, J., Cashman, K.V., Rust, A. and Witham, F. (2010) A case for CO_2-rich arc magmas. *Earth Planet. Sci. Lett.* **290**, 289-301.

Bodnar, R.J., Binns, P.R. and Hall, D.L. (1989) Synthetic fluid inclusions - VI. Quantitative evaluation of the decrepitation behaviour of fluid

inclusions in quartz at one atmosphere confining pressure. *J. Metamorphic Geology* **7**, 229-242.

Brooker, R., Holloway, J.R. and Hervig, R. (1998) Reduction in piston-cylinder experiments: The detection of carbon infiltration into platinum capsules. *American Mineralogist* **83**, 985-994.

Brooker, R.A., Kohn, S.C., Holloway, J.R., McMillan, P.F. and Carroll, M.R. (1999) Solubility, speciation and dissolution mechanisms for CO_2 in melts on the $NaAlO_2$-SiO_2 join. *Geochimica et Cosmochimica Acta* **63**, 3549-3565.

Burke, E.A.J. (2001) Raman microspectrometry of fluid inclusions. *Lithos* **55**, 139-158.

Burton, M.R., Sawyer, G.M. and Granieri, D. (2013) Deep carbon emissions from volcanoes, In *Reviews in Mineralogy & Geochemistry*, (Eds. Hazen, R.M., Jones, A.P., Baross, J.A.). Mineralogial Society of America, Virginia, pp. 323-354.

Catalli, K. and Williams, Q. (2005) A high-pressure phase transition of calcite-III. *American Mineralogist* **90**, 1679-1682.

Cerfontain, M.B., Meijer, R., Kapteijn, F. and Moulijn, J.A. (1987) Alkali-catalyzed carbon gasification in CO-CO_2 mixtures: An extended model for the oxygen exchange and gasification reaction. *Journal of Catalysis* **107**, 173-180.

Cho, G., Yen, B.K. and Klug, C.A. (2008) Structural characterization of sputtered hydrogenated amorphous carbon films by solid state nuclear magnetic resonance. *Journal of Applied Physics* **104**, 013531.

Cody, G.D. and Alexander, C.M.O.D. (2005) NMR studies of chemical structural variation of insoluble organic matter from different

carbonaceous chondrite groups. *Geochimica et Cosmochimica Acta* **69**, 1085-1097.

Cody, G.D., Heying, E., Alexander, C.M.O., Nittler, L.R., Kilcoyne, A.L.D., Sandford, S.A. and Stroud, R.M. (2011) Establishing a molecular relationship between chondritic and cometary organic solids. *Proceedings of the National Academy of Sciences of the United States of America* **108**, 19171-19176.

Davis, A.R. and Oliver, B.G. (1972) A vibrational-spectroscopic study of the species present in the CO_2−H_2O system. *Journal of Solution Chemistry* **1**, 329-339.

Dixon, J.E. and Clague, D.A. (2001) Volatiles in basaltic glasses from Loihi seamount, Hawaii: Evidence for a relatively dry plume component. *J. Petrol.* **42**, 627-654.

Eggler, D.H. and Kadik, A.A. (1979) System $NaAlSi_3O_8$-H_2O-CO_2 to 20 kbar pressure: 1. Compositional and thermodynamic relations of liquids and vapors coexisting with albite. *American Mineralogist* **64**, 1036-1048.

Eggler, D.H. and Rosenhauer, M. (1978) Carbon-dioxide in silicate melts: 2. Solubilites of CO_2 and H_2O in $CaMgSi_2O_6$ (diopside) liquids and vapors at pressure to 40 kb. *American Journal of Science* **278**, 64-94.

Etesse, P., Zega, J.A. and Kobayashi, R. (1992) High pressure nuclear magnetic resonance measurement of spin–lattice relaxation and self-diffusion in carbon dioxide. *Journal of Chemical Physics* **97**, 2022.

Ettinger, R., Blume, P., Patterson, A. and Lauterbur, P.C. (1960) ^{13}C chemical shifts in CO and CO_2. *Journal of Chemical Physics* **33**, 1597-1598.

Feng, J., Lee, Y.J., Reeder, R.J. and Phillips, B.L. (2006) Observation of bicarbonate in calcite by NMR spectroscopy. *American Mineralogist* **91**, 957-960.

Fine, G. and Stolper, E. (1985) The speciation of carbon-dioxide in sodium aluminosilicate glasses. *Contributions to Mineralogy and Petrology* **91**, 105-121.

Freund, F. (1981) Mechanism of the water and carbon dioxide solubility in oxides and silicates and the role of O^-. *Contributions to Mineralogy and Petrology* **76**, 474-482.

Freund, F., Kathrein, H., Wengeler, H., Knobel, R. and Reinen, H.J. (1980) Carbon in solid solution in forsterite--a key to the untractable nature of reduced carbon in terrestrial and cosmogenic rocks. *Geochimicah et Cosmochimica Acta* **44**, 1319-1333.

Frisch, M.J., et al. (2004) Gaussian 03, Revision C.02. Gaussian, Inc., Wallingford CT.

Fyfe, W.S. (1970) Lattice energies, phase transformations and volatiles in the mantle. *Physics of the Earth and Planetary Interiors* **3**, 196-200.

Garrabos, Y., Echargui, M.A. and Marsault-Herail, F. (1989) Comparison between the density effects on the levels of the Raman spectra of the Fermi resonance doublet of the $^{12}C^{16}O_2$ and $^{13}C^{16}O_2$ molecules. *The Journal of Chemical Physics* **91**, 5869-5881.

Gerlach, T.M., McGee, K.A., Elias, T., Sutton, A.J. and Doukas, M.P. (2002) Carbon dioxide emission rate of Kīlauea Volcano: Implications for primary magma and the summit reservoir. *J. Geophys. Res.: Solid Earth* **107**, 2189.

Green, H.W. (1972) A CO_2 charged asthenosphere. *Nature Phys. Sic.* **238**, 2-5.

Hazen, R.M., Downs, R.T., Jones, A.P. and Kah, L. (2013) Carbon mineralogy and crystal chemistry, In *Reviews in Mineralogy and Geochemistry*, (Eds. Hazen, R.M., Jones, A.P., Baross, J.A.). Mineralogical Society of America, Virginia, pp. 7-46.

Herzfeld, J. and Berger, A.E. (1980) Sideband intensities in NMR spectra of samples spinning at the magic angle. *The Journal of Chemical Physics* **73**, 6021-6030.

Jäger, C., Henning, T., Schlögl, R. and Spillecke, O. (1999) Spectral properties of carbon black. *Journal of Non-Crystallin Solids* **258**, 161-179.

Jambon, A. (1994) Earth degassing and large-scale geochemical cycling of volatile elements, In *Reviews in Mineralogy and Geochemistry*, (Eds. Carroll, M.R., Holloway, J.R.). Mineralogical Society of America, Washington, pp. 479-517.

Jones, A.R., Winter, R., Greaves, G.N. and Smith, I.H. (2005) ^{23}Na, ^{29}Si, and ^{13}C MAS NMR investigation of glass-forming reactions between Na_2CO_3 and SiO_2. *Journal of Physical Chemistry B* **109**, 23154-23161.

Kadik, A., Pineau, F., Litvin, Y., Jendrzejewski, N., Martinez, I. and Javoy, M. (2004) Formation of carbon and hydrogen species in magmas at low oxygen fugacity. *Journal of Petrology* **45**, 1297-1310.

Kaminski, É. and Jaupart, C. (1997) Expansion and quenching of vesicular magma fragments in Plinian eruptions. *J. Geophys. Res.: Solid Earth* **102**, 12187-12203.

Kanowski, M., Vieth, H.M., Lüders, K., Buntkowsky, G., Belz, T., Werner, H., Wohlers, M. and Schlögl, R. (1997) The structure of fullerene black and the incorporation of C_{60} investigated by ^{13}C NMR. *Carbon* **35**, 685-695.

Keppler, H., Wiedenbeck, M. and Shcheka, S.S. (2003) Carbon solubility in olivine and the mode of carbon storage in the Earth's mantle. *Nature* **424**, 414-416.

Kim, E.J. and Lee, S.K. (2011) Atomic structure of dissolved carbon in enstatite: Raman spectroscopy and quantum chemical calculations of NMR chemical shift. *Journal of Mineralogical Society of Korea* **24**, 289-300.

Kirkpatrick, R.J. and Brow, R.K. (1995) Nuclear-magnetic-resonance investigation of the structures of phosphate and phospahte-containing glasses: A review. *Solid State Nuclear Magnetic Resonance* **5**, 9-21.

Kirkpatrick, R.J., Oestrike, R., Weiss, C.A., Smith, K.A. and Oldfield, E. (1986) High-resolution ^{27}Al and ^{29}Si NMR spectroscopy of glasses and crystals along the join $CaMgSi_2O_6$-$CaAl_2SiO_6$. *American Mineralogist* **71**, 705-711.

Kobayashi, T., Yamamoto, J., Hirajima, T., Ishibashi, H., Hirano, N., Lai, Y., Prikhod'ko, V.S. and Arai, S. (2012) Conformity and precision of CO_2 densimetry in CO_2 inclusions: Microthermometry versus Raman microspectroscopic densimetry. *Journal of Raman Spectroscopy* **43**, 1126-1133.

Kohn, S.C., Brooker, R.A. and Dupree, R. (1991) ^{13}C MAS NMR - A method for studying CO_2 speciation in glasses. *Geochimica et Cosmochimica Acta* **55**, 3879-3884.

Kwak, J.H., Hu, J.Z., Hoyt, D.W., Sears, J.A., Wang, C.M., Rosso, K.M. and Felmy, A.R. (2010) Metal carbonation of forsterite in supercritical CO_2 and H_2O using solid state ^{29}Si, ^{13}C NMR spectroscopy. *Journal of Physical Chemistry C* **114**, 4126-4134.

Lee, B.H. and Lee, S.K. (2009) Effect of lattice topology on the adsorption of benzyl alcohol on kaolinite surfaces: Quantum chemical calculations of geometry optimization, binding energy, and NMR chemical shielding. *American Mineralogist* **94**, 1392-1404.

Lee, S.K. (2010) Effect of pressure on structure of oxide glasses at high pressure: Insights from solid-state NMR of quadrupolar nuclides. *Solid State Nuclear Magnetic Resonance* **38**, 45-57.

Lee, S.K. (2011) Simplicity in melt densification in multicomponent magmatic reservoris in Earth's interior revealed by multinuclear magnetic resonance. *Proceedings of the National Academy of Sciences of the United States of America* **108**, 6847-6852.

Lee, S.K. and Ahn, C.W. (2014) Probing of 2 dimensional confinement-induced structural transitions in amorphous oxide thin film. *Sci. Rep.* **4**, 4200.

Lee, S.K., Cody, G.D., Fei, Y.W. and Mysen, B.O. (2004) Nature of polymerization and properties of silicate melts and glasses at high pressure. *Geochim. Cosmochim. Ac.* **68**, 4189-4200.

Lee, S.K., Lee, S.B., Park, S.Y., Yi, Y.S. and Ahn, C.W. (2009) Structure of amorphous aluminum oxide. *Phys. Rev. Lett.* **103**.

Lee, S.K., Park, S.Y., Yi, Y.S. and Moon, J. (2010) Structure and disorder in amorphous alumina thin films: Insights from high-resolution solid-state NMR. *The Journal of Physical Chemistry C* **114**, 13890-13894.

Lee, S.K., Yi, Y.S., Cody, G.D., Mibe, K., Fei, Y. and Mysen, B.O. (2012) Effect of network polymerization on the pressure-induced structural changes in sodium aluminosilicate glasses and melts: ^{27}Al and ^{17}O solid-state NMR study. *The Journal of Physical Chemistry C* **116**, 2183-2191.

Lin, F., Bodnar, R.J. and Becker, S.P. (2007) Experimental determination of the Raman CH_4 symmetric stretching (v_1) band position from 1–650 bar and 0.3–22°C: Application to fluid inclusion studies. *Geochim. Cosmochim. Acta* **71**, 3746-3756.

Lin, Y., Zhang, L., Mao, H.-k., Chow, P., Xiao, Y., Baldini, M., Shu, J. and Mao, W.L. (2011) Amorphous diamond: A high-pressure superhard carbon allotrope. *Phys. Rev. Lett.* **107**.

Lloyd, A.S., Ruprecht, P., Hauri, E.H., Rose, W., Gonnermann, H.M. and Plank, T. (2014) NanoSIMS results from olivine-hosted melt embayments: Magma ascent rate during explosive basaltic eruptions. *J. Volcanol. Geoth. Res.* **283**, 1-18.

Mathez, E.A., Dietrich, V.J. and Irving, A.J. (1984) The geochemistry of carbon in mantle peridotites. *Geochimica et Cosmochimica Acta* **48**, 1849-1859.

Mikhail, S., Shahar, A., Hunt, S.A., Jones, A.P. and Verchovsky, A.B. (2011) An experimental investigation of the pressure effect on stable isotope fractionation at high temperature: Implications for mantle processes and core formation in celestial bodies from 1 GPa and up to 25 GPa, 42nd Lunar and Planetary Science Conference, The Woodlands, Texas.

Mookherjee, M. (2011) Elasticity and anisotropy of Fe_3C at high pressures. *American Mineralogist* **96**, 1530-1536.

Mookherjee, M., Nakajima, Y., Steinle-Neumann, G., Glazyrin, K., Wu, X., Dubrovinsky, L., McCammon, C. and Chumakov, A. (2011) High-pressure behavior of iron carbide (Fe_7C_3) at inner core conditions. *Journal of Geophysical Research: Solid Earth* **116**, B04201.

Moore, J.K., Surface, J.A., Brenner, A., Skemer, P., Conradi, M.S. and Hayes, S.E. (2015) Quantitative identification of metastable magnesium carbonate minerals by solid-state ^{13}C NMR spectroscopy. *Environmental Science & Technology* **49**, 657-664.

Morizet, Y., Brooker, R.A. and Kohn, S.C. (2002) CO_2 in haplo-phonolite melt: solubility, speciation and carbonate complexation. *Geochimica et Cosmochimica Acta* **66**, 1809-1820.

Morizet, Y., Paris, M., Gaillard, F. and Scaillet, B. (2009) Raman quantification factor calibration for CO-CO_2 gas mixture in synthetic fluid inclusions: Application to oxygen fugacity calculation in magmatic systems. *Chemical Geology* **264**, 58-70.

Morizet, Y., Paris, M., Gaillard, F. and Scaillet, B. (2010) C-O-H fluid solubility in haplobasalt under reducing conditions: An experimental study. *Chemical Geology* **279**, 1-16.

Mysen, B. (2013) Structure–property relationships of COHN-saturated silicate melt coexisting with COHN fluid: A review of in-situ, high-temperature, high-pressure experiments. *Chemical Geology* **346**, 113-124.

Mysen, B.O., Arculus, R.J. and Eggler, D.H. (1975) Solubility of carbon-dioxide in melts of andesite, tholeiite, and olivine nephelinite composition to 30 kbar pressure. *Contributions to Mineralogy and Petrology* **53**, 227-239.

Mysen, B.O., Fogel, M.L., Morrill, P.L. and Cody, G.D. (2009) Solution behavior of reduced C-O-H volatiles in silicate melts at high pressure and temperature. *Geochimica et Cosmochimica Acta* **73**, 1696-1710.

Mysen, B.O., Kumamoto, K., Cody, G.D. and Fogel, M.L. (2011) Solubility and solution mechanisms of C–O–H volatiles in silicate melt with

variable redox conditions and melt composition at upper mantle temperatures and pressures. *Geochimica et Cosmochimica Acta* **75**, 6183-6199.

Mysen, B.O. and Richet, P. (2005) Volatiles I. The system C-O-H-S, In *Silicate Glasses and Melts*. Elsevier.

Ni, H.W. and Keppler, H. (2013) Carbon in silicate melts, In *Reviews in Mineralogy and Geochemistry*, (Eds. Hazen, R.M., Jones, A.P., Baross, J.A.). Mineralogical Society of America, Virginia, pp. 251-287.

Oganov, A.R., Hemley, R.J., Hazen, R.M. and Jones, A.P. (2013) Structure, bonding, and mineralogy of carbon at extreme conditions, In *Reviews in Mineralogy and Geochemistry*, (Eds. Hazen, R.M., Jones, A.P., Baross, J.A.). Mineralogical Society of America, Virginia, pp. 47-77.

Pan, H., Pruski, M., Gerstein, B.C., Li, F. and Lannin, J.S. (1991) Local coordination of carbon atoms in amorphous carbon. *Phys. Rev. B* **44**, 6741-6745.

Papenguth, H.W., Kirkpatrick, R.J., Montez, B. and Sandberg, P.A. (1989) ^{13}C MAS NMR spectroscopy of inorganic and biogenic carbonates. *American Mineralogist* **74**, 1152-1158.

Parfitt, E.A. and Wilson, L. (2008) The role of volatiles, In *Fundamentals of Physical Volcanology*. Blackwell Science, pp. 64-76.

Pawley, A.R., Holloway, J.R. and McMillan, P.F. (1992) The effect of oxygen fugacity on the solubility of carbon oxygen fluids in basaltic melt. *Earth and Planetary Science Letters* **110**, 213-225.

Phillips, B.L., Xu, H., Heaney, P.J. and Navrotsky, A. (2000) ^{29}Si and ^{27}Al MAS-NMR spectroscopy of β-eucryptite ($LiAlSiO_4$): The enthalpy of Si,Al ordering. *American Mineralogist* **85**, 181-188.

Pretsch, E., Buhlmann, P. and Badertscher, M. (2009) Structure Determination of Organic Compounds - Tables of Spectral Data, 4th, revised and enlarged edition ed. Springer, Berlin.

Resing, H.A. (1969) NMR Relaxation in adamantane and hexamethylenetetramine: Diffusion and rotation. *Molecular Crystals* **9**, 101-132.

Richet, P. and Bottinga, Y. (1984) Anorthite, andesine, wollastonite, diopside, cordierite, and pyrope: Thermodynamics of melting, glass transitions, and properties of the amorphous phases. *Earth and Planetary Science Letters* **67**, 415-432.

Rockafellow, E.M., Fang, X., Trewyn, B.G., Schmidt-Rohr, K. and Jenks, W.S. (2009) Solid-state ^{13}C NMR characterization of carbon-modified TiO_2. *Chemistry of Materials: A Publication of the American Chemical Society* **21**, 1187-1197.

Rohrbach, A. and Schmidt, M.W. (2011) Redox freezing and melting in the Earth's deep mantle resulting from carbon-iron redox coupling. *Nature* **472**, 209-212.

Rosso, K.M. and Bodnar, R.J. (1995) Microthermometric and Raman spectroscopic detection limits of CO_2 in fluid inclusions and the Raman spectroscopic characterization of CO_2. *Geochimica et Cosmochimica Acta* **59**, 3961-3975.

Rust, A.C. and Cashman, K.V. (2011) Permeability controls on expansion and size distributions of pyroclasts. *J. Geophys. Res.: Solid Earth* **116**, B11202.

Santillán, J., Catalli, K. and Williams, Q. (2005) An infrared study of carbon-oxygen bonding in magnesite to 60 GPa. *American Mineralogist* **90**, 1669-1673.

Santoro, M., Gorelli, F., Haines, J., Cambon, O., Levelut, C. and Garbarino, G. (2011) Silicon carbonate phase formed from carbon dioxide and silica under pressure. *Proceedings of the National Academy of Sciences of the United States of America* **108**, 7689-7692.

Seitz, J.C., Pasteris, J.D. and Chou, I. (1996) Raman spectrscopic characterization of gas mixtures. II quantitative composition and pressure determination of the CO_2-CH_4 system. *American Journal of Science* **296**, 577-600.

Sen, S., Widgeon, S.J., Navrotsky, A., Mera, G., Tavakoli, A., Ionescu, E. and Riedel, R. (2013) Carbon substitution for oxygen in silicates in planetary interiors. *Proceedings of the National Academy of Sciences* **110**, 15904-15907.

Seto, Y., Hamane, D., Nagai, T. and Fujino, K. (2008) Fate of carbonates within oceanic plates subducted to the lower mantle, and a possible mechanism of diamond formation. *Phys. Chem. Miner.* **35**, 223-229.

Shcheka, S.S., Wiedenbeck, M., Frost, D.J. and Keppler, H. (2006) Carbon solubility in mantle minerals. *Earth and Planetary Science Letters* **245**, 730-742.

Shindo, K., Kondo, T. and Sakurai, Y. (2011) ^{1}H NMR study of hydrogen stored in activated carbon powder prepared by mechanical milling. *J. Alloy. Compd.* **509**, 4534-4537.

Si, Y. and Samulski, E.T. (2008) Synthesis of water soluble graphene. *Nano Lett.* **8**, 1679-1682.

Sides, I., Edmonds, M., Maclennan, J., Houghton, B.F., Swanson, D.A. and Steele-MacInnis, M.J. (2014) Magma mixing and high fountaining during the 1959 Kīlauea Iki eruption, Hawai'i. *Earth Planet. Sci. Lett.* **400**, 102-112.

Stebbins, J.F. (1995) Dynamics and structure of silicate and oxide melts: Nuclear magnetic resonance studies. *Structure, Dynamics and Properties of Silicate Melts* **32**, 191-246.

Stebbins, J.F. and Xue, X. (2014) NMR Spectroscopy of Inorganic Earth Materials, In *Reviews in Mineralogy and Geochemistry*, (Eds. Henderson, G.S., Neuville, D.R., Downs, R.T.). Mineralogical Society of America, Virginia, U.S.A., pp. 605-653.

Stolper, E., Fine, G., Johnson, T. and Newman, S. (1987) Solubility of carbon dioxide in albitic melt. *American Mineralogist* **72**, 1071-1085.

Sugioka, I. and Bursik, M. (1995) Explosive fragmentation of erupting magma. *Nature* **373**, 689-692.

Tangeman, J.A., Phillips, B.L., Navrotsky, A., Weber, J.K.R., Hixson, A.D. and Key, T.S. (2001) Vitreous forsterite (Mg_2SiO_4): Synthesis, structure, and thermochemistry. *Geophys. Res. Lett.* **28**, 2517-2520.

Taylor, R., Hare, J.P., Abdul-Sada, A.K. and Kroto, H.W. (1990) Isolation, separation and characterisation of the fullerens C_{60} and C_{70}: The third form of carbon. *J. Chem. Soc., Chem. Commun.*, 1423-1425.

Tingle, T.N. and Aines, R.D. (1988) Beta-track autoradiography and infrared-spectroscopy bearing on the solubility of CO_2 in albite melt at 2 GPa and 1450 °C. *Contributions to Mineralogy and Petrology* **100**, 222-225.

Tossell, J.A. (1995) Calculation of the ^{13}C NMR shieldings of the CO_2 complexes of aluminosilicates. *Geochimica et Cosmochimica Acta* **59**, 1299-1305.

Tsong, I.S.T. and Knipping, U. (1986) Solute carbon and carbon segregation in magnesium-oxide signle-crystals - A secondary ion mass-spectrometry study - comment. *Phys. Chem. Miner.* **13**, 277-279.

Tsong, I.S.T., Knipping, U., Loxton, C.M., Magee, C.W. and Arnold, G.W. (1985) Carbon on surfaces of magnesium oxide and olivine single crystals. Diffusion from the bulk or surface contamination? *Phys. Chem. Miner.* **12**, 261-270.

Wallace, P.J. (2005) Volatiles in subduction zone magmas: concentrations and fluxes based on melt inclusion and volcanic gas data. *Journal of Volcanology and Geothermal Research* **140**, 217-240.

Wen, N. and Brooker, M.H. (1995) Ammonium Carbonate, Ammonium Bicarbonate, and Ammonium Carbamate Equilibria: A Raman Study. *The Journal of Physical Chemistry* **99**, 359-368.

Wright, R.B. and Wang, C.H. (1973) Density effect on the Fermi resonance in gaseous CO_2 by Raman scattering. *The Journal of Chemical Physics* **58**, 2893-2895.

Zhang, C. and Duan, Z.H. (2010) GFluid: An Excel spreadsheet for investigating C-O-H fluid composition under high temperatures and pressures. *Computers & Geosciences* **36**, 569-572.

Zhang, Y. and Zindler, A. (1993) Distribution and evolution of carbon and nitrogen in Earth. *Earth and Planetary Science Letters* **117**, 331-345.

Chapter 3. Effect of pressure on the short-range structure and speciation of carbon in alkali silicate and aluminosilicate glasses and melts at high pressure up to 8 GPa: ^{13}C, ^{27}Al, ^{17}O and ^{29}Si solid-state NMR study

Eun Jeong Kim, Yingwei Fei, and Sung Keun Lee

Published in *Geochimica et Cosmochimica Acta*, 2018, v. 224, 327–343

Abstract

Despite the pioneering efforts to explore the nature of carbon in carbon-bearing silicate melts under compression, *experimental* data for the speciation and the solubility of carbon in silicate melts above 4 GPa have not been reported. Here, we explore the speciation of carbon and pressure-induced changes in network structures of carbon-bearing silicate (Na_2O-$3SiO_2$, NS3) and sodium aluminosilicate ($NaAlSi_3O_8$, albite) glasses quenched from melts at high pressure up to 8 GPa using multi-nuclear solid-state NMR. The ^{27}Al triple quantum (3Q) MAS NMR spectra for carbon-bearing albite melts revealed the pressure-induced increase in the topological disorder around 4 coordinated Al ($^{[4]}Al$) without forming $^{[5,6]}Al$. These structural changes are similar to those in volatile-free albite melts at high pressure, indicating that the addition of CO_2 in silicate melts may not induce any additional increase in the topological disorder around Al at high pressure. ^{13}C MAS NMR spectra for carbon-bearing albite melts show multiple carbonate species, including $^{[4]}Si(CO_3)^{[4]}Si$, $^{[4]}Si(CO_3)^{[4]}Al$, $^{[4]}Al(CO_3)^{[4]}Al$, and free CO_3^{2-}. The fraction of $^{[4]}Si(CO_3)^{[4]}Al$ increases with

increasing pressure, while those of other bridging carbonate species decrease, indicating that the addition of CO_2 may enhance mixing of Si and Al at high pressure. A noticeable change is not observed for ^{29}Si NMR spectra for the carbon-bearing albite glasses with varying pressure at 1.5 to 6 GPa. These NMR results confirm that the densification mechanisms established for fluid-free, polymerized aluminosilicate melts can be applied to the carbon-bearing albite melts at high pressure.

In contrast, the ^{29}Si MAS NMR spectra for partially depolymerized, carbon-bearing NS3 glasses show that the fraction of $^{[5,6]}Si$ increases with increasing pressure at the expense of Q^3 species ($^{[4]}Si$ species with one non-bridging oxygen as the nearest neighbor). The pressure-induced increase in topological disorder around Si is evident from an increase in peak width of $^{[4]}Si$ with pressure. ^{17}O NMR spectrum shows that the fraction of Na·O-$^{[5]}Si$ in carbon-bearing NS3 glasses is less than that of carbon-free NS3 glasses at 6 GPa potentially due to the formation of bridging carbonate species. While its presence is not evident from the ^{17}O NMR spectrum primarily due to low carbon concentration, ^{13}C MAS NMR results imply the formation of bridging carbonates, $^{[4]}Si(CO_3)^{[4]}Si$, above 6 GPa. The spin-lattice relaxation time (T_1) of CO_2 in albite melts increases with increasing pressure from 42 s (at 1.5 GPa) to 149 s (at 6 GPa). Taking the pressure-induced change in T_1 of carbon species into consideration, total carbon content in carbon-bearing albite melts increases with pressure from ~1 wt% at 1.5 GPa to ~4.1 wt% at 6 GPa. The results also reveal a noticeable drop in the peak intensity of free carbonates in carbon-bearing NS3 melts at 6 GPa, implying a potential non-linear change in the carbon solubility with pressure. The current results of carbon speciation in the silicate melts above 4 GPa provide an improved

link among the atomic configurations around carbon species, their carbon contents, and isotope composition of carbon-bearing melts in the upper mantle.

3.1. Introduction

CO_2 is among the most abundant volatile components in Earth's interior, and understanding the nature of carbon (e.g., speciation, solubility) in silicate melts at high pressure is essential to unraveling the property changes in carbon-bearing silicate melts in the mantle. The presence of CO_2 molecule and/or other carbon-bearing species in silicate melts changes the stability field of silicate crystals (Mysen and Richet, 2005), which controls the composition of partial melts generated by decompressional melting beneath the mid-ocean ridge (e.g., Dasgupta and Hirschmann, 2006; Dasgupta et al., 2013; Eggler, 1976; Evans et al., 1999; Wallace, 2005). The addition of CO_2 with H_2O in peridotitic melts is expected to decrease the solidus, which may have contributed to the presence of a low-velocity zone in the asthenosphere (e.g., Dasgupta et al., 2004; Eggler, 1976; Evans et al., 1999; Gu et al., 2005; Lee, 2010; Massuyeau et al., 2015; Song et al., 2004). The dissolved CO_2 in silicate melts affects the viscosity of silicate melts: the viscosity of $KAlSi_3O_8$ melts shows non-linear behavior as the viscosity decreases with increasing CO_2 content up to 5 wt% and then increases with more CO_2 in the melts, perhaps because of the complex role of CO_2 in silicate melts (White and Montana, 1990). In contrast, the viscosity of $NaAlSi_3O_8$ (albite) melts continuously decreases with increasing CO_2 contents in the silicate melts (Brearley and Montana, 1989).

Whereas the focus of the study is to reveal the effect of pressure on the speciation of carbon in silicate melts, carbon speciation has strong implications for carbon solubility in melts. The solubility of CO_2 in the silicate melts up to ~ 3.5 GPa has been experimentally explored. Here, we briefly summarize the solubility of carbon in silicate melts below 3.5 GPa. The total solubility of carbon in basaltic melts linearly increases up to 0.5 wt% with increasing pressure up to 0.2 GPa (Parfitt and Wilson, 2008). The solubility of carbon in the silicate melts tends to increase with increasing pressure, the ratio of non-bridging oxygen over tetrahedron (NBO/T), and the fraction of Mg and Ca, but it decreases with increasing temperature, the SiO_2 content, and the Na content (e.g., Eggler and Kadik, 1979; Eggler and Rosenhauer, 1978; Fine and Stolper, 1985; Kohn et al., 1991; Morizet et al., 2010; Mysen et al., 1975; Nowak et al., 2004). For instance, the total solubility of carbon species in synthesized $NaAlSi_4O_{10}$ melts increases up to 1.0 wt% at 2.5 GPa (Fine and Stolper, 1985), while the solubility in albite melts increases up to 2.5 wt% at 3.5 GPa (Brooker et al., 1999). In the natural olivine nephelinite-composition melts, the solubility ranges up to 17.7 wt% with increasing pressure up to 3 GPa (Eggler and Kadik, 1979; Kohn et al., 1991; Mysen et al., 1975).

The mechanisms for dissolving CO_2 and other carbon species (e.g., CO_3^{2-}, CO, and CH_4) into silicate melt are relatively well understood in the pressure range up to 3.5 GPa (Behrens et al., 2004; Blank and Brooker, 1994; Brooker et al., 1999; Kohn et al., 1991; Morizet et al., 2002; Morizet et al., 2014a; Morizet et al., 2015; Mysen et al., 1976; Mysen et al., 2009; Mysen et al., 2011; Pan et al., 1991; Tossell, 1995). FTIR and Raman spectroscopies are extensively used to identify the speciation and exact structural information

of carbon in silicate glasses and melts (Brooker et al., 1999; Burke, 2001; Hacura et al., 1990; Morizet et al., 2009; Moussallam et al., 2016; Mysen et al., 2009; Ni and Keppler, 2013; Pawley et al., 1992; Rosso and Bodnar, 1995; Seitz et al., 1996). Those studies found diverse molecular species (superscript mol), such as CO_2^{mol} and CO^{mol}, and other structurally bound species, such as bridging carbonate species and dissolved CO_2 (a molecule weakly bound to the bridging oxygen in the silicate network). In addition, the information from these vibrational spectroscopies can be useful in inferring the pressure conditions and slight changes in the topology of carbon species with increasing pressure and temperature. For instance, the peak splitting in the main CO_2 Raman peak (at 1337 cm^{-1}, i.e., the Fermi resonance) in fluid inclusions provides the internal pressure of the fluid inclusion (Bakker, 2003; Bodnar, 2003; Rosso and Bodnar, 1995; Seitz et al., 1996), and the gap between the two split carbonate peaks (at ~ 1500 cm^{-1}) in the FTIR spectra can give insights into the distortion of carbonate species in the silicate glasses (Brooker et al., 1999; Morizet et al., 2002).

NMR spectroscopy is complementary to the vibrational spectroscopy. It provides direct, element-specific, and quantitative information of atomic structures around nuclides of interest in silicate melts and glasses (e.g., Kirkpatrick and Brow, 1995; Kohn et al., 1991; Lee et al., 2001; Lee and Stebbins, 2003; Malfait et al., 2012; Papenguth et al., 1989; Park and Lee, 2012; Phillips et al., 2000; Stebbins, 1995b; Stebbins and Xue, 2014; Xue et al., 1989). ^{13}C NMR in particular has been effective in identifying carbon species in silicate melts and glasses (Cody et al., 2011; Herzfeld and Berger, 1980; Kohn et al., 1991; Morizet et al., 2014b; Morizet et al., 2015; Mysen, 2012). Previous studies on ^{13}C magic angle spinning (MAS) NMR have identified

CO_2 (at ~ 125 ppm), CO_3^{2-} (at ~ 160–170 ppm), and CO species (~ 184 ppm) in silicate glasses (Brooker et al., 1999; Feng et al., 2006; Kim et al., 2016; Kohn et al., 1991; Mysen, 2013; Tossell, 1995). The bridging carbonate ions that are linked to two framework cations, such as $^{[4]}Si(CO_3)^{[4]}Si$, $^{[4]}Si(CO_3)^{[4]}Al$, or $^{[4]}Al(CO_3)^{[4]}Al$, and the free carbonate ions that are near the network-modifying cations were proposed from the compositional dependence of carbonate peaks in NMR spectra (Brooker et al., 1999). The presence of the molecular CH_4 and CH_3 functional groups that are bound to the silicon tetrahedron is characterized by peaks at -5.4 and -2.1 ppm, respectively (Mysen, 2012). Because of the large ^{13}C chemical shift anisotropy of CO_2 (Herzfeld and Berger, 1980), the presence of spinning side bands of CO_2 in ^{13}C MAS NMR spectra indicates whether CO_2 is in a free-gas phase, such as in fluid inclusions, or within the silicate network and bound to the bridging oxygen (Kim et al., 2016; Kohn et al., 1991) (see section 3.2.2 for details).

On the basis of these experimental studies, two mechanisms for dissolving CO_2 into silicate glasses (i.e., solubility mechanisms) have been proposed (Fine and Stolper, 1985; Kohn et al., 1991; Morizet et al., 2015; Tossell, 1995): CO_2 dissolves as molecular CO_2 weakly bound to the bridging oxygen (depolymerization of silicate melts) or as CO_3^{2-} by transforming two non-bridging oxygen into bridging oxygen (polymerization of silicate melts) (Morizet et al., 2015; Tossell, 1995). The formation of bridging CO_3^{2-} [such as $^{[4]}Si(CO_3)^{[4]}Si$] in silicate melts may change the NBO/T in silicate melts, accounting for the observed changes in melt viscosity (e.g., Lee, 2011; Stebbins, 1995a). The formation of bridging carbonates, such as $^{[4]}Si(CO_3)^{[4]}Si$ and $^{[4]}Si(CO_3)^{[4]}Al$, also affects the atomic

environments of Al and Si. ^{27}Al triple quantum magic angle spinning (3QMAS) NMR has provided the details of Al coordination environments and their topological disorder (e.g., the increased dispersion of bond angle and length distributions) in carbon-free silicate glasses (e.g., Edén, 2015; Florian et al., 2007; Jaworski et al., 2012; Kim and Lee, 2013; Lee et al., 2016; Malfait et al., 2012; McMillan and Kirkpatrick, 1992; Neuville et al., 2008; Park and Lee, 2014; Stebbins et al., 2008). The changes in the coordination number of Al in silicate glasses are also observed with increasing pressure in the ^{27}Al 3QMAS NMR spectra (Allwardt et al., 2007; Gaudio et al., 2015; Lee, 2010; Lee et al., 2004). The degree of polymerization of silicate melts decreases with increasing pressure above 5–8 GPa at constant melt composition (Lee, 2011). The ^{29}Si MAS NMR studies at high pressure show the formation of highly coordinated Si in silicate glasses upon compression (Xue et al., 1991). Whether the network modification from the dissolved CO_2 in silicate glasses quenched from melts at high pressure can be seen in the ^{27}Al 3QMAS and ^{29}Si MAS NMR spectra remains to be investigated.

While experimental progress has been made in the carbon-bearing glasses and melts below 3.5 GPa, no experimental data for carbon-bearing silicate glasses above 3.5 GPa have been reported because the conventional piston-cylinder high-pressure apparatus is often operated below 4 GPa (e.g., Brooker et al., 1998; Brooker et al., 1999; Malfait et al., 2012; Morizet et al., 2007; Morizet et al., 2015). Whereas the experimental data have not been available for the speciation of carbon in silicate melts above 4 GPa, theoretical calculations using molecular dynamics (MD) simulation for carbon-bearing silicate melts up to 15 GPa has predicted that the total solubility of CO_2 increases with increasing pressure and is dependent on the

composition of silicate melts (Guillot and Sator, 2011; Vuilleumier et al., 2015). For example, first-principle MD simulation has shown that the proportion of CO_2 in kimberlite melts could reach up to ~ 4% at 12 GPa, while that in basaltic melts would be ~ 15% at the same pressure (Vuilleumier et al., 2015). MD simulation for carbon-bearing silicate melts at high pressure up to 15 GPa has shown that the fraction of CO_2^{mol} over $CO_2^{mol} + CO_3^{2-}$ in rhyolitic, mid-ocean ridge basalts and kimberlitic melts is in the range of 0.25–0.38 at 12 GPa (Guillot and Sator, 2011). The fraction of CO_3^{2-} is not a simple linear increase with pressure, but it drastically increases above 5 GPa (Guillot and Sator, 2011). The results also showed that free carbonate ions are dominant species in carbon-bearing kimberlite melts (75.4%) and about 52% of carbonate ions in basaltic melts at 12 GPa would be bound to one non-bridging oxygen atom in the silicate network (Vuilleumier et al., 2015). Based on these studies, it has been predicted that the degree of polymerization is positively correlated with the concentration of carbonate ions (Guillot and Sator, 2011; Vuilleumier et al., 2015). The fraction of bridging carbonate ions increases with increasing NBO/T, resulting in decreasing NBO/T in the system (Vuilleumier et al., 2015). As the NBO/T in silicate melts tends to decrease with increasing pressure, regardless of the melt composition (Lee, 2011), the presence of carbonate ions in silicate melts facilitates the reduction of NBO with pressure. To identify the effect of carbon species in the silicate network at high pressure, we need direct information about the bonds and coordination of carbon species in the silicate glasses and melts.

In this study, we explore the structures of silicate glasses quenched from melts at high pressure (topological disorder and coordination

environments of the framework cations) and speciation of carbon in silicate glasses quenched from melts at pressures up to 8 GPa in the sodium trisilicate binary system (Na_2O-$3SiO_2$, NS3) and the sodium aluminosilicate ternary system ($NaAlSi_3O_8$, albite), using high-resolution multi-nuclear (^{29}Si, ^{27}Al, ^{17}O, and ^{13}C) solid-state NMR. We seek to reveal the pressure-induced structural changes of carbon species in silicate melts in the upper mantle (up to 240 km depth), such as the formation of bridging carbonates up to 8 GPa. We also explore the effect of pressure on the spin-lattice relation time (T_1) of CO_2 in albite melts and derive quantitative information about the speciation and connectivity of carbon in silicate melts. We report the first experimental results of detailed coordination environments of framework cations (Si and Al) at high pressure above 4 GPa up to 8 GPa. We then discuss the effect of the structural changes in thermodynamic properties (i.e., solubility, isotope fractionation) of carbon-bearing silicate melts.

3.2. Experimental Methods

3.2.1. Sample preparation

Albite glass was synthesized from powdered Na_2CO_3, Al_2O_3, and SiO_2. About 0.2 wt% of Co oxides was added to enhance the spin-lattice relaxation, allowing us to collect spectra with improved signal-to-noise ratio in the same experimental time. The Na_2CO_3, Al_2O_3, and SiO_2 powders were dried overnight at 300 °C, and the weighted powders were mixed in an agate mortar. The mixture was decarbonated in a Pt crucible at 850 °C for 30 min, fused at 1300 °C for 1 h at ambient pressure, and then quenched into glasses by dropping the Pt crucible into distilled water. Albite glasses at 1.5 and 6 GPa were synthesized from two ^{13}C-dopped stating materials,

prepared by adding powdered 99.7% enriched $Na_2{}^{13}CO_3$ (2.71 wt% and 16.63 wt%, respectively), balanced with Al_2O_3 and SiO_2 powders, into the pre-synthesized albite glass. The amount of $Na_2{}^{13}CO_3$ needed for saturation of $^{13}CO_2$ in albite glass was estimated from the linear extrapolation of previous results (Brooker et al., 1999; Stolper et al., 1987). Because the carbon solubility in silicate melts has only been available up to 4 GPa, the amount of $Na_2{}^{13}CO_3$ in the starting oxide-carbonate mixture above 4 GPa needs to be assumed. Here, a factor of 2 was multiplied to the predicted solubility of $^{13}CO_2$ in albite glasses at 6 GPa from the previous study to ensure that the system was saturated with the CO_2. Although the presence of void space and/or fluid inclusion is not observed in the carbon-bearing albite glasses at 6 GPa, the calculated carbon contents in albite melts at 6 GPa are similar to the predicted solubility of carbon in albite melts at 6 GPa (see section 3.3.5 for the estimation of carbon contents). After each of the starting materials was loaded into a Pt capsule and sealed, the samples were loaded into a piston cylinder and a multi-anvil apparatus at the Geophysical Laboratory with a 1/2-inch assembly and an 18/11 (octahedron edge length/truncated edge length of the anvils) assembly, respectively. The samples were fused at 1.5 GPa and 1400 °C in the piston-cylinder apparatus for 25 min and at 6 GPa and 1700 °C in the multi-anvil device for 30 min, and then quenched to glasses by turning off the power. The initial quenching rate was approximately 500 °C/s. The carbon-free albite glass sample at 8 GPa was previously synthesized (Lee et al., 2004).

NS3 glasses were synthesized in the same manner as the synthesis of albite glasses using Na_2CO_3 and SiO_2. The amount of Na_2CO_3 needed for saturation of $^{13}CO_2$ in NS3 glass for 4, 6, and 8 GPa was estimated from the

Table 3.1. Experimental condition on carbon-bearing silicate glasses quenched from melts at high pressure.

	Albite glass		NS3 glass		
Pressure	1.5 GPa	6 GPa	4 GPa	6 GPa	8 GPa
wt% of $^{13}CO_2$ ($Na_2{}^{13}CO_3$)	0.76 wt% (2.71 wt%)	4.66 wt% (16.63 wt%)	0.09 wt% (0.39 wt%)	0.18 wt% (0.75 wt%)	0.27 wt% (1.13 wt%)
T, time	1350 °C, 25 min	1700 °C, 30 min	1400 °C, 30 min	1400 °C, 30 min	1400 °C, 30 min
Apparatus	Piston cylinder	Multi-anvil press	Multi-anvil press	Multi-anvil press	Multi-anvil press

* The amount of Na_2CO_3 needed for saturation of $^{13}CO_2$ in albite and NS3 melts was estimated from previous study (Brooker et al., 1999; Mysen et al., 2009; Stolper et al., 1987), and the factor of 2 was multiplied.

linear extrapolation of previous solubility data from melts formed in reduced conditions with an iron-wüstite buffer (IW, f_{O2} value of ~ -12) (Mysen et al., 2009). Note that carbon solubility into melts also depends on oxygen fugacity (f_{O2}). For instance, the solubility of carbon in Na_2O-$4SiO_2$ (NS4) melts in magnesite-hematite buffer (MH with estimated f_{O2} value of ~-4) is reported to be twice larger than that in iron-wüstite buffer (Mysen et al., 2011). The estimated f_{O2} in the current experiment was similar to that of C-CO (CCO) buffer (with estimated f_{O2} value of ~-7.5) (Zhang and Duan, 2010). Taking these into consideration, the amount of $Na_2{}^{13}CO_3$ in the starting NS3 glasses was calculated as a factor of 2 multiplied to the predicted solubility of carbon in NS3 glasses in reduced conditions (Mysen et al., 2009). 0.39, 0.75, and 1.13 wt% of $Na_2{}^{13}CO_3$ (corresponding to 0.09,

0.18, and 0.27 wt% of $^{13}CO_2$, respectively) were added to a pre-synthesized glass for experiments at 4, 6, and 8 GPa, respectively. The presence of void space was observed in carbon-bearing NS3 glasses quenched from melts at 6 GPa, suggesting that the NS3 glasses at 6 GPa is saturated with carbon under the current oxygen fugacity conditions. The samples were loaded into a multi-anvil device at the Geophysical Laboratory with the 18/11 assembly. All the samples were fused at approximately 1400 °C for 30 min and then quenched to glasses. Table 3.1 shows experimental conditions on carbon-bearing silicate glasses quenched from melts at high pressure.

^{17}O-enriched NS3 glasses used for experiments at 6 GPa were synthesized in the same manner as the synthesis of NS3 glasses, using $Na_2{}^{13}CO_3$ and ^{17}O-enriched SiO_2 obtained from hydrolysis of 40% ^{17}O water with $SiCl_4$. The recovered samples were used for NMR experiments without grinding them into powder in order to avoid hydration and minimize the structural changes that might be associated with crushing and grinding. A previous study for ^{27}Al NMR of albite glasses at high pressure showed a potential drop in melt pressure during rapid quenching of the melts (Gaudio et al., 2015). The pressure conditions of the current study could also be slightly lower, leading to less fraction of highly-coordinated network-forming cations (e.g., $^{[5,6]}Al$) and lowering the solubility of total carbon in the silicate melts at high pressure. The glasses quenched from melts at high pressure preserve pressure-induced structural transitions in super-cooled melts (e.g., Lee, 2010; Xue et al., 1991). Therefore, the solubility and speciation of carbon in the glasses could be somewhat different from those in the melts. See supplementary materials 3.S1 for the effect of quench on the solubility of CO_2 in silicate melts and glasses.

Due to the difficulty in the sample synthesis of fluid-bearing silicate glasses at high pressure using multi-anvil press and the relatively long NMR data acquisition time for the ~ mg of sample (see, e.g., Lee, 2010 for the detailed review), it is challenging to get the sufficient spectral data. We have limited our study to 4, 6, and 8 GPa at which sufficient amount of sample can be synthesized in our largest sample assembly. Further study with more structural information at varying pressure conditions is desirable, but additional technical development and/or application of high-field NMR are required for sufficient number of NMR data acquisition.

3.2.2. NMR spectroscopy

The recent breakthroughs in high-resolution, solid-state NMR including multiple quantum magic angle spinning (MQMAS) NMR allowed us to explore the effect of pressure on the speciation of carbon in silicate glasses quenched from melt at high pressure by detecting tens of ppm of the nuclide (particularly, quadrupolar nuclides) of interest from ~5–15 mg of a sample (Kelsey et al., 2009; Lee, 2010; Lee et al., 2012a; Lee et al., 2010; Stebbins and Xue, 2014). The ^{13}C NMR study of carbon-bearing silicate glasses at high pressure has been challenging because of the relatively low natural abundance of ^{13}C combined with small high-pressure sample and the relaxation time of carbon species under varying pressure conditions. NMR spectroscopy is sensitive only to ^{13}C, whose natural abundance is only 1.1%. Combined with the solubility of CO_2 in silicate glasses (several wt%), the detectable carbon species in carbon-bearing silicate glasses would be at the level of hundreds of ppm. Therefore, samples should be enriched in ^{13}C in order to see the atomic structure using the solid-state NMR. The

relaxation time for carbon species is relatively long; for example, the T_1 for Na_2CO_3, $CaCO_3$, and $MgCO_3$ are ~ 1729 s, ~ 6418 s, and ~ 78 s, respectively (Moore et al., 2015). A long relaxation time for carbon species leads to time-consuming experimental schedules if the experiment is to get high-resolution NMR spectra from ^{13}C MAS NMR experiments. The T_1 of the nuclide of interest increases with increasing pressure, resulting in a signal decrease at high pressure under the same experimental conditions. Taking into consideration the T_1 relaxation time and recycle delay time of previous ^{13}C MAS NMR experiments for C-bearing enstatite at 1.5 GPa, we used 5 s of recycle delay time for conventional ^{13}C MAS NMR experiment (Kim et al., 2016). In the current study, ^{13}C MAS NMR spectra were collected on a Varian solid-state NMR 400 system (9.4 T) at a Larmor frequency of 100.582 MHz using a 3.2 mm Varian double-resonance probe (Seoul National University, Korea). A radio frequency pulse length of 1.3 μs was used, which corresponds to a 30° tip angle. Sample spinning speeds of 11 kHz for albite glasses and 17 kHz for NS3 glasses were used. Scans of free-induction decay (FID) that ranged from approximately 120,000 scans to 86,400 scans (5 to 7 days) were averaged to achieve the signal-to-noise ratio shown in the ^{13}C MAS NMR spectra. The spectra were referenced to solid adamantane (ADM), which is 38.6 ppm away from tetramethylsilane (TMS). We performed the identical ^{13}C MAS NMR experiments on the empty rotor to check the intensity of carbon background signal in the spectra as a stator and a rotor of NMR probes have carbon background signals. The background signal from the rotor and stator was subtracted from the collected ^{13}C spectra.

^{27}Al MAS NMR spectra were collect on the same NMR system at

Seoul National University at a Larmor frequency of 104.23 MHz using a 3.2 mm Varian double-resonance probe. The ^{27}Al 3QMAS NMR spectra were collected using a fast-amplitude modulation (FAM)-based shifted-echo pulse sequence (0.3 s relaxation delay – 3 μs pulse for 3Q excitation – t1 delay – FAM pulse train with a 0.7 μs pulse – echo delay – 15 us soft pulse for echo reconversion – t2 acquisition) (Baltisberger et al., 1996; Lee et al., 2009; Madhu et al., 1999). Collected for 28 hrs, 1,248 scans were averaged to achieve the current signal-to-noise ratio (with a minimum contour line of 4%) in the ^{27}Al 3QMAS NMR spectra. The ^{27}Al NMR spectra were referenced to an external 0.1 M $AlCl_3$ solution.

A ^{17}O 3QMAS NMR spectrum for NS3 glasses at 6 GPa was collected on a Varian solid-state NMR 400 system (9.4 T) at a Larmor frequency of 54.24 MHz. The ^{17}O 3QMAS NMR spectrum was collected using a FAM-based shifted-echo pulse sequence (3.3 μs pulse for 3Q excitation – t1 delay – FAM pulse train with a 1 μs pulse – echo delay – 11 μs soft pulse for echo reconversion – t2 acquisition) with a relaxation delay of 1 s. The ^{17}O NMR spectrum was measured using tap water as the external reference.

We collected ^{29}Si MAS NMR spectra at 9.4 T (Varian NMR spectrometer) using a single-pulse sequence (1.9 μs, a 30° tip angle) with a relaxation delay of 30 s at a Larmor frequency of 79.49 MHz. Sample spinning speeds of 11 kHz and approximately 20,000 scans (7 days) of FID were averaged to achieve the signal-to-noise ratio shown in the ^{29}Si MAS NMR spectra. The ^{29}Si MAS NMR spectra were referenced to TMS.

3.3. Results

3.3.1. ^{27}Al 3QMAS NMR results: Pressure-induced topological disorder in Al in carbon-bearing albite glasses quenched from melts at high pressure up to 6 GPa

Figure 3.1 presents the ^{27}Al 3QMAS NMR spectra for carbon-bearing albite glasses quenched from melts at 1.5 GPa and 6 GPa, and those for carbon-free albite glasses quenched from melts at 1 atm and 8 GPa (See Figure 3.S1 for ^{27}Al 1D MAS NMR spectra). Two Al-coordination environments—mostly $^{[4]}$Al and a small fraction of $^{[5]}$Al at 8 GPa—were resolved. These peak assignments are based on previous NMR studies on crystalline and glassy aluminosilicates (e.g., Baltisberger et al., 1996; Edén, 2015; Kelsey et al., 2008; McMillan and Kirkpatrick, 1992; Neuville et al., 2008; Toplis et al., 2000 and references therein).

The formation of highly coordinated Al (e.g., $^{[5, 6]}$Al) is not observed in carbon-bearing albite melts up to 6 GPa, while the peak width in the MAS dimension (y axis) increases from 60 ppm (~ 10–70 ppm) to 90 ppm (~ -20–70 ppm) with increasing pressure. The peak width in the MAS dimension of $^{[4]}$Al in the 3QMAS NMR spectra contains information about the magnitudes of quadrupolar interactions of Al and its topological disorder, such as changes in bond lengths and bond angles around Al environments and changes in isotropic chemical shifts (e.g., Edén, 2015; Lee, 2010; Park and Lee, 2012). Therefore, the increase in the peak width in the MAS dimension in the ^{27}Al 3QMAS NMR data suggests the pressure-induced topological disorder of Al in albite melts, such as distortion in Al polyhedron and Al-O bond length changes. Previous studies of the albite glasses quenched from melts at 8 GPa have suggested the formation of five

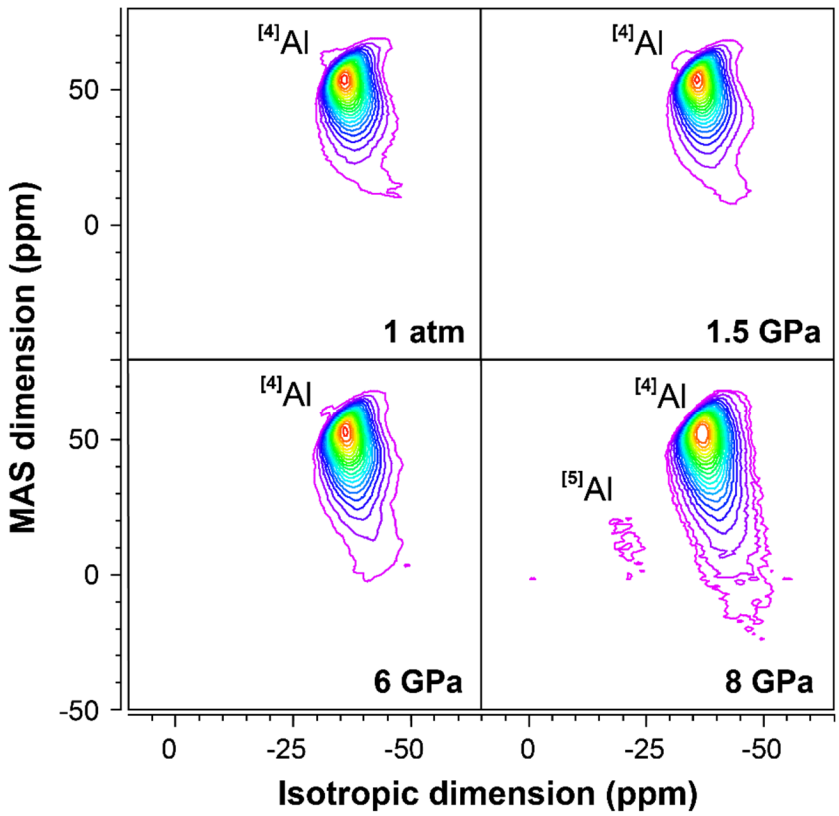

Figure 3.1. ^{27}Al 3QMAS NMR spectra for carbon-bearing albite glasses quenched from melts at 1.5 and 6 GPa and for carbon-free albite melts at 1 atm and 8 GPa.

coordinated Al in the system (Gaudio et al., 2015; Lee et al., 2004). The increases in the peak width in the MAS dimension of carbon-free albite melts and carbon-bearing albite melts seem to be identical, regardless of the presence of volatile species in the glass, indicating that the solubility of CO_2 in silicate melts may not result in any additional effect on the topological changes of Al in albite melts. See supplementary materials 3.S2 for the pressure-induced structural changes and the effect of carbon content on the structural evolution of Al.

3.3.2. ^{29}Si MAS NMR results: carbon-bearing Na_2O-3SiO_2 and albite glasses quenched from melts at high pressure

Figure 3.2a shows the ^{29}Si MAS NMR spectra of the carbon-bearing Na_2O-3SiO_2 (sodium trisilicate, NS3) glass up to 8 GPa. In the ^{29}Si MAS NMR spectra, peaks corresponding to the $^{[4]}$Si, $^{[5]}$Si, and $^{[6]}$Si are observed at ~ -90, -150, and -200 ppm, respectively (Kirkpatrick et al., 1986; Stebbins, 1995b and references therein). The ^{29}Si MAS NMR spectra for volatile-free NS3 glasses quenched from melts at high pressure have not been available, the presence of highly coordinated Si has been indicated from the decrease in NBO in volatile-free NS3 glasses quenched from melts at high pressure up to 10 GPa (Lee, 2011; Lee et al., 2003). Those for volatile-free sodium disilicate (NS2) and sodium tetrasilicate (NS4) melts at high pressure also showed the presence of highly coordinated Si above 6 GPa with 1.0%–8.5% of $^{[5,6]}$Si in the system (Xue et al., 1991).

The changes in the distribution of Q^n species in $^{[4]}$Si in carbon-bearing silicate melts are also shown in carbon-bearing NS3 glasses quenched from melts at high pressure. The ^{29}Si MAS NMR spectrum for carbon- bearing

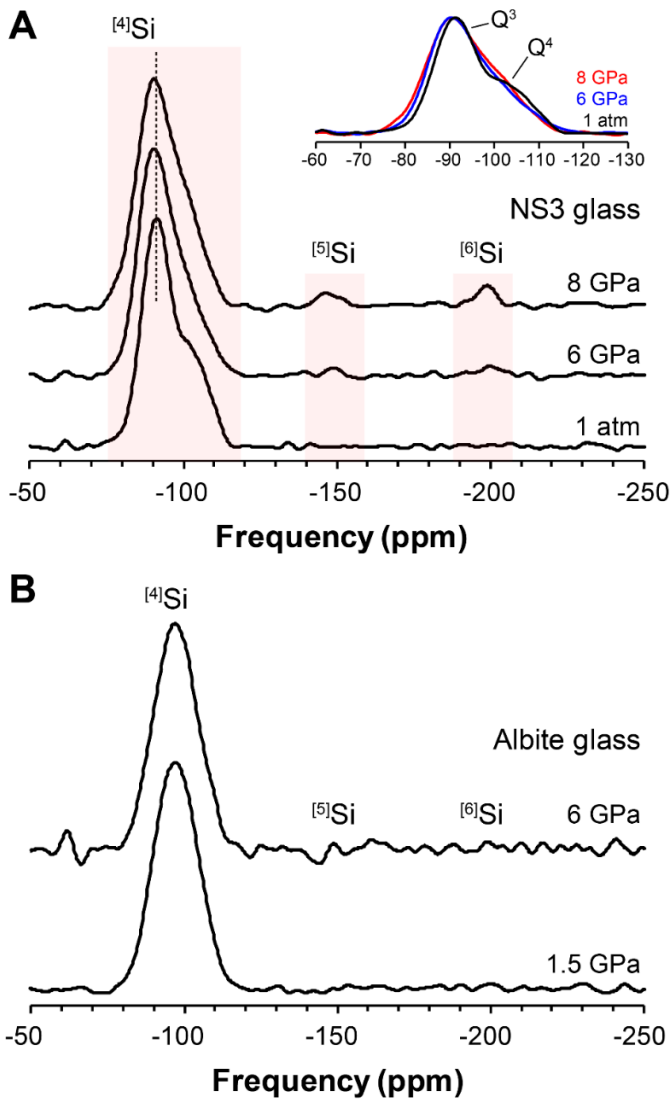

Figure 3.2. (A) ^{29}Si MAS NMR spectra for carbon-bearing NS3 (Na_2O-$3SiO_2$) glasses quenched from melts at 1 atm, 6, and 8 GPa in the range of -50 – -250 ppm. Inset shows ^{29}Si MAS NMR spectra for carbon-bearing NS3 melts at 1 atm, 6, and 8 GPa in the range of -60 – -130 ppm. (B) ^{29}Si MAS NMR spectra for carbon-bearing albite glasses quenched from melts at 1.5 and 6 GPa.

NS3 glasses at 1 atm shows a peak maximum at -91.4 ppm, with partially resolved peaks corresponding to Q^3 (~ -91 ppm) and Q^4 (~ -101 ppm) species (Maekawa et al., 1991). Those for NS3 glasses at 6 GPa and 8 GPa show that the peak maxima shift to a less negative frequency region, from -91.4 ppm at 1 atm to -90.7 ppm and -90.4 ppm at 6 and 8 GPa, respectively. The observed peak shifts toward higher frequency may result from the pressure-induced distortion of Si tetrahedron with increasing pressure, such as increases in Si-O-Si angles and Si-O bond lengths. It has been shown that the ^{29}Si MAS NMR peak positions of α-cristobalite and vitreous silica tend to decrease with increasing Si-O-Si angle (Mauri et al., 2000; Radeglia and Engelhardt, 1985) and that the chemical shift of silicate minerals decreases with increasing Si-O bond lengths (Skibsted et al., 1990). As also previously discussed in the carbon-free silicate glasses, the distribution of the bond angle and bond lengths of Si tetrahedron became wider with increasing pressure, indicating a pressure-induced increase in topological disorder (Xue et al., 1991), leading to an overall increase in the topological entropy with pressure (Lee, 2010; 2011)

The peak widths of $^{[4]}$Si are influenced by the disproportionation of Q^n species (the changes in the Q^n species into Q^{n-1}+Q^{n+1}) (Stebbins, 2016) and the pressure-induced changes in the Q^n species (Xue et al., 1991). Although the assessment of the fraction of each Q^n species is difficult due to peak overlap, the simulation results for ^{29}Si MAS NMR spectra for carbon-bearing NS3 glasses provide insight into pressure-induced changes in Q^n species (See supplementary materials 3.S3 and Figure 3.S2). The apparent increase of peak intensity at around -85 ppm (Q^2 species) and -100 ppm (Q^4 species)

with increasing pressure is observed in Figure 3.2a. This may be explained by the following mass balance equation:

$$2Q^3 = Q^2 + Q^4. \quad (1)$$

The similar disproportionation reaction has also been observed in carbon-free NS2 and NS4 glasses at high pressure up to 10 GPa (Xue et al., 1991; Xue et al., 1989). The changes in the fraction of Q^n species in carbon-baring silicate melts in the current study may also result from the formation of highly coordinated Si at high pressure. The proposed formation mechanism for highly coordinated Si is

$$Q^3 + Q^4 = Q^{4*} + {}^{[5]}Si \quad (2)$$

$$2Q^3 + Q^4 = 2Q^{4*} + {}^{[6]}Si, \quad (3)$$

where Q^{4*} is a SiO_4 species with three $^{[4]}Si$ and one $^{[5,6]}Si$ (Wolf et al., 1990; Xue et al., 1991). As also evidenced from the formation of $^{[5.6]}Si$ in the carbon bearing silicate glasses at high pressure (Figure 3.2a), the formation of Q^{4*} species in the glasses may contribute to the observed peak shift toward less negative frequency region (~1 ppm, Figure 3.2a) because a decrease in Si-O bond lengths and the reduction of Si-O-Si bond angle in Q^{4*} is expected by the formation of $^{[5,6]}Si$ as the next-nearest neighbors. The trend is consistent with previous studies for carbon-free NS2 glasses (Xue et al., 1989).

We note that the observed shift in ^{29}Si NMR spectra for the glass studied here is somewhat smaller than that reported from nephelinite melts (alkali silicate glasses with varying types of non-network formers, such as K and Na) at pressures up to 300 MPa (Morizet et al., 2014a). Although the differences in melt composition and pressure condition between the current study and the earlier study prohibit direct comparison, we did not observe any noticeable change in the NMR peak position with pressure for NS3

glasses quenched from melts at high pressure up to 8 GPa. The observed difference between these studies may also be due to the water content in the nephelinite melts.

Figure 3.2b shows the ^{29}Si MAS NMR spectra for carbon-bearing albite glasses quenched from melts at 1.5 and 6 GPa. The spectra for carbon-bearing albite melts show that only the $^{[4]}$Si environment is present up to 6 GPa: the ^{29}Si NMR spectrum for carbon-bearing albite melts at 6 GPa is largely identical to that at 1.5 GPa (Figure 3.2b). Together with the pressure-induced topological disorder of Al in albite melts (Figure 3.1), the absence of changes in the ^{29}Si MAS NMR spectra for albite melts at 1.5 and 6 GPa suggests that the densification mechanisms in sodium aluminosilicate melts change the Al environments (including bond lengths and angles), rather than the Si environment, as is also well understood in carbon-free aluminosilicate melts (e.g., Lee, 2010; Lee et al., 2004; Yarger et al., 1995 and references therein). The results show that the densification mechanism for aluminosilicate melts at high pressure can also be applied to the carbon-bearing aluminosilicate melts.

3.3.3. ^{17}O NMR results: oxygen environments in carbon-bearing Na_2O-$3SiO_2$ glasses quenched from melts at high pressure

Figure 3.3 shows the ^{17}O 3QMAS NMR spectrum for carbon-bearing NS3 glasses at 6 GPa, which indicates the presence of Na$\cdots$O-$^{[4]}$Si, $^{[4]}$Si-O-$^{[4]}$Si, and Na$\cdots$O-$^{[5]}$Si (See Figure 3.S3 for ^{17}O 1D MAS NMR spectrum). The feature is similar to that observed for carbon-free NS3 glasses (Lee, 2004). However, the observed peak intensity of Na$\cdots$O-$^{[5]}$Si in this study is twice smaller than that in previous study (Lee, 2004). This difference in NBO

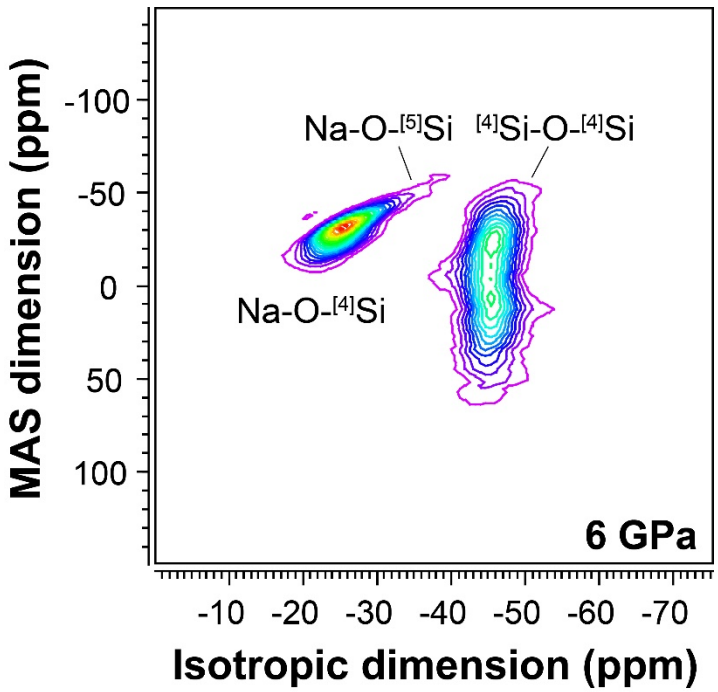

Figure 3.3. ^{17}O 3QMAS NMR spectrum for carbon-bearing NS3 melts at 6 GPa.

(Na ··O-[5]Si) is partly due to the difference in the magnetic field studied (9.4 T NMR in this study and 7.1 T in the previous study) because fraction of the larger C_q sites (e.g. [4]Si-O-[4]Si) can be somewhat underestimated at lower magnetic field, and therefore NBO fraction can be overestimated. Furthermore, a decrease in Na ··O-[5]Si in carbon-bearing NS3 glasses may be because the oxygen has been consumed to form bridging carbonate, prohibiting the formation of highly coordinated Si linked with non-bridging oxygen. Our preliminary quantum chemical calculation shows that peak position of ^{17}O in carbonate–[4]Si is ~160 ppm in the MAS dimension of the spectra, consistent with the assignment in the previous experimental study (Morizet et al., 2017), but its presence is not clear. Note that it is challenging to detect a change in the oxygen site fraction of approximately 1 mol% in the oxygen environment from the ^{17}O 3QMAS NMR spectra (Du and Stebbins, 2005; Lee et al., 2016; Park and Lee, 2014). See section 3.4.3 for origin of the presence of bridging carbonate ions in NS3 glasses upon compression and 3.S4 for the estimation of bridging oxygen with silicate and carbonates.

3.3.4. ^{13}C MAS NMR results of carbon-bearing albite glasses quenched from melts at high pressure

Figure 3.4a shows the ^{13}C MAS NMR spectra for carbon-bearing albite glasses quenched from melts at 1.5 and 6 GPa. Based on previous ^{13}C MAS NMR studies for diverse carbon-bearing silicate glasses, the trends observed in the quantum chemical calculations, and the changes in peak shape with increasing Al contents, the peaks at ~125 ppm, 150–170 ppm, and 181–185 ppm can be assigned to CO_2 bound to the silicate network, CO_3^{2-}, and dissolved CO in an albite melt system, respectively (Feng et al.,

2006; Jones et al., 2005; Kim et al., 2016; Kohn et al., 1991; Moore et al., 2015; Morizet et al., 2007; Morizet et al., 2010; Morizet et al., 2014a; Mysen et al., 2011; Papenguth et al., 1989; Tossell, 1995). The background-subtracted ^{13}C MAS NMR spectra in Figure 3.4b show at least four different peaks for CO_3^{2-} species, the carbonate peaks at 171, 165, 160, and 155 ppm, assigned to the free carbonates, $^{[4]}Al(CO_3)^{[4]}Al$, $^{[4]}Si(CO_3)^{[4]}Al$, and $^{[4]}Si(CO_3)^{[4]}Si$, respectively (Brooker et al., 1999) (See Figure 3.8 for deconvolution of NMR spectra). CO_2 is the dominant species among the carbon species in carbon-bearing albite melts at high pressure. The fraction of CO_2 and CO_3^{2-} increases with increasing pressure, while that of CO decreases because of the thickness of the graphite heater compared with that of the sample and the increased strength of the carbon infiltration effect in the piston cylinder (1.5 GPa) compared to that in multi-anvil press (6 GPa). See section 3.4.5 for additional discussion. The spectra in Figure 3.4 also revealed the changes of carbonate species at different pressures. The fraction of $^{[4]}Si(CO_3)^{[4]}Al$ increases with increasing pressure, while those of $^{[4]}Si(CO_3)^{[4]}Si$ and $^{[4]}Al(CO_3)^{[4]}Al$ decrease slightly with increasing pressure. This indicates that an addition of CO_2 results in an enhanced mixing between Si and Al at high pressure. See section 3.4.4 for detailed fractional changes of carbonate species with increasing pressure.

The CO_2 peak shows strong spinning side bands on each side (~ 240 ppm and ~ 20 ppm) and relatively large ^{13}C NMR chemical shift anisotropy (~ 260-270 ppm) (Ettinger et al., 1960; Kohn et al., 1991). The presence of spinning side bands of CO_2 reflects that CO_2 is bound to the silicate glass network and that the degree of freedom of CO_2 decreases (Ettinger et al., 1960; Herzfeld and Berger, 1980; Kohn et al., 1991). To identify the atomic

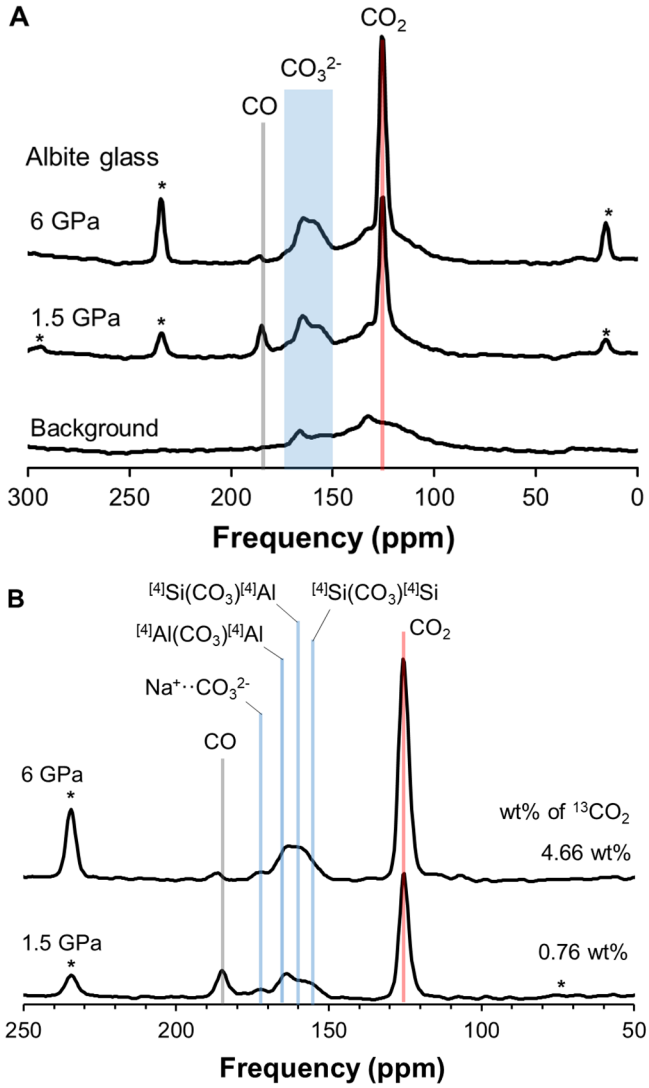

Figure 3.4. (A) Background-included and (B) background-subtracted ^{13}C MAS NMR spectra for carbon-bearing albite melts at 1.5 and 6 GPa. The spectra are normalized with the weight of the samples. Spinning sidebands are marked with an asterisk. The numbers labeled on the right side of the spectra refer to the amount of input CO_2 in the system. See section 2.2 for the measurement of background signal.

configuration of CO, it is necessary to confirm whether CO is structurally incorporated or exsolved in the silicate network, for which the spinning sidebands patterns and the FWHM of the peak can be used. For instance, structurally bound CO results in the emergence of strong spinning sideband patterns, as expected from its large ^{13}C chemical shift anisotropy (335 ± 20 ppm) (Gibson et al., 1977), while molecular CO, such as CO inclusion, may not show spinning sidebands (Kim et al., 2016). The expected positions of the spinning sidebands for CO in albite melts are at ~ 290 ppm and ~ 70 ppm. Thus, the presence of the spinning side bands of CO in albite melts at 1.5 GPa suggests its incorporation into the network. The incorporation of CO into the silicate network can also be confirmed by FWHM. A previous ^{13}C MAS NMR spectrum for carbon-bearing fluid inclusion in crystalline $MgSiO_3$ at 1.5 GPa showed that the molecular CO in fluid inclusion has a sharp peak with FWHM of ~ 0.6 ppm (Kim et al., 2016), while CO in albite glasses quenched from melts at both 1.5 and 6 GPa (Figure 3.4b) has a relatively broad FWHM of ~ 5 ppm. The lack of sharp peak due to CO, therefore, indicates that carbon-bearing albite melts at 6 GPa do not have fluid inclusion with molecular CO. Although the detailed atomic configurations around the dissolved CO remain to be confirmed, based on the NMR characteristics (e.g., spinning side bands and FWHM) of the CO peak, the CO may have a moderate degree of interaction with nearby bridging oxygens.

In order to have quantitative estimation of the carbon species fractions, the T_1 relaxation time of CO should be considered in quantifying the carbon species in albite melts. The interaction between CO_2 and the silicate network may also affect the decrease in peak intensity with

increasing pressure, such as that which occurs with an increase in T_1 relaxation time. These aspects were discussed in the following sections (e.g., see section 3.3.6 and 3.4.5 for the saturation-recovery experiments for CO_2, quantification of carbon species in albite melts at high pressure, and the presence of CO in albite melts at high pressure).

3.3.5. ^{13}C MAS NMR results for carbon-bearing NS3 glasses quenched from melts at high pressure up to 8 GPa

Figure 3.5 shows the ^{13}C MAS NMR spectra for carbon-bearing NS3 glasses quenched from melts at 4, 6, and 8 GPa. The observed peak at ~ 171 ppm can be assigned to the free carbonates (Morizet et al., 2014a; Tossell, 1995). The free carbonate peak shifts to lower frequency with increasing pressure, with the peak positions from 171.7 ppm at 4 GPa to 170.2 ppm at 8 GPa, respectively. The peak shift of carbonates in scapolite (a solid-solution of $Na_4Al_3Si_9O_{24}Cl$ and $Ca_4Al_6Si_6O_{24}CO_3$) showed ~ 3 ppm peak shift to the lower frequencies when the planar carbonates were bent less than 3° to the (001) plane (Kohn et al., 1991; Sherriff et al., 1987). If the peak shift of carbonates in NS3 glasses is due to the bending of carbonate species upon compression, the bending of free carbonates in NS3 melts would be less than 3° with increasing pressure. The peak intensity of free carbonates shows non-linear changes with increasing pressure: the peak intensity of free carbonates decreases from 4 GPa to 6 GPa and then increases to 8 GPa (see Table 3.S1 for the simulation parameters and results). These aspects and its implications were discussed in the following sections (see section 3.4.6). In addition, the signal at ~ 161 ppm, the peak position for bridging carbonates [e.g., $^{[4]}Si(CO_3)^{[4]}Si$], apparently increases with increasing pressure above 6 GPa. While this position is within the errors because of the

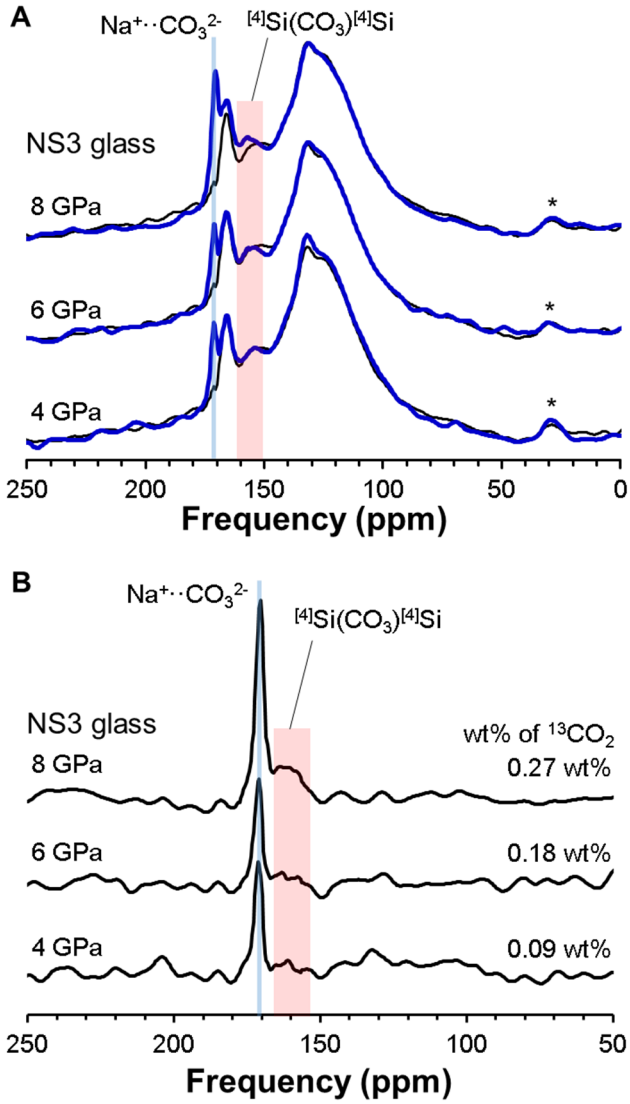

Figure 3.5. (A) ^{13}C MAS NMR spectra for carbon-bearing NS3 melts at 4, 6, and 8 GPa (blue) and background (black). (B) background-subtracted ^{13}C MAS NMR spectra for carbon-bearing NS3 melts at 4, 6, and 8 GPa. Spinning sidebands are marked with an asterisk. The numbers labeled on the right side of the spectra refer to the amount of input CO_2 in the system. See section 2.2 for the measurement of background signal.

peak overlap, these two phenomena—the peak shift of free carbonates toward low frequency and the manifestation of bridging carbonates at high pressure above 6 GPa—may be related to the pressure-induced distortion of carbonates and the formation of bridging oxygen with the silicate network in the carbon. See section 3.4.2 and 3.4.3 for peak assignment and supplementary materials 3.S5 for the simulation results.

3.3.6. Quantitative measurements of the speciation of carbon in albite melts by ^{13}C MAS NMR spectra using ^{13}C spin-lattice (T_1) relaxation results and analyses

The initial $^{13}CO_2$ contents in albite glasses are 0.76 and 4.66 wt% at 1.5 and 6 GPa, respectively. Whereas the initial input of carbon in albite glasses quenched from melts at 6 GPa is approximately six times larger than that at 1.5 GPa, the total peak intensity of carbon species in carbon-bearing albite melts (with a 5 s delay time) increases ~ 1.6 times from the sample at 1.5 GPa to the sample at 6 GPa (Figure 3.4). This result may be due to a relatively small increase in the carbon solubility into the silicate melts at high pressure or primarily due to the pressure-induced changes in the spin-lattice relaxation time. As for the latter, ^{13}C MAS NMR spectroscopy is a quantitative analysis tool that is used when the relaxation delay time of the experimental conditions is sufficiently long (e.g., longer than three times the T_1 relaxation time). As the delay time of 5 s was chosen from the experimental conditions for CO_2 in fluid inclusion in enstatite at 1.5 GPa (Kim et al., 2016), calibration of peak intensity with the spin-lattice relation time (T_1) is necessary. It has been observed that the T_1 relaxation time of carbon species increases with increasing pressure partly due to an increase

in network rigidity with pressure, reducing the peak intensity with increasing pressure (Kim et al., 2016). Therefore, ^{13}C saturation-recovery experiments were performed to determine whether the origin of the reduction of peak intensity is from the differences in the T_1 relaxation time or from the lower solubility of carbon in albite glasses.

Figure 3.6 shows the peak intensity of the ^{13}C NMR signal (M) normalized with respect to the peak area of a fully relaxed spectrum (M_0) with varying delay times (τ, time between $\pi/2$ pulse and π pulse in T_1 relaxation time measurement). The spin-lattice relaxation time can be described using the following equation (Abragam, 1961):

$$M / M_0 = 1 - exp[-(\tau / T_1)] \quad (4)$$

As shown in Figure 3.6, the ^{13}C NMR peak intensities of CO_2 for carbon-bearing albite glasses at 1.5 and 6 GPa were well fitted with 42 s and 149 s of T_1 relaxation time, respectively. From the calculated T_1 relaxation time of CO_2 for carbon-bearing albite glasses, the estimated normalized peak intensity of CO_2 with respect to the fully relaxed maximum peak intensity is ~ 0.16 at 1.5 GPa. Because of the difference in T_1, the estimated normalized peak intensity of CO_2 at 6 GPa is estimated to be ~ 0.06 at 6 GPa, indicating that the peak intensity is largely underestimated. The difference in the intensity ratios of CO_2 at 1.5 and 6 GPa is ~ 2.8 from the normalized peak intensity of CO_2 with respect to the fully relaxed maximum peak intensity, and ~ 3.5 from the differences in the T_1 relaxation time. The T_1 relaxation time for CO_2 in albite glasses at 6 GPa is approximately three times longer than that at 1.5 GPa, so its peak intensity at 6 GPa is underestimated (~ 1/3 of the intensity at 1.5 GPa) when identical NMR acquisition condition (i.e., relaxation delay of 5 s) is used. Therefore, it is

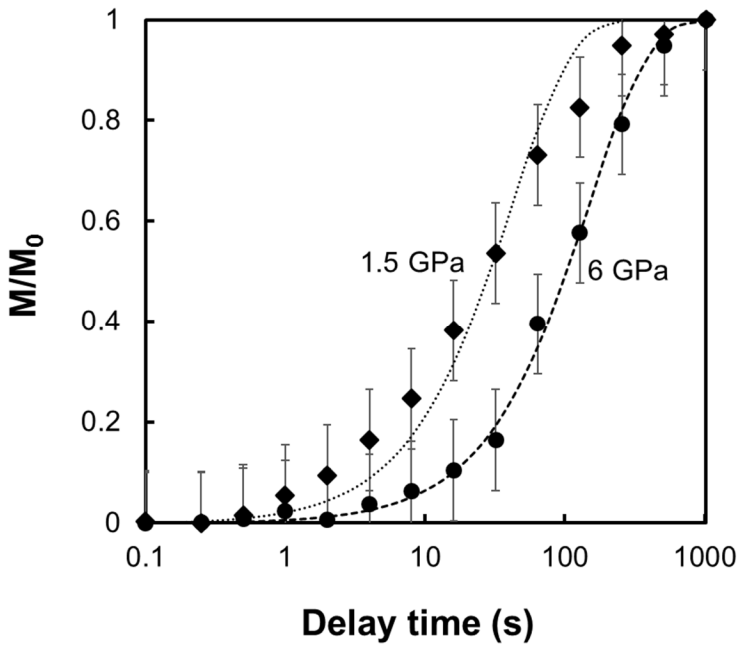

Figure 3.6. Saturation-recovery of CO_2 in the carbon-bearing albite melts at 1.5 GPa and 6 GPa. Diamonds and circles refer to the normalized peak intensity of carbon-bearing albite glasses at 1.5 and 6 GPa, respectively, with varying delay time. Solid lines and dashed lines refer to calculated peak intensity, following the spin-lattice relaxation time equation. Error bars represent a 10% error.

essential to calibrate the intensity at different pressures by determining the effect of pressure on the estimated T_1 relaxation time.

Figure 3.7 illustrates the total carbon content and the relative amount of each carbon species (calibrated with difference in T_1 relaxation time with pressure) in carbon-bearing albite melts with increasing pressure. Solubility data for carbon-bearing albite melts is available up to 3.5 GPa (Brooker et al., 1999; Stolper et al., 1987). We calculated the proportion of each carbon species in carbon-bearing albite melts from the peak area of each carbon species from the ^{13}C MAS NMR spectra. The T_1 for CO and CO_3^{2-} species has not been measured because of their low S/N ratio and intensities. Nevertheless, we assumed similar changes in pressure-induced T_1 relaxation times for CO and CO_3^{2-} (~ 3 times longer with increasing pressure from 1.5 to 6 GPa).

Taking into consideration of the T_1 relaxation time of CO_2 and similar increases in the relaxation times for other carbon species, the estimated amount of CO_2, CO_3^{2-}, and CO at 1.5 GPa are 0.52, 0.34, and 0.14 wt%, respectively. The calibrated amount of CO_2, CO_3^{2-}, and CO at 6 GPa are 2.69, 1.32, and 0.08 wt%, respectively. The total amount of carbon species in carbon-bearing albite glasses at 6 GPa is ~ 4.10 wt%. The calculated carbon contents in the current study are generally consistent with the previous studies (Brooker et al., 1999; Stolper et al., 1987). The current results may present a minimum solubility and thus the actual solubility of total carbon in albite melts up to 6 GPa is higher than 4 wt%. Note that without taking the T_1 relaxation time of CO_2 into consideration, the CO_2 contents in albite melts at 6 GPa (marked as raw data in Figure 3.7) would be 0.95 wt%, and the total amount of carbon would be ~ 1.44 wt%, which is far below the

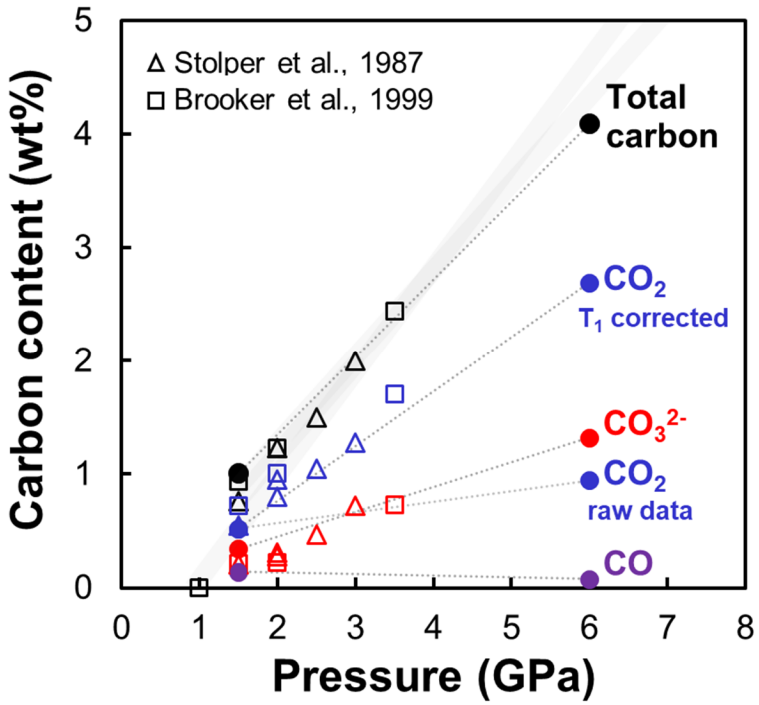

Figure 3.7. Carbon contents in the albite melts with increasing pressure. Black, blue, red, and violet closed circles refer to total carbon content and the amount of CO_2, CO_3^{2-}, and CO species in albite glasses calculated from ^{13}C MAS NMR spectra, respectively. Open triangles and rectangles refer to data from Stolper et al. (1987) and Brooker et al. (1999), respectively.

input amount of carbon in the albite glasses at 6 GPa. Recent ^{13}C NMR study presented a calibration curve between ^{13}C abundance and ^{13}C MAS NMR peak intensity of ADM-SiO_2 mixture (Kim et al., 2016). Using this calibration curve, the calculated carbon contents in the carbon-bearing albite glasses is similar to the amount of ^{13}C initially added in the starting silicates.

Note again that the focus of the study is to explore the effect of pressure on carbon species in silicate melts and thus, quantitative estimation of the solubility may not be fully achievable based on current data alone. Nevertheless, the speciation of carbon and the abundance of each carbon species in silicate melts at high pressure has been successfully calculated by using ^{13}C NMR. These structural data are critical for understanding the solubility and the dissolution mechanism of carbon in silicate melts above 4 GPa. As the consideration the spinning sidebands does not affect the simulation results significantly (e.g., Lee and Ahn, 2014), the proportion of each carbon species in carbon-bearing albite glasses was calculated from the peak area of each carbon species without the consideration of the spinning sidebands. The estimated fractions of CO_2, CO_3^{2-}, and CO from the modified ^{13}C MAS NMR spectrum are 52, 34, and 14% at 1.5 GPa, and 66, 32, and 2% at 6 GPa, respectively, with a ± 10% error bar. Because the exact T_1 times for CO and CO_3^{2-} species are not available, the estimated fractions of carbon species may be subject to a larger uncertainty despite smaller uncertainty in the fitting results. Therefore, the proportions reported here are mainly for the semi-quantitative discussion. Despite the uncertainty, the trend of changes of carbonate species with increasing pressure is evident from the ^{13}C MAS NMR spectra. The fraction of CO_2 in albite melts, taking T_1 time into consideration, matches well with the theoretical results of the fraction

of CO_2 (~ 60% among the carbon species) in rhyolite melts at 5 GPa that were calculated using the MD simulation (Guillot and Sator, 2011). Previous study showed that the fraction of CO_3^{2-} to total carbon contents in albite glasses increased from 23–27% at 1.5 GPa to 27–34% at 3 GPa using IR spectroscopy (Stolper et al., 1987). However, the current results showed that the calibrated fraction of carbonates slightly decreases from ~34 % at 1.5 GPa to ~32 % at 6 GPa. This is consistent with the result for the carbon-bearing albite glasses using ^{13}C NMR spectroscopy (Brooker et al., 1999). The observed difference between the IR result and the study may reside in the difference in analytical methods.

3.4. Discussion

3.4.1. ^{13}C NMR peak assignment of bridging carbonate ions in carbon-bearing albite and NS3 glasses

The ^{13}C NMR peak assignment of the carbonate groups in silicate glasses has been performed using the quantum chemical calculations and the experimental NMR study (Kohn et al., 1991; Morizet et al., 2014b; Tossell, 1995). We assigned the peaks at 165, 160, and 155 ppm to $^{[4]}Al(CO_3)^{[4]}Al$, $^{[4]}Si(CO_3)^{[4]}Al$, and $^{[4]}Si(CO_3)^{[4]}Si$, respectively, based on the increase in the peak intensity at 165 ppm when the fraction of Al_2O_3 in the $NaAlO_2$-SiO_2 system increased (Brooker et al., 1999). A previous theoretical study based on the Hartree-Fock level of theory and the 6-31G* basis set suggested that $^{[4]}Al(CO_3)^{[4]}Al$, $^{[4]}Si(CO_3)^{[4]}Si$, and $^{[4]}Si(CO_3)^{[4]}Al$ would correspond to 168.4, 167.5, and 163.6 ppm, respectively (Tossell, 1995). Although the peak positions by simulations and experimental measurements are slightly different, the trends are in good agreement

(Morizet et al., 2015). The calculated chemical shifts for carbonate species linked to the silicate network can vary with the basis sets and the level of theory used for quantum chemical calculations (Frisch et al., 2004; Lee and Lee, 2009). Furthermore, the model clusters for the simulation did not include either network-modifying cations or charge-balancing cations (Tossell, 1995). The changes in the presence of charge-balancing cations would result in a shift in the peak position, which may explain the difference in the chemical shift values.

The signal at ~ 161 ppm in ^{13}C MAS NMR spectra for carbon-bearing NS3 glasses apparently increases with increasing pressure above 6 GPa (Figure 3.5). From the peak assignment of bridging carbonates in Na-aluminosilicates, the $^{[4]}Si(CO_3)^{[4]}Si$ peak is shown at ~155 ppm. In Al-free NS3 glasses, the absence of Al and charge-balancing Na in this system may lead to an increase in chemical shifts of the bridging carbonates $^{[4]}Si(CO_3)^{[4]}Si$ in the system. The peak at ~ 161 ppm in ^{13}C MAS NMR in NS3 glasses is likely to be due to $^{[4]}Si(CO_3)^{[4]}Si$.

3.4.2. ^{13}C NMR peak assignment of free carbonate ions in carbon-bearing NS3 glasses

The possible carbonate species in silicate melts are non-bridging carbonates, bridging carbonates, and free carbonate. The free carbonate is the carbonate ion that is charge-balancing with network-modifying cations, and that have no bridging oxygen in the carbon units linked with the silicate network (Brooker et al., 1999; Guillot and Sator, 2011; King and Holloway, 2002; Nowak et al., 2004; Vuilleumier et al., 2015). The ^{13}C chemical shift of the free carbonate in carbonate minerals ranges from ~ 166 to ~ 171 ppm

(Feng et al., 2006; Jones et al., 2005; Kwak et al., 2010; Moore et al., 2015; Papenguth et al., 1989).

The ^{13}C MAS NMR spectra for carbon-bearing NS3 glasses at high pressure up to 8 GPa (Figure 3.5) show the presence of a peak at ~ 171 ppm, indicating the presence of free carbonate ions in the glasses. The peak shift from 171.7 ppm at 4 GPa toward 170.2 ppm at 8 GPa is likely caused by the pressure-induced changes in the bending of free carbonates in NS3 glasses and/or the shortening of C-O bond lengths. The peak shift in free carbonates to the lower frequency has been interpreted as a distortion of carbonate species (Kohn et al., 1991; Sherriff et al., 1987). Reduction of the C-O bond length from 1.310 Å to 1.265 Å changes the isotropic chemical shift of the free carbonates from 187.7 ppm to 170.5 ppm (Tossell, 1995).

3.4.3. Origin of the presence of bridging carbonate ions in NS3 glasses upon compression

As shown in Figure 3.5b, the peak intensity of $^{[4]}Si(CO_3)^{[4]}Si$ increases with increasing pressure. However, the presence of bridging carbonates in ^{17}O 3QMAS NMR spectrum is not clear in the spectra. Based on ^{13}C NMR spectra for carbon-bearing NS3 glasses, a non-negligible fraction of carbon is expected to play a role as a bridging carbonates in NS3 glasses (Figure 3.S4). Therefore, the absence of clear spectroscopic evidence for the bridging carbonates in ^{17}O NMR is mainly due to the low total carbon concentration, especially considering possible peak overlap.

Note that the formation of bridging carbonates consumes the non-bridging oxygen in the system, and the degree of polymerization of silicate melts would increase. This is consistent with the increase in Q^4 species with

increasing pressure from 6 GPa to 8 GPa (Figure 3.2 and Figure 3.S2). In addition, as non-bridging oxygen is necessary to form the highly coordinated Si, it prohibits the formation of highly coordinated Si linked with non-bridging oxygen. Thus the formation of bridging carbonates accounts for the difference in the peak intensity decrease of Na···O-$^{[5]}$Si in ^{17}O 3QMAS NMR spectrum in Figure 3.3 and that of carbon-free NS3 glasses at 6 GPa (Lee, 2004).

3.4.4. The speciation of carbonates in albite glasses quenched from melt at high pressure

The carbon-bearing albite glasses quenched from melts at high pressure contain four distinct carbonate species, bridging carbonates [$^{[4]}$Al(CO_3)$^{[4]}$Al, $^{[4]}$Si(CO_3)$^{[4]}$Al, and $^{[4]}$Si(CO_3)$^{[4]}$Si] and non-bridging carbonates (Figure 3.4b). Here, the fraction of each carbonate species was obtained by fitting the ^{13}C MAS NMR spectra using four Gaussian functions representing $^{[4]}$Al(CO_3)$^{[4]}$Al (165 ppm), $^{[4]}$Si(CO_3)$^{[4]}$Al (160 ppm), $^{[4]}$Si(CO_3)$^{[4]}$Si (155 ppm), and free carbonates (~ 171 ppm) (Figure 3.8). The peak widths of each peak were fixed with FWHM of ~ 6 ppm. Figure 3.8 shows the CO_3^{2-} ion population for various carbonate species as a function of pressure. Here, we assume no differential relaxation time for distinct carbonate species at constant pressure condition. Due to the overlaps of the observed peaks, the estimated proportion of each carbonate species is not unique. Therefore, the following description is intended only as a semi-quantitative discussion. The uncertainty is estimated as 5% based on the simulation results with different factors (peak position and widths). The proportion of $^{[4]}$Al(CO_3)$^{[4]}$Al, $^{[4]}$Si(CO_3)$^{[4]}$Al, $^{[4]}$Si(CO_3)$^{[4]}$Si, and non-bridging

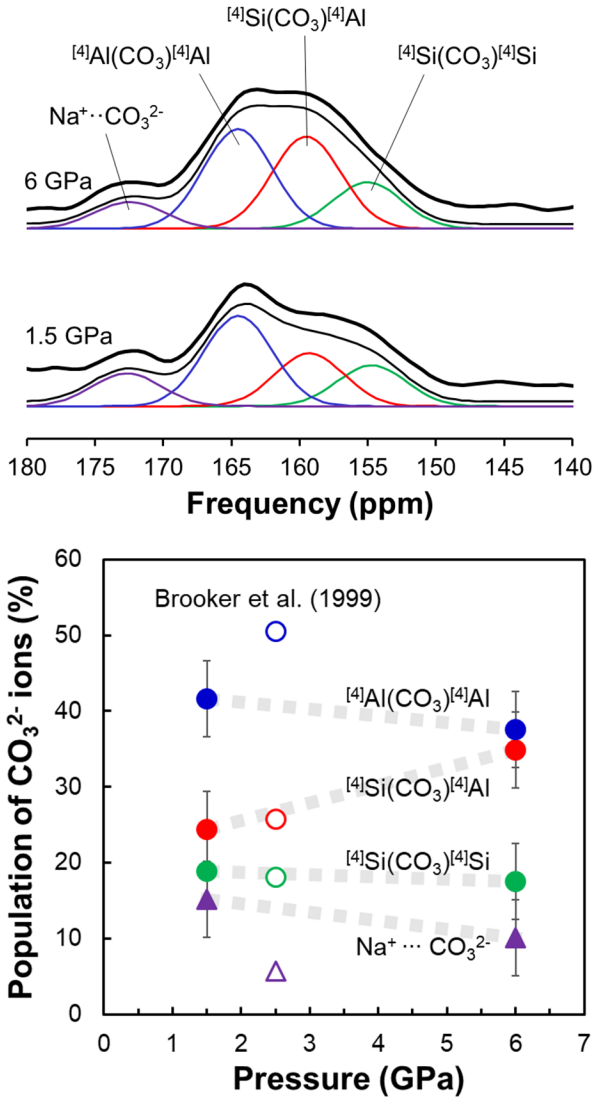

Figure 3.8. (Top) Simulation results for ^{13}C MAS NMR spectra for carbonates in carbon-bearing albite melts with varying pressure at 1.5 and 6 GPa. Green, red, blue, purple, and black lines correspond to $^{[4]}Si(CO_3)^{[4]}Si$, $^{[4]}Si(CO_3)^{[4]}Al$, $^{[4]}Al(CO_3)^{[4]}Al$, free carbonates ($Na\cdot\cdot CO_3^{2-}$), and total simulation results, respectively. (Bottom) Variations in the CO_3^{2-} ion population with pressure in carbon-

bearing albite melts. Blue, red, and green circles refer to $^{[4]}Al(CO_3)^{[4]}Al$, $^{[4]}Si(CO_3)^{[4]}Al$, and $^{[4]}Si(CO_3)^{[4]}Si$, respectively. Violet triangles denote free CO_3^{2-} ions near the non-bridging oxygen in network polyhedra, charge-balancing with the Na^+ ions. Open symbols refer to data from Brooker et al. (1999).

carbonates at 1.5 GPa are ~ 42 ± 5%, ~ 24 ± 5%, ~ 19 ± 5%, and ~ 15 ± 5%, respectively, while those at 6 GPa are ~ 38 ± 5%, ~ 35 ± 5%, ~ 18 ± 5%, and ~ 10 ± 5%, respectively. Among the four distinct carbonate species, the fraction of $^{[4]}Si(CO_3)^{[4]}Al$ appears to increase with increasing pressure, while the fractions of the other carbonate species decrease with increasing pressure. The fractions of $^{[4]}Si(CO_3)^{[4]}Al$ and $^{[4]}Si(CO_3)^{[4]}Si$ from Brooker et al. (1999) at lower pressure conditions are generally consistent with the current data.

Previous MD simulation has reported that the fraction of CO_3^{2-} over total carbon species (CO_2 + CO_3^{2-}) in rhyolitic melts (Al/Si of ~ 0.21) would be 38% at 5 GPa and 48% at 8 GPa (Guillot and Sator, 2011), which is similar to the calculated fraction of total carbonates in albite glasses at 6 GPa (~ 32%, in this study). While MD simulation reported the total carbon contents in silicate melts at high pressure up to 15 GPa (Guillot and Sator, 2011; Vuilleumier et al., 2015), the speciation of carbonate ions in rhyolitic melts was available only at 2 GPa (Guillot and Sator, 2011). About 40% of carbonate ions are involved in free carbonate bonds in rhyolitic melts at 2 GPa and 1473 K (in MD simulation). Compared with the fraction of free carbonate species in albite glasses at 1.5 GPa (~ 15 ± 5%, in this study), the differences in the MD simulation and the ^{13}C MAS NMR results may be due

to differences in the relaxation of each carbon species, the Al/Si ratio in the silicate system, the composition of cations. Further studies of relaxation of each carbonate species with varying compositions are needed to resolve the differences. The glasses studied here represent the structures of the super-cooled liquids at the glass transition temperature that are much lower than that of liquids and partly the difference in temperature condition between glasses and melts.

3.4.5. Presence of CO in albite glasses quenched from melts at high pressure

Figure 3.4b shows the presence of CO and the spinning side bands for CO in carbon-bearing albite melts at 1.5 GPa (~ 290 ppm and ~ 70 ppm) (see section 3.3.4). The presence of CO in the system is thought to be due to carbon diffusion throughout the Pt capsule (Brooker et al., 1998; Lurn, 1989; Morizet et al., 2015), which reduces CO_2 and CO_3^{2-} to CO. Indeed, carbon infiltration from the graphite heater into Pt capsules was observed during the synthesis of CO_2-bearing nephelinite-composition melts using ^{13}C-enriched Na_2CO_3 (99%) as a carbon reservoir (Brooker et al., 1998), as evidenced by a gradual decrease in ^{12}CO from the Pt tube wall to the sample in the piston cylinder experiments (Brooker et al., 1998). Note that the ^{13}C-enriched Na_2CO_3 (99%) was also used to synthesize carbon-bearing albite melts at high pressure up to 6 GPa in this study. ^{13}CO in albite glasses quenched from melts at 1.5 GPa is due to carbon diffused into the sample. In our previous study, the presence of ^{12}CO and ^{13}CO was observed in fluid inclusions in crystalline $MgSiO_3$ by Raman spectroscopy (Kim et al., 2016). Preliminary Raman spectra for carbon-bearing albite glasses at 1.5 GPa

showed the presence of CH_4. Because ^{13}C-enriched $Na_2{}^{13}CO_3$ (99.7%) was used for the synthesis of carbon-bearing albite glasses, the sample was sealed in the Pt tube, and CH_4 was not observed in ^{13}C MAS NMR spectra, the presence of $^{12}CH_4$ thus indicates a potential confamination by carbon infiltration from the graphite furnace.

The observed peak shift of CO from 181 ppm at 1.5 GPa to 185 ppm at 6 GPa (Figure 3.4b) suggests the pressure-induced structural changes of CO in albite melts, as the peak shift of carbonate in the ^{13}C MAS NMR spectra indicates the distortion of carbonates (Kohn et al., 1991; Sherriff et al., 1987). As mentioned in section 3.3.4, CO in albite melts at 6 GPa appears to be bound to the silicate network. If the CO dissolves in the silicate network, the peak shift may indicate the pressure-induced structural changes in CO that is bound to the silicate network. Previous quantum chemical calculations for CO_3^{2-} and $C(OH)_4$ show that the increase of C-O bond lengths results in the increase of isotropic chemical shifts (Kim et al., 2016; Tossell, 1995). If the trend is similar in a CO molecule, the peak shift to the higher frequency region (positive frequency) of CO in albite glasses upon compression may indicate the decrease of the C-O bond length of dissolved CO in carbon-bearing albite glasses with increasing pressure.

3.4.6. Effect of carbon speciation on the properties and isotope composition in silicate melts at high pressure

In this section, we further discuss the structural origins of the pressure-induced changes in carbon solubility in silicate melts at high pressure above 4 GPa and geochemical implications. Recent study suggested that the composition of partial melt formed from the subducting

oceanic crust and the pelitic sediments can be rhyolitic at 2–3 GPa (Duncan and Dasgupta, 2017). The recent field study showed that composition of melt inclusion in the subducted carbonate rock in Kokchetav massif (with the estimated peak pressure of 4.5–6.0 GPa) is reported to be granitic (Korsakov and Hermann, 2006). Furthermore, the high-pressure melting experiment of mineral assemblage relevant to basalts, together with clay minerals and $CaCO_3$, confirmed the formation of rhyolitic melts containing up to 10% of CO_2 at 2.5–5.0 GPa (Thomsen and Schmidt, 2008). Whereas the experimental confirmation at higher pressure may be necessary, the melt composition of the subducting oceanic crust containing $CaCO_3$ and other clay minerals could be rhyolitic at the extended pressure condition. As the albite melts serve the model system for rhyolitic melts, the current results for the carbon-bearing albite melts formed at 6 GPa would, therefore, be useful to infer the carbon speciation and the carbon carrying capacity of rhyolitic melts formed by the partial melting of the oceanic crust with the politic sediments.

Earlier studies at low pressure showed that CO_2 dissolves as bridging carbonate units like $Si(CO_3)Si$ and $Al(CO_3)Si$ into silicate network in depolymerized glasses and as molecular CO_2 bound near the bridging oxygen, such as Si-O-Si, in polymerized melts (e.g., Eggler and Kadik, 1979; Fine and Stolper, 1985; Holloway and Blank, 1994; King and Holloway, 2002; Morizet et al., 2002; Morizet et al., 2014b; Mysen, 2012; Mysen et al., 1975; Mysen et al., 1976; Ni and Keppler, 2013). These observations are generally consistent with our high-pressure results. Unexpected differences include a decrease in peak intensity of free-carbonates in the NS3 melts at 6 GPa. Note again that the reduction in solubility has also been inferred from

the formation of void in the Pt capsule of carbon-bearing NS3 glasses quenched from melt at 6 GPa (section 3.2.1). The origin of the observed void may be from the excess molecular carbon species, such as gas phase CO_2. The presence of a void inside the Pt capsule is evident only in the carbon-bearing NS3 melts at 6 GPa. The reduction in peak intensity may result from the discontinuous drop in the solubility of carbon in NS3 melts with increasing pressure and the formation of bridging carbonates at 6 GPa. The solubility of carbon in some depolymerized silicate melts may change non-linearly with increasing pressure and show a potential drop in the solubility. This non-linear change in the carbon solubility needs to be taken into consideration in order to understand fluid-induced melting relations in mantle peridotite deep below mid-ocean ridge.

The observed changes in the carbon species imply the complex changes in melt viscosity of fluid-bearing silicate melts at high pressure. As the melt viscosity largely depends on the degree of polymerization of silicate melts with the formation of $Si(CO_3)Si$, it is important to identify the formation of bridging carbonates and its effect on the polymerization of silicate melts at high pressure. The extent of polymerization increases either by forming bridging Si-O-Si bond or by reducing the fraction of NBO species: as for the former, the formation of $Si(CO_3)Si$ may not be regarded as polymerization process because its formation of $Si(CO_3)Si$ bond in silicate melts does not form a Si-O-Si bond. On the other hand, the formation of $Si(CO_3)Si$ reduces NBO fraction, contributing to an overall increase in the network polymerization. Depending on pressure and composition, the fractions of diverse bridging carbonates may control the melt viscosity. Although the bond strength of the bridging carbonates (Si-O-C bonds) is

expected to be weaker than that of the Si-O-Si or Si-O-Al bonds, the fraction of Si-O-C bonds above a certain threshold value may lead to the increase in viscosity. Therefore, the formation of bridging carbonates in silicate melts can be used as a structural proxy for the increase in polymerization of silicate melts and the viscosity at an elevated pressure conditions.

The estimated speciation of carbon in silicate melts in the current study allows us to infer the carbon isotope composition in the Earth interior. Recent experimental studies on the isotope fractionation of carbon between silicate melts and fluids have shown that the $\delta^{13}C$ in CH_4 and CO_3^{2-} in the silicate melts is higher than that in the coexisting C-O-H fluids, and the differences in $\delta^{13}C$ between reduced silicate melts and fluids decrease with increasing temperature (Mysen, 2016, 2017). These studies addressed the importance of carbon speciation in carbon isotope composition of melts, fluids, and thus mantle rocks. The electronic structures around an isotope of interest play a dominant role in determining the equilibrium isotope fractionation and thus the isotope composition of the melts, fluids, and minerals (e.g., Deines, 2004; Schauble et al., 2006; Seo et al., 2007). Each carbon species in the carbon-bearing silicate melts has unique atomic structures and configurations around carbon. For instance, the C-O bond lengths in bridging carbonates $Si(CO_3)Si$, (C-O bond in Si-O-C), and free carbonates is 1.313 Å and 1.265 Å, respectively (Tossell, 1995), and bridging carbonates have two more covalence bonds with network forming cations. As also demonstrated in crystalline calcite, pressure-induced changes in atomic structures around C atom in the carbonate units result in a significant carbon isotope fractionation (Deines, 2004). Therefore, while further theoretical confirmation is necessary, the formation of bridging

carbonates and its strong interaction with silicate network at high pressure above 6 GPa may further contribute to the pressure-induced changes in isotope fractionation factors in the melts in the upper mantle.

3.5. Conclusion

We explore the speciation and the solubility of carbon in silicate melts and the related-structural changes of silicate networks in binary sodium silicate and ternary sodium aluminosilicate glasses quenched from melts at high pressure up to 8 GPa. The ^{13}C MAS NMR spectra for carbon-bearing albite melts provide quantitative information about the speciation of carbon in the silicate melts at high pressure by measuring the peak intensity for carbon species and taking into consideration the spin-lattice relaxation time. The calibrated fraction of CO_2 in albite melts matches well with the theoretical results of the fraction of CO_2 in rhyolite melts at 5 GPa. The fraction of $^{[4]}Si(CO_3)^{[4]}Al$ in carbon-bearing albite melts increases with increasing pressure. The spectral patterns of network-forming cations (Al and Si) in carbon-bearing silicate melts and those in volatile free silicate melts are rather similar. Therefore, the addition of CO_2 in the studied melts does not lead to an additional change in the network structure in the carbon-bearing albite melts. The ^{29}Si MAS NMR spectra for carbon-bearing NS3 melts show the increase of Q^4 species with increasing pressure from 1 atm to 8 GPa. The ^{13}C MAS NMR spectra for carbon-bearing NS3 melts show the formation of bridging carbonates $^{[4]}Si(CO_3)^{[4]}Si$, which can be used as a structural proxy for the increase in the polymerization of silicate melts at high pressure. The combination of high-resolution solid-state NMR and high-pressure synthesis using multi-anvil press could provide a powerful

tool for understanding the detailed structures around cations and anions in carbon-bearing silicate melts above 4 GPa and revealing the atomistic origins of the pressure-induced changes in melt properties in the upper mantle.

Appendix

3.S1. Effect of quench on the solubility of carbon in silicate melts and glasses

The solubility and speciation of carbon in the glasses could be somewhat different from those in the melts. Here, we briefly discussed the several factors that may contribute to potential changes in element solubility upon quenching of silicate melts. Quench-induced changes in atomic structures around carbon (and thus the carbon speciation) will affect the changes in carbon solubility during quenching. The atomic structure of glasses represents that of super-cooled liquids at the glass transition temperature (T_g) below which the melt structure is frozen at high pressure (e.g., Lee, 2010, 2011; Stebbins, 2016; Xue et al., 1991). The change in Q^n species in silicate melts can indeed vary with T_g: the proportion of Q^4 species in Na_2O-$2SiO_2$ melts at 1 atm increases from 6.4 (at T_g of 450 °C) to 7.9% (at 530 °C) (Stebbins, 1988). It is thus expected that above the melting temperature the fraction of Q^4 species can also increase. Although the direct comparison of the structure of melts and glasses at high pressure is difficult, similar structural changes of melts during quenching would be expected. The MD simulation showed that the population of CO_2 over total carbon in rhyolitic melts increases from 62 to 84% with increasing temperature from 1473 to 2273 K while the fraction of NBO in silicate network increases from 6.7 to 11.7% (Guillot and Sator, 2011), leading to the changes in the carbon solubility. The MD simulation for basaltic melts predicted that the solubility of carbon at 8 GPa varies ~ 5% with increasing temperature from 1673 to 2273 K (Guillot and Sator, 2011). The temperature drop during melt-quench would affect overall solubility. Taking these into consideration, while the

changes in speciation and solubility during quenching are expected, the changes during quenching with the given temperature window are not significant. The trend observed in the quenched glasses can therefore reflect those in the silicate melts at high pressure.

3.S2. The pressure-induced structural changes and the effect of carbon content on the structural evolution of Al

Previous studies on the carbon-free Na-silicate and Na-aluminosilicate glasses with increasing pressure up to 10 GPa addressed the effect of pressure on the changes in the degree of polymerization and Al coordination environment at high pressure (Lee et al., 2004; Lee et al., 2003; Lee et al., 2012b). The degree of polymerization (X_{NBO}) at 1 atm plays an important role in the formation of highly coordinated Al in oxide melts: the formation of highly coordinated Al increases with increasing NBO/T of aluminosilicate glasses and the Al content in the silicate melts at 1 atm (Kelsey et al., 2009; Lee, 2010; Lee et al., 2004a; Navrotsky, 1995; Yarger et al., 1995). Therefore, the current experimental results for the carbon-bearing silicate melts at high pressure allow us to explore the pressure-induced structural changes and the effect of carbon content on the structural evolution, separately.

3.S3. The changes of Q^n species in NS3 glasses quenched from melts at high pressure and the effect of Co on the relaxation time of Q^n species

Figure 3.S2 presents the simulation results for the ^{29}Si MAS NMR spectra for carbon-bearing NS3 glasses quenched from melts at high pressure. Each peak is modeled with the Gaussian functions. There is a

moderate degree of uncertainty associated with the fitting results due to severe overlaps. The peak position of Q^2, Q^3, and Q^4 species were well constrained to -78 – -80 ppm, -90 – -92 ppm, -102.5 – -104.5 ppm, respectively. The peak widths of Q^2, Q^3, and Q^4 species were also relatively well-constrained from 11.4 ppm to 11.7 ppm. The simulation of the spectrum with such constraints may reduce the overall quality of the fit. However, the purpose of the simulation is to provide a general trend of changes in Q^n species with varying pressure. Taking into the consideration the uncertainties of peak position and widths of Q^n species with varying pressure, we obtained the following simulation results from ^{29}Si MAS NMR spectra for carbon-bearing NS3 glasses at high pressure up to 8 GPa. The fraction of Q^2 and Q^4 species slightly increases from 2 to 5%, and from 28 to 29%, respectively, while that of Q^3 species decreases from 70 to 66% with increasing pressure.

For the simulation, here we assume that the relaxation times of Q^n species are identical. We note that in sodium silicate glasses, no differential relaxation has been reported with varying concentrations of paramagnetic elements (Sen and Stebbins, 1994). Therefore, the presence of Co does not induce differential relaxation between Q^3 and Q^4 species in carbon-bearing NS3 glasses.

3.S4. The estimation of bridging oxygen with silicate and carbonates

The calculated mol% of input amount of CO_2 in NS3 glasses at 6 GPa is 1.7 mol%. As ^{17}O-enriched SiO_2 (40% enriched) was used as an oxygen reservoir in the carbon-bearing NS3 glasses, ~ 0.7–1.4 mol% of bridging oxygen with silicate and carbonate is expected to be observed in the ^{17}O

3QMAS NMR spectrum. This change in carbonate species in the oxygen environment is not trivial to detect.

3.S5. The speciation of carbonates in NS3 glasses quenched from melts at high pressure

The carbon-bearing NS3 glasses quenched from melts at high pressure contain two carbonate species, bridging carbonates [$^{[4]}$Si(CO_3)$^{[4]}$Si] and free carbonates (Figure 3.S4). As the NS3 glasses only has Si as a network former cation, the fraction of each carbonate species was obtained by fitting the ^{13}C MAS NMR spectra using two Gaussian functions representing $^{[4]}$Si(CO_3)$^{[4]}$Si, and free carbonates. The peak position and widths of Gaussian functions were determined by the previous peak assignment used in Figure 3.8. As for the low signal-to-noise ratio of the spectra, we should mention that the estimated fraction of carbonate species in carbon-bearing NS3 glasses has intrinsic uncertainty. Pronounced peak overlap among species also makes it difficult to provide fully quantitative spectral analyses. Therefore, the proportions of each carbonate species reported here are for the semi-quantitative discussion only.

Detailed information of the fitting parameters for ^{13}C MAS NMR spectra is given in Table 3.S1. The peak intensity of free carbonates decreases from 94 C atom/g × 10^{-23} at 4 GPa to 85 C atom/g × 10^{-23} at 6 GPa, and then increases to 160 C atom/g × 10^{-23} at 8 GPa, while that of bridging carbonate increases with increasing pressure from 33 C atom/g × 10^{-23} at 4 GPa to 73 C atom/g × 10^{-23} at 8 GPa. The fraction of bridging carbonates slightly increases from 26 % at 4 GPa to 31% at 8 GPa.

Table 3.S1. Simulation parameters and results for ^{13}C MAS NMR spectra for carbon-bearing NS3 glasses quenched from melts at high pressure up to 8 GPa.

Pressure (GPa)	Free carbonate	Bridging carbonate	Free carbonate		Bridging carbonate
	Fraction (%)*	Fraction (%)*	Intensity (C atom/g × 10^{-23})	Peak position (ppm)[a]	Intensity (C atom/g × 10^{-23})[a,b]
4	74.0 ± 5.0	26.0 ± 5.0	94	171.3 ± 0.3	33
6	72.0 ± 5.0	28.0 ± 5.0	85	171.3 ± 0.3	33
8	68.7 ± 5.0	31.3 ± 5.0	160	170.6 ± 0.3	73

* The uncertainty of 5% was estimated from the uncertainty in NMR processing condition, difference between experimental and fitted spectra, and possible artifacts resulting from fixed fitting parameters.

[a] The FWHM is set to 4 ppm.

[b] The FWHM and the peak position for bridging carbonates is set to 8.2 ppm and 160.0 ppm, respectively.

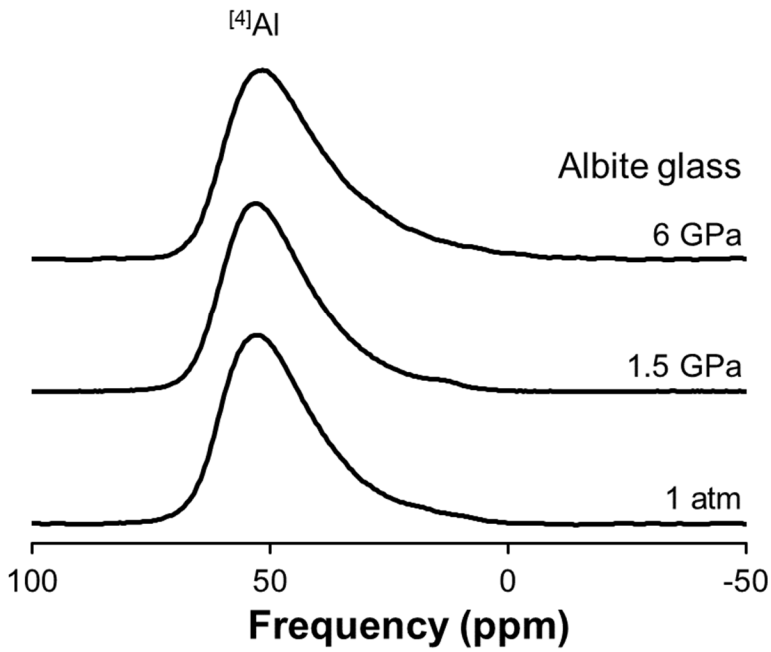

Figure 3.S1. ^{27}Al MAS NMR spectra for carbon-bearing albite glasses at 1.5 and 6 GPa and that for carbon-free albite glasses at 1 atm.

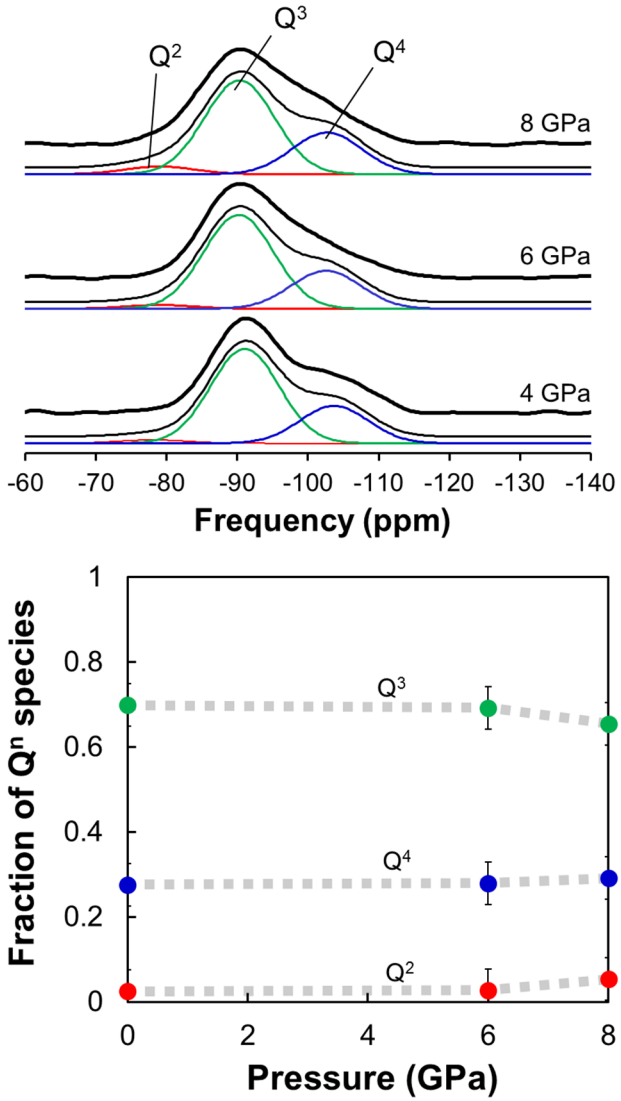

Figure 3.S2. (Top) ^{29}Si MAS NMR spectra and simulation results for carbon-bearing NS3 glasses with varying pressure up to 8 GPa. Red, green, and blue lines correspond to Q^2, Q^3, and Q^4 species, respectively. (Bottom) Population of Si atom species for carbon-bearing NS3 glasses with varying pressure up to 8 GPa. Red, green, and blue circles correspond to Q^2, Q^3, and Q^4 species, respectively.

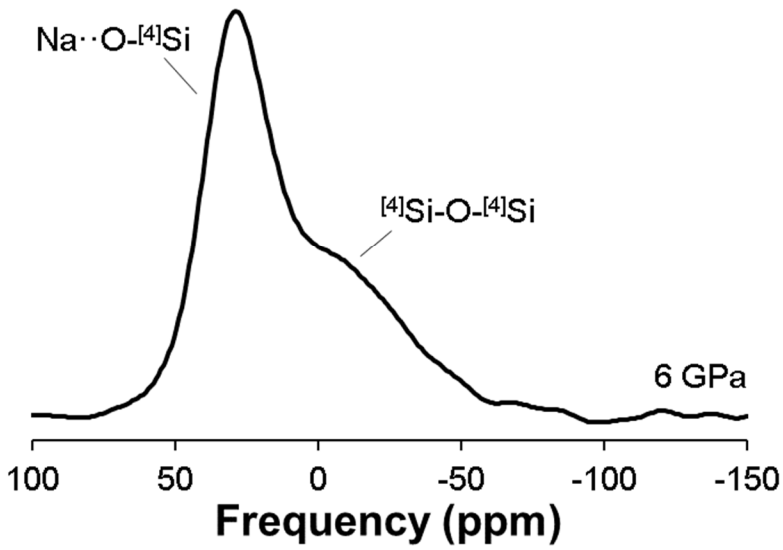

Figure 3.S3. ^{17}O MAS NMR spectrum for carbon-bearing NS3 glasses at 6 GPa.

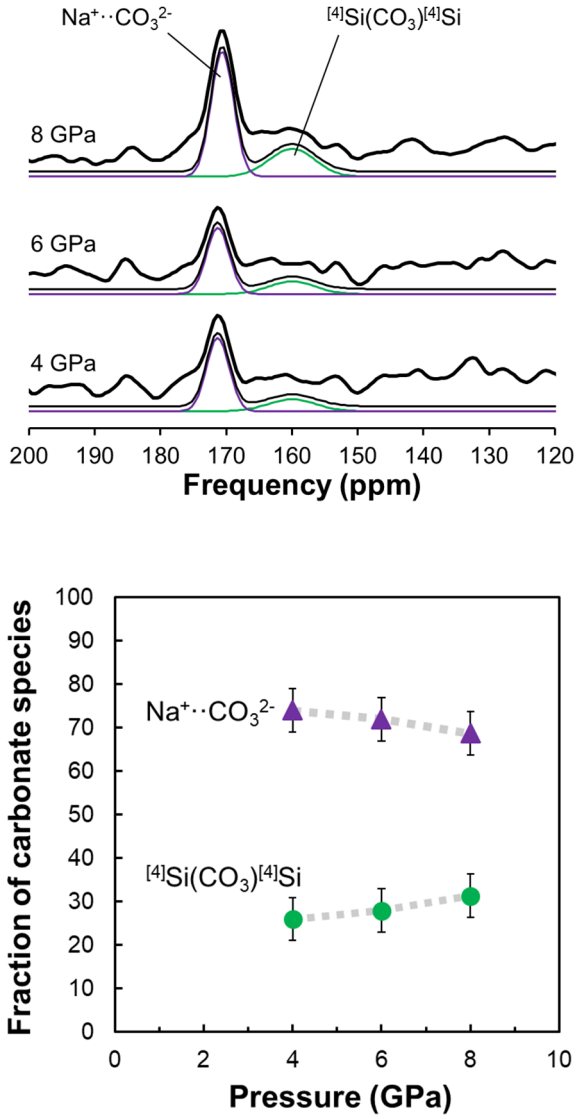

Figure 3.S4. (Top) Simulation results for ^{13}C MAS NMR spectra for carbon-bearing NS3 glasses at high pressure up to 8 GPa. Violet and green lines correspond to free carbonates and bridging carbonates, respectively. (Bottom) The population of carbon species in carbon-bearing NS3 glasses. Violet and green circles correspond to free carbonates and bridging carbonates, respectively.

References

Abragam, A. (1961) The Principles of Nuclear Magnetism. Oxford University Press, London, England.

Allwardt, J.R., Stebbins, J.F., Terasaki, H., Du, L.-S., Forst, D.J., Withers, A.C., Hirschmann, M.M., Suzuki, A. and Ohtani, E. (2007) Effect of structure transitions on properties of high-pressure silicate melts: ^{27}Al NMR, glass densities, and melt viscosities. *American Mineralogist* **92**, 1093-1104.

Bakker, R.J. (2003) Package FLUIDS 1. Computer programs for analysis of fluid inclusion data and for modelling bulk fluid properties. *Chemical Geology* **194**, 3-23.

Baltisberger, J.H., Xu, Z., Stebbins, J.F., Wang, S.H. and Pines, A. (1996) Triple-quantum two-dimensional ^{27}Al magic angle spinning nuclear magnetic resonance spectroscopic study of aluminosilicate and aluminate crystals and glasses. *J Am Chem Soc* **118**, 7209-7214.

Behrens, H., Ohlhorst, S., Holtz, F. and Champenois, M. (2004) CO_2 solubility in dacitic melts equilibrated with H_2O-CO_2 fluids: Implications for modeling the solubility of CO_2 in silicic melts. *Geochimica et Cosmochimica Acta* **68**, 4687-4703.

Blank, J.G. and Brooker, R.A. (1994) Experimental studies of carbon dioxide in silicate melts: Solubility, speciation, and stable carbon isotope behavior, In *Volatiles in Magmas*, (Eds. Carroll, M.R., Holloway, J.R.).

Bodnar, R.J. (2003) Introduction to fluid inclusions, In *Fluid Inclusions: Analysis and Interpretation*, (Eds. Samson, I., Anderson, A., Marshall, D.). Mineral. Assoc. Canada, pp. 1-8.

Brearley, M. and Montana, A. (1989) The effect of CO_2 on the viscosity of silicate liquids at high pressure. *Geochimica et Cosmochimica Acta* **53**, 2609-2616.

Brooker, R., Holloway, J.R. and Hervig, R. (1998) Reduction in piston-cylinder experiments: The detection of carbon infiltration into platinum capsules. *American Mineralogist* **83**, 985-994.

Brooker, R.A., Kohn, S.C., Holloway, J.R., McMillan, P.F. and Carroll, M.R. (1999) Solubility, speciation and dissolution mechanisms for CO_2 in melts on the $NaAlO_2$-SiO_2 join. *Geochimica et Cosmochimica Acta* **63**, 3549-3565.

Burke, E.A.J. (2001) Raman microspectrometry of fluid inclusions. *Lithos* **55**, 139-158.

Cody, G.D., Heying, E., Alexander, C.M.O., Nittler, L.R., Kilcoyne, A.L.D., Sandford, S.A. and Stroud, R.M. (2011) Establishing a molecular relationship between chondritic and cometary organic solids. *Proceedings of the National Academy of Sciences* **108**, 19171-19176.

Dasgupta, R. and Hirschmann, M.M. (2006) Melting in the Earth's deep upper mantle caused by carbon dioxide. *Nature* **440**, 659-662.

Dasgupta, R., Hirschmann, M.M. and Withers, A.C. (2004) Deep global cycling of carbon constrained by the solidus of anhydrous, carbonated eclogite under upper mantle conditions. *Earth Planet. Sci. Lett.* **227**, 73-85.

Dasgupta, R., Maillik, A., Tsuno, K., Withers, A.C., Hirth, G. and Hirschmann, M.M. (2013) Carbon-dioxide-rich silicate melt in the Earth's upper mantle. *Nature* **493**, 211-215.

Deines, P. (2004) Carbon isotope effects in carbonate systems. *Geochimica et Cosmochimica Acta* **68**, 2659-2679.

Du, L.-S. and Stebbins, J.F. (2005) Network connectivity in aluminoborosilicate glasses: A high-resolution ^{11}B, ^{27}Al and ^{17}O NMR study. *Journal of Non-Crystalline Solids* **351**, 3508-3520.

Duncan, M.S. and Dasgupta, R. (2017) Rise of Earth's atmospheric oxygen controlled by efficient subduction of organic carbon. *Nature Geoscience* **10**, 387-392.

Edén, M. (2015) Chapter Four - ^{27}Al NMR Studies of Aluminosilicate Glasses, In *Annual Reports on NMR Spectroscopy*, (Ed. Graham, A.W.). Academic Press, pp. 237-331.

Eggler, D.H. (1976) Does CO_2 cause partial melting in the low-velocity layer of the mantle? *Geology* **4**, 69-72.

Eggler, D.H. and Kadik, A.A. (1979) System $NaAlSi_3O_8$-H_2O-CO_2 to 20 kbar pressure 1. Compositional and thermodynamic relations of liquids and vapors coexisting with albite. *American Mineralogist* **64**, 1036-1048.

Eggler, D.H. and Rosenhauer, M. (1978) Carbon-dioxide in silicate melts 2. Solubilites of CO_2 and H_2O in $CaMgSi_2O_6$ (diopside) liquids and vapors at pressure to 40 kb. *American Journal of Science* **278**, 64-94.

Ettinger, R., Blume, P., Patterson, A. and Lauterbur, P.C. (1960) C-13 chemical shifts in CO and CO_2. *J. Chem. Phys.* **33**, 1597-1598.

Evans, R.L., et al. (1999) Asymmetric Electrical Structure in the Mantle Beneath the East Pacific Rise at 17°S. *Science* **286**, 752-756.

Feng, J., Lee, Y.J., Reeder, R.J. and Phillips, B.L. (2006) Observation of bicarbonate in calcite by NMR spectroscopy. *American Mineralogist* **91**, 957-960.

Fine, G. and Stolper, E. (1985) The speciation of carbon-dioxide in soium aluminosilicate glasses. *Contributions to Mineralogy and Petrology* **91**, 105-121.

Florian, P., Sadiki, N., Massiot, D. and Coutures, J.P. (2007) Al-27 NMR study of the structure of lanthanum- and yttrium-based aluminosilicate glasses and melts. *J. Phys. Chem. B* **111**, 9747-9757.

Frisch, M.J., et al. (2004) Gaussian 03, Revision C.02. Gaussian, Inc., Wallingford CT.

Gaudio, S.J., Lesher, C.E., Maekawa, H. and Sen, S. (2015) Linking high-pressure structure and density of albite liquid near the glass transition. *Geochimica et Cosmochimica Acta* **157**, 28-38.

Gibson, A.A.V., Scott, T.A. and Fukushima, E. (1977) Anisotropy of the chemical shift tensor for solid carbon monoxide. *Journal of Magnetic Resonance* **27**, 29-33.

Gu, Y.J., Lerner-Lam, A.L., Dziewonski, A.M. and Ekström, G. (2005) Deep structure and seismic anisotropy beneath the East Pacific Rise. *Earth and Planetary Science Letters* **232**, 259-272.

Guillot, B. and Sator, N. (2011) Carbon dioxide in silicate melts: A molecular dynamics simulation study. *Geochimica et Cosmochimica Acta* **75**, 1829-1857.

Hacura, A., Bródka, A., Nikiel, L. and Baglin, F.G. (1990) High pressure Raman study of fermi resonance spectrum in gaseous carbon dioxide. *J. Mol. Struct.* **218**, 297-302.

Herzfeld, J. and Berger, A.E. (1980) Sideband intensities in NMR spectra of samples spinning at the magic angle. *J Chem Phys* **73**, 6021-6030.

Holloway, J.R. and Blank, J.G. (1994) Application of experimental results to C-O-H species in natrual melts, In *Volatiles in Magmas*. Mineralogical Soc America, Washington, pp. 187-230.

Jaworski, A., Stevensson, B., Pahari, B., Okhotnikov, K. and Eden, M. (2012) Local structure and Al/Si ordering in lanthanum aluminosilicate glasses explored by advanced ^{27}Al NMR experiments and molecular dynamics simulations. *Physical Chemistry Chemical Physics* **14**, 15866-15878.

Jones, A.R., Winter, R., Greaves, G.N. and Smith, I.H. (2005) ^{23}Na, ^{29}Si, and ^{13}C MAS NMR investigation of glass-forming reactions between Na_2CO_3 and SiO_2. *J. Phys. Chem. B* **109**, 23154-23161.

Kelsey, K.E., Allwardt, J.R. and Stebbins, J.F. (2008) Ca–Mg mixing in aluminosilicate glasses: An investigation using ^{17}O MAS and 3QMAS and ^{27}Al MAS NMR. *Journal of Non-Crystalline Solids* **354**, 4644-4653.

Kelsey, K.E., Stebbins, J.F., Mosenfelder, J.L. and Asimow, P.D. (2009) Simultaneous aluminum, silicon, and sodium coordination changes in 6 GPa sodium aluminosilicate glasses. *American Mineralogist* **94**, 1205-1215.

Kim, E.J., Fei, Y. and Lee, S.K. (2016) Probing carbon-bearing species and CO_2 inclusions in amorphous carbon-$MgSiO_3$ enstatite reaction products at 1.5 GPa: Insights from ^{13}C high-resolution solid-state NMR. *American Mineralogist* **101**, 1113-1124.

Kim, H.N. and Lee, S.K. (2013) Effect of particle size on phase transitions in metastable alumina nanoparticles: A view from high-resolution solid-state ^{27}Al MAS and 3QMAS NMR. *American Mineralogist* **98**, 1198-1210.

King, P.L. and Holloway, J.R. (2002) CO_2 solubility and speciation in intermediate (andesitic) melts: the role of H_2O and composition. *Geochimica et Cosmochimica Acta* **66**, 1627-1640.

Kirkpatrick, R.J. and Brow, R.K. (1995) Nuclear-magnetic-resonance investigation of the structures of phosphate and phospahte-containing glasses: A review. *Solid State Nuclear Magnetic Resonance* **5**, 9-21.

Kirkpatrick, R.J., Oestrike, R., Weiss, C.A., Smith, K.A. and Oldfield, E. (1986) High-resolution ^{27}Al and ^{29}Si NMR spectroscopy of glasses and crystals along the join $CaMgSi_2O_6$-$CaAl_2SiO_6$. *American Mineralogist* **71**, 705-711.

Kohn, S.C., Brooker, R.A. and Dupree, R. (1991) ^{13}C MAS NMR - A method for studying CO_2 speciation in glasses. *Geochimica et Cosmochimica Acta* **55**, 3879-3884.

Korsakov, A.V. and Hermann, J. (2006) Silicate and carbonate melt inclusions associated with diamonds in deeply subducted carbonate rocks. *Earth and Planetary Science Letters* **241**, 104-118.

Kwak, J.H., Hu, J.Z., Hoyt, D.W., Sears, J.A., Wang, C.M., Rosso, K.M. and Felmy, A.R. (2010) Metal carbonation of forsterite in supercritical CO_2 and H_2O using solid state ^{29}Si, ^{13}C NMR spectroscopy. *Journal of Physical Chemistry C* **114**, 4126-4134.

Lee, B.H. and Lee, S.K. (2009) Effect of lattice topology on the adsorption of benzyl alcohol on kaolinite surfaces: Quantum chemical calculations of geometry optimization, binding energy, and NMR chemical shielding. *American Mineralogist* **94**, 1392-1404.

Lee, S.K. (2004) Structure of silicate glasses and melts at high pressure: Quantum chemical calculations and solid-state NMR. *J. Phys. Chem. B* **108**, 5889-5900.

Lee, S.K. (2010) Effect of pressure on structure of oxide glasses at high pressure: Insights from solid-state NMR of quadrupolar nuclides. *Solid State Nucl. Mag. Reson.* **38**, 45-57.

Lee, S.K. (2011) Simplicity in melt densification in multicomponent magmatic reservoirs in Earth's interior revealed by multinuclear magnetic resonance. *Proceedings of the National Academy of Sciences* **108**, 6847-6852.

Lee, S.K., Cody, G.D., Fei, Y.W. and Mysen, B.O. (2004) Nature of polymerization and properties of silicate melts and glasses at high pressure. *Geochimica et Cosmochimica Acta* **68**, 4189-4200.

Lee, S.K., Fei, Y.W., Cody, G.D. and Mysen, B.O. (2003) Order and disorder in sodium silicate glasses and melts at 10 GPa. *Geophysical Research Letters* **30**, 1845.

Lee, S.K., Kim, H.-I., Kim, E.J., Mun, K.Y. and Ryu, S. (2016) Extent of Disorder in Magnesium Aluminosilicate Glasses: Insights from ^{27}Al and ^{17}O NMR. *Journal of Physical Chemistry C* **120**, 737-749.

Lee, S.K., Musgrave, C.B., Zhao, P.D. and Stebbins, J.F. (2001) Topological disorder and reactivity of borosilicate glasses: Quantum chemical calculations and O-17 and B-11 NMR study. *J. Phys. Chem. B* **105**, 12583-12595.

Lee, S.K., Park, S.Y., Kim, H.-I., Tschauner, O., Asimow, P., Bai, L., Xiao, Y. and Chow, P. (2012a) Structure of shock compressed model basaltic glass: Insights from O K-edge X-ray Raman scattering and high-

resolution ^{27}Al NMR spectroscopy. *Geophysical Research Letters* **39**, L05306.

Lee, S.K., Park, S.Y., Yi, Y.S. and Moon, J. (2010) Structure and disorder in amorphous alumina thin films: Insights from high-resolution solid-state NMR. *Journal of Physical Chemistry C* **114**, 13890-13894.

Lee, S.K. and Stebbins, J.F. (2003) The distribution of sodium ions in aluminosilicate glasses: A high-field Na-23 MAS and 3QMAS NMR study. *Geochimica et Cosmochimica Acta* **67**, 1699-1709.

Lee, S.K., Yi, Y.S., Cody, G.D., Mibe, K., Fei, Y. and Mysen, B.O. (2012b) Effect of network polymerization on the pressure-induced structural changes in sodium aluminosilicate glasses and melts: ^{27}Al and ^{17}O solid-state NMR study. *Journal of Physical Chemistry C* **116**, 2183-2191.

Lurn, R.W. (1989) Natural versus experimental control of oxidation state: Effects on the composition and speciation of COH fluids. *American Mineralogist* **74**, 50-57.

Maekawa, H., Maekawa, T., Kawamura, K. and Yokokawa, T. (1991) The structural groups of alkali silicate glasses determined from 29Si MAS-NMR. *J. Non-Cryst. Solids* **127**, 53-64.

Malfait, W.J., Verel, R., Ardia, P. and Sanchez-Valle, C. (2012) Aluminum coordination in rhyolite and andesite glasses and melts: Effect of temperature, pressure, composition and water content. *Geochimica et Cosmochimica Acta* **77**, 11-26.

Massuyeau, M., Gardés, E., Morizet, Y. and Gaillard, F. (2015) A model for the activity of silica along the carbonatite–kimberlite–mellilitite–basanite melt compositional joint. *Chemical Geology* **418**, 206-216.

Mauri, F., Pasquarello, A., Pfrommer, B.G., Yoon, Y.-G. and Louie, S.G. (2000) Si-O-Si bond-angle distribution in vitreous silica from first-principles ^{29}Si NMR analysis. *Physical Review B* **62**, R4786-R4789.

McMillan, P.F. and Kirkpatrick, R.J. (1992) Al coordination in magnesium aluminosilicate glasses. Mineralogical Society of America, Washington, DC, ETATS-UNIS.

Moore, J.K., Surface, J.A., Brenner, A., Skemer, P., Conradi, M.S. and Hayes, S.E. (2015) Quantitative identification of metastable magnesium carbonate minerals by solid-state ^{13}C NMR spectroscopy. *Environmental Science & Technology* **49**, 657-664.

Morizet, Y., Brooker, R.A. and Kohn, S.C. (2002) CO_2 in haplo-phonolite melt: solubility, speciation and carbonate complexation. *Geochimica et Cosmochimica Acta* **66**, 1809-1820.

Morizet, Y., Nichols, A.R.L., Kohn, S.C., Brooker, R.A. and Dingwell, D.B. (2007) The influence of H_2O and CO_2 on the glass transition temperature: insights into the effects of volatiles on magma viscosity. *Eur. J. Mineral.* **19**, 657-669.

Morizet, Y., Paris, M., Gaillard, F. and Scaillet, B. (2009) Raman quantification factor calibration for CO-CO_2 gas mixture in synthetic fluid inclusions: Application to oxygen fugacity calculation in magmatic systems. *Chemical Geology* **264**, 58-70.

Morizet, Y., Paris, M., Gaillard, F. and Scaillet, B. (2010) C-O-H fluid solubility in haplobasalt under reducing conditions: An experimental study. *Chemical Geology* **279**, 1-16.

Morizet, Y., Paris, M., Gaillard, F. and Scaillet, B. (2014a) Carbon dioxide in silica-undersaturated melt Part II: Effect of CO_2 on quenched glass structure. *Geochim. Cosmochim. Acta* **144**, 202-216.

Morizet, Y., Paris, M., Gaillard, F. and Scaillet, B. (2014b) Carbon dioxide in silica-undersaturated melt. Part I: The effect of mixed alkalis (K and Na) on CO_2 solubility and speciation. *Geochimica et Cosmochimica Acta* **141**, 45-61.

Morizet, Y., Paris, M., Sifré, D., Di Carlo, I. and Gaillard, F. (2017) The effect of Mg concentration in silicate glasses on CO_2 solubility and solution mechanism: Implication for natural magmatic systems. *Geochimica et Cosmochimica Acta* **198**, 115-130.

Morizet, Y., Vuilleumier, R. and Paris, M. (2015) A NMR and molecular dynamics study of CO_2-bearing basaltic melts and glasses. *Chemical Geology* **418**.

Moussallam, Y., et al. (2016) The molecular structure of melts along the carbonatite–kimberlite–basalt compositional joint: CO_2 and polymerisation. *Earth and Planetary Science Letters* **434**, 129-140.

Mysen, B. (2013) Structure–property relationships of COHN-saturated silicate melt coexisting with COHN fluid: A review of in-situ, high-temperature, high-pressure experiments. *Chemical Geology* **346**, 113-124.

Mysen, B. (2016) Experimentally-determined carbon isotope fractionation in and between methane-bearing melt and fluid to upper mantle temperatures and pressures. *Earth and Planetary Science Letters* **445**, 28-35.

Mysen, B. (2017) Experimental, in-situ carbon solution mechanisms and isotope fractionation in and between (C–O–H)-saturated silicate melt

and silicate-saturated (C–O–H) fluid to upper mantle temperatures and pressures. *Earth and Planetary Science Letters* **459**, 352-361.

Mysen, B.O. (2012) Silicate-COH melt and fluid structure, their physicochemical properties, and partitioning of nominally refractory oxides between melts and fluids. *Lithos* **148**, 228-246.

Mysen, B.O., Arculus, R.J. and Eggler, D.H. (1975) Solubility of carbon-dioxide in melts of andesite, tholeiite, and olivine nephelinite composition to 30 kbar pressure. *Contributions to Mineralogy and Petrology* **53**, 227-239.

Mysen, B.O., Eggler, D.H., Seitz, M.G. and Holloway, J.R. (1976) Carbon dioxide in silicate melts and crystals. Part I. Solubiltiy measurements. *American Journal of Science* **276**, 455-479.

Mysen, B.O., Fogel, M.L., Morrill, P.L. and Cody, G.D. (2009) Solution behavior of reduced C-O-H volatiles in silicate melts at high pressure and temperature. *Geochimica et Cosmochimica Acta* **73**, 1696-1710.

Mysen, B.O., Kumamoto, K., Cody, G.D. and Fogel, M.L. (2011) Solubility and solution mechanisms of C–O–H volatiles in silicate melt with variable redox conditions and melt composition at upper mantle temperatures and pressures. *Geochimica et Cosmochimica Acta* **75**, 6183-6199.

Mysen, B.O. and Richet, P. (2005) Volatiles I. The system C-O-H-S, In *Silicate Glasses and Melts*. Elsevier.

Neuville, D.R., Cormier, L., Montouillout, V., Florian, P., Millot, F., Rifflet, J.-C. and Massiot, D. (2008) Structure of Mg-and Mg/Ca aluminosilicate glasses: ^{27}Al NMR and Raman spectroscopy investigations. *American Mineralogist* **93**, 1721-1731.

Ni, H.W. and Keppler, H. (2013) Carbon in silicate melts, In *Reviews in Mineralogy and Geochemistry*, (Eds. Hazen, R.M., Jones, A.P., Baross, J.A.). Mineralogical Society of America, Virginia, pp. 251-287.

Nowak, M., Schreen, D. and Spickenbom, K. (2004) Argon and CO_2 on the race track in silicate melts: A tool for the development of a CO, speciation and diffusion model. *Geochimica et Cosmochimica Acta* **68**, 5127-5138.

Pan, V., Holloway, J.R. and Hervig, R.L. (1991) The pressure and temperature dependence of carbon dioxide solubility in tholeiitic basalt melts. *Geochimica et Cosmochimica Acta* **55**, 1587-1595.

Papenguth, H.W., Kirkpatrick, R.J., Montez, B. and Sandberg, P.A. (1989) ^{13}C MAS NMR spectroscopy of inorganic and biogenic carbonates. *American Mineralogist* **74**, 1152-1158.

Parfitt, E.A. and Wilson, L. (2008) The role of volatiles, In *Fundamentals of Physical Volcanology*. Blackwell Science, pp. 64-76.

Park, S.Y. and Lee, S.K. (2012) Structure and disorder in basaltic glasses and melts: Insights from high-resolution solid-state NMR study of glasses in diopside–Ca-tschermakite join and diopside–anorthite eutectic composition. *Geochim. Cosmochim. Acta* **80**, 125-142.

Park, S.Y. and Lee, S.K. (2014) High-resolution solid-state NMR study of the effect of composition on network connectivity and structural disorder in multi-component glasses in the diopside and jadeite join: Implications for structure of andesitic melts. *Geochim. Cosmochim. Acta* **147**, 26-42.

Pawley, A.R., Holloway, J.R. and McMillan, P.F. (1992) The effect of oxygen fugacity on the solubility of carbon oxygen fluids in basaltic melt. *Earth and Planetary Science Letters* **110**, 213-225.

Phillips, B.L., Xu, H., Heaney, P.J. and Navrotsky, A. (2000) ^{29}Si and ^{27}Al MAS-NMR spectroscopy of β-eucryptite ($LiAlSiO_4$): The enthalpy of Si,Al ordering. *American Mineralogist* **85**, 181-188.

Radeglia, R. and Engelhardt, G. (1985) Correlation of Si-O-T (T = Si or Al) angles and ^{29}Si NMR chemical shifts in silicates and aluminosilicates. Interpretation by semi-empirical quantum-chemical considerations. *Chemical Physics Letters* **114**, 28-30.

Rosso, K.M. and Bodnar, R.J. (1995) Microthermometric and Raman spectroscopic detection limits of CO_2 in fluid inclusions and the Raman spectroscopic characterization of CO_2. *Geochimica et Cosmochimica Acta* **59**, 3961-3975.

Schauble, E.A., Ghosh, P. and Eiler, J.M. (2006) Preferential formation of ^{13}C-^{18}O bonds in carbonate minerals, estimated using first-principles lattice dynamics. *Geochimica et Cosmochimica Acta* **70**, 2510-2529.

Seitz, J.C., Pasteris, J.D. and Chou, I. (1996) Raman spectrscopic characterization of gas mixtures. II quantitative composition and pressure determination of the CO_2-CH_4 system. *American Journal of Science* **296**, 577-600.

Sen, S. and Stebbins, J.F. (1994) Phase separation, clustering, and fractal characteristics in glass: A magic-angle-spinning NMR spin-lattice relaxation study. *Physical Review B* **50**, 822-830.

Seo, J.H., Lee, S.K. and Lee, I. (2007) Quantum chemical calculations of equilibrium copper(I) isotope fractionations in ore-forming fluids. *Chem. Geol.* **243**, 225-237.

Sherriff, B.L., Grundy, H.D. and Hartman, J.S. (1987) Occupancy of T sites in the scapolite series; a multinuclear NMR study using magic-angle spinning. *Canadian Mineralogist* **25**, 717-730.

Skibsted, J., Hjorth, J. and Jakobsen, H.J. (1990) Correlation between ^{29}Si NMR chemical shifts and mean Si-O bond lengths for calcium silicates. *Chemical Physics Letters* **172**, 279-283.

Song, T.-R.A., Helmberger, D.V. and Grand, S.P. (2004) Low-velocity zone atop the 410-km seismic discontinuity in the northwestern United States. *Nature* **427**, 530-533.

Stebbins, J.F. (1988) Effects of temperature and composition on silicate glass structure and dynamics: Si-29 NMR results. *Journal of Non-Crystalline Solids* **106**, 359-369.

Stebbins, J.F. (1995a) Dynamics and structure of silicate and oxide melts: Nuclear magnetic resonance studies, In *Structure, Dynamics, and Properties of Silicate Melts*, (Eds. Stebbins, J.F., McMillan, P.F., Dingwell, D.B.). Mineralogical Society of America, Wasington, DC, pp. 191-246.

Stebbins, J.F. (1995b) Nuclear magnetic resonance spectroscopy of silicates and oxides in geochemistry and geophysics, In *Mineral Physics & Crystallography: A Handbook of Physical Constants*. American Geophysical Union, pp. 303-331.

Stebbins, J.F. (2016) Glass structure, melt structure, and dynamics: Some concepts for petrology. *American Mineralogist* **101**, 753-768.

Stebbins, J.F., Dubinsky, E.V., Kanehashi, K. and Kelsey, K.E. (2008) Temperature effects on non-bridging oxygen and aluminum coordination number in calcium aluminosilicate glasses and melts. *Geochimica et Cosmochimica Acta* **72**, 910-925.

Stebbins, J.F. and Xue, X. (2014) NMR Spectroscopy of Inorganic Earth Materials, In *Reviews in Mineralogy and Geochemistry*, (Eds. Henderson, G.S., Neuville, D.R., Downs, R.T.). Mineralogical Society of America, Virginia, U.S.A., pp. 605-653.

Stolper, E., Fine, G., Johnson, T. and Newman, S. (1987) Solubility of carbon dioxide in albitic melt. *American Mineralogist* **72**, 1071-1085.

Thomsen, T.B. and Schmidt, M.W. (2008) Melting of carbonated pelites at 2.5–5.0 GPa, silicate–carbonatite liquid immiscibility, and potassium–carbon metasomatism of the mantle. *Earth and Planetary Science Letters* **267**, 17-31.

Toplis, M.J., Kohn, S.C., Smith, M.E. and Poplett, I.J. (2000) Letter. Fivefold-coordinated aluminum in tectosilicate glasses observed by triple quantum MAS NMR. *American Mineralogist* **85**, 1556-1560.

Tossell, J.A. (1995) Calculation of the C-13 NMR shieldings of the CO_2 complexes of aluminosilicates. *Geochimica et Cosmochimica Acta* **59**, 1299-1305.

Vuilleumier, R., Seitsonen, A.P., Sator, N. and Guillot, B. (2015) Carbon dioxide in silicate melts at upper mantle conditions: Insights from atomistic simulations. *Chemical Geology* **418**, 77-88.

Wallace, P.J. (2005) Volatiles in subduction zone magmas: concentrations and fluxes based on melt inclusion and volcanic gas data. *Journal of Volcanology and Geothermal Research* **140**, 217-240.

White, B.S. and Montana, A. (1990) The effect of H_2O and CO_2 on the viscosity of sanidine liquid at high pressures. *J. Geophys. Res.-Solid Earth* **95**, 15683-15693.

Xue, X.Y., Stebbins, J.F., Kanzaki, M., McMillan, P.F. and Poe, B. (1991) Pressure-induced silicon coordination and tetrahedral structural-changes in alkali oxide-silica melts up to 12 GPa - NMR, Raman, and infrared-spectroscopy. *American Mineralogist* **76**, 8-26.

Xue, X.Y., Stebbins, J.F., Kanzaki, M. and Tronnes, R.G. (1989) Silicon coordination and speciation changes in a silicate liquid at high pressures. *Science* **245**, 942-944.

Yarger, J.L., Smith, K.H., Nieman, R.A., Diefenbacher, J., Wolf, G.H., Poe, B.T. and McMillan, P.F. (1995) Al coordination changes in high-pressure aluminosilicate liquids. *Science* **270**, 1964-1967.

Chapter 4. Effect of chemical disorder on structural changes in Na-Li silicate glasses quenched from melts at high pressure

Eun Jeong Kim, Yong Hyun Kim, and Sung Ken Lee

This study is currently ongoing, and thus the part of results and their discussion are presented here.

Abstract

Despite the importance of the mixed-cation effect on the structural changes of silicate glasses quenched from high-pressure melts, that of Na-Li silicate glasses quenched from melts at high pressures has not yet been studied. In this study, we explore the mixed-cation effect on the chemical disorder and structural changes of Na-Li trisilicate (NLS3) glasses at high pressures up to 8 GPa using solid-state nuclear magnetic resonance (NMR) and Raman spectroscopy. While the ^{29}Si magic angle spinning (MAS) NMR spectra of the NLS3 glasses show a relatively constant ratio of highly-coordinated Si at high pressures (>6 GPa), regardless of the lithium content (X_{Li}), the ^{17}O 3 quantum MAS NMR spectra show changes in (Na,Li)-O-Si with increasing X_{Li} and pressure. The ^{7}Li MAS NMR spectra of the NLS3 glasses show continuous changes of the peak position and widths with varying pressures and $X_{Li.}$ The spin-spin relaxation time (T_2) of the NLS3 glasses changes with increasing pressure and X_{Li}: The increase of T_2 with increasing pressure indicates that the cation disorder changes from a

random distribution to a chemical order above 6 GPa (X_{Li} = 0.25) and with increasing pressure from 1 atm to 6 GPa (X_{Li} = 0.50 and 0.75). According to the T_2 values of ^{7}Li in ^{7}Li NMR, together with the ^{29}Si MAS NMR spectra, the cation diffusion in mixed-alkali glasses with cations of different radii is interrupted at high pressures due to changes in the cation disorder and connectivity of the silicate network.

Keywords: chemical disorder, high pressure, glass structure, solid-state NMR

4.1. Introduction

Unveiling the cation disorder and structural changes in mixed-alkali silicate glasses is key to understanding the transport properties of silicate glasses, such as ion diffusion within silicate glasses. The structure of mixed-cation silicate glasses also provides insights into composition-induced complex changes in the properties of diverse technologically important multicomponent silicate glasses and natural melts in the Earth's interior. Among those mixed-alkali silicate glasses, mixed Li-Na silicate glasses and their end members have been widely used for solid electrolytes in batteries (Chen and Du, 2015; Masquelier and Croguennec, 2013; Ravaine, 1980; Tuller et al., 1980) due to the high diffusion rate of Li (Chen and Du, 2015; Masquelier and Croguennec, 2013; Tuller et al., 1980) and partly, to the absence of a grain boundary (Ravaine, 1980). Alkali silicate glasses are also used as substrates for ion implantation in semiconductor device fabrication (Snoeks et al., 1996) and as dielectric applications by the electric field-induced softening (McLaren et al., 2017; Pinter et al., 2018). Although Li is

minor element in magma, the Li content in silicate melts gives insight into the fractionation process of the magma (Herd et al., 2005) with the compatibility of Li in hydrous fluids in basaltic magma and its incompatibility in pyroxene minerals. Due to its compatibility, the concentration of Li tends to increase in partial melts (Marschall et al., 2017). The distribution of Li in these silicate melts, formed during the partial melting, is important to understand the fractionation process of the silicate melt itself and the diffusion of network-modifying cations at high pressure.

The "mixed-cation effect" in silicate melts represents considerable changes in the transport properties of melts with intermediate compositions as compared to those of end-members (Habasaki et al., 1996; Kjeldsen et al., 2014; Le Losq and Neuville, 2013; Moynihan et al., 1976; Rouse et al., 1978; Sen et al., 1996). The mixed-cation effect depends on the degree of cation intermixing as cation hopping from one site to another is more difficult between dissimilar pairs (e.g., Na-Li) than between similar pairs (e.g., Na-Na) (Sen et al., 1996; Xu and Stebbins, 1995). The proportion of dissimilar pairs depends on the degree of cation disorder; for instance, chemically ordered glasses contain the most abundant dissimilar pairs while phase-separated glasses have the least dissimilar pairs (Lee et al., 2003b). Previous studies have also reported that mixed-cation silicate glasses with different cation radii may have a greater tendency to relax toward the super-cooled liquid state than the silicate glasses containing a single type of network-modifying cations (Phillips, 1996; Welch et al., 2013; Yu et al., 2018; Yu et al., 2015). This is because the mixing of two cations with different radii results in local stress around the cations, and cation diffusion is enhanced in the mixed-cation glasses to reduce this local stress, hence result in changes to

the transport properties of the glasses at ambient temperatures.

Previous studies have investigated the structure of silicate melts and the mixed-cation effect in various oxide glasses quenched from these melts using theoretical calculations, such as molecular dynamic simulations (Cormack and Du, 2001; Habasaki and Hiwatari, 2003), and experimental techniques, such as X-ray scattering (Cormier and Cuello, 2013; Greaves, 1998; Lee et al., 2007), X-ray absorption spectroscopy (Greaves, 1998), neutron diffraction (Cormier et al., 2010; Cormier and Cuello, 2013), and high-resolution solid-state nuclear magnetic resonance (NMR) (Behrends and Eckert, 2011; Florian et al., 1996; Kaneko et al., 2017; Lee and Stebbins, 2006; Minami et al., 2014; Neuville et al., 2008; Ollier et al., 2004; Park and Lee, 2016; Schneider et al., 2013; Tsuchida et al., 2012; Tsuchida et al., 2010; Vessal and Greaves, 1992). Of these experimental techniques, high-resolution ^{17}O NMR yields specific information on the degree of cation disorder by proving the proportion of cation distribution around non-bridging oxygens (NBOs) and bridging oxygens (BOs). Previous studies on ^{17}O NMR have analyzed the effects of the ionic radius and cation field strength on the degree of cation disorder in various mixed-cation silicate glasses, such as Na-Ba (Lee et al., 2003b; Park and Lee, 2016), Na-Ca (Lee and Stebbins, 2003; Lee and Sung, 2008), Na-K (Florian et al., 1996), Mg-Ca (Allwardt and Stebbins, 2004), Ba-Ca (Stebbins et al., 1997), and Li-K silicate glasses (Balasubramanian and Rao, 1995). (See Table 1 in Park and Lee (2016) for previous studies on the distribution of various mixed-cations in silicate glasses.) However, ^{17}O NMR studies on Na-Li silicate glasses were not undertaken due to the similar isotropic chemical shifts of the Na-O-Si and Li-O-Si peak positions (e.g., Na-O-Si in $Na_2Si_2O_5$ glass with δ_{iso} of 39

ppm and Li-O-Si in $Li_2Si_2O_5$ glass with δ_{iso} of ~42 ppm) (Lee and Stebbins, 2003; Maekawa et al., 1996; Park and Lee, 2016).

Due to the shortcomings of ^{17}O NMR in analyzing Na-Li silicate systems, the distribution of Na and Li cations in Na-Li silicate glasses at 1 atm was studied using diverse NMR techniques in ^{7}Li NMR (Ali et al., 1995; Gee and Eckert, 1996; Gee et al., 1997). The peak intensities in the NMR spectra are related to the interactions between similar and dissimilar pairs, which indicate the chemical disorder of these cations, such as chemical order, random distribution, and phase separation (e.g., Lee et al., 2010a). Based on a comparison between the estimated NMR peak intensity and the experimental results, it was deduced that the mixing of Na and Li cations in Na-Li silicate glasses is likely to be random at 1 atm (Gee et al., 1997). While the Li K-edge X-ray scattering spectra have been used to study the Li configuration in Li-bearing alkali borate glasses at high pressures up to 5 GPa (Lee et al., 2007) and the ^{7}Li and ^{23}Na spin-spin relaxation time for Li and Na metal, respectively, have been reported up to 0.7 GPa (Hultzsch and Barnes, 1962), the distribution of Li in Na-Li silicate glasses and other glass systems has not been studied at high pressure using NMR and other spectroscopic methods.

Structural changes affecting the transport properties of silicate melts include the formation of highly coordinated network-forming cations, decrease in the fraction of NBO, and chemical disorder of network-modifying cations, such as the mixed-cation effect. For instance, the formation of $^{[5]}Si$ in silicate melts at high pressure is suggested to be a major factor controlling viscous flow in silicate melts (Angell et al., 1982; Poe et al., 1997; Stebbins, 2016; Xue et al., 1991); further, the continuous transition

between $^{[5]}$Si or $^{[5]}$Al and $^{[4,6]}$Si or $^{[4,6]}$Al may promote the diffusion of network-modifying cations around network-forming cations (Xue et al., 1991) and the fraction of $^{[5]}$Si and $^{[5]}$Al is closely related to the O^{2-} diffusivity at high pressure (Poe et al., 1997). Furthermore, the reduction of NBO with increasing pressure is suggested as a possible mechanism for changing in the melt viscosity at high pressures (Lee, 2010; Lee et al., 2008a).

The other factor, the chemical disorder of network-modifying cations, also affects the transport properties. The distribution of cations in silicate glasses seems to be systematic with varying the difference between cation radii. For instance, cations with the same valence states but different ionic radii (under 0.4 Å) seem to be distributed randomly in ternary silicate glasses, such as Na-Li, Na-K, Ca-Mg, and Ca-Ba (Allwardt and Stebbins, 2004; Dupree et al., 1990; Florian et al., 1996; Stebbins et al., 1997), while those with different valence states and a large difference in ionic radii (up to 0.6 Å) seem to have a preference to form dissimilar pairs (Allwardt et al., 2003; Lee et al., 2003b; Lee and Stebbins, 2003).

The degree of chemical disorder in the alkaline-earth elements in silicate glasses changes with increasing pressure and with different cation field strengths. Previous research has reported a preference for dissimilar pairs in Na-Ca silicate glasses at 1 atm based on the fractions of Na-O-$^{[4]}$Si and (Ca,Na)-O-$^{[4]}$Si (Lee and Stebbins, 2003), and the fraction of Na-O-$^{[4]}$Si decreases more than that of (Ca,Na)-O-$^{[4]}$Si at high pressures up to 8 GPa, as cations with higher cation field strengths are more stable with highly coordinated networks (Lee et al., 2008a), leading to a pressure-induced chemical disorder in the network-modifying cations in silicate melts (Lee et al., 2008a). In addition, previous studies on binary alkali silicate glasses at

high pressures show that the fractions of $^{[5]}$Si and $^{[6]}$Si increase as the cation radius increases from 1.02 Å (Na^+) to 1.38 Å (K^+) in binary Na-tetrasilicate and K-tetrasilicate glasses quenched from melts at high pressures up to 12 GPa (Xue et al., 1991). While the experimental results have revealed the effect of the cation field strength in mixed-cation effects and the effect of the cation radius in binary alkali silicate glasses at high pressures, experimental verification of the pressure-induced changes to the chemical disorder with different cation radii remains to be explored.

In this study, we aim to identify the effect of the cation radius on the mixing of cations in mixed-alkali silicate glasses quenched from melts at high pressures and the relevant changes in silicon and oxygen environments using solid-state NMR and Raman spectroscopy. Particularly, we report the first ^{7}Li magic angle spinning (MAS) and ^{7}Li spin-echo NMR spectra for glasses under compression of up to 8 GPa. The comparison of the ^{7}Li NMR and ^{17}O 3 quantum (3Q) MAS NMR spectra was also reported to explain the structural changes of the silicate network with varying Li content.

4.2. Experimental methods

4.2.1. Sample preparation

Na-Li silicate glasses of different Li content [$(Na_2O)_{1-x} \cdot (Li_2O)_x \cdot 3SiO_2$, NLS3], with $X_{Li} = Li_2O/(Na_2O + Li_2O)$ of 0.25, 0.50, and 0.75, were synthesized from powdered Na_2CO_3, Li_2CO_3, and SiO_2. About 0.2 wt.% of Co oxide was added to enhance the spin-lattice relaxation. The Na_2CO_3, Li_2CO_3, and SiO_2 powders were dried overnight at 300 °C and the weighed powders were mixed by grinding them in an agate mortar. The mixtures were decarbonated in a Pt crucible at 750–850 °C for 1 h, fused at 1000–

1300 °C for 30 min at ambient pressure, and then quenched into glasses by plugging the bottom of the crucible into distilled water. The glasses were visually transparent and exhibited constant extinction in cross-polarized light. The starting materials of the glasses were loaded into a multi-anvil apparatus with a 14/8 (octahedron edge length/truncated edge length of the anvils) "G2" assembly. The samples were fused at approximately 1723–1923 K for 5 min and quenched into glasses at pressures of 6 and 8 GPa. Note that the structure of the glasses quenched from the melts represents that of the super-cooled liquids near the glass-transition temperature (T_g) (e.g., Stebbins, 2016); therefore, the structure of the glasses is often studied to understand the characteristics of silicate melts in ambient- and high-pressure conditions. The initial quench rate was estimated to be larger than 500 °C/s. The volumes of the sample chambers of the 14/8 G2 assembly are typically about 30 mm^3. The ^{17}O-enriched NLS3 glasses used for the experiments at 6 GPa were fabricated using the same procedure as that used for synthesizing the NLS3 glasses. In this case, the Na_2CO_3, Li_2CO_3, and ^{17}O-enriched SiO_2 acquired from the hydrolysis of 40% ^{17}O water with $SiCl_4$ were used as the starting materials. The X-ray powder diffraction and ^{29}Si MAS NMR spectra of the glasses at 1 atm and high pressures do not show any evidence for the presence of crystalline impurities.

4.2.2. NMR spectroscopy

The ^7Li, ^{29}Si MAS, and ^{17}O 3QMAS NMR spectra were collected on a Varian solid-state NMR 400 system (9.4 T) at Larmor frequencies of 155.46 MHz for ^7Li, 79.47 MHz for ^{29}Si, and 54.23 MHz for ^{17}O nuclides. The ^7Li MAS NMR spectra were collected using a 3.2-mm Varian double-resonance

probe at a spinning speed of 15 kHz. A single-pulse sequence with an approximate 30° pulse (0.5 μs) and a recycle delay of 1 s were used to collect the ^{7}Li MAS NMR spectra. The spectra were referenced to a 1 M LiCl solution. While the typical 90° pulse lengths were 9–12 μs for ^{7}Li (Gee and Eckert, 1996), separate nutation NMR experiments were also performed to verify the 360° pulse lengths of the NLS3 glasses; the measured 90° and 180° pulses are 3 and 6 μs, respectively. The ^{7}Li spin-spin relaxation experiments were performed using a spin-echo pulse sequence [90°-t_1-180°-t_2] with a 5-s recycle delay to pin down the distribution of Li in the NLS3 glasses. ^{29}Si MAS NMR spectra were collected using a 3.2-mm Varian double-resonance probe at a spinning speed of 11 kHz. A single-pulse sequence with a 30° pulse (1.2 μs) and delay time of 30 s was used. Tetramethylsilane (TMS) was used as the external reference. The ^{17}O MAS and 3QMAS NMR spectra were collected using a 3.2-mm Varian double-resonance probe at a spinning speed of 15 kHz. The ^{17}O MAS NMR spectra were collected using a single-pulse sequence with an approximate 30° pulse (1.2 μs) and a recycle delay of 1 s. The ^{17}O 3QMAS NMR spectra were obtained using a fast-amplitude modulation (FAM)-based shifted-echo pulse sequence with a relaxation delay of 1 s – 3.3 μs pulse for 3Q excitation – t1 delay – FAM pulse train with a 1 μs pulse – echo delay – 11 μs soft pulse for echo reconversion – t2 acquisition.

4.3. Results

4.3.1. Structural changes in Si in NLS3 glasses: Insights from ^{29}Si MAS NMR

Figure 4.1 shows the ^{29}Si MAS NMR spectra of the X_{Li} = 0.25 glass

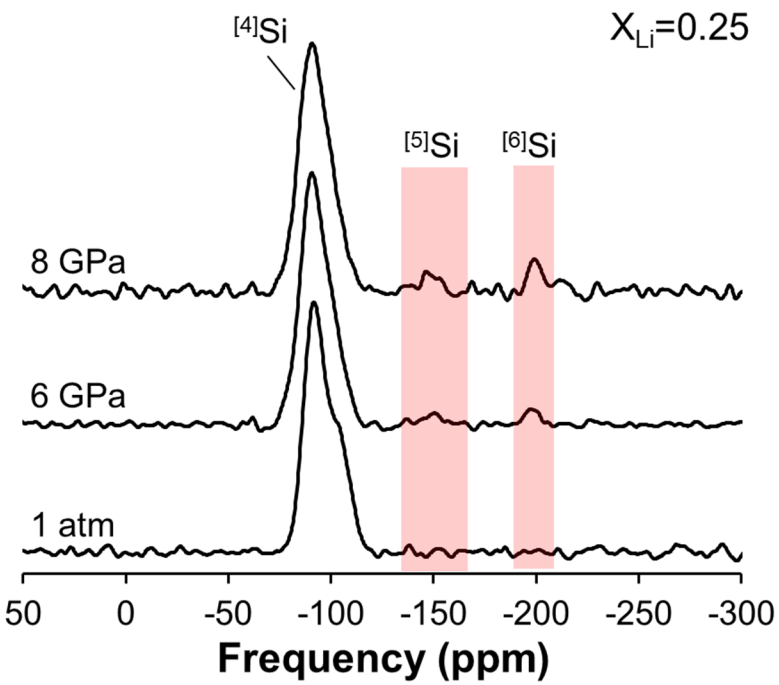

Figure 4.1. ^{29}Si MAS NMR spectra of NLS3 glasses with X_{Li} = 0.25 at different pressures.

Table 4.1. The estimated fractions of $^{[5]}$Si and $^{[6]}$Si in Na-Li trisilicate glasses quenched from melts at high pressures. The fractions are estimated from the peak areas in the ^{29}Si MAS NMR spectra.

X_{Li}	Pressure	$^{[5]}$Si	$^{[6]}$Si
0.25	1 atm	< 0.05	< 0.05
	6 GPa	3.2	2.7
	8 GPa	5	7.4
0.50	1 atm	< 0.05	< 0.05
	6 GPa	3.1	2.6
0.75	1 atm	<0.05	<0.05
	6 GPa	2.5	2.5

with increasing pressures up to 8 GPa. $^{[4]}$Si is dominant at 1 atm and the Q^3 and Q^4 species of the silicate melts are partially resolved at 1 atm (~–90 ppm for Q^3 species and ~–100 ppm for Q^4 species). The peak for $^{[4]}$Si becomes unresolved and asymmetric above 6 GPa and the peak maximum of $^{[4]}$Si shifts towards higher frequencies (less negative chemical shift) with an increase in pressure from –91.8 ppm at 1 atm to –90.6 ppm at 8 GPa. The spectra at high pressure also show the presence of 4-, 5-, and 6-coordinated Si. Particularly, the fraction of the highly coordinated Si (e.g., $^{[5,6]}$Si) increases with increasing pressure and the estimated fraction of $^{[5,6]}$Si in NLS3 glasses at 6 GPa is comparable to that in the sodium trisilicate (NS3) glasses at 6 GPa (Kelsey et al., 2009; Lee, 2004; Lee et al., 2003a). Table 4.1 lists the estimated fractions of $^{[5,6]}$Si in the NLS3 glasses.

Figure 4.2a shows the ^{29}Si MAS NMR spectra of the NLS3 glasses with varying X_{Li} at 1 atm in the chemical shift range of –50 to –150 ppm. The peak intensity of the Q^2 and Q^4 species in the NLS3 melts at 1 atm increases with increasing X_{Li}. The increase in the Q^2 and Q^4 species with increasing X_{Li} is due to the disproportionation of the silicate melts with an increase in the cation field strength (Maekawa et al., 1991; Stebbins, 2016). For example, the fractionation of the Q^n species in M_2O-SiO_2 is ideally identical regardless of the network-modifying cation (M), but the fractions of the Q^2 and Q^4 species in the M_2O-$4SiO_2$ glasses increase with increasing cation field strength, from potassium to lithium (Maekawa et al., 1991). Therefore, the systematic increase in the Q^2 and Q^4 species over the Q^3 species with increasing X_{Li} at 1 atm is due to the larger field strength of Li^+ (~1.83) than that of Na^+ (~0.96). See the supplementary information for simulation results on the estimated fractions of Q^n species at 1 atm (Table 4.S1 and Figure 4.S1).

Figure 4.2b shows the ^{29}Si MAS NMR spectra of the NLS3 glasses with varying X_{Li} at 6 GPa. The spectra show the presence of highly coordinated Si in the NLS3 glasses for all compositions at 6 GPa. The fraction of $^{[5,6]}$Si in the NLS3 glasses is estimated from the peak intensity of the ^{29}Si MAS NMR spectra. Though the changes are within a defined error margin, the $^{[5,6]}$Si fraction seems to decrease with increasing X_{Li} from 0.25 to 0.75 (Table 4.1). The estimated fraction of $^{[5,6]}$Si in NLS3 glasses is 5.0%–5.9%, which is consistent with the reported fraction of $^{[5,6]}$Si in sodium trisilicate glasses at 6 GPa (~4.6%) (Kelsey et al., 2009) and with the trend reported for Na- and K-tetrasilicate glasses and Na-trisilicate glasses at high pressures (Kelsey et al., 2009; Lee et al., 2004, 2006; Lee et al., 2003a; Xue et al., 1991).

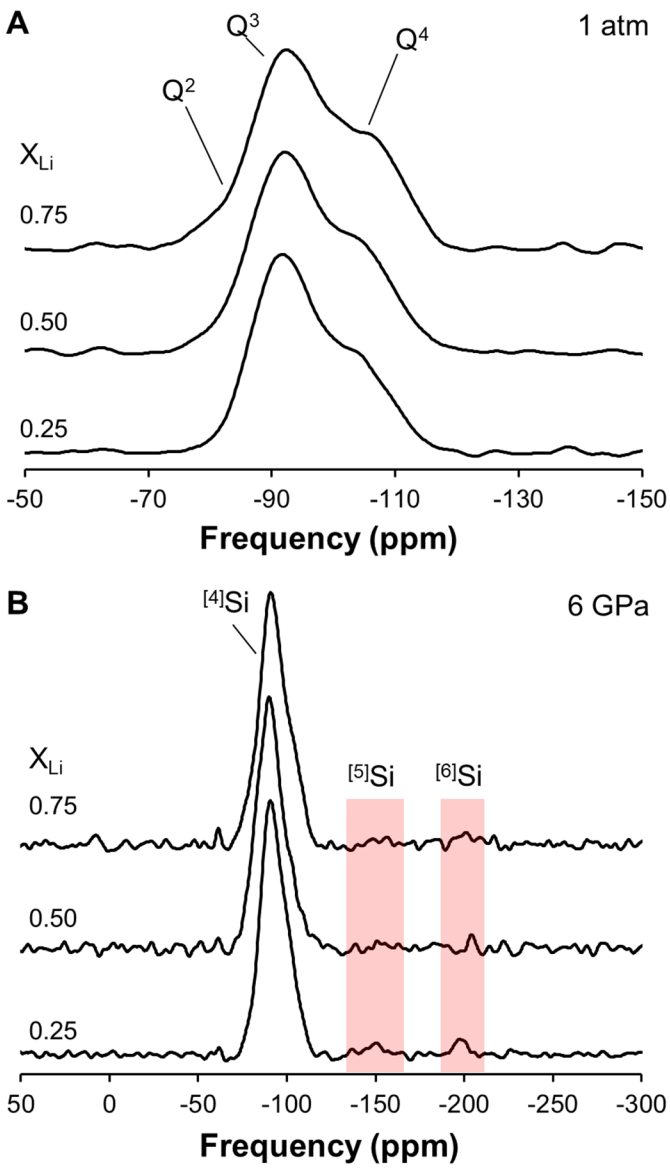

Figure 4.2. ^{29}Si MAS NMR spectra of NLS3 glasses with varying X_{Li} (a) at 1 atm and (b) at 6 GPa.

4.3.2. Structure of Li^+ in NLS3 glasses quenched from melts at high pressures: Insights from ^7Li MAS NMR results

Figures 4.3a and b show the ^7Li MAS NMR spectra of NLS3 glasses with varying X_{Li} (from 0.25 to 0.75) at 1 atm and at 6 GPa, respectively. The peak shape in the ^7Li MAS NMR spectra is Lorentzian broadening, which may indicate a moderately high mobility for Li^+. While an earlier pioneering study reported that the peak shift is negligible with varying X_{Li} (from X_{Li} = 0.2 to 1) in Na-Li disilicate glasses (Ali et al., 1995), we observed small changes of the peak position with varying X_{Li}. The peak maxima shift towards lower frequencies (the more negative region), from 0.3 ppm to 0.1 ppm, with an increase in X_{Li} from 0.25 to 0.75 at 1 atm, and from 0.3 ppm to -0.1ppm with increasing X_{Li} from 0.25 to 0.75 at 6 GPa, respectively. The degree of peak shift slightly increases with increasing pressure from 1 atm to 6 GPa. Peak position and the isotropic chemical shift (δ_{iso}) of ^7Li generally decrease with an increase in the coordination number of ^7Li and the distance between ^7Li and oxygen (Li-O distance) (Alam et al., 2012; Park and Lee, 2016; Stebbins, 1998; Xu et al., 2007). This trend is also observed in ^6Li (Xu and Stebbins, 1995), ^{23}Na (Tsuchida et al., 2010), and ^{109}Ag NMR experiments (Tsuchida et al., 2012). Therefore, the peak shift to lower frequencies (negative frequency region) in ^7Li MAS NMR spectra for NLS3 glasses at 1 atm and at 6 GPa indicates that the average coordination number of Li and/or the Li-O distance in mixed Na-Li silicate glasses may increase with increasing X_{Li}.

Figure 4.3c shows the ^7Li MAS NMR spectra of NLS3 glasses with X_{Li} = 0.25 at different pressures up to 8 GPa. The peak maxima of ^7Li in NLS3 glasses with X_{Li} = 0.25 slightly shifts to lower frequencies from 0.3 ppm at 1

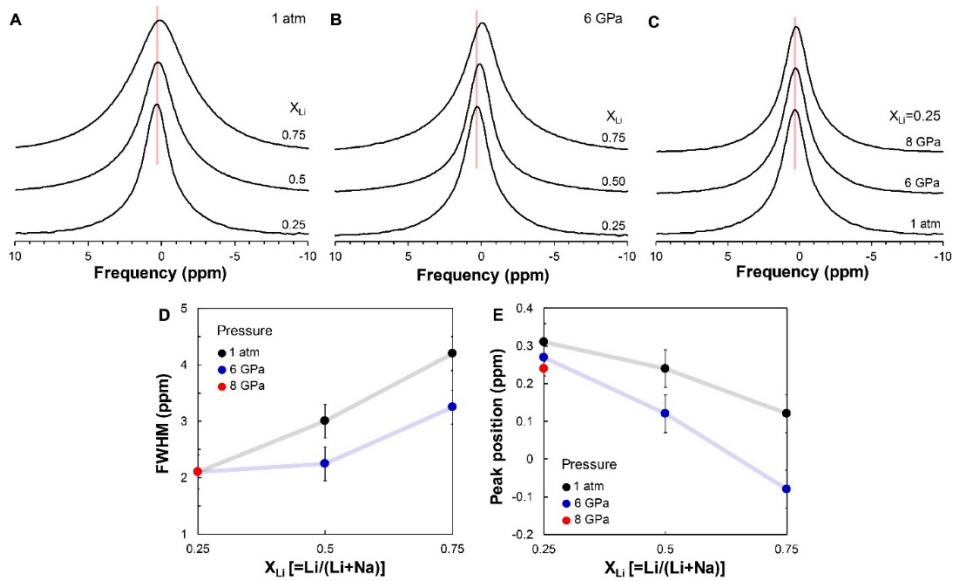

Figure 4.3. (a) ^{7}Li MAS NMR spectra of NLS3 glasses with varying X_{Li} at 1 atm. (b) ^{7}Li MAS NMR spectra of NLS3 glasses with X_{Li} = 0.25 and at different pressure up to 8 GPa. (c) ^{7}Li MAS NMR spectra of NLS3 glasses with varying X_{Li} at 6 GPa. (d) FWHM of ^{7}Li in NLS3 glasses with different X_{Li} and at different pressures. (e) Peak position of ^{7}Li in NLS3 glasses with varying X_{Li} and pressure.

Table 4.2. Peak maxima in the ^{7}Li MAS NMR spectra of Na-Li trisilicate glasses with different compositions and at different pressures.

Pressure \ X_{Li}	0.25	0.50	0.75
1 atm	0.31	0.24	0.12
6 GPa	0.27	0.12	-0.08
8 GPa	0.24		

atm to 0.2 ppm at 8 GPa, while the peak widths remain constant (~2.1 ppm). The observed changes in the peak shift in NLS3 glasses with X_{Li} = 0.25 at different pressures from 1 atm to 8 GPa are similar to those in NLS3 glasses with varying X_{Li} from 0.25 to 0.50 at 1 atm (see Fig. 4.3e and Table 4.2 for changes in the peak maxima in the ^{7}Li MAS NMR spectra of NLS3 glasses of different compositions and at different pressures). The rather small but systematic and continuous changes of the peak position with increasing pressure indicates that the distribution of Na and Li in the NLS3 glasses prefers substantial mixing rather than the phase separation at high pressure as the phase-separated glasses would show abrupt changes of the peak position with increasing Li content (Ali et al., 1995; Gee and Eckert, 1996; Gee et al., 1997).

While a possible solutions for obtaining the ^{7}Li MAS NMR spectra at a higher resolution is to conduct NMR experiments in high magnetic fields, which reduces quadrupolar broadening and increases the split of nuclear spin states (Levitt, 2005), the ^{7}Li MAS NMR spectra of NLS3 glasses obtained at 14.1 T showed little difference in the peak position and width when compared with the values obtained at 9.4 T (Figure 4.S2) as the

quadrupolar coupling constant (C_q) for ^{7}Li is relatively small (-3.7 × 10^{-2} Q) (Park and Lee, 2016) and the effect of the field on the quadrupolar nuclide is negligible for ^{7}Li.

The full-width at half-maximum (FWHM) of the ^{7}Li MAS NMR spectra increases from 2.2 ppm to 4.8 ppm with increasing X_{Li} from 0.25 to 0.75 at 1 atm (Figure 4.3d). While the FWHM of NLS3 glasses with X_{Li} = 0.25 is relatively constant with varying pressure up to 8 GPa (~ 2.1 ppm), the FWHM of NLS3 glasses with X_{Li} = 0.50 and 0.75 decreases with increasing pressure from 1 atm to 6 GPa for NLS3 glasses. The peak width of the ^{7}Li MAS NMR spectra is controlled by the temperature-related Li mobility, such as the increased Li mobility due to spinning-induced heating during magic angle spinning (Dodd et al., 2000; Elbayed et al., 2005; Kim and Lee, 2013; Park and Lee, 2016), and dipolar interactions between ^{7}Li nuclides with varying Li content (MacKenzie and Meinhold, 1994; Yap and Elliott, 1995). As the experimental conditions (e.g., temperature of the NMR probe and the spinning speed) are identical for all NLS3 glasses at 1 atm and at high pressure, the changes in the peak widths are related to the dipolar interactions between ^{7}Li nuclides in NLS3 glasses. The magnitude of the dipolar coupling increases with decreasing the distance between lithium cations (Yap and Elliott, 1995). As the increase of Li content induces the decrease of the Li-Li distance, the observed increase in the peak width with increasing X_{Li} evidently shows the decrease in the distance between Li cations. The reduction of the peak width with increasing pressure is first reported in this study. This might be related to the increase in the distance between Li cations, such as changes in the cation mixing behavior from random to chemically ordered.

4.3.3. Distribution of ^{7}Li in NLS3 glasses: Insights from spin-spin relaxation of ^{7}Li in NLS3 glasses

Figure 4.4a shows the ^{7}Li NMR spectra of NLS3 glasses with X_{Li} in the range of 0.25–0.75 with increasing echo time (τ). Increasing the lithium content at the same pressure decreases the time required for the dephasing of transverse magnetization by approximately six times (e.g., from 6.5 ms for X_{Li} = 0.25 at 1 atm to 1.1 ms for X_{Li} = 0.75 at 1 atm).

Figure 4.4b shows the calculated ^{7}Li spin-spin relaxation time (T_2) curves of NLS3 glasses with varying X_{Li} and pressures up to 8 GPa; the integrated peak areas in Figure 4a were used to calculate the T_2 time. The total peak area in the ^{7}Li NMR signals is normalized with respect to the peak area of a fully relaxed spectrum (M/M_0). The ^{7}Li peak intensity is simulated by the following equation:

$$M/M_0 = 1 - exp[-(\tau/T_2)]$$

where T_2 is the spin-spin relaxation time constant. See Table 4.3 for a simulation parameter. The T_2 time of ^{7}Li depends on the interactions between the Li cations, such as Li-Li distances (Ali et al., 1995; Gee et al., 1997). The average Li-Li distance varies with Li content, cation disorder, and pressure. The increase in X_{Li} decreases the Li-Li distance, resulting in the decrease in the T_2 time. When X_{Li} is identical, the distribution of Li cations can affect the T_2 time. The distribution of cations can be divided into three types: chemical order (preference to form Na-Li dissimilar pairs), random distribution, and phase separation (preference to form Na-Na and Li-Li similar pairs). The distributions of cations vary continuously from one another, and the extent of cation distribution can be parameterized by Q_m, which is used to describe Al avoidance, from Q_m = -1 (phase separation), Q_m

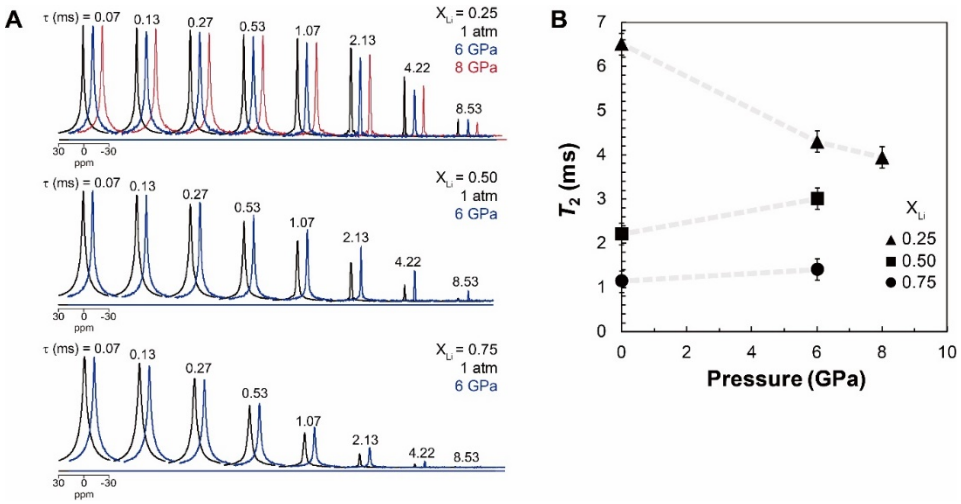

Figure 4.4. (A) Evolution of the ^{7}Li NMR spectra of NLS3 glasses with different X_{Li} and at pressures up to 8 GPa. The black, blue, and red lines represent the peak intensity of ^{7}Li NMR spectra at 1 atm, 6 GPa, and 8 GPa, respectively. (B) ^{7}Li T_2 curves at X_{Li} = 0.25, 0.50, and 0.75 as a function of pressure up to 8 GPa.

Table 4.3. A simulation parameter for the integrated peak area of the recovered ^{7}Li NMR signal with respect to the echo time (τ).

X_{Li}	Pressure	T_2 (ms)
0.25	1 atm	6.50 ± 0.20
	6 GPa	4.30 ± 0.20
	8 GPa	3.94 ± 0.20
0.50	1 atm	2.20 ± 0.20
	6 GPa	3.00 ± 0.20
0.75	1 atm	1.15 ± 0.20
	6 GPa	1.40 ± 0.20

= 0 (random distribution), to Q_m = 1 (chemical order).(Lee et al., 2010b) The average Li-Li distance is the longest in chemical order (Q_m = 1) and is the shortest in phase separation (Q_m = -1). Therefore, the T_2 time for ^{7}Li decreases in the order of chemical order, random distribution, and phase separation at 1 atm at the same X_{Li} value. **T**he increase in pressure also affects the T_2 time. **T**he free volume in glass reduces with increasing pressure, which in turn reduces the Li-Li distance. The T_2 of ^{7}Li decreases with the reduction of the Li-Li distance when there is no change in the cation distribution and Li content. The observed changes in the T_2 with increasing pressure show nonsystematic changes with increasing X_{Li}. The T_2 in the NLS3 glasses (X_{Li} = 0.25) decreases with increasing pressure and the degree of T_2 decrease reduce at pressures above 6 GPa. The slope of T_2 for X_{Li} = 0.25 at 6–8 GPa decreases less than that at 1 atm–6 GPa. The changes in the T_2 decrease at X_{Li} = 0.25 may be related to the decrease of the free volume reduction with increasing pressure as the second-order derivatives

of the volume over pressure is positive. Whereas, the T_2 at X_{Li} = 0.50 and 0.75 increases with increasing pressure from 1 atm to 6 GPa and the degree of the increase of the T_2 time is higher for X_{Li} = 0.50. As the pressure increase would result in the reduction of the Li-Li distance when the cation disorder does not change, the increase of T_2 with increasing pressure indicates the changes in cation disorder upon compression. As the distribution of Na and Li in the Na-Li silicate glasses at 1 atm is random (Ali et al., 1995; Gee et al., 1997), the increase in the spin-spin relaxation time with respect to pressure for X_{Li} = 0.50 and 0.75 may indicate the reduction of Li-Li pairs and/or the increase of the Li-Li distance, which means the cation disorder changes from random to chemical order. Further MD simulations on the distribution of Li and Na in Na-Li silicate glasses is needed to confirm the variations in T_2 with varying pressure and chemical disorder of cations

The presence of inhomogeneity can be also obtained by the comparison with FWHM in MAS NMR spectra and calculated FWHM from T_2. The FWHM can be estimated from T_2 with $1/\pi T_2$ (in Hz) when the nuclide of interest decays homogenously (Levitt, 2005). Generally, the peak width in MAS NMR spectra is broader than the calculated FWHM from T_2 due to the inhomogeneous broadening. The broadening is due to the inhomogeneity of magnetic field by the volume of the sample, errors from the apparatus, and/or susceptibility effects (Levitt, 2005). As the ^{7}Li MAS NMR experiments and the ^{7}Li spin-echo experiments were performed in the same NMR instrument, we assume that the changes between the FWHM from MAS NMR spectra and that calculated from T_2 are from the macroscopic property changes in magnetic field in the sample. Figure 4.S5 shows the changes of FWHM in ^{7}Li MAS NMR spectra and that calculated

from T_2. Though the slope of FWHM with respect to pressure changes non-linearly with varying X_{Li}, the differences between FWHM in ^{7}Li MAS NMR spectra and that calculated from T_2 decrease with increasing pressure regardless of X_{Li}. As the experiments were performed in the same NMR apparatus, the reduction of peak widths gap indicates the reduction of inhomogeneous decays of Li in NLS3 glasses, and this may be related to the changes in Li environments, such as the changes in distribution of Li and Na from random distribution to chemical ordering.

This ^{7}Li NMR data may provide insights into the distribution of mixed cations at high pressure with respect to the cation field strength. A previous study on the effect of pressure on the mixed Na-Ca silicate glasses at high pressure showed the effect of cation charge on the distribution of Na and Ca (Lee et al., 2008a). The cation radii (r) of Na and Ca are similar (~ 1.0 Å) but the charge (Z) is different; therefore, Ca^{2+} has a higher cation field strength (Z/r^2). The ^{17}O 3QMAS NMR spectra for Na-Ca silicate glasses showed the presence of Na-NBO and (Na,Ca)-NBO at 1 atm (Lee et al., 2008a). The cation with a higher cation field strength is more stable with highly coordinated Si, resulting in the drastic decrease of Na-NBO and negligible changes of the fraction of (Na,Ca)-NBO with increasing pressure from 1 atm to 6 GPa (Lee et al., 2008a). The decrease of Na-NBO over (Na,Ca)-NBO indicates that the distribution of mixed cations changes toward more cation ordering with increasing pressure. Assuming that the pressure-induced cation disorder shows a systematic change with respect to the cation field strength, the fractions of Na-NBO would decrease and that of (Na,Li)-NBO would increase, as shown in (Na,Ca)-trisilicate glasses at high pressure (Lee et al., 2008b). The increase of (Na,Li)-NBO at high

pressure is also related to the chemical ordering of Na and Li at high pressure. The increase of Na-Li dissimilar pairs at the same pressure would increase the Li-Li distance, resulting in the increase of T_2 of ^{7}Li at high pressure.

4.3.4. Fraction of non-bridging oxygen in NLS3 glasses at high pressures: Insights from ^{17}O 3QMAS NMR results

Figure 4.S3 represents the ^{17}O MAS NMR spectra of NLS3 glass with varying X_{Li} and pressure up to 6 GPa. The spectra indicate the partially resolved Si-O-Si (BO) as well as (Na,Li)-O-Si [(Na,Li)-NBO, at around 30 ppm]. The peak assignment is based on the previous ^{17}O NMR studies on crystalline and amorphous Na and Li silicates (Maekawa et al., 1996; Maekawa et al., 1991; Park and Lee, 2016). The peak widths of both NBO and BO in the ^{17}O MAS NMR spectra increase with increasing pressure. The peak maxima of (Na,Li)-NBO at 1 atm are ~27 ppm regardless of X_{Li}. As the isotropic chemical shifts (δ_{iso}) of Li-NBO [Li-O-Si in $Li_2Si_2O_5$ with δ_{iso} of ~42 ppm] and Na-NBO [Na-O-Si in $Na_2Si_2O_5$ glass with δ_{iso} of 39 ppm] are similar, it is difficult to distinguish Li-NBO from Na-NBO and (Na,Li)-NBO here. The peak for (Na,Li)-NBO shifts to a higher frequency (positive frequency) with increasing pressure up to 6 GPa; the peak maxima shifts from 27 ppm to 32 ppm (X_{Li} = 0.25) and from 27 ppm to 34 ppm (X_{Li} = 0.50) with increasing pressure from 1 atm to 6 GPa, respectively. This may be related to the formation of new oxygen sites such as (Na,Li)-O-$^{[5,6]}$Si (Lee, 2004; Lee et al., 2003a). However, due to the peak overlap and similar peak positions among different NBO and BO sites in MAS NMR spectra, it is hard to obtain quantitative information on the presence of oxygens linked to

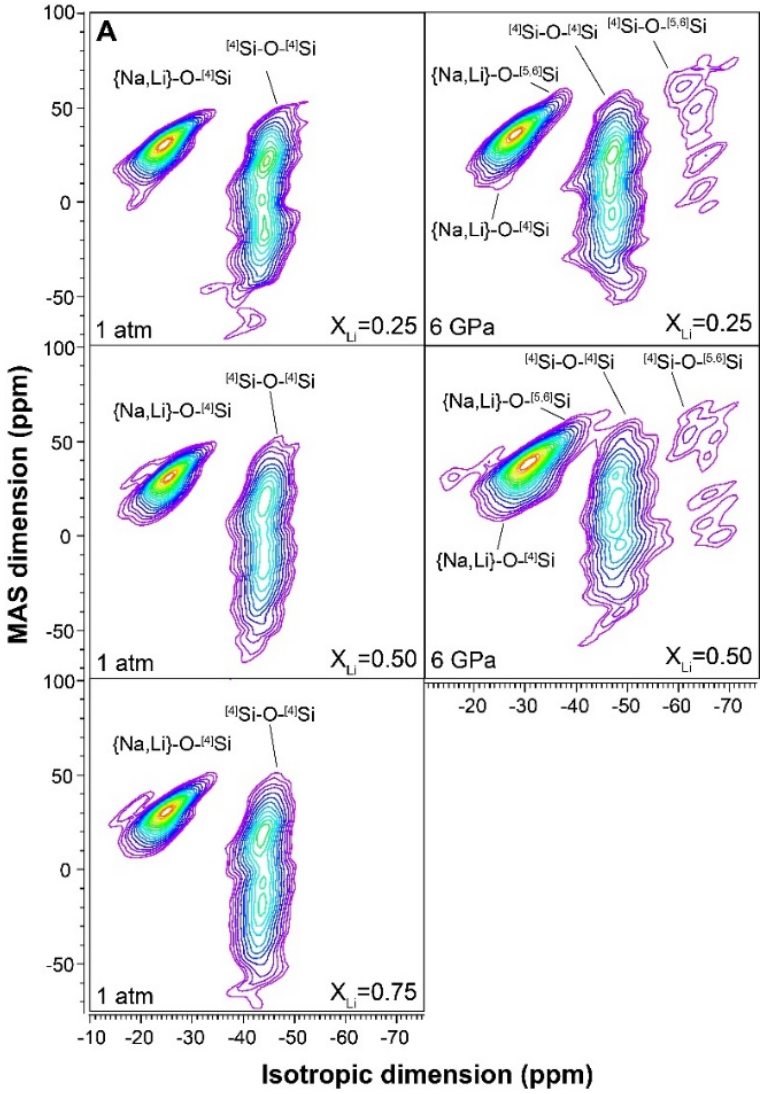

Figure 4.5. (A) ^{17}O 3QMAS NMR spectra of NLS3 glasses with varying X_{Li} and at different pressures up to 6 GPa. Contour lines are drawn at 5% increments from 13 to 93% of the relative intensity, with added lines at 5%, 7%, and 10% to show low-intensity peaks better.

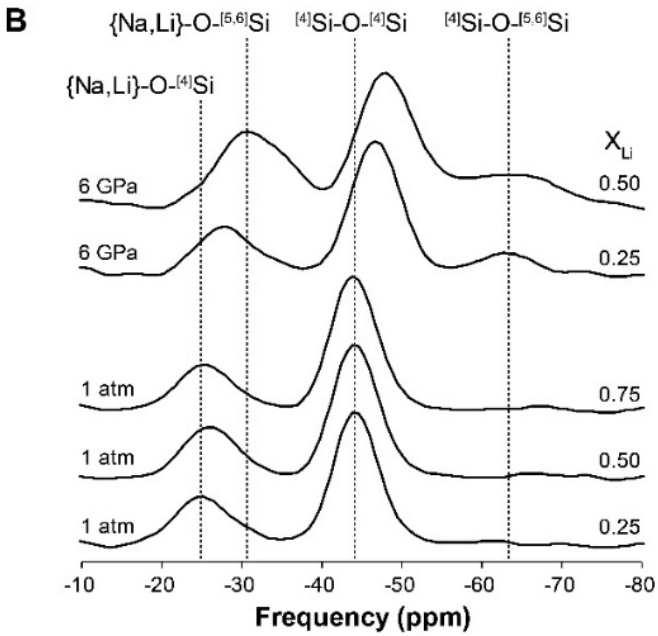

Figure 4.5. (B) Total isotropic projection of the ^{17}O 3QMAS NMR spectra of NLS3 glasses at different pressures and X_{Li} values.

[5,6]Si, such as [4]Si-O-[5,6]Si and (Na,Li)-O-[5,6]Si, in the ^{17}O MAS NMR spectra.

Figure 4.5a shows the ^{17}O 3QMAS NMR spectra of NLS3 glasses quenched from melts at high pressures from 1 atm to 6 GPa and with varying X_{Li} from 0.25 to 0.75. While a distinction between Li-NBO and Na-NBO is still difficult in the ^{17}O 3QMAS NMR spectra, four peaks corresponding to (Na,Li)-O-[4]Si (~–25 ppm at 1 atm in the isotropic dimension and ~30 ppm at 1 atm in the MAS dimension), (Na,Li)-O-[5,6]Si (~–36 ppm in the isotropic dimension and ~53 ppm in the MAS dimension at 6 GPa), [4]Si-O-[4]Si (~–44 ppm at 1 atm in the isotropic dimension), and [4]Si-O-[5,6]Si (~–63 ppm at 6 GPa in the isotropic dimension) are well resolved. The peaks corresponding to the NBOs and BOs shift to a lower frequency region (negative chemical shift, more shielded) in the isotropic

dimension and to a higher frequency region in the MAS dimension with increasing pressure. The increase in δ_{iso} of $^{[4]}$Si-O-$^{[4]}$Si is observed with increasing pressure from 1 atm to 6 GPa, probably due to an increase in Si-O distance (Lee et al., 2003a). The ^{17}O δ_{iso} of the NBO for NLS3 glass at 6 GPa is larger than that at 1 atm, implying decreasing (Na,Li)-O distance or the increasing average number of Na and Li around the NBO. The (Na,Li)-O-$^{[4]}$Si and (Na,Li)-O-$^{[5,6]}$Si for NLS3 glass at 6 GPa are both more shielded (negative frequency) than (Na,Li)-O-$^{[4]}$Si for NLS3 glasses at 1 atm, which can be attributed to the increase in the Si-O distance for (Na,Li)-O-$^{[5,6]}$Si (Lee et al., 2003a). Figure 4.5b shows the total isotropic projection of the ^{17}O 3QMAS NMR spectra of NLS3 glasses. As mentioned earlier, the peaks of (Na,Li)-O-Si and Si-O-Si shift to lower frequency regions in the isotropic dimension. The peak shifts of the NLS3 glasses from 1 atm to 6 GPa for both NBO and BO are ~–3 ppm for X_{Li} = 0.25 and ~–4 ppm for X_{Li} = 0.50, respectively. While the isotropic projection of the ^{17}O 3QMAS NMR spectra for the NLS3 glasses at 1 atm shows almost identical peak widths and shape; an apparent increase in the peak width is observed in the isotropic dimension at 6 GPa and the peak width broadening in X_{Li} = 0.50 is larger than that in X_{Li} = 0.25 at 6 GPa. Furthermore, $^{[4]}$Si-O-$^{[4]}$Si in NLS3 glass with X_{Li} = 0.50 showed a pressure-induced increase in peak asymmetry. Previous theoretical calculations on bridging oxygen clusters with Na^+ and Li^+ reported that the quadrupolar coupling constant (C_q) of the Na-containing bridging oxygen (Na-BO) cluster is higher than that of the Li-BO cluster and the quadrupolar asymmetry constant (η_q) of Na-BO cluster is lower than that of Li-BO cluster (Vermillion et al., 1998). The difference is negligible when Na-BO or Li-BO distance is larger than 2.5 Å (Vermillion et al., 1998).

Therefore, based on the theoretical calculation data, the observed changes in the peak widths and symmetry with increasing pressure and X_{Li} may be related to the decrease in distance between (Na,Li) and bridging oxygen and changes in C_q and η with respect to Na and Li.

Figure 4.6 (a) shows the fraction of oxygen clusters in the NLS3 glasses with varying X_{Li} and at different pressures. These values are estimated from the isotropic projection of the ^{17}O 3QMAS NMR spectra. The fractions of different oxygen environments are simulated using four Gaussian functions representing (Na,Li)-O-$^{[4]}$Si, (Na,Li)-O-$^{[5,6]}$Si, $^{[4]}$Si-O-$^{[4]}$Si, and $^{[4]}$Si-O-$^{[5,6]}$Si. The peak position and width of each peak during spectral simulation are based on previous ^{17}O NMR studies (Lee et al., 2008a; Park and Lee, 2016) and those shown in the current ^{17}O 3QMAS NMR spectra. The simulation of the isotropic projection of the ^{17}O 3QMAS NMR spectra gives quantitative information on the oxygen clusters in the system. For the trisilicate glasses, the expected NBO fraction [i.e., NBO/(NBO + BO)] is 29% and the calculated fraction of NBO in NLS3 glasses at 1 atm is ~28%–30%, similar to the nominal NBO ratio.

Figure 4.6 (b) shows the estimated fractions of different oxygen environments with respect to pressure and X_{Li}. The fraction of the BO is almost identical with varying X_{Li}. As the pressure increases, the fractions of $^{[4]}$Si-O-$^{[4]}$Si and (Na,Li)-O-$^{[4]}$Si decrease and the fractions of $^{[4]}$Si-O-$^{[5,6]}$Si and (Na,Li)-O-$^{[5,6]}$Si increase. The estimated fraction of $^{[4]}$Si-O-$^{[4]}$Si at 6 GPa is ~50%–60% and that of (Na,Li)-O-$^{[4]}$Si is ~20%–23%. Previous quantum chemical calculations on the energy differences of oxygen clusters showed that the fraction of $^{[4]}$Si-O-$^{[4]}$Si decreases and that of $^{[5,6]}$Si-O-$^{[4]}$Si increases with increasing the chemical disorder of cations, and the distribution

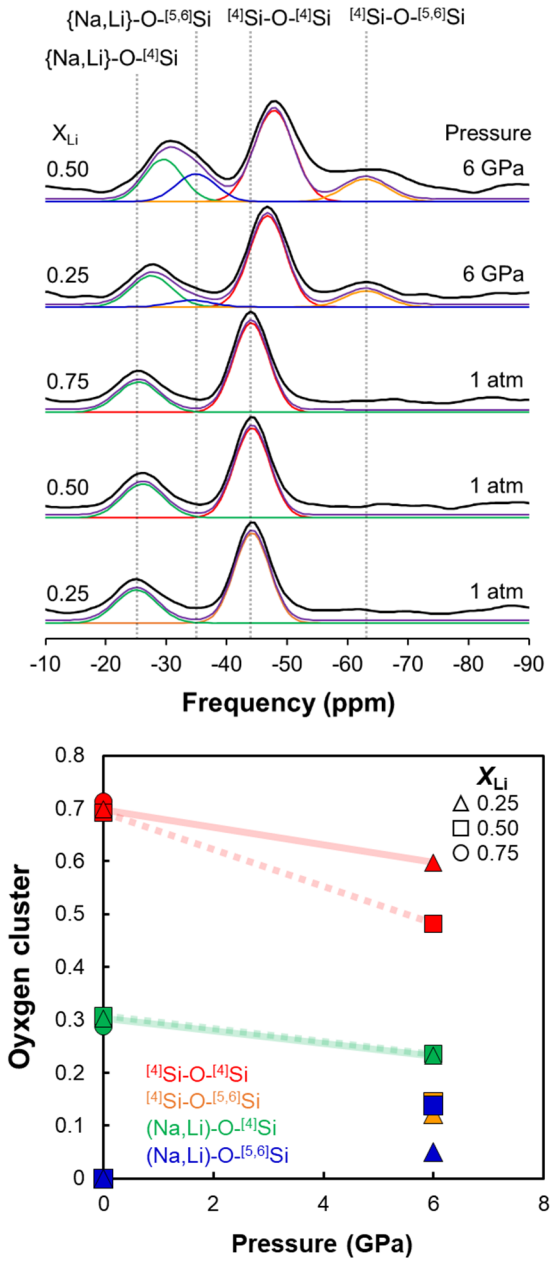

Figure 4.6. (Top) Simulation for the total isotropic projection of the ^{17}O 3QMAS NMR spectra of NLS3 glasses at different X_{Li} and pressures. (Bottom) The estimated oxygen fraction in NLS3 glasses as a function of pressure and X_{Li}.

of network polyhedra in sodium trisilicate glasses at 10 GPa is not completely random but favors formation of oxygen linking dissimilar Si pairs such as $^{[5,6]}$Si-O-$^{[4]}$Si (Lee et al., 2003a). The estimated oxygen cluster fractions in the NLS3 glasses is similar to those obtained in sodium trisilicate glasses at 10 GPa (Lee et al., 2003a), indicating chemically ordered silicate network polyhedra in NLS3 glasses at high pressure. Therefore, not only the cations but also the silicate network polyhedra seem to become chemically ordered upon compression.

4.3.5. Distribution of mixed cations of different ionic radii in silicate melts at high pressures

Previous molecular dynamic simulations suggested that the smaller the cation radius, the higher the number of diffusion channels formed for network-modifying cations at 1 atm (Habasaki and Hiwatari, 2003; Habasaki et al., 1996). The segregation of the Q^2 species can generate the diffusion channels for cations, and the degree of disproportionation of Q^3 into Q^2 and Q^4 increases with increasing the cation field strength (Maekawa et al., 1991). The observed diffusion channels in the MD simulation is relevant to the disproportionation of silicate glasses with respect to cation radius. In addition, the formation of $^{[5]}$Si in the silicate melts is suggested as an activated complex for cation diffusion, which may increase the diffusion of network modifying cations (Xue et al., 1991) and oxygens (Poe et al., 1997). The presence of $^{[5]}$Si is observed in all NLS3 glasses (Fig. 4.2). Therefore, the diffusion of both network-modifying cations and oxygens would be less difficult at high pressures.

Based on the T_2 time of ^{7}Li (Fig. 4.3), the distribution of Li in NLS3

glasses changes from random distribution to chemical order with increasing pressure. As the cation field strength of Li^+ is higher than that of Na^+, this is consistent with the previous experimental data on the (Na,Ca)-silicate glasses at high pressure (Lee et al., 2008a), showing the preference of oxygen clusters with dissimilar cation pairs and indicating the increase of chemical ordering in network modifying cations at high pressure. Moreover, the estimated fraction of $^{[4]}$Si-O-$^{[4]}$Si and (Na,Li)-O-$^{[4]}$Si is similar to those calculated for chemically ordered silicon network polyhedra (Lee et al., 2003a). Together with the chemical ordering of network modifying cations, the ordering of network former polyhedra results in the reduction of the activity coefficient of silica, resulting in the changes to the composition of partial melts at high pressure (Lee et al., 2003a).

4.4. Conclusion

In this study, we explored the effect of pressure on the cation mixing and the structural changes of NLS3 melts at high pressures up to 8 GPa using solid-state NMR and Raman spectroscopy. The ^{29}Si MAS NMR spectra of the NLS3 glasses indicate the presence of 4-, 5-, and 6-coordinated Si at high pressures above 6 GPa, regardless of X_{Li}. The total fraction of highly coordinated Si decreased with increasing X_{Li} in the melts at 6 GPa. The ^{7}Li MAS NMR spectra of NLS3 glasses shows that the peak position gradually shifts to a lower frequency (negative region) with increasing pressure in all NLS3 glasses. The spin-spin relaxation time of the NLS3 glasses with X_{Li} = 0.25 underwent a continuous decrease with an increase in pressure, while the degree of the slope increased above 6 GPa. However, the T_2 of the NLS3 glasses with X_{Li} = 0.50 and 0.75 increased with increasing

pressure from 1 atm to 6 GPa, indicating a cation disorder change from random distribution at 1 atm to chemical order at 6 GPa. The ^{17}O 3QMAS NMR spectra showed the various oxygen sites in the NLS3 glasses, and the estimated oxygen cluster fraction based on the isotropic projection of the ^{17}O 3QMAS NMR spectra implies that the network former polyhedra becomes chemically ordered with increasing pressure. Based on the T_2 of ^{7}Li in the ^{7}Li NMR and ^{29}Si MAS NMR spectra, it is deduced that the diffusion of cations with smaller radii would be interrupted at high pressures due to changes in cation disorder and changes to the silicate network.

Appendix

4.S1. Simulation results of the ^{29}Si MAS NMR spectra of NLS3 glasses

Table 4.S1 and Figure 4.S1 show the simulation results of the estimated fractions of the Q^n species. Note that it is difficult to obtain quantitative information on the changes in the Q^n species with respect to pressure due to the pressure-induced shifting of the peak positions of the Si environments in NLS3 glasses at high pressures. For example, a previous study reported that the peak position for the Q^4 species in the wadeite-type $K_2Si_4O_9$ mineral, which contains $^{[4]}$Si-O-$^{[6]}$Si bonds, shifted to -96 ppm, a shift of ~10 ppm from the general peak position for the Q^4 species (Maekawa et al., 1991). As the pressure-induced distortion of the network polyhedra and the changes of the Si-O bond lengths induce the peak broadening of silicate glasses at high pressure as well, the simulation results for the ^{29}Si MAS NMR spectra of NLS3 glasses quenched from melts at high pressure are not unique. Therefore, here we report the simulation results for NLS3 glasses at 1 atm which can be used for quantitative discussion.

The proportion of Q^n species varies with the NBO/T ratio, T_g, and the cation field strength (see Stebbins (2016) and the references therein). In glasses with the same NBO/T ratio, the increase in the Q^2 and Q^4 species due to consumption of the Q^3 species is related to a disproportionation reaction, which generally takes place upon an increase in the T_g and/or at higher field strengths (the charge over the square of the ionic radius) of the modifier cations (Larson et al., 2006; Maekawa et al., 1991; Stebbins, 2016; Xue et al., 1989), and the increase of cation field strengths may enhance the disproportionation (Maekawa et al., 1991; Stebbins, 2016; Voigt et al., 2005). The simulation results for the NLS3 glasses at 1 atm are in good agreement

with previous studies on binary Na- and Li-silicate glasses (Maekawa et al., 1991; Stebbins, 2016; Voigt et al., 2005). The simulated fraction of the Q^2 species in NLS3 glasses with X_{Li} = 0.25 at 1 atm is 1.1% and that of the Q^4 species is 33.1%, while those of the Q^2 and Q^4 species in NLS3 glasses with X_{Li} = 0.75 are 7.3% and 35.6%, respectively.

4.S2. The structural role of cations in silicate melts at high pressures: Insights from Raman spectroscopy

The Raman spectra of the Na-Li trisilicate glasses were collected on a micro Raman spectrometer at the Seoul National University. Raman analysis was conducted on chunks of the samples. The spectra were collected using the following conditions: laser wavelength of 488 nm, exposure time of 4 s, 120 accumulation runs, and a grating groove density of 1800/500 L/mm. The spectral resolution was ~0.55–0.85 cm^{-1}/pixel and the spectrometer slit width was 250 μm. The typical spectral width was ~940 cm^{-1} (centered at 600 cm^{-1}) and ~890 cm^{-1} (centered at 900 cm^{-1}). A beam diameter of 3.1 μm (using 50× microscope objectives), laser power of 24 mW, and beam scattering of 1 mrad were used. The estimated reproducibility of the recorded peak positions in the spectra was less than 0.5 cm^{-1}.

Although the Raman spectra do not provide quantitative information on the structural changes of materials of interest, the changes observed in the vibrational modes indeed provide qualitative information on the structural changes. Figure 4.S4 shows the Raman spectra of NLS3 glasses quenched from melts at high pressures with varying X_{Li} and significant changes have been observed in NLS3 glasses with varying X_{Li} and pressure.

Generally, the vibrational modes between 200–600 cm^{-1} are assigned to the Si-O-Si bending vibrations of the Q^n species and those between 900–1200 cm^{-1} are assigned to the symmetric Si-O vibrations of the Q^n species (Xue et al., 1991). The Raman spectra of NLS3 glasses at 1 atm with varying X_{Li} are generally consistent with those of Li trisilicate and Na silicate glasses (Hass, 1970; Matson et al., 1983; McMillan et al., 1989; Seuthe et al., 2013; Wolf et al., 1990; Xue et al., 1991). A broad peak near 430 cm^{-1} is related to the Si-O-Si bending vibrations of the Q^4 species (Matson et al., 1983; Xue et al., 1991). The vibrational modes near ~540 cm^{-1} correspond to the Si-O-Si bending of the Q^3 species and the shoulder peak at ~600 cm^{-1} is due to Si-O-Si bending vibrations with a narrow Si-O-Si angle associated with the Q^2 species or three-membered Si tetrahedral rings (Wolf et al., 1990; Xue et al., 1991). The vibrational band near ~780 cm^{-1} may correspond to the vibrational motion of Si within a Si tetrahedron (McMillan, 1984; Xue et al., 1991). The peak at ~950 cm^{-1} corresponds to the symmetric Si-O stretching vibrations of the Q^2 species. The NLS3 glasses at 1 atm show a strong high frequency peak at ~1090 cm^{-1}, attributable to the symmetric Si-O vibrations of the Q^3 species (Xue et al., 1991). The shoulder peak at ~1150 cm^{-1} observed in the Raman spectra of the NLS3 melts at 1 atm is assigned to the symmetric Si-O stretching vibrations of the Q^4 species (Hehlen and Neuville, 2015). See Table 4.S2 for additional details on the Raman modes corresponding to binary Na- and Li-silicate glasses and SiO_2 glasses.

While the relative peak intensities of the Q^2 and Q^4 species increase with an increase in X_{Li} at 1 atm, only the relative peak intensities of the stretching vibrational mode of the Q^2 with respect to that of the Q^3 increases with increasing X_{Li}. This is similar to that obtained from the ^{29}Si MAS NMR

spectra (Fig. 4.2a and Fig. 4.S1), showing the increase of Q^2 species with respect to Q^3 species in the NLS3 glasses at 1 atm with increasing X_{Li}. The changes in the relative intensities of the Q^2 and Q^4 species in bending and stretching vibrational modes change with increasing pressure. In the NLS3 glasses at 6 GPa, only the changes in the bending vibrations of the Q^4 and Q^3 species at ~400–550 cm^{-1} were observed and those in the stretching vibration are negligible for all Q^n species. Therefore, we assumed that the changes in the bending vibration in NLS3 glasses is more observable than those in the stretching vibration with increasing pressure.

4. S3. The relationship between Li-Li distance and T_2 time in ^{7}Li NMR spectra

Solid-state NMR provides element-specific information on the short-range structure of nuclides of interest. The information of specific dissimilar pairs can be obtained using double resonance NMR experiments. The interaction between dissimilar pairs can be measured by the second moment M_2, which affects the decrease of the peak intensity in spin-echo double resonance experiments in NMR and can be described as follows:

$$M_{2,\,IS} = 4/15 * \gamma_i^2 \gamma_s^2 \hbar S(S+1)\Sigma(1/r_{is}^6)$$

Here, γ_i and γ_i denote the gyromagnetic ratio of the nuclide i and s, $\hbar$ is the Plank constant divided by 2π ($h/2\pi$), S is the spin number of the nuclide S, and r_{is} is the distance between the i and s nuclides. The second moment varies with the distance between the two nuclides r_{is}. The overall intensity in the NMR spin-echo experiment can be explained as follows:

$$S/S_0 = 1 - f\{1 - \exp[-M_2(2\tau)^2/2]\}$$

where f indicates the efficiency of the ^{7}Li π pulse, 2τ represents the time to

acquire an echo pulse, and M_2 is the second moment in the spin-echo experiments. Therefore, the estimation of r_{is} based on the changes to S/S_0 in the spin-echo experiments would give insights into the distribution of Li and Na in Na-Li silicate glasses at high pressures, up to 8 GPa.

The spin-echo NMR experiments measures the spin-spin relaxation time (T_2) of nuclides of interest. Here, the information of one specific nuclide, such as the distance between Li cations can be obtained from the T_2 relaxation time with following second moment values of the nuclide of interests (Yap and Elliott, 1995):

$$M_{2,\,II} = 12/25 * \gamma_i^4 \hbar I(I+1)\Sigma(1/r_{ii}^6)$$

Here, r_{ii} represent the distance between similar pairs, such as i-i pairs. The decrease of peak intensity can be fitted with following equations

$$S/S_0 = 1 - f\{1 - \exp[-M_{2,\,II}(2\tau)^2/2]\}$$

$$= \exp(-t/T_2)$$

and therefore, the distance between Li-Li pairs can be obtained from T_2 measurements using solid-state NMR.

Table 4.S1. The estimated fraction of Q_n species in Na-Li trisilicate glasses at 1 atm. The values are obtained by the simulation of peak areas of ^{29}Si MAS NMR spectra.

X_{Li}	Q^2	Q^3	Q^4
0.25	1.1	65.7	33.1
0.50	5.2	60.1	34.7
0.75	6.5	57.5	36.0

Table 4.S2. Raman modes corresponding to binary Na- and Li-silicate glasses and SiO_2 glasses.

Composition	ν_1 (cm^{-1})	Modes	Ref.
Li-silicate glasses	~380	Si-O-H wagging	(1)
Li-silicate glasses	440	Symmetric motion of the bridging oxygen, ν_s(Si-O-Si) (transverse optical splitting)	(2)
Li-silicate glasses	430–500	Si-O-Si bending vibration of linkages associated with the predominant Q^4 species	(1), (5)
Li-silicate glasses	490	Symmetric motion of the bridging oxygen, ν_s(Si-O-Si) (longitudinal optical splitting)	(2)
Li-silicate glasses		D1 defect, 4-membered rings of SiO_4 tetrahedra	(1)
$Na_2Si_2O_5$ glass	562	Si-O-Si bending vibration of linkages associated with the predominant Q^3 species	(5)
$Na_2Si_2O_5$ glass	600	Si-O-Si vibration of linkages associated with the Q^2 species	(5)
		The presence of three-membered siloxane rings containing both Q^4 and Q^3 species	(1)
$MgSiO_3$ garnet	600	Bending vibration of $^{[4]}$Si-O-$^{[6]}$Si	(4)
SiO_2 glass	740	Si motion against its tetrahedral oxygen cage	(3)
$Na_2Si_2O_5$ glass	772	Si motion against its tetrahedral oxygen cage	(5)
$Na_2Si_2O_5$ glass	940	Si-O stretching of Q^2 species	(5)
	1060	Antisymmetric Si-O-Si stretching mode ν_{as}(Si-O-Si) (longitudinal optical splitting)	(2)
$Na_2Si_2O_5$ glass	1090	Si-O stretching of Q^3 species	(5)
	1190	Antisymmetric Si-O-Si stretching mode ν_{as}(Si-O-Si) (transverse optical splitting)	(2)
	1100	$[Si_2O_5]_n^{2-}$ sheet unit	(2)

(1) Seuthe et al. (2013); (2) Matson et al. (1983); (3) McMillan (1984); (4) McMillan et al. (1989) (5) Xue et al. (1991)

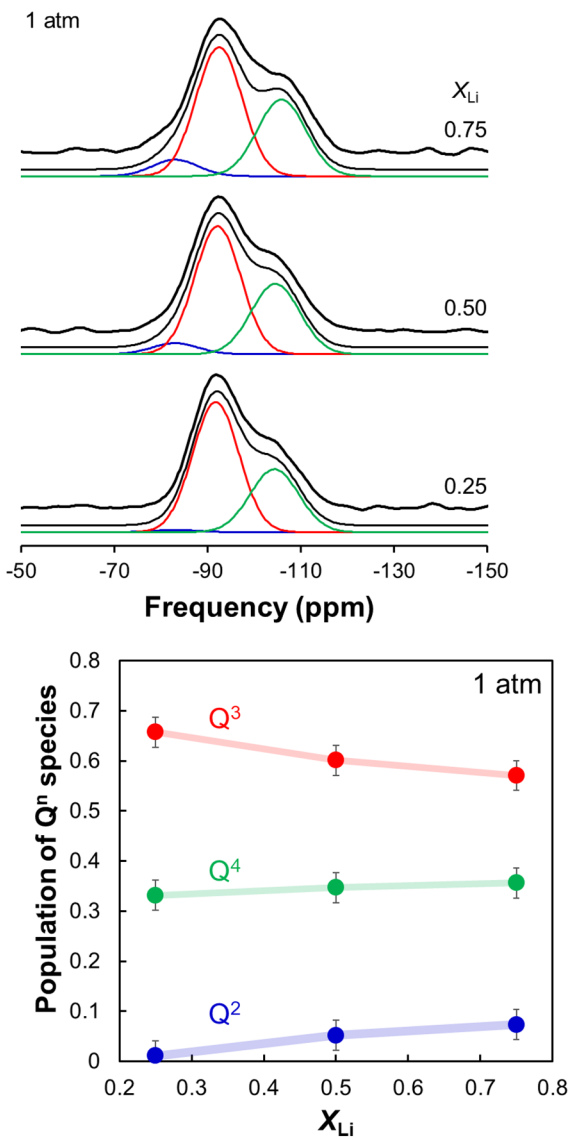

Figure 4.S1. (Left) Simulation results of the ^{29}Si MAS NMR spectra of NLS3 glasses with varying X_{Li}. The thick black lines refer to experimental data. The thin blue, red, green, and black lines correspond to Q^2, Q^3, Q^4, and total simulation results, respectively. (Right) Variations in the Q^n fraction with respect to X_{Li} in the NLS3 glasses. The blue, red, and green colors correspond to Q^2, Q^3, and Q^4, respectively.

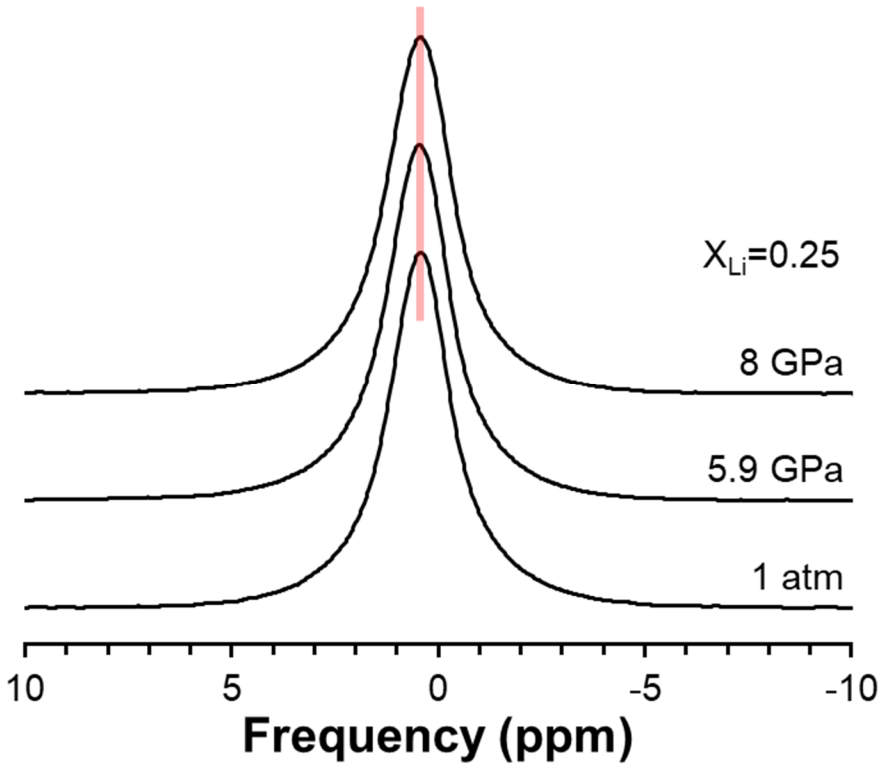

Figure 4.S2. ^{7}Li MAS NMR spectra of NLS3 glasses with X_{Li} = 0.25 at 14.1 T.

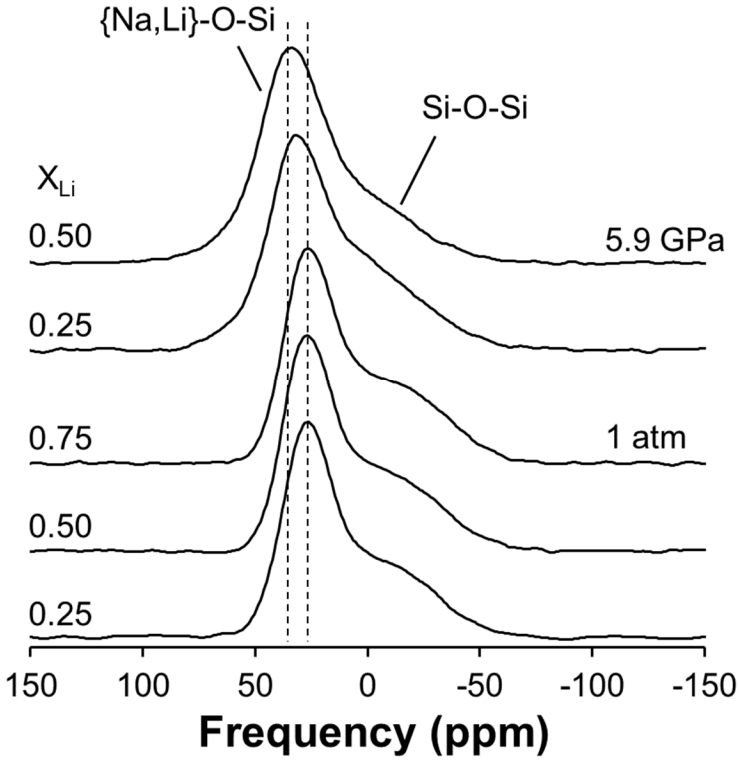

Figure 4.S3. ^{17}O MAS NMR spectra of NLS3 glasses with varying pressure and X_{Li} at 9.4 T.

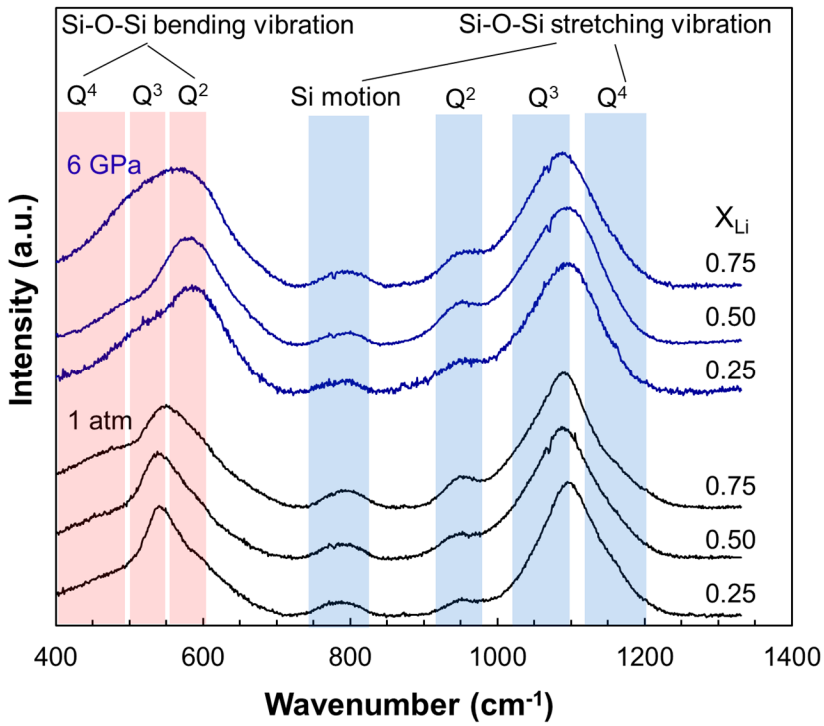

Figure 4.S4. Raman spectra of NLS3 glasses with varying X_{Li} and at different pressures up to 6 GPa.

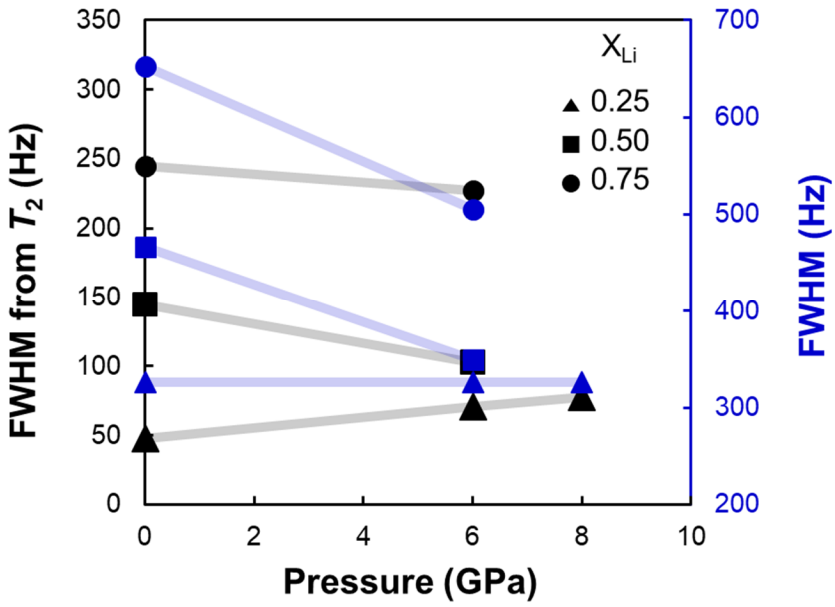

Figure 4.S5. Full-width at half-maximum (FWHM) in ^{7}Li MAS NMR spectra (blue) and those derived from T_2 of ^{7}Li NMR spectra (black). Triangles, squares, and circles refer to X_{Li} = 0.25, 0.50, and 0.75, respectively.

References

Alam, T.M., Jenkins, J.E., Bolintineanu, D.S., Stevens, M.J., Frischknecht, A.L., Buitrago, C.F., Winey, K.I., Opper, K.L. and Wagener, K.B. (2012) Heterogeneous coordination environments in lithium-neutralized ionomers identified using ^{1}H and ^{7}Li MAS NMR. *Materials* **5**, 1508.

Ali, F., Chadwick, A.V., Greaves, G.N., Jermy, M.C., Ngai, K.L. and Smith, M.E. (1995) Examination of the mixed-alkali effect in (Li,Na) disilicate glasses by nuclear magnetic resonance and conductivity measurements. *Solid State Nuclear Magnetic Resonance* **5**, 133-143.

Allwardt, J.R., Lee, S.K. and Stebbins, J.F. (2003) Bonding preferences of non-bridging O atoms: Evidence from 17O MAS and 3QMAS NMR on calcium aluminate and low-silica Ca-aluminosilicate glasses. *American Mineralogist* **88**, 949-954.

Allwardt, J.R. and Stebbins, J.F. (2004) Ca-Mg and K-Mg mixing around non-bridging O atoms in silicate glasses: An investigation using ^{17}O MAS and 3QMAS NMR. *American Mineralogist* **89**, 777-784.

Angell, C.A., Cheeseman, P.A. and Tamaddon, S. (1982) Pressure enhancement of ion mobilities in liquid silicates from computer simulation studies to 800 kilobars. *Science* **218**, 885-887.

Balasubramanian, S. and Rao, K.J. (1995) A molecular dynamics study of the mixed alkali effect in silicate glasses. *Journal of Non-Crystalline Solids* **181**, 157-174.

Behrends, F. and Eckert, H. (2011) Mixed-alkali effects in aluminophosphate glasses: A re-examination of the system $[xNa_2O(1-x)Li_2O]_{0.46}[yAl_2O_3(1-y)P_2O_5]_{0.54}$. *The Journal of Physical Chemistry C* **115**, 17175-17183.

Chen, C.-h. and Du, J. (2015) Lithium ion diffusion mechanism in lithium lanthanum titanate solid-state electrolytes from atomistic simulations. *Journal of the American Ceramic Society* **98**, 534-542.

Cormack, A.N. and Du, J. (2001) Molecular dynamics simulations of soda–lime–silicate glasses. *Journal of Non-Crystalline Solids* **293**, 283-289.

Cormier, L., Calas, G. and Cuello, G.J. (2010) Structural study of Ca–Mg and K–Mg mixing in silicate glasses by neutron diffraction. *Journal of Non-Crystalline Solids* **356**, 2327-2331.

Cormier, L. and Cuello, G.J. (2013) Structural investigation of glasses along the $MgSiO_3$–$CaSiO_3$ join: Diffraction studies. *Geochimica et Cosmochimica Acta* **122**, 498-510.

Dodd, A.J., van Eck, E.R.H., Jak, M.J.G., Kelder, E.M. and Schoonman, J. (2000) NMR study of ionic distribution in Li-doped BPO_4. *Journal of Solid State Chemistry* **153**, 282-286.

Dupree, R., Holland, D. and Mortuza, M.G. (1990) A MAS-NMR investigation of lithium silicate glasses and glass ceramics. *Journal of Non-Crystalline Solids* **116**, 148-160.

Elbayed, K., Dillmann, B., Raya, J., Piotto, M. and Engelke, F. (2005) Field modulation effects induced by sample spinning: application to high-resolution magic angle spinning NMR. *Journal of Magnetic Resonance* **174**, 2-26.

Florian, P., Vermillion, K.E., Grandinetti, P.J., Farnan, I. and Stebbins, J.F. (1996) Cation distribution in mixed alkali disilicate glasses. *J Am Chem Soc* **118**, 3493-3497.

Gee, B. and Eckert, H. (1996) Cation distribution in mixed-alkali silicate glasses. NMR studies by ^{23}Na-{^{7}Li} and ^{23}Na-{^{6}Li} spin echo double resonance. *The Journal of Physical Chemistry* **100**, 3705-3712.

Gee, B., Janssen, M. and Eckert, H. (1997) Local cation environments in mixed alkali silicate glasses studied by multinuclear single and double resonance magic-angle spinning NMR. *Journal of Non-Crystalline Solids* **215**, 41-50.

Greaves, G.N. (1998) Structural studies of the mixed alkali effect in disilicate glasses. *Solid State Ionics* **105**, 243-248.

Habasaki, J. and Hiwatari, Y. (2003) Fast and slow dynamics in single and mixed alkali silicate glasses. *Journal of Non-Crystalline Solids* **320**, 281-290.

Habasaki, J., Okada, I. and Hiwatari, Y. (1996) Relaxation processes and the mixed alkali effect in alkali metasilicate glasses, Materials Research Society Online Proceeding LIbrary Archive, pp. 91-104.

Hass, M. (1970) Raman spectra of vitreous silica, germania and sodium silicate glasses. *Journal of Physics and Chemistry of Solids* **31**, 415-422.

Hehlen, B. and Neuville, D.R. (2015) Raman response of network modifier cations in alumino-silicate glasses. *The Journal of Physical Chemistry B* **119**, 4093-4098.

Herd, C.D.K., Treiman, A.H., McKay, G.A. and Shearer, C.K. (2005) Light lithophile elements in martian basalts: Evaluating the evidence for magmatic water degassing. *Geochimica et Cosmochimica Acta* **69**, 2431-2440.

Hultzsch, R.A. and Barnes, R.G. (1962) Pressure dependence of self-diffusion in lithium and sodium. *Physical Review* **125**, 1832-1842.

Kaneko, S., Tokuda, Y., Takahashi, Y., Masai, H. and Ueda, Y. (2017) Structural analysis of mixed alkali borosilicate glasses containing Cs^+ and Na^+ using strong magnetic field magic angle spinning nuclear magnetic resonance. *Journal of Asian Ceramic Societies* **5**, 7-12.

Kelsey, K.E., Stebbins, J.F., Mosenfelder, J.L. and Asimow, P.D. (2009) Simultaneous aluminum, silicon, and sodium coordination changes in 6 GPa sodium aluminosilicate glasses. *American Mineralogist* **94**, 1205-1215.

Kim, H.N. and Lee, S.K. (2013) Atomic structure and dehydration mechanism of amorphous silica: Insights from ^{29}Si and ^{1}H solid-state MAS NMR study of SiO_2 nanoparticles. *Geochim. Cosmochim. Ac.* **120**, 39-64.

Kjeldsen, J., Smedskjaer, M.M., Mauro, J.C. and Yue, Y. (2014) On the origin of the mixed alkali effect on indentation in silicate glasses. *Journal of Non-Crystalline Solids* **406**, 22-26.

Larson, C., Doerr, J., Affatigato, M., Feller, S., Holland, D. and Smith, M.E. (2006) A ^{29}Si MAS NMR study of silicate glasses with a high lithium content. *Journal of Physics: Condensed Matter* **18**, 11323.

Le Losq, C. and Neuville, D.R. (2013) Effect of the Na/K mixing on the structure and the rheology of tectosilicate silica-rich melts. *Chemical Geology* **346**, 57-71.

Lee, S.K. (2004) Structure of silicate glasses and melts at high pressure: Quantum chemical calculations and solid-state NMR. *The journal of Physical Chemistry B* **108**, 5889-5900.

Lee, S.K. (2010) Effect of pressure on structure of oxide glasses at high pressure: Insights from solid-state NMR of quadrupolar nuclides. *Solid State Nuclear Magnetic Resonance* **38**, 45-57.

Lee, S.K., Cody, G.D., Fei, Y.W. and Mysen, B.O. (2004) Nature of polymerization and properties of silicate melts and glasses at high pressure. *Geochimica et Cosmochimica Acta* **68**, 4189-4200.

Lee, S.K., Cody, G.D., Fei, Y.W. and Mysen, B.O. (2006) The effect of Na/Si on the structure of sodium silicate and aluminosilicate glasses quenched from melts at high pressure: A multi-nuclear (Al-27, Na-23, O-17) 1D and 2D solid-state NMR study. *Chem. Geol.* **229**, 162-172.

Lee, S.K., Cody, G.D., Fei, Y.W. and Mysen, B.O. (2008a) Oxygen-17 nuclear magnetic resonance study of the structure of mixed cation calcium-sodium silicate glasses at high pressure: Implications for molecular link to element partitioning between silicate liquids and crystals. *The journal of Physical Chemistry B* **112**, 11756-11761.

Lee, S.K., Cody, G.D., Fei, Y.W. and Mysen, B.O. (2008b) Oxygen-17 nuclear magnetic resonance study of the structure of mixed cation calcium-sodium silicate glasses at high pressure: Implications for molecular link to element partitioning between silicate liquids and crystals. *J. Phys. Chem. B* **112**, 11756-11761.

Lee, S.K., Eng, P.J., Mao, H.K., Meng, Y. and Shu, J. (2007) Structure of alkali borate glasses at high pressure: B and Li K-edge inelastic X-ray scattering study. *Phys. Rev. Lett.* **98**.

Lee, S.K., Fei, Y.W., Cody, G.D. and Mysen, B.O. (2003a) Order and disorder in sodium silicate glasses and melts at 10 GPa. *Geophysical Research Letters* **30**.

Lee, S.K., Kim, H.N., Lee, B.H., Kim, H.I. and Kim, E.J. (2010a) Nature of Chemical and Topological Disorder in Borogermanate Glasses: Insights from B-11 and O-17 Solid-State NMR and Quantum Chemical Calculations. *The Journal of Physical Chemistry B* **114**, 412-420.

Lee, S.K., Kim, H.N., Lee, B.H., Kim, H.I. and Kim, E.J. (2010b) Nature of Chemical and Topological Disorder in Borogermanate Glasses: Insights from B-11 and O-17 Solid-State NMR and Quantum Chemical Calculations. *J. Phys. Chem. B* **114**, 412-420.

Lee, S.K., Mysen, B.O. and Cody, G.D. (2003b) Chemical order in mixed-cation silicate glasses and melts. *Physical Review B* **68**.

Lee, S.K. and Stebbins, J.F. (2003) Nature of cation mixing and ordering in Na-Ca silicate glasses and melts. *J. Phys. Chem. B* **107**, 3141-3148.

Lee, S.K. and Stebbins, J.F. (2006) Disorder and the extent of polymerization in calcium silicate and aluminosilicate glasses: O-17 NMR results and quantum chemical molecular orbital calculations. *Geochim. Cosmochim. Ac.* **70**, 4275-4286.

Lee, S.K. and Sung, S.Y. (2008) The Effect of Network-modiying Cations on the Structure and Disorder in Peralkaline Ca-Na Aluminosilicate Glasses: O-17 3QMAS NMR Study. *Chemical Geology* **256**, 325-332.

Levitt, M.H. (2005) Spin Dynamics: Basics of nuclear magnetic resonance. John Wiley & Sons, LTD, Chichester.

MacKenzie, K.J.D. and Meinhold, R.H. (1994) The thermal reactions of synthetic hectorite studied by ^{29}Si, ^{25}Mg, and ^{7}Li magic angle spinning nuclear magnetic resonance. *Thermochimica Acta* **232**, 85-94.

Maekawa, H., Florian, P., Massiot, D., Kiyono, H. and Nakamura, M. (1996) Effect of alkali metal oxide on ^{17}O NMR parameters and Si−O−Si angles

of alkali metal disilicate glasses. *The Journal of Physical Chemistry* **100**, 5525-5532.

Maekawa, H., Maekawa, T., Kawamura, K. and Yokokawa, T. (1991) The structural groups of alkali silicate glasses determined from ^{29}Si MAS-NMR. *Journal of Non-Crystalline Solids* **127**, 53-64.

Marschall, H.R., Wanless, V.D., Shimizu, N., Pogge von Strandmann, P.A.E., Elliott, T. and Monteleone, B.D. (2017) The boron and lithium isotopic composition of mid-ocean ridge basalts and the mantle. *Geochimica et Cosmochimica Acta* **207**, 102-138.

Masquelier, C. and Croguennec, L. (2013) Polyanionic (phosphates, silicates, sulfates) frameworks as electrode materials for rechargeable Li (or Na) batteries. *Chemical Reviews* **113**, 6552-6591.

Matson, D.W., Sharma, S.K. and Philpotts, J.A. (1983) The structure of high-silica alkali-silicate glasses. A Raman spectroscopic investigation. *Journal of Non-Crystalline Solids* **58**, 323-352.

McLaren, C., Roling, B., Raj, R. and Jain, H. (2017) Mechanism of electric field-induced softening (EFIS) of alkali silicate glasses. *Journal of Non-Crystalline Solids* **471**, 384-395.

McMillan, P. (1984) Structural studies of silicate glasses and melts - applications and limitations of Raman spectroscopy. *American Mineralogist* **69**, 622-644.

McMillan, P.F., Akaogi, M., Ohtani, E., Williams, Q., Nieman, R. and Sato, R. (1989) Cation disorder in garnets along the $Mg_3Al_2Si_3O_{12}$-$Mg_4Si_4O_{12}$ join: an Infrared, Raman and NMR study. *Phys. Chem. Miner.* **16**, 428-435.

Minami, T., Tokuda, Y., Masai, H., Ueda, Y., Ono, Y., Fujimura, S. and Yoko, T. (2014) Structural analysis of alkali cations in mixed alkali silicate

glasses by ^{23}Na and ^{133}Cs MAS NMR. *Journal of Asian Ceramic Societies* **2**, 333-338.

Moynihan, C.T., Easteal, A.J., Tran, D.C., Wilder, J.A. and Donovan, E.P. (1976) Heat capacity and structural relaxation of mixed-alkali glasses. *Journal of the American Ceramic Society* **59**, 137-140.

Neuville, D.R., Cormier, L., Montouillout, V., Florian, P., Millot, F., Rifflet, J.-C. and Massiot, D. (2008) Structure of Mg- and Mg/Ca aluminosilicate glasses: ^{27}Al NMR and Raman spectroscopy investigations. *American Mineralogist* **93**, 1721-1731.

Ollier, N., Charpentier, T., Boizot, B., Wallez, G. and Ghaleb, D. (2004) A Raman and MAS NMR study of mixed alkali Na-K and Na-Li aluminoborosilicate glasses. *Journal of Non-Crystalline Solids* **341**, 26-34.

Park, S.Y. and Lee, S.K. (2016) Effects of difference in ionic radii on chemical ordering in mixed-cation silicate glasses: Insights from solid-state ^{17}O and ^{7}Li NMR of Li-Ba silicate glasses. *Journal of the American Ceramic Society*.

Phillips, J.C. (1996) Stretched exponential relaxation in molecular and electronic glasses. *Reports on Progress in Physics* **59**, 1133-1207.

Pinter, L., Biesuz, M., Sglavo, V.M., Saunders, T., Binner, J., Reece, M. and Grasso, S. (2018) DC-electro softening in soda lime silicate glass: An electro-thermal analysis. *Scripta Materialia* **151**, 14-18.

Poe, B.T., McMillan, P.F., Rubie, D.C., Chakraborty, S., Yarger, J. and Diefenbacher, J. (1997) Silicon and oxygen self-diffusivities in silicate liquids measured to 15 gigapascals and 2800 kelvin. *Science* **276**, 1245-1248.

Ravaine, D. (1980) Glasses as solid electrolytes. *Journal of Non-Crystalline Solids* **38-39**, 353-358.

Rouse, G.B., Miller, P.J. and Risen, W.M. (1978) Mixed alkali glass spectra and structure. *Journal of Non-Crystalline Solids* **28**, 193-207.

Schneider, J., Tsuchida, J. and Eckert, H. (2013) Cation size effects in mixed-ion metaphosphate glasses: structural characterization by multinuclear solid state NMR spectroscopy. *Physical Chemistry Chemical Physics* **15**, 14328-14339.

Sen, S., George, A.M. and Stebbins, J.F. (1996) Ionic conduction and mixed cation effect in silicate glasses and liquids: ^{23}Na and ^{7}Li NMR spin-lattice relaxation and a multiple-barrier model of percolation. *Journal of Non-Crystalline Solids* **197**, 53-64.

Seuthe, T., Grehn, M., Mermillod-Blondin, A., Eichler, H.J., Bonse, J. and Eberstein, M. (2013) Structural modifications of binary lithium silicate glasses upon femtosecond laser pulse irradiation probed by micro-Raman spectroscopy. *Optical Materials Express* **3**, 755-764.

Snoeks, E., Kik, P.G. and Polman, A. (1996) Concentration quenching in erbium implanted alkali silicate glasses. *Optical Materials* **5**, 159-167.

Stebbins, J.F. (1998) Cation sites in mixed-alkali oxide glasses: correlations of NMR chemical shift data with site size and bond distance. *Solid State Ionics* **112**, 137-141.

Stebbins, J.F. (2016) Glass structure, melt structure, and dynamics: Some concepts for petrology. *American Mineralogist* **101**, 753-768.

Stebbins, J.F., Oglesby, J.V. and Xu, Z. (1997) Disorder among network-modifier cations in silicate glasses: New constraints from triple-quantum ^{17}O NMR, American Mineralogist, p. 1116.

Tsuchida, J., Schneider, J., Deshpande, R.R. and Eckert, H. (2012) Cation distribution and local order in mixed sodium metaphosphate glasses. *The Journal of Physical Chemistry C* **116**, 24449-24461.

Tsuchida, J., Schneider, J., Orlandi de Oliveira, A., Rinke, M.T. and Eckert, H. (2010) Sodium distribution in mixed alkali K-Na metaphosphate glasses. *Physical Chemistry Chemical Physics* **12**, 2879-2887.

Tuller, H.L., Button, D.P. and Uhlmann, D.R. (1980) Fast ion transport in oxide glasses. *Journal of Non-Crystalline Solids* **40**, 93-118.

Vermillion, K.E., Florian, P. and Grandinetti, P.J. (1998) Relationships between bridging oxygen ^{17}O quadrupolar coupling parameters and structure in alkali silicates. *The Journal of Chemical Physics* **108**, 7274-7285.

Vessal, B. and Greaves, G.N. (1992) Cation microsegregation and ionic mobility in mixed alkali glasses. *Nature* **356**, 504.

Voigt, U., Lammert, H., Eckert, H. and Heuer, A. (2005) Cation clustering in lithium silicate glasses: Quantitative description by solid-state NMR and molecular dynamics simulations. *Physical Review B* **72**.

Welch, R.C., et al. (2013) Dynamics of glass relaxation at room temperature. *Phys. Rev. Lett.* **110**, 265901.

Wolf, G.H., Durben, D.J. and McMillan, P. (1990) High-pressure Raman spectroscopic study of sodium tetrasilicate ($Na_4Si_4O_9$) glass. *The Journal of Chemical Physics* **93**, 2280.

Xu, X., Wen, Z., Wu, X., Yang, X. and Gu, Z. (2007) Lithium ion-conducting glass–ceramics of $Li_{1.5}Al_{0.5}Ge_{1.5}(PO_4)_{3-x}Li_2O$ (x=0.0–0.20) with good electrical and electrochemical properties. *Journal of the American Ceramic Society* **90**, 2802-2806.

Xu, Z. and Stebbins, J.F. (1995) Cation dynamics and diffusion in lithium orthosilicate: Two-dimensional lithium-6 NMR. *Science* **270**, 1332.

Xue, X.Y., Stebbins, J.F., Kanzaki, M., McMillan, P.F. and Poe, B. (1991) Pressure-induced silicon coordination and tetrahedral structural-changes in alkali oxide-silica melts up to 12 GPa - NMR, Raman, and infrared-spectroscopy. *American Mineralogist* **76**, 8-26.

Xue, X.Y., Stebbins, J.F., Kanzaki, M. and Tronnes, R.G. (1989) Silicon coordination and speciation changes in a silicate liquid at high pressures. *Science* **245**, 942-944.

Yap, A.T.W. and Elliott, S.R. (1995) A study of the mixed-alkali effect in disilicate glasses using 7Li nuclear magnetic resonance. *Journal of Non-Crystalline Solids* **192-193**, 207-211.

Yu, Y., Mauro, J. and Bauchy, M. (2018) Stretched exponential relaxation of glasses: Origin of the mixed-alkali effect. *American Ceramic Society Bulletin* **96**, 34-36.

Yu, Y., Wang, M., Zhang, D., Wang, B., Sant, G. and Bauchy, M. (2015) Stretched exponential relaxation of glasses at low temperature. *Physical Review Letter* **115**, 165901.

Chapter 5. Speciation of carbon in aluminosilicate glasses and crystals at high pressure up to 14 GPa: Insights from ^{13}C solid-state NMR and Raman spectroscopy

Eun Jeong Kim and Sung Keun Lee

This study is currently ongoing, and thus the part of results and their discussion are presented here.

5.1. Introduction

Mantle is the largest carbon reservoir in the Earth interior (Dasgupta and Hirschmann, 2010; Kelemen and Manning, 2015). The presence of carbon species and their cycle in the mantle affects the oxygen fugacity of the mantle and the geophysical and geochemical properties of silicate melts at high pressure. For example, redox reaction of CO_2 and/or carbonates with transition metal cations in the silicate minerals is one of the mechanisms to control the oxygen fugacity of the mantle (Stagno et al., 2013) and recent study reported the presence of highly oxidized garnet with diamond inclusions which is expected to have been in the boundary of upper mantle and mantle transition zone (Xu et al., 2017), indicating the importance of carbon species in controlling oxygen fugacity in the mantle up to the boundary of upper mantle and transition zone. The presence of CO_2 or carbonates in silicate melts affect the viscosity of silicate melts and the transport of carbon species (Luth, 2003; Mysen and Richet, 2005). Previous study reported the low-velocity zone atop ~410 km depth, which

may be induced by the volatile-induced silicate melts at ~330–410 km depth in the mantle (Revenaugh and Sipkin, 1994).

Carbon species exists mostly as accessory minerals in the grain boundaries of silicate crystals such as graphite, diamonds, and carbonate minerals (Hazen and Schiffries, 2013; Keppler et al., 2003; Luth, 2003; Shcheka et al., 2006). Once those carbon species form carbon-bearing silicate melts, the mobility of carbon species itself and the viscosity of silicate melts increases. During the dissolution of carbon species, especially for neutral carbon species, the following reaction occurs:

$$C + O_2 = CO_2$$

where O_2 is from the redox reaction of transition metals in the silicate crystals and/or can be free oxygens in the silicate melts. While the redox reaction of carbon species and transition metals in the silicate crystals has been studied at high pressure up to 11 GPa (Stagno and Frost, 2010; Stagno et al., 2013; Tao et al., 2017), interaction between silicate melts and carbon species has been studied up to 4 GPa due to the difficulties in synthesizing the sample (Brooker et al., 1999; Kohn et al., 1991; Morizet et al., 2017a; Ni and Keppler, 2013).

Previous studies have reported the carbon environments in silicate melts with varying pressure, temperature, and composition of silicate melts at high pressure up to 4 GPa (Behrens et al., 2004; Blank and Brooker, 1994; Brooker et al., 1999; Kohn et al., 1991; Morizet et al., 2002; Morizet et al., 2014a; Morizet et al., 2015; Mysen et al., 1976; Mysen et al., 2009; Mysen et al., 2011; Pan et al., 1991; Tossell, 1995). In the oxidized conditions with H_2O, major carbon species are CO_2 and $CO_3^{2=}$ while CH_4, graphite, and CO are the major carbon species in the reduced conditions (Mysen et al., 2011). As

the carbon species varies with the presence of H_2O and the changes in oxygen fugacity, previous studies have also investigated the speciation of carbon in silicate melts without the presence of water to simplify the systems (e.g., Blank and Brooker, 1994; Brooker et al., 2001; Brooker et al., 1999). In the absence of H_2O in the system, CO_2 and CO_3^{2-} are the major carbon species in the carbon-bearing silicate glasses. The fraction of CO_2 over CO_3^{2-} in silicate melts increases with decreasing the fraction of non-bridging oxygen over tetrahedron (NBO/T) and only carbonate species are observed in depolymerized silicate melts at high pressure (e.g., Behrens et al., 2004; Eggler and Rosenhauer, 1978; Kadik et al., 2004; Morizet et al., 2010; Morizet et al., 2017b; Mysen et al., 1975).

Peak widths of carbonate species in ^{13}C MAS NMR spectra changes with varying network modifying cations and the NBO/T ratio (Morizet et al., 2014b). The reported increase of peak widths is related to the changes of network modifying cations from Na^+ and/or K^+ to Ca^{2+} and/or Mg^{2+} and the structural changes of silicate melts with varying NBO/T ratio. Previous study on the peak widths of carbonate minerals in ^{13}C MAS NMR showed that the peak width of carbonate minerals is the sharpest in sodium carbonates (~0.8 ppm of full-widths at half-maximum) and increases with the changes of cations from Na^+ to Ca^{2+} and Mg^{2+} (Papenguth et al., 1989). Assuming that the effect of cations on the structural changes of carbonate minerals can be applied to the structural changes of carbon-bearing silicate melts with varying cations, the changes of Na^+ to Ca^{2+} and/or Mg^{2+} in silicate melts would result in the increase of peak widths in ^{13}C MAS NMR spectra. This may make the analysis on the carbon species in carbon-bearing silicate melts more difficult. The peak widths in NMR spectra generally

increases with increasing pressure due to the pressure-induced topological disorder of network-forming species. Therefore, to minimize the effect of cations on the peak broadening, we chose binary- to ternary-silicate glasses as a model system to understand the carbon environments in silicate melts at high pressure, and Na-silicate melts system was chosen as the model system.

The natural magma systems contain both CO_2 and H_2O and the estimated CO_2/H_2O ratio in the mid-ocean ridge basalt and oceanic island basalts are in the range of 0.2–4 (Hirschmann and Dasgupta, 2009). Although the model system in the study does not contain H_2O, the obtained structural information on the speciation of carbon in carbon-bearing sodium silicate melts at high pressure above 4 GPa up to 14 GPa would provide insights into pressure-induced structural changes of carbon in silicate glasses and the effect of carbon species on the structural changes of silicate melts and crystals at high pressure up to 14 GPa.

Although the absence of H_2O and the presence of CO_2 in the silicate melts is different from the natural magma systems, the obtained structural information on the speciation of carbon in carbon-bearing sodium silicate melts at high pressure above 4 GPa up to 14 GPa would provide insights into pressure-induced structural changes of carbon in silicate glasses and the effect of carbon species on the structural changes of silicate melts and crystals at high pressure up to 14 GPa. In this study, we aim to identify the speciation of carbon in crystalline and amorphous sodium aluminosilicate at high pressure up to 14 GPa and the carbon-induced structural changes of silicate melts. We also discuss the changes of oxygen fugacity with the changes in the carbon species and the formation of silicate melts at high

pressure.

5.2. Experimental methods

5.2.1. Sample preparation

Sodium trisilicate glasses (Na_2O-$3SiO_2$, NS3) were synthesized from powdered Na_2CO_3 and SiO_2 at 1 atm. About 0.2 wt.% of Co oxides was added to enhance the spin-lattice relaxation. The mixture of Na_2CO_3 and SiO_2 was decarbonated in a Pt crucible at 800 °C for 1 h, and fused at 1000 °C for 30 min. The amount of carbon needed for saturation of $^{13}CO_2$ in NS3 glasses was predicted from the linear extrapolation of previous studies (Mysen et al., 2009) as the solubility data are only available up to 4 GPa. The factor of 6 was multiplied to the predicted carbon solubility in NS3 glasses in reduced conditions (Mysen et al., 2009; Mysen et al., 2011). Due to the absence of H_2O, only CO_2 and CO_3^{2-} species are expected to observed and the estimated f_{O2} was similar to those in previous study (Kim et al., 2018), around C-CO (CCO) buffer (f_{O2} = ~ -7.5) based on the fraction of each carbon species formed in the silicate melts (Zhang and Duan, 2010). The 99.7% ^{13}C-enriched $Na_2{}^{13}CO_3$ was used for carbon reservoir in the sample. The amounts of $Na_2{}^{13}CO_3$ added to a pre-synthesized glass are 11.2 and 16.3 wt% (3.5 and 5.2 wt% of CO_2) for 9.2 GPa and 14 GPa, respectively, balanced with SiO_2, into the pre-starting glasses at 1 atm. The samples were loaded into a 1100-ton multi-anvil apparatus in Seoul National University with 14/8 (octahedron edge length/truncated edge length of the anvils) assembly. The samples were fused at 9.2 GPa and 14 GPa at the temperature ranging from 1700–1900 °C for 5 min, and then quenched to glasses by turning off the power. The initial quenching rate was approximately

500 °C/s.

Carbon-bearing albite glasses ($NaAlSi_3O_8$) at 9.2 GPa and aluminosilicate crystals ($NaAlSi_3O_8$) at 14 GPa were synthesized from the mixture of $Na_2{}^{13}CO_3$, Al_2O_3, and SiO_2. The amount of $Na_2{}^{13}CO_3$ needed for saturation of $^{13}CO_2$ in albite glasses calculated from the linear extrapolation of previous studies (Brooker et al., 1999; Stolper et al., 1987) was higher than the direct mixing of powdered $Na_2{}^{13}CO_3$, Al_2O_3, and SiO_2 (~7.9 wt% of $^{13}CO_2$). The mixtures were ground in the agate mortar for 30 min and then loaded into Pt capsule. The samples were loaded in a 1100-ton multi-anvil press in Seoul National University and then synthesized in the same manner as the synthesis of NS3 glasses at high pressure.

5.2.2. NMR spectroscopy

The ^{13}C, ^{29}Si, and ^{27}Al MAS NMR spectra were collected on a Varian solid-state NMR 400 system (9.4 T) at Larmor frequencies of 100.582 MHz for ^{13}C, 79.47 MHz for ^{29}Si, and 104.23 MHz for ^{27}Al nuclides using a 3.2-mm double resonance probe. The ^{13}C MAS NMR spectra were collected with a single-pulse sequence with an approximately 30° pulse (0.5 μs), a recycle delay of 1 s, and at a speed of 17 kHz. Approximately 35,000 scans (~ 3 days) of FID were averaged to achieve the signal-to-noise ratio shown in the ^{13}C MAS NMR spectra. The spectra were referenced to solid adamantane (ADM), which is 38.6 ppm away from tetramethylsilane (TMS). The ^{29}Si MAS NMR spectra were collected at a spinning speed of 11 kHz with a single-pulse sequence with a 30° pulse (1.2 μs) and delay time of 30 s. Tetramethylsilane (TMS) was used as the external reference. ^{27}Al MAS and 3QMAS NMR spectra were collected a spinning speed of 17 kHz. ^{27}Al MAS

NMR spectra were collected using a single-pulse sequence with an approximately 30° pulse (1.2 μs) and a recycle delay of 1 s. ^{27}Al 3QMAS NMR spectra were obtained using a fast-amplitude modulation (FAM)-based shifted-echo pulse sequence with a relaxation delay of 0.3 s – 3 μs pulse for 3Q excitation – t1 delay – FAM pulse train with a 0.7 μs pulse – echo delay – 15 μs soft pulse for echo reconversion – t2 acquisition (Baltisberger et al., 1996; Lee et al., 2009; Madhu et al., 1999).The ^{27}Al NMR spectra were referenced to an external 0.1 M $AlCl_3$ solution.

5.2.3. Raman spectroscopy

The Raman spectra of carbon-bearing aluminosilicate crystals were collected on a micro Raman spectrometer at the Seoul National University. The sample was polished Raman analysis was conducted on chunks of the samples. The crystalline aluminosilicates were fixed in an epoxy resin and were polished using 200 mech, 600 mesh, 1500 mesh powders for 30 min and 6000 mesh powders for 2 h, respectively. The spectra were collected using the following conditions: laser wavelength of 488 nm, exposure time of 4 s, 100 accumulation runs, and a grating groove density of 1800/500 L/mm. The spectral resolution was ~0.55–0.85 cm^{-1}/pixel and the spectrometer slit width was 250 μm. The typical spectral width was ~940 cm^{-1} (centered at 600 cm^{-1}) and ~840 cm^{-1} (centered at 1400 cm^{-1}), and ~780 cm^{-1} (centered at 2200 cm^{-1}), respectively. A beam diameter of 3.1 μm (using 50x microscope objectives), laser power of 36 mW, and beam scattering of 1 mrad were used. The estimated reproducibility of the recorded peak positions in the spectra was less than 0.5 cm^{-1}.

5.2.4. SEM/EDS analysis

The backscattered (BSE) images and EDS analysis on the C-bearing aluminosilicate crystals were obtained from JSM-6380 in Seoul National University. The sample was coated with Pt (10 nm-thick) to see carbon signal from EDS analysis. The voltage of 20 kV, the spot size of 60, and working distance of 10 mm was used.

5.3. Results

5.3.1. Characterization of C-bearing aluminosilicate crystals at 14 GPa

Figure 5.1 a-c shows stereoscopic micrographs of C-bearing albite glasses at 9.2 GPa and those of C-bearing aluminosilicate crystals at 14 GPa. The C-bearing albite glasses at 9.2 GPa is a chunk of glass showing vitreous luster on the surface while the C-bearing aluminosilicate glasses at 14 GPa consists of a mixture of greyish smooth grains and whitish rough grains, and the surface of the sample, which was in contact with the Pt tube, had a black speckled pattern. The polished surface of C-bearing aluminosilicate crystals at 14 GPa in figure 5.1.d shows the distribution of greyish smooth grains and whitish rough grains and the proportion of greyish smooth grains is ~40%. Figure 5.1.c-g show the BSE images of C-bearing aluminosilicate crystals synthesized at 14 GPa. The greyish grains are recognized with their larger grains (5–15 μm) and euhedral to subhedral grain shape in the BSE images while whitish rough grains are composed of very fine (< 1 μm × 10 μm) columnar grains. Compared with the BSE images of C-bearing aluminosilicate crystals, that of C-bearing albite glasses quenched from melts at 9.2 GPa shows a relatively uniform surface and the contrast of the image is monotonic due to its homogeneous composition

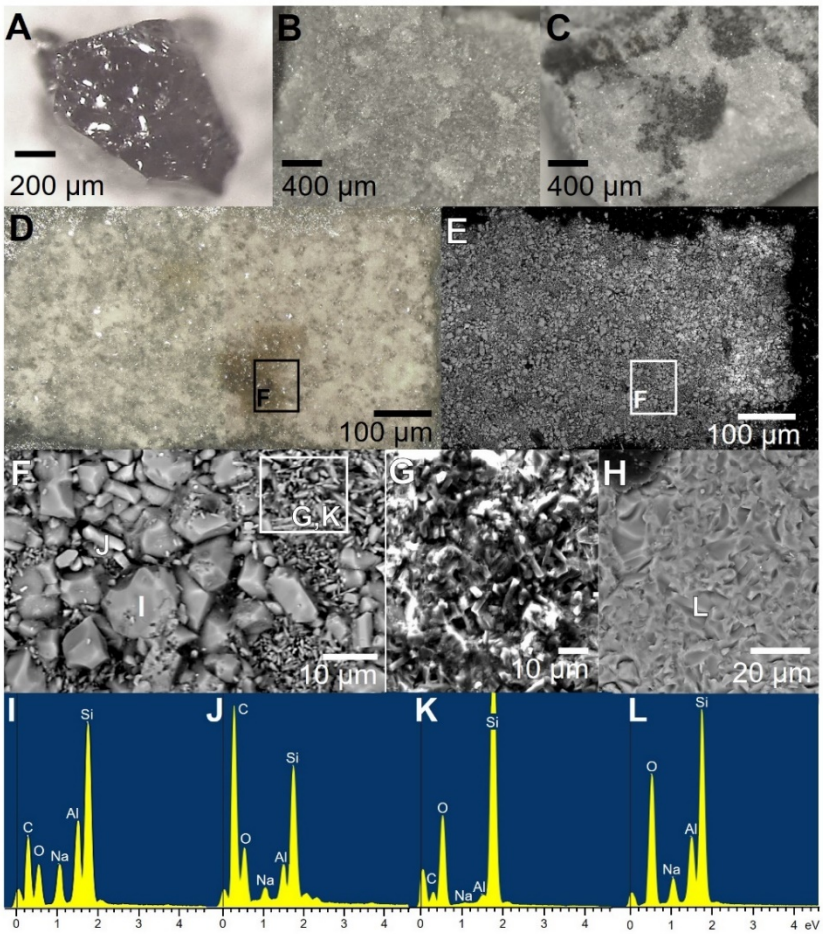

Figure 5.1. Stereoscopic micrographs of (a) C-bearing aluminosilicate glasses at 9.2 GPa and (b) C-bearing aluminosilicate glasses and crystals at 14 GPa inside and (c) outside. (d) A stereoscopic micrograph of C-bearing aluminosilicate crystals and glasses synthesized at 14 GPa. (e) BSE image of C-bearing aluminosilicate crystals and glasses synthesized at 14 GPa. (f) Close-up view of transparent particles (5–15 µm). (g) Close-up view of small white particles in fig. e. (h) BSE image of C-bearing albite glasses at 9.2 GPa. (i-l) EDS patterns of labelled particles in fig. f and h.

(Figure 5.1.h). The EDS analyses of point i-l in Fig. 5.1.f and Fig. 5.1.h are shown in figure 5.1.(i–l). The grain in point i in figure 5.1.f shows the EDS pattern of jadeite ($NaAlSi_2O_6$) and point j shows EDS pattern of albite-like aluminosilicate composition ($NaAlSi_{3.5}O_9$) with intense carbon signal. The EDS patterns in figure 5.1.k is obtained from whitish rough area in figure 5.1.g, which shows the silica-rich aluminosilicate composition ($NaAlSi_{33.8}O_{70}$), which is similar to SiO_2. The obtained EDS patterns of C-bearing albite glasses at 9.2 GPa shows the $Na_6Al_{7.7}Si_{23.9}O_{65.4}$ composition, which is similar to albite ($NaAlSi_3O_8$) and the observed EDS patterns are relatively consistent within the given area in figure 5.1.h.

5.3.2. Raman spectra

Figure 5.2 shows the Raman spectra for C-bearing albite glasses at 9.2 GPa, C-bearing aluminosilicate crystals at 14 GPa, and Na_2CO_3 powder at 1atm as a reference. The inset shows stereoscopic micrographs of C-bearing aluminosilicate crystals and the numbers labeled on the right indicate the area where Raman spectra obtained (see the labels #1 to #4 on the right side of the spectra). The Raman spectra for C-bearing aluminosilicate crystals show the presence of multiple mineral phases including jadeite, stishovite, cubic graphite, nano-diamonds, and small portion of glasses and reveal heterogeneous distribution of these minerals and glasses which can be expected by the different colors in the stereoscopic micrographs. The peak assignments are based on the previous Raman data on each mineral. The peak at 415, 430, 525, 580, 590, 690, 710, 790, 990, ~1010, ~1070 cm^{-1} are assigned to A_g symmetry of jadeite (Prencipe et al., 2014). The vibrational modes of stishovite are shown at 589 cm^{-1} for E_g symmetry mode and 753

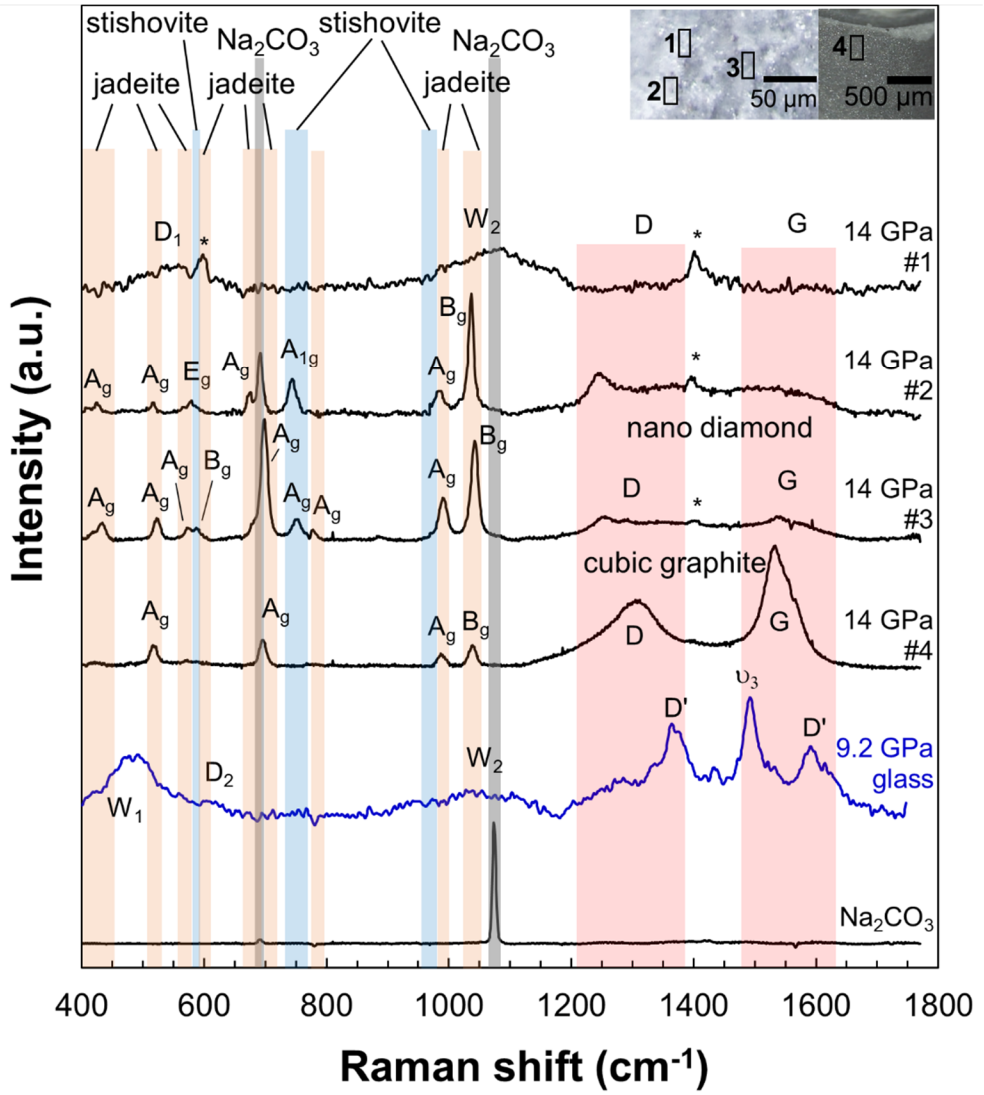

Figure 5.2. Raman spectra for C-bearing aluminosilicate crystals and glasses at 14 GPa, C-bearing albite glasses at 9.2 GPa, and Na_2CO_3 at 1 atm. Inset images were obtained from C-bearing aluminosilicate crystals and glasses at 14 GPa (left: inside, right: outside). Asterisks refer to central spike in Raman spectra.

cm^{-1} of A_{1g} mode, respectively (Hemley, 1987). While Na_2CO_3 was added as a carbon reservoir in the mixture, the presence of Na_2CO_3 was not observed in the synthesized product in Raman spectra. The broad peaks at ~1350 cm^{-1} and ~1580 cm^{-1} are assigned as D and G bands of cubic graphite, respectively (Hanfland et al., 1989; Knight and White, 1989; Perraki et al., 2006; Vidano and Fischbach, 1978). The peaks at ~1250, ~1290, ~1350, and ~1530 cm^{-1} corresponds to B_{2g}, A_{1g}, E_{1g} of hexagonal diamonds, and G band of residual graphite, respectively (Goryainov et al., 2014). See section 5.4.1 for the peak assignment of cubic graphite and nano-diamonds in Raman spectra. The peaks for disordered graphite are only observed at the surface of the sample (black speckled area) and the vibrational modes of nano-diamonds are only observed inside of the sample. The Raman spectra for glassy part in C-bearing aluminosilicate crystals show broad vibrational peaks at ~590 cm^{-1} and ~1100 cm^{-1} which are assigned as vibrational mode of "defect" bands (D_1) and (Al,Si)-O-(Al,Si) stretching (W_2), respectively (McKeown et al., 1984). The vibrational modes of glass in C-bearing aluminosilicate crystal is similar to those of Si-rich sodium aluminosilicate glasses ($Na_{3.07}Al_{0.05}Si_{3.06}O_8$) (McKeown et al., 1984). While the intensity of stretching modes are weaker, the Raman spectra for C-bearing albite glasses at 9.2 GPa show peaks at ~450 cm^{-1} , ~600 cm^{-1}, and ~1050 cm^{-1} are generally consistent with previous studies on albite glasses (McKeown et al., 1984) and additional peaks at ~1370 cm^{-1}, ~1470 cm^{-1}, and ~1600 cm^{-1} are assigned as disordered sp^2 band (D') and υ_3 in carbon (Ferrari and Robertson, 2001; Schindler and Vohra, 1995; Vidano and Fischbach, 1978). Note that the presence of carbonate minerals is not observed in either glassy part of C-bearing aluminosilicate crystals at 14 GPa or C-bearing albite glasses at 9.2

GPa.

5.3.3. ^{13}C MAS NMR spectra of C-bearing aluminosilicate glasses and crystals at high pressure

Figure 5.3 shows the ^{13}C MAS NMR spectra of C-bearing albite glasses at 9.2 GPa and C-bearing aluminosilicate crystals at 14 GPa, and those of C-bearing albite glasses at 1.5 and 6 GPa, reported in previous study (Kim et al., 2018). The peaks at ~125 ppm and 150–170 ppm are assigned as dissolved CO_2 and carbonates species in C-bearing albite glasses at high pressure based on the previous ^{13}C NMR studies and quantum chemical calculations (Feng et al., 2006; Jones et al., 2005; Kim et al., 2016; Kohn et al., 1991; Moore et al., 2015; Morizet et al., 2007; Morizet et al., 2010; Morizet et al., 2014a; Mysen et al., 2011; Papenguth et al., 1989; Tossell, 1995). While the dissolved CO_2 is the dominant carbon species in albite glasses at high pressure up to 9.2 GPa and the fraction of bridging carbonate drastically increases with increasing pressure from 6 GPa to 9.2 GPa. In addition, the peak widths of CO_2 increase from 4 ppm at 1.5 and 6 GPa to 8 ppm at 9.2 GPa, respectively, while the peak position of CO_2 is almost constant (125.4 ppm at 1.5 and 6 GPa and 125.7 ppm at 9.2 GPa, respectively). The chemical shift anisotropy of CO_2 seems to change with increasing pressure from 6 GPa to 9.2 GPa. As the current spectra only shows 2–3 spinning sidebands, it is difficult to analyze CSA patterns of CO_2 systematically. Further ^{13}C MAS NMR experiments on the carbon-bearing albite glasses with spinning speed of ~6–7 kHz would provide the information on the chemical shift anisotropy of dissolved CO_2 at high pressure. See section 5.4.2 for detailed discussion on the peak broadening of

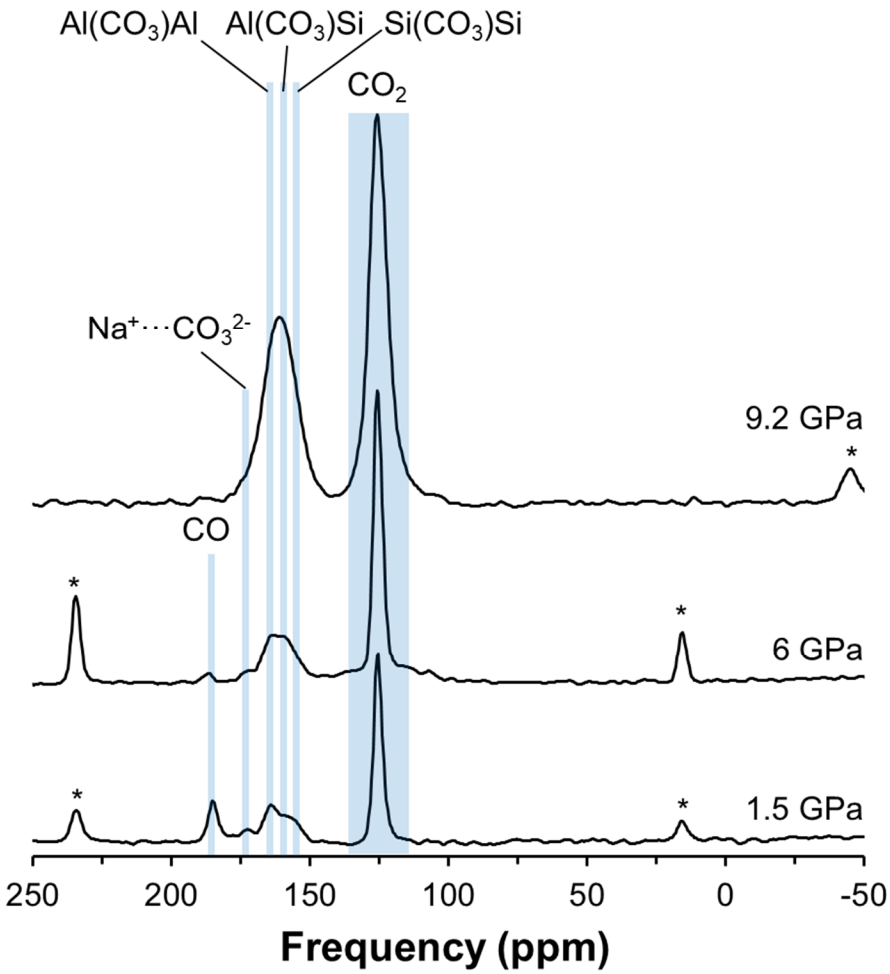

Figure 5.3. ^{13}C MAS NMR spectra for C-bearing albite glasses at high pressure up to 9.2 GPa. The data of 1.5 and 6 GPa are from Kim et al. (2018). The peak intensities are in the absolute value, corrected to the sample weight. The asterisks refer to spinning side bands.

$^{13}CO_2$ in C-bearing albite glasses at high pressure. The broad peak at ~150–170 ppm is assigned for bridging carbonates, such as $^{[4]}Al(CO_3)^{[4]}Al$, $^{[4]}Si(CO_3)^{[4]}Al$, and $^{[4]}Si(CO_3)^{[4]}Si$, at 165, 160, and 155 ppm, respectively (Brooker et al., 1999). As the pressure-induced peak shift of carbonate species is hard to be distinguished due to the peak overlap, we assume that the peak positions of bridging carbonate species, such as $^{[4]}Al(CO_3)^{[4]}Al$, $^{[4]}Si(CO_3)^{[4]}Al$, and $^{[4]}Si(CO_3)^{[4]}Si$, remain constant with increasing pressure. While the peak intensity for carbonate species including bridging and non-bridging carbonates increases with increasing pressure, the fraction of $^{[4]}Si(CO_3)^{[4]}Al$ increases the most with increasing pressure. The presence of CO is not observed in C-bearing albite glasses at 9.2 GPa which is mainly due to the changes in the assembly sets (from those using graphite heater to those using Re heater).

Figure 5.4 shows the ^{13}C MAS NMR spectra of C-bearing aluminosilicate crystals ($NaAlSi_2O_6 + SiO_2$) at 14 GPa, C-bearing albite glasses at 9.2 GPa, and Na_2CO_3 at 1 atm. The ^{13}C MAS NMR spectra for C-bearing aluminosilicate crystals show peaks at 164.5 ppm and ~35 ppm. The peak at ~35 ppm in the ^{13}C MAS NMR spectra for C-bearing aluminosilicate crystals at 14 GPa is assigned as nano-diamonds based on the previous studies (Donnet et al., 2000; Duncan, 1987; Panich, 2017; Shames et al., 2002). Peak assignment for the peak at 164.5 ppm with peak widths of ~5 ppm is rather difficult. The peak position and widths in Na_2CO_3 in Figure 5.4 is 170.8 ppm and ~1.7 ppm, respectively, and the reported peak position and widths of Na_2CO_3 are 169.7 ppm and 0.8 ppm and those of $CaCO_3$ are 167.5 ppm and 1.0 ppm, respectively (Papenguth et al., 1989). The peak position of carbonates in scapolite (a solid-solution of $Na_4Al_3Si_9O_{24}Cl$ and

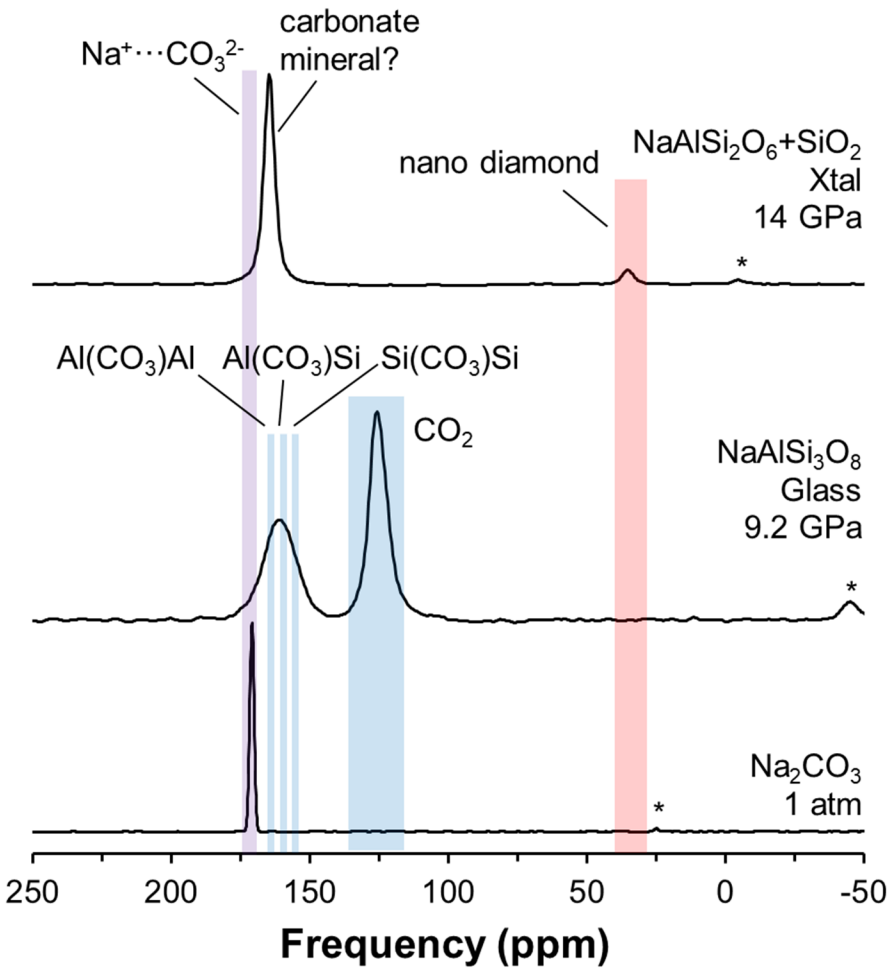

Figure 5.4. ^{13}C MAS NMR spectra for C-bearing aluminosilicate crystals ($NaAlSi_2O_6$ + SiO_2) at 14 GPa, C-bearing albite glasses at high pressure up to 9.2 GPa, and Na_2CO_3. The peak intensities are normalized to its highest height. Asterisks refer to spinning side bands.

$Ca_4Al_6Si_6O_{24}CO_3$) showed ~ 3 ppm peak shift to the lower frequencies (~163.8 ppm) when the planar carbonates were bent less than 3° to the (001) plane (Kohn et al., 1991; Sherriff et al., 1987). Therefore, the peak at 164.5 ppm may be due to the carbonate minerals liked to silicon or aluminum tetrahedra at high pressure and/or carbonate minerals with off-planar carbonate structure (distorted structure) at high pressure.

5.3.4. ^{27}Al 3QMAS NMR spectra and ^{29}Si MAS NMR spectra of C-bearing aluminosilicate glasses and crystals at high pressure

Figure 5.5a shows the ^{27}Al MAS NMR spectra of C-free albite glasses at 1 atm and C-bearing albite glasses at high pressure up to 9.2 GPa. While the small fraction of $^{[5]}$Al is observed in C-free albite glasses at 8 GPa (Lee, 2004), the current ^{27}Al MAS NMR spectra show that only $^{[4]}$Al exists in C-bearing albite glasses at high pressure. The peak assignment is based on previous NMR studies on aluminosilicates crystals and glasses (e.g., Baltisberger et al., 1996; Edén, 2015; Kelsey et al., 2008; McMillan and Kirkpatrick, 1992; Neuville et al., 2008; Toplis et al., 2000 and references therein). The peak position shifts to lower frequency region (negative frequency) from ~54 ppm at 1.5 GPa to ~50 ppm at 9.2 GPa and the peak widths increases with increasing pressure. The ^{27}Al 3QMAS NMR spectra in Figure 5.5b shows the increase of peak widths in both MAS dimension (y axis) and isotropic dimension (X axis) with increasing pressure: from 60 ppm (~10–70 ppm) to 80 ppm (~ -10–70 ppm) in MAS dimension and from ~17 ppm (-47 – -30 ppm) to 25 ppm (~-50 – -25 ppm) in isotropic dimension, respectively. The increase of peak widths is related to the increase

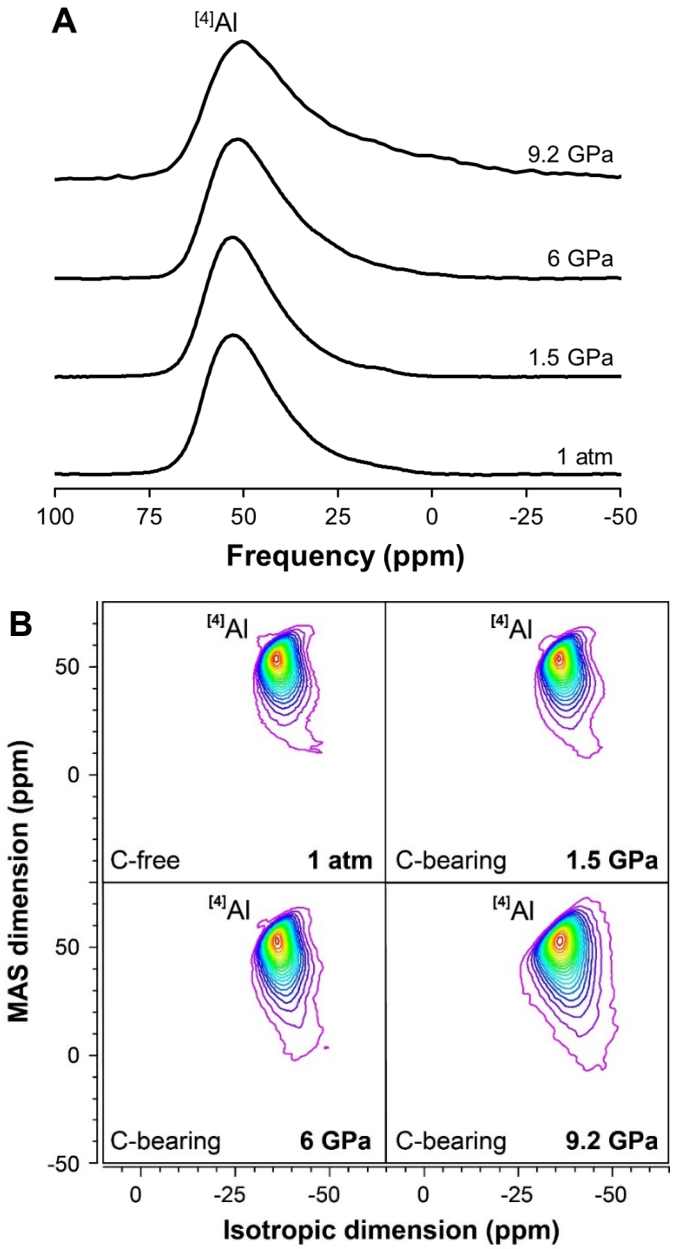

Figure 5.5. (A) ^{27}Al MAS and (B) 3QMAS NMR spectra for C-free albite glasses at 1 atm and C-bearing albite glasses at high pressure up to 9 GPa.

topological disorder, such as changes in Al-O bond lengths and/or bond angle around Al environments (e.g., Edén, 2015; Lee, 2010; Park and Lee, 2012). As the fraction of $^{[4]}Al(CO_3)^{[4]}Si$ increases the most with increasing pressure (Figure 5.3), the increase of topological disorder of Al in C-bearing albite glasses suggest that the carbon-induced topological disorder of Al in albite melts at high pressure.

Figure 5.6 shows the ^{29}Si MAS NMR spectra of C-bearing albite glasses at 9.2 GPa and C-bearing aluminosilicate crystals at 14 GPa, and those of C-bearing albite glasses at 1.5 and 6 GPa from previous study (Kim et al., 2018). The ^{29}Si MAS NMR spectra for C-bearing albite glasses at high pressure show only the $^{[4]}Si$ environment at high pressure up to 9.2 GPa. While the peak for $^{[4]}Si$ in C-bearing albite glasses at 6 GPa is identical to that at 1.5 GPa, the peak position shifts to lower frequency (negative region, ~1 ppm) and peak widths increase from 16 ppm to 20 ppm with increasing pressure from 6 GPa to 9.2 GPa, respectively. Together with the pressure-induced topological disorder of Al in C-bearing albite glasses at high pressure (Figure 5.5), the absence of highly coordinated Al and Si in albite glasses at 9.2 GPa suggests that the formation of bridging carbonate species in silicate melts change both Al and Si environments, evidenced by the peak broadening with increasing pressure up to 9.2 GPa, and the Al environments changes first from 6 GPa and then the Si environments starts to change from 9.2 GPa (e.g., Lee, 2010; Lee et al., 2004; Yarger et al., 1995 and references therein). The formation of highly coordinated Al and Si is still absent at 9.2 GPa, and this may indicate that the densification mechanism for C-bearing aluminosilicate melts may be different from that for C-free aluminosilicate melts at high pressure.

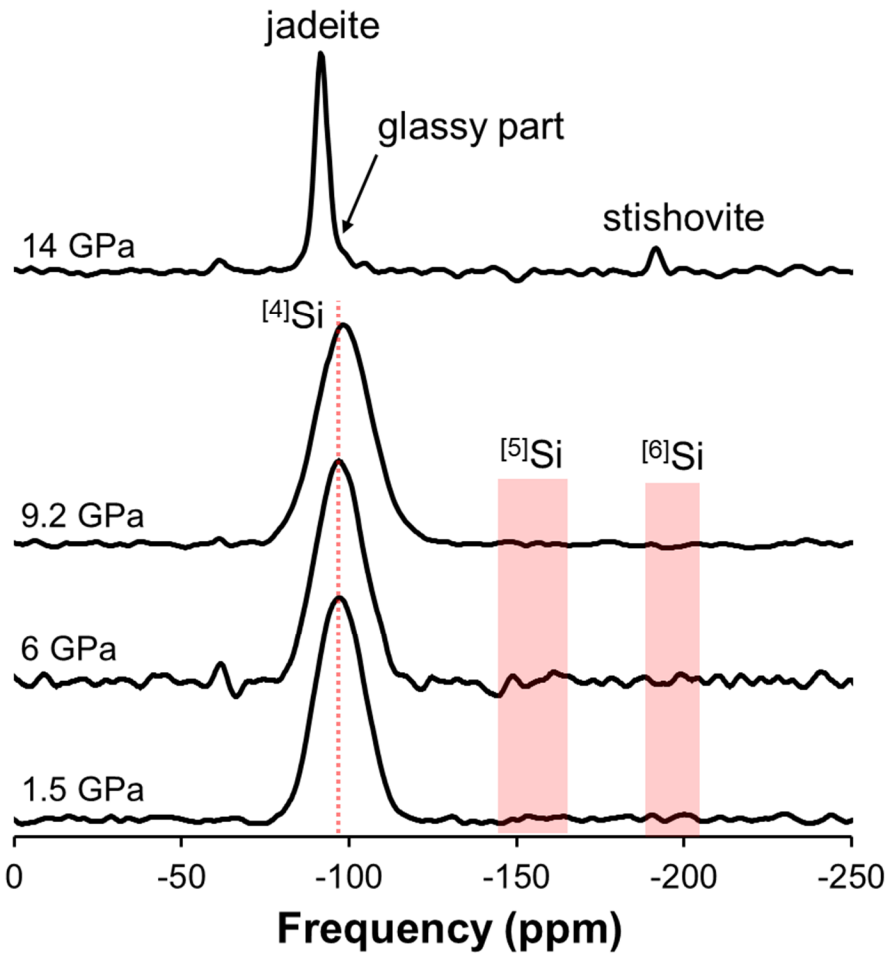

Figure 5.6. ^{29}Si MAS NMR spectra for C-bearing aluminosilicate crystals ($NaAlSi_2O_6$ + SiO_2) at 14 GPa, C-bearing albite glasses at high pressure up to 6 GPa.

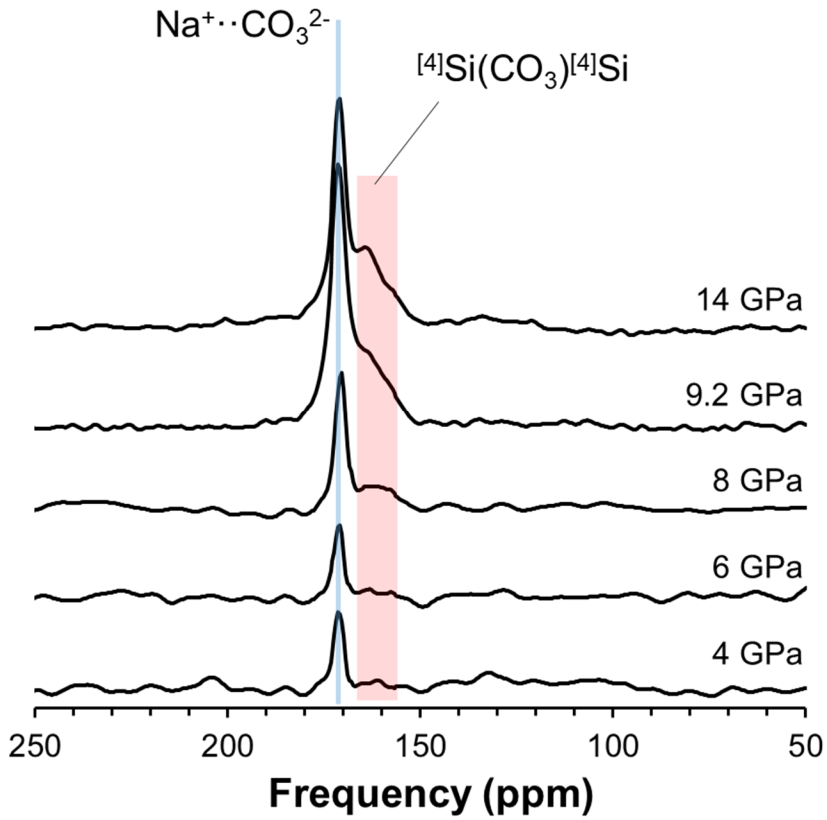

Figure 5.7. ^{13}C MAS NMR spectra for C-bearing sodium trisilicate (NS3) glasses quenched from melts at high pressure up to 14 GPa.

5.3.5. ^{13}C and ^{29}Si MAS NMR spectra of C-bearing alkali silicate glasses at high pressure

Figure 5.7 shows the ^{13}C MAS NMR spectra of C-bearing NS3 glasses at high pressure up to 14 GPa. The peak at ~171 ppm is assigned as free carbonates and that at ~160 ppm is assigned as bridging carbonates $^{[4]}Si(CO_3)^{[4]}Si$ as there is only one network-former cation in this glass (Morizet et al., 2014a; Tossell, 1995). Whereas the peak for free carbonates shifts to lower frequency region (negative frequency) from 171.7 ppm to

170.2 ppm with increasing pressure from 4 to 8 GPa, respectively, the peak for free carbonates at 9.2 and 14 GPa seems to shift back to 171.2 and 170.8 ppm, respectively. The increase of peak widths from ~2.5 ppm up to 8 GPa to ~4 ppm at 9.2 and 14 GPa is also observed. The peak at ~160 ppm gradually increases with increasing pressure and shifts toward higher frequency region (positive frequency) with increasing pressure above 9.2 GPa.

Figure 5.8 shows the ^{29}Si MAS NMR spectra of C-bearing NS3 glasses at high pressure up to 14 GPa. The peaks for $^{[4]}$Si, $^{[5]}$Si, and $^{[6]}$Si are observed at ~-90, -150, and -200 ppm, respectively, based on the previous studies on crystalline and amorphous silicates (Kirkpatrick et al., 1986; Stebbins, 1995 and references therein). While the peak position of $^{[4]}$Si slightly shift to higher frequency region (from -91.4 ppm at 4 GPa to -90.4 ppm at 8 GPa) (Kim et al., 2018), further increase of pressure result in the peak shift to lower frequency region from -90.4 ppm at 8 GPa to -96.2 ppm at 14 GPa, respectively. The formation of $^{[4]}$Si linked to $^{[6]}$Si makes the longer and more ionic bonds, resulting in the decreasing of chemical shielding and peak shift to higher frequency (positive region) (Kanzaki et al., 1998; Skibsted et al., 1990; Xue et al., 1991). The peak shift to lower frequency is related to the shorter and more covalent bonds and the increase of chemical shielding. As the bond lengths of C-O in carbonates (~1.3 Å) are shorter than those of Si-O (~1.6 Å in $^{[4]}$Si and ~1.8 Å in $^{[6]}$Si) (Effenberger et al., 1981; Smith et al., 1983; Tossell, 1995), the peak shift to lower frequency in ^{29}Si MAS NMR spectra may be related to the formation of bridging carbonates $^{[4]}$Si(CO_3)$^{[4]}$Si. This is consistent with previous study on carbon-bearing basaltic glasses at high pressure up to 3 GPa, showing the peak shift toward negative frequency

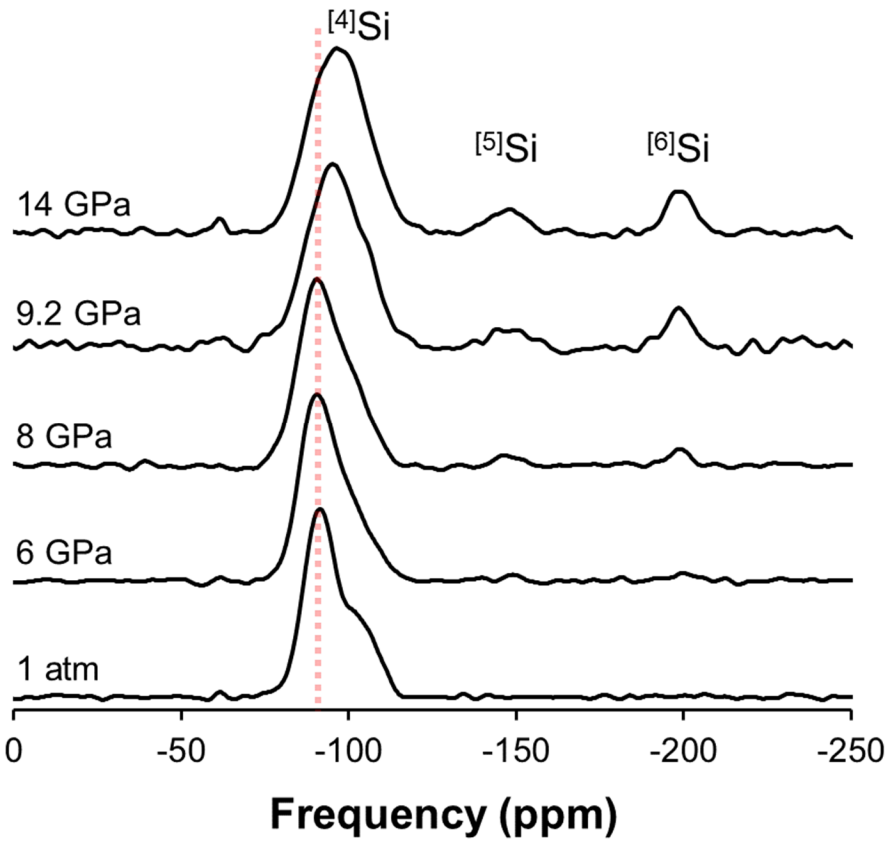

Figure 5.8. ^{29}Si MAS NMR spectra for C-bearing sodium trisilicate (NS3) glasses quenched from melts at high pressure up to 14 GPa.

with increasing pressure (Morizet et al., 2015). In ^{13}C MAS NMR spectra, on the other hand, the peak for bridging carbonates seems to shift to higher frequency region with increasing pressure. This may be related to the formation of bridging carbonates not only $^{[4]}Si(CO_3)^{[4]}Si$ but also $^{[4]}Si(CO_3)^{[5,6]}Si$ and the increase of C-O bond lengths with increasing pressure. Further studies on the NMR chemical shielding of $^{[4]}Si(CO_3)^{[5,6]}Si$ by quantum chemical calculations are needed to confirm the origin of non-linear peak shift in C-bearing NS3 glasses at high pressure.

5.3.6. Quantification of carbon species in albite glasses by ^{13}C MAS NMR spectra

The quantitative measurements of carbon species in albite glasses are based on the peak intensity of central peak and spinning side bands and the measured T_1 of each carbon species in ^{13}C MAS NMR spectra. The measured T_1 times of CO_2 and CO_3^{2-} in C-bearing albite glasses at 9.2 GPa are ~30 s and ~28 s, respectively. Compared with the previous T_1 of CO_2 in C-bearing albite glasses at 1.5 and 6 GPa (43 s and ~140 s, respectively), the T_1 at 9.2 GPa is much shorter due to the higher Co contents in the sample (~0.4% of Co due to the detection limit of the scale). The peak area of CO_2 and CO_3^{2-} are normalized by the measured T_1 at 9.2 GPa. Note that the measure T_1 of CO_2 and CO_3^{2-} are relatively similar and we used the same T_1 for CO_2 and CO_3^{2-} in C-bearing albite glasses at 1.5 and 6 GPa due to the difficulties in the fitting of T_1 for CO_3^{2-} with low signal to noise ratio (Kim et al., 2018). Therefore, an assumption for using the same T_1 for CO_2 and CO_3^{2-} in C-bearing albite glasses at high pressure up to 6 GPa may not result in the severe error in the quantification of carbon species at high pressure.

Figure 5.9 shows the carbon contents of CO_2, CO_3^{2-}, and CO in albite glasses at high pressure up to 9.2 GPa taking into consideration the T_1 time of carbon species. The estimated amount of CO_2, CO_3^{2-}, and CO at 9.2 GPa are 4.12, 3.03, and 0.04 wt%, respectively. The calculated carbon contents in the current study (9.2 GPa) together with the previous data from Kim et al. (2018) is generally consistent with the trend observed in previous theoretical calculations (Guillot and Sator, 2011). The fraction of CO_3^{2-} increases from ~31% at 1.5 GPa, ~27 % at 6 GPa to ~42% at 9.2 GPa, which clearly shows the drastic increase of carbonates above 6 GPa, similar to the previous study (Guillot and Sator, 2011).

While the estimated fraction of carbon species in carbon-bearing albite glasses at high pressure up to 9.2 GPa gradually increases with increasing pressure from ~1.4 wt% at 1.5 GPa to ~7.9 wt% at 9.2 GPa, respectively, the actual carbon contents carried by silicate melts would be different from those estimated from ^{13}C MAS NMR spectra. Note that carbon carrying capacity of silicate melts only provides the information on the maximum carbon contents that can be carried by the silicate melts and actual carbon contents in silicate melts from in the mantle vary with its location. Recent study suggested the dissolution of carbon species into water and transport of carbon species into mantle wedge during the subduction of oceanic crust (e.g., Sverjensky et al., 2014) while some argued that there is no significant transfer of carbon species into the mantle wedge (Dasgupta and Hirschmann, 2010; Kelemen and Manning, 2015; Kerrick and Connolly, 2001). Based on these experimental data, the estimated carbon flux between subducting oceanic crust and mantle wedge at depth < 60–70 km varies from 0.06 to 6 Mt C/y (Kelemen and Manning, 2015). It is difficult

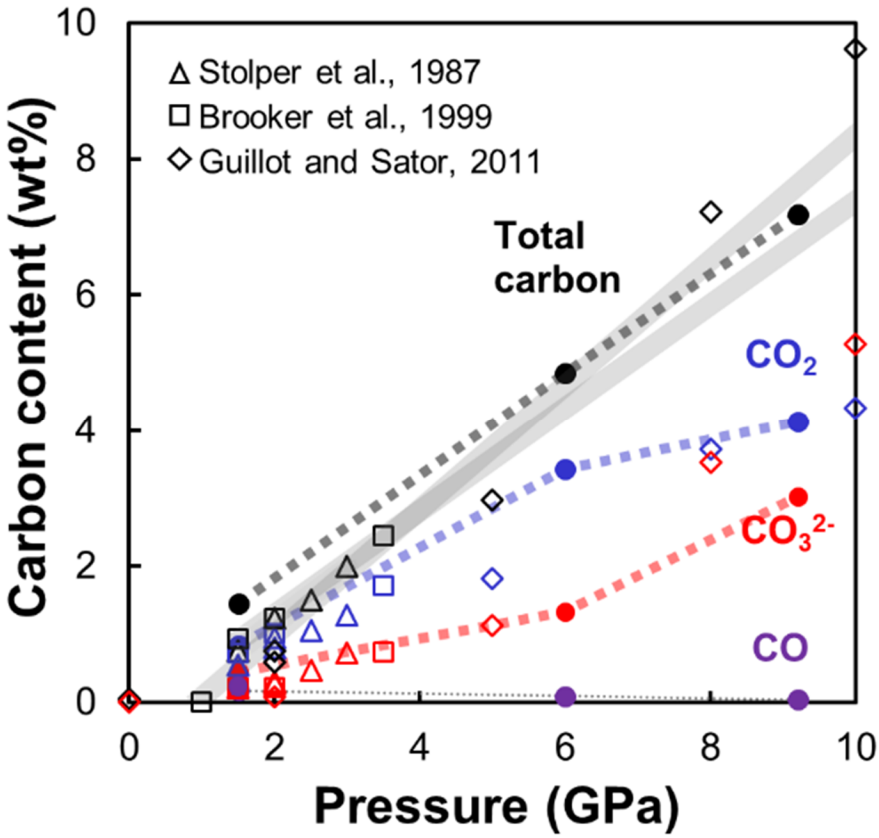

Figure 5.9. Carbon contents in the C-bearing albite glasses with increasing pressure up to 9.2 GPa. Black, blue, red, and violet closed circles correspond to total carbon, CO_2 CO_3^{2-}, and CO contents in albite glasses calculated from ^{13}C MAS NMR spectra, respectively. Open triangle, rectangle, and diamonds correspond to previous data from Stolper et al. (1987), Brooker et al. (1999), and Guillot and Sator (2011), respectively.

to estimate the actual carbon contents in the silicate melts from in the mantle based on the current study because of the heterogeneity in the distribution of carbon species in the mantle and difficulties in the estimating the remnant carbon species in the subducting slab. Therefore, although the estimated carbon carrying capacity of carbon-bearing albite melts gradually increases up to ~7.9 wt% with increasing pressure up to 9.2 GPa, the actual carbon contents in silicate melts formed at ~9 GPa may be different from those estimated in the current study. Based on the reported carbon contents in the fertile mantle, the average carbon contents in basaltic melts are estimated as ~0.2 wt% (Ni and Keppler, 2013).

5.4. Discussion

5.4.1. Peak assignment of graphite and nano-diamond quenched from high pressure and high temperature conditions

The peak assignment in the Raman spectra of C-bearing aluminosilicate glasses at 14 GPa is based on the previous Raman studies on diamond, lonsdaleite, and graphite (Ferrari and Robertson, 2001; Goryainov et al., 2014; Knight and White, 1989; Kuzmany et al., 2004; Schindler and Vohra, 1995; Vidano and Fischbach, 1978) and previous ^{13}C NMR studies on nano-diamonds (Donnet et al., 2000; Komatsu et al., 2007; Panich, 2017; Shames et al., 2002). The broad peak at ~1540 cm^{-1} in Raman spectra for the surface of the C-bearing aluminosilicate crystals is assigned as G bands of cubic graphite, respectively (Hanfland et al., 1989; Knight and White, 1989; Perraki et al., 2006; Vidano and Fischbach, 1978). The G band of cubic graphite shows asymmetric feature (longer tails to the higher frequencies) and this may be due to the presence of D' bands at ~ 1600 cm^{-1} which is

related to the structural disorder of graphite (Vidano and Fischbach, 1978).

Previous studies on nano-diamond showed three peaks for nano-diamonds at ~1150, ~1350, and ~1550 cm^{-1} where the presence of a peak at ~1150 cm^{-1} is the key to find nano-diamonds (Ferrari and Robertson, 2004; Kuzmany et al., 2004; Prawer et al., 2000; Schindler and Vohra, 1995). The obtained Raman spectra for C-bearing aluminosilicate glasses at 14 GPa shows peaks at ~1250, ~1290, ~1350, and ~1530 cm^{-1}, and vibrational modes at ~1250 cm^{-1} is ~100 cm^{-1} away from the reported peak position of nano-diamonds. Previous study on the high-pressure experiment on polycrystalline pyrolytic graphite at room temperature reported the presence of intermediate structures between diamond and graphite, showing bands at 1250 cm^{-1}, 1294 cm^{-1}, 1326 cm^{-1}, and 1574 cm^{-1} (Schindler and Vohra, 1995), which is lonsdaleite, often called as hexagonal diamonds (Goryainov et al., 2014; Hazen et al., 2013). Both diamonds and lonsdaleite consist of sp^3 bonding of carbon while the stacking sequence of diamonds is a three-layer sequence, filling all the empty site of the first layer, that of lonsdaleite is a two-layer sequence that one empty site exists when stacking one graphene-like layer to another (Hazen et al., 2013). Lonsdaleite is often observed in shock-compressed meteorites, where the impact of pressure and temperature is short (Hazen et al., 2013). Here, we heated the C-bearing aluminosilicate crystals for 5 min at 14 GPa, which is short for crystal formation. The heating of graphite at 2300 °C at 15–18 GPa for 10–10000 s made mixtures of cubic- and hexagonal-diamonds of 10–30 nm size (Sumiya, 2004). Therefore, heating of 5 min at 14 GPa may be too short to form cubic-diamonds in the system. The residence time of carbon species in the mantle is several millions of years, which is much longer than our

experimental heating conditions. In geological conditions, the formation of cubic diamonds is expected. While the crystal structure of cubic- and hexagonal diamonds are different, peak assignment of nano-diamonds in ^{13}C MAS NMR spectra does not show the differences in cubic- and hexagonal-diamonds as both diamonds have a same sp^3 bonding and their differences are in the stacking sequences of the layers. Therefore, it is necessary to use Raman spectroscopy or X-ray diffractions to identify the exact structure of nano-diamonds in the sample.

5.4.2. Peak broadening of CO_2 in C-bearing albite glasses with increasing pressure

The peak widths of CO_2 in C-bearing albite glasses increase from 4 ppm to 8 ppm with increasing pressure from 6 GPa to 9.2 GPa, respectively, while the peak position is unchanged with respect to the pressure (Figure 5.3). The peak broadening of dissolved CO_2 may be related to the increase of spin-lattice relaxation time (T_1) of CO_2 with increasing pressure (Etesse et al., 1992) and/or pressure-induced topological disorder of CO_2. Previous study reported that the spin-relaxation time of gas phase CO_2 increases with increasing pressure and the changes of spin-relaxation time of CO_2 with respect to pressure show a threshold pressure that sudden increase of T_1 occurred (Etesse et al., 1992). In addition, the diffusion of dissolved CO_2 would decrease with increasing pressure and various topologically different CO_2–bridging oxygen (BO) site would exist with increasing pressure, such as variations dihedral angle of CO_2–BO and CO_2–BO bond lengths, resulting in the broadening of peak above 6 GPa. It is interesting to note that the variations in CO_2–BO bond lengths seems not to result in the peak shift to

the lower frequency (negative region, more shielded) until the bond lengths of CO_2–BO decreases below a threshold length as the peak position of CO_2 in fluid inclusion in enstatite at 1. 5 GPa and that of dissolved CO_2 in albite glasses at 1.5 GPa is identical (Kim et al., 2016, 2018). The additional interaction between CO_2–BO occurs in dissolved CO_2 in albite glasses at 1.5 GPa only causes the presence of spinning side bands. Therefore, it seems that the distance between CO_2–BO seems to have negligible effect on the chemical shift of CO_2 in ^{13}C MAS NMR spectra at high pressure up to 9.2 GPa. Therefore, the non-linear changes in T_1 of CO_2 with increasing pressure and the topological disorder between CO_2-BO with increasing pressure would result in the peak broadening of CO_2 in albite glasses with increasing pressure.

5.4.3. Redox reaction of carbon and the oxygen fugacity of mantle

Redox reaction of carbon species is one of the well-known processes to control the oxygen fugacity of mantle (Stagno et al., 2013) and the increase of atmospheric oxygen during the early Earth (Duncan and Dasgupta, 2017; Ruhl and Kürschner, 2011). The redox reaction of carbon species in mantle minerals are usually related to the redox reaction of transition metals in minerals as followed (Stagno et al., 2013).

$MgSiO_3 + MgCO_3 = Mg_2SiO_4 + C + O_2$

enstatite magnesite olivine diamond

$4Fe_2SiO_4 + 2FeSiO_3 + O_2 = 2Fe_3Fe_2^{3+}Si_3O_{12}$

olivine orthopyroxene garnet

In the current study, we used Na_2CO_3 as a carbon reservoir and we obtained cubic graphite, hexagonal diamonds, and unidentified carbonate minerals

after the reaction of $Na_2CO_3 + Al_2O_3 + SiO_2$ at 14 GPa. The formations of both carbonate minerals and hexagonal nano-diamonds are observed, and this can be explained in the following equation

$$3\ CO_2 = C + 2\ CO_3^{2-}$$

Based on the equation, the formation of graphite with carbonate minerals may not form free oxygen when the fraction of carbonate minerals over nano-diamonds ($X_{carbonate}/X_{diamond}$) equals 2. On the other hand, the free oxygen would be formed even with the presence of carbonate minerals when $X_{carbonate}/X_{diamond}$ is less than 2. Together with the peak intensity of carbonate minerals and nano-diamonds in ^{13}C MAS NMR spectra, the estimated $X_{carbonate}/X_{diamond}$ is ~15. Therefore, the presence of free oxygen by the formation of nano-diamonds would be negligible in the current sodium aluminosilicate glasses and crystals at high pressure.

When the presence of neutral carbon species is observed with the presence of silicate melts and the absence of carbonate minerals, this may have an implication on the free oxygen in the silicate melts at high pressure. Silicate melts contains some amounts of free oxygen depending on the composition of silicate melts (Lee and Kim, 2015; Stebbins, 2017) and the estimated fraction of free oxygen in lead-disilicate glasses is ~6% (Lee and Kim, 2015) and the fraction of free oxygen decreases with increasing the fraction of SiO_2 in the silicate melts (Stebbins, 2017). We put 7.9 wt% of CO_2 in the C-bearing aluminosilicate crystals and glasses at 14 GPa. Assuming that the all the CO_2 transforms into $C + O_2$, the amount of free oxygen produced is ~6.9 mol%, which is similar to the fraction of free oxygen in lead disilicate glasses (Lee and Kim, 2015). However, as the presence of new carbonate species are observed in ^{13}C MAS NMR spectra (Figure 5.4) and the proportion of nano-

diamonds are one-tenth of that of carbonate species at high pressure, the produced free oxygen should be less than 0.7 mol%. Though the fraction of aluminosilicate glasses in the sample is relatively low (~10%) based on the peak intensity of glass in ^{29}Si MAS NMR spectra (Figure 5.6), 0.7 mol% of free oxygen could be consumed in silicate melts. This experiment may indicate that the formation of silicate melts at high pressure can also affect the oxygen fugacity of the mantle by storing free oxygen in the magma. The volcanic eruption of magma containing excess free oxygen may result in the release of O_2 in the proto-atmosphere without the presence of O_2 releasing living organisms. The recent study reported inorganic processes in the formation of O_2 in the atmosphere (Hu et al., 2016). The presence of FeO_2 in the lower mantle was observed at ~76 GPa and the upwelling of FeO_2 through the magma eruption may cause the release of excess O_2 to the atmosphere as the Fe_2O_3 and Fe_3O_4 is stable at lower pressure (Hu et al., 2016). The presence of the redox reaction of carbon species with silicate melt may also be applicable to the inorganic formation of O_2 in the atmosphere. The previous study reported the episodic subduction of crust during Precambrian period (~1.1, 1.9–2.1, 2.7, and 3.5 Ga) based on the apparent polar wander angular velocities and Nb/Th ratio (O'Neil et al., 2007). The reported episodic subduction of crust at ~2.7 and ~3.5 Ga may be related to the emission of oxygen to the proto-atmosphere with volcanic activities in the arc. Thus, the current result may also imply the effect of silicate melts on the redox reaction of inorganic carbon species at high pressure and the effect of inorganic carbon species on the formation of O_2 in the proto-atmosphere.

5.5. Conclusion

In this study, we identify the pressure-induced speciation of carbon in binary sodium silicate glasses and ternary sodium aluminosilicate glasses and crystals at high pressure up to 14 GPa. In both systems, the fraction of bridging carbonates increases with increasing pressure. In polymerized albite glasses at 9.2 GPa, the peak widths of CO_2 increase almost twice to those at 6 GPa, which may be related to the increase of T_1 time of CO_2 and pressure-induced topological disorder of CO_2 weakly bound to bridging oxygen. The formation of highly coordinated Al and Si is not observed in C-bearing albite glasses at high pressure up to 9.2 GPa while the topological disorder of both network formers increases with increasing pressure, evidenced by the increase of peak widths. In depolymerized sodium silicate glasses, the peak position of bridging carbonates seems to shift towards higher frequency region in ^{13}C MAS NMR spectra and that of $^{[4]}Si$ shifts towards lower frequency region. This may be related to the formation of bridging carbonates and the shielding and deshielding effect on each nuclide. In C-bearing aluminosilicate crystals and glasses at 14 GPa, the presence of nano-diamonds is observed in both Raman and ^{13}C NMR spectra. As the Na_2CO_3 was used as a carbon reservoir, the formation of nano-diamonds indicates that free oxygens are stored in the silicate melts. This implies that the formation of silicate melts at high pressure may result in the reduction of carbon species from carbonates to diamonds without the redox reaction with metal ions and affects the oxygen fugacity in the mantle.

References

Baltisberger, J.H., Xu, Z., Stebbins, J.F., Wang, S.H. and Pines, A. (1996) Triple-quantum two-dimensional ^{27}Al magic angle spinning nuclear magnetic resonance spectroscopic study of aluminosilicate and aluminate crystals and glasses. *J Am Chem Soc* **118**, 7209-7214.

Behrens, H., Ohlhorst, S., Holtz, F. and Champenois, M. (2004) CO_2 solubility in dacitic melts equilibrated with H_2O-CO_2 fluids: Implications for modeling the solubility of CO_2 in silicic melts. *Geochimica et Cosmochimica Acta* **68**, 4687-4703.

Blank, J.G. and Brooker, R.A. (1994) Experimental studies of carbon dioxide in silicate melts: Solubility, speciation, and stable carbon isotope behavior, In *Volatiles in Magmas*, (Eds. Carroll, M.R., Holloway, J.R.).

Brooker, R.A., Kohn, S.C., Holloway, J.R. and McMillan, P.F. (2001) Structural controls on the solubility of CO_2 in silicate melts Part II: IR characteristics of carbonate groups in silicate glasses. *Chemical Geology* **174**, 241-254.

Brooker, R.A., Kohn, S.C., Holloway, J.R., McMillan, P.F. and Carroll, M.R. (1999) Solubility, speciation and dissolution mechanisms for CO_2 in melts on the $NaAlO_2$-SiO_2 join. *Geochimica et Cosmochimica Acta* **63**, 3549-3565.

Dasgupta, R. and Hirschmann, M.M. (2010) The deep carbon cycle and melting in Earth's interior. *Earth and Planetary Science Letters* **298**, 1-13.

Donnet, J.-B., Fousson, E., Delmotte, L., Samirant, M., Baras, C., Wang, T.K. and Eckhardt, A. (2000) ^{13}C NMR characterization of nanodiamonds. *Comptes Rendus de l'Académie des Sciences - Series IIC - Chemistry* **3**, 831-838.

Duncan, M.S. and Dasgupta, R. (2017) Rise of Earth's atmospheric oxygen controlled by efficient subduction of organic carbon. *Nature Geoscience* **10**, 387-392.

Duncan, T.M. (1987) ^{13}C chemical shieldings in solids. *Journal of Physical and Chemical Reference Data* **16**, 125-151.

Edén, M. (2015) Chapter Four - ^{27}Al NMR Studies of Aluminosilicate Glasses, In *Annual Reports on NMR Spectroscopy*, (Ed. Graham, A.W.). Academic Press, pp. 237-331.

Effenberger, H., Mereiter, K. and Zemann, J. (1981) Crystal structure refinements of magnesite, calcite, rhodochrosite, siderite, smithonite, and dolomite, with discussion of some aspects of the stereochemistry of calcite type carbonates. *Zeitschrift für Kristallographie-Crystalline Materials* **156**, 233-244.

Eggler, D.H. and Rosenhauer, M. (1978) Carbon-dioxide in silicate melts 2. Solubilites of CO_2 and H_2O in $CaMgSi_2O_6$ (diopside) liquids and vapors at pressure to 40 kb. *American Journal of Science* **278**, 64-94.

Etesse, P., Zega, J.A. and Kobayashi, R. (1992) High pressure nuclear magnetic resonance measurement of spin-lattice relaxation and selfdiffusion in carbon dioxide. *J Chem Phys* **97**, 2022-2029.

Feng, J., Lee, Y.J., Reeder, R.J. and Phillips, B.L. (2006) Observation of bicarbonate in calcite by NMR spectroscopy. *American Mineralogist* **91**, 957-960.

Ferrari, A.C. and Robertson, J. (2001) Origin of the 1150 cm^{-1} Raman mode in nanocrystalline diamond. *Physical Review B* **63**, 121405.

Ferrari, A.C. and Robertson, J. (2004) Raman spectroscopy of amorphous, nanostructured, diamond–like carbon, and nanodiamond. *Philosophical Transactions of the Royal Society of London. Series A: Mathematical, Physical and Engineering Sciences* **362**, 2477-2512.

Goryainov, S.V., Likhacheva, A.Y., Rashchenko, S.V., Shubin, A.S., Afanas'ev, V.P. and Pokhilenko, N.P. (2014) Raman identification of lonsdaleite in Popigai impactites. *Journal of Raman Spectroscopy* **45**, 305-313.

Guillot, B. and Sator, N. (2011) Carbon dioxide in silicate melts: A molecular dynamics simulation study. *Geochimica et Cosmochimica Acta* **75**, 1829-1857.

Hanfland, M., Beister, H. and Syassen, K. (1989) Graphite under pressure: Equation of state and first-order Raman modes. *Physical Review B* **39**, 12598-12603.

Hazen, R.M., Downs, R.T., Jones, A.P. and Kah, L. (2013) Carbon mineralogy and crystal chemistry, In *Reviews in Mineralogy and Geochemistry*, (Eds. Hazen, R.M., Jones, A.P., Baross, J.A.). Mineralogical Society of America, Virginia, pp. 7-46.

Hazen, R.M. and Schiffries, C.M. (2013) Why deep carbon?, In *Carbon in Earth*, (Eds. Hazen, R.M., Jones, A.P., Baross, J.A.). Mineralogical Society of America, Virginia, U.S.A.

Hemley, R.J. (1987) Pressure dependence of Raman spectra of SiO_2 polymorphs: a-quartz, coesite, and stishovite, In *High-Pressure Research in Mineral Physics*, (Eds. Manghnani, M.H., Syono, Y.). Americal Geophysical Union, Washington D.C., U.S.A., pp. 347-359.

Hirschmann, M.M. and Dasgupta, R. (2009) The H/C ratios of Earth's near-surface and deep reservoirs, and consequences for deep Earth volatile cycles. *Chemical Geology* **262**, 4-16.

Jones, A.R., Winter, R., Greaves, G.N. and Smith, I.H. (2005) ^{23}Na, ^{29}Si, and ^{13}C MAS NMR investigation of glass-forming reactions between Na_2CO_3 and SiO_2. *J. Phys. Chem. B* **109**, 23154-23161.

Kadik, A., Pineau, F., Litvin, Y., Jendrzejewski, N., Martinez, I. and Javoy, M. (2004) Formation of carbon and hydrogen species in magmas at low oxygen fugacity. *J. Petrol.* **45**, 1297-1310.

Kanzaki, M., Xue, X. and Stebbins, J.F. (1998) Phase relations in Na_2O–SiO_2 and $K_2Si_4O_9$ systems up to 14 GPa and ^{29}Si NMR study of the new high-pressure phases: implications to the structure of high-pressure silicate glasses. *Physics of the Earth and Planetary Interiors* **107**, 9-21.

Kelemen, P.B. and Manning, C.E. (2015) Reevaluating carbon fluxes in subduction zones, what goes down, mostly comes up. *Proceedings of the National Academy of Sciences* **112**, E3997-E4006.

Kelsey, K.E., Allwardt, J.R. and Stebbins, J.F. (2008) Ca–Mg mixing in aluminosilicate glasses: An investigation using ^{17}O MAS and 3QMAS and ^{27}Al MAS NMR. *Journal of Non-Crystalline Solids* **354**, 4644-4653.

Keppler, H., Wiedenbeck, M. and Shcheka, S.S. (2003) Carbon solubility in olivine and the mode of carbon storage in the Earth's mantle. *Nature* **424**, 414-416.

Kerrick, D.M. and Connolly, J.A.D. (2001) Metamorphic devolatilization of subducted oceanic metabasalts: implications for seismicity, arc magmatism and volatile recycling. *Earth Planet. Sci. Lett.* **189**, 19-29.

Kim, E.J., Fei, Y. and Lee, S.K. (2016) Probing carbon-bearing species and CO_2 inclusions in amorphous carbon-$MgSiO_3$ enstatite reaction products at 1.5 GPa: Insights from ^{13}C high-resolution solid-state NMR. *American Mineralogist* **101**, 1113-1124.

Kim, E.J., Fei, Y. and Lee, S.K. (2018) Effect of pressure on the short-range structure and speciation of carbon in alkali silicate and aluminosilicate glasses and melts at high pressure up to 8 GPa: ^{13}C, ^{27}Al, ^{17}O and ^{29}Si solid-state NMR study. *Geochimica et Cosmochimica Acta* **224**, 327-343.

Kirkpatrick, R.J., Oestrike, R., Weiss, C.A., Smith, K.A. and Oldfield, E. (1986) High-resolution ^{27}Al and ^{29}Si NMR spectroscopy of glasses and crystals along the join $CaMgSi_2O_6$-$CaAl_2SiO_6$. *American Mineralogist* **71**, 705-711.

Knight, D.S. and White, W.B. (1989) Characterization of diamond films by Raman spectroscopy. *Journal of Materials Research* **4**, 385-393.

Kohn, S.C., Brooker, R.A. and Dupree, R. (1991) ^{13}C MAS NMR - A method for studying CO_2 speciation in glasses. *Geochimica et Cosmochimica Acta* **55**, 3879-3884.

Komatsu, N., Kadota, N., Kimura, T. and Osawa, E. (2007) Solution-phase ^{13}C NMR spectroscopy of detonation nanodiamond. *Chemistry Letters* **36**, 398-399.

Kuzmany, H., Pfeiffer, R., Salk, N. and Günther, B. (2004) The mystery of the 1140 cm^{-1} Raman line in nanocrystalline diamond films. *Carbon* **42**, 911-917.

Lee, S.K. (2004) Structure of silicate glasses and melts at high pressure: Quantum chemical calculations and solid-state NMR. *The journal of Physical Chemistry B* **108**, 5889-5900.

Lee, S.K. (2010) Effect of pressure on structure of oxide glasses at high pressure: Insights from solid-state NMR of quadrupolar nuclides. *Solid State Nuclear Magnetic Resonance* **38**, 45-57.

Lee, S.K., Cody, G.D., Fei, Y.W. and Mysen, B.O. (2004) Nature of polymerization and properties of silicate melts and glasses at high pressure. *Geochimica et Cosmochimica Acta* **68**, 4189-4200.

Lee, S.K., Deschamps, M., Hiet, J., Massiot, D. and Park, S.Y. (2009) Connectivity and Proximity between Quadrupolar Nuclides in Oxide Glasses: Insights from through-Bond and through-Space Correlations in Solid-State NMR. *J. Phys. Chem. B* **113**, 5162-5167.

Lee, S.K. and Kim, E.J. (2015) Probing metal-bridging oxygen and configurational disorder in amorphous lead silicates: Insights from ^{17}O solid-state nuclear magnetic Resonance. *J. Phys. Chem. C* **119**, 748-756.

Luth, R.W. (2003) Mantle volatiles--Distribution and consequences, In *Treatise on Geochemistry*, (Eds. Heinrich, D.H., Karl, K.T.). Pergamon, Oxford, pp. 319-361.

Madhu, P.K., Goldbourt, A., Frydman, L. and Vega, S. (1999) Sensitivity enhancement of the MQMAS NMR experiment by fast amplitude modulation of the pulses. *Chemical Physics Letters* **307**, 41-47.

McKeown, D.A., Galeener, F.L. and Brown, G.E. (1984) Raman studies of Al coordination in silica-rich sodium aluminosilicate glasses and some related minerals. *Journal of Non-Crystalline Solids* **68**, 361-378.

McMillan, P.F. and Kirkpatrick, R.J. (1992) Al coordination in magnesium aluminosilicate glasses. *American mineralogist* **77**, 898-900.

Moore, J.K., Surface, J.A., Brenner, A., Skemer, P., Conradi, M.S. and Hayes, S.E. (2015) Quantitative identification of metastable magnesium carbonate minerals by solid-state ^{13}C NMR spectroscopy. *Environmental Science & Technology* **49**, 657-664.

Morizet, Y., Brooker, R.A. and Kohn, S.C. (2002) CO_2 in haplo-phonolite melt: solubility, speciation and carbonate complexation. *Geochimica et Cosmochimica Acta* **66**, 1809-1820.

Morizet, Y., Florian, P., Paris, M. and Gaillard, F. (2017a) ^{17}O NMR evidence of free ionic clusters $M^{n+}CO_3^{2-}$ in silicate glasses: Precursors for carbonate-silicate liquids immiscibility. *American Mineralogist* **102**, 1561-1564.

Morizet, Y., Nichols, A.R.L., Kohn, S.C., Brooker, R.A. and Dingwell, D.B. (2007) The influence of H_2O and CO_2 on the glass transition

temperature: insights into the effects of volatiles on magma viscosity. *Eur. J. Mineral.* **19**, 657-669.

Morizet, Y., Paris, M., Gaillard, F. and Scaillet, B. (2010) C-O-H fluid solubility in haplobasalt under reducing conditions: An experimental study. *Chemical Geology* **279**, 1-16.

Morizet, Y., Paris, M., Gaillard, F. and Scaillet, B. (2014a) Carbon dioxide in silica-undersaturated melt Part II: Effect of CO_2 on quenched glass structure. *Geochim. Cosmochim. Acta* **144**, 202-216.

Morizet, Y., Paris, M., Gaillard, F. and Scaillet, B. (2014b) Carbon dioxide in silica-undersaturated melt. Part I: The effect of mixed alkalis (K and Na) on CO_2 solubility and speciation. *Geochimica et Cosmochimica Acta* **141**, 45-61.

Morizet, Y., Paris, M., Sifré, D., Di Carlo, I. and Gaillard, F. (2017b) The effect of Mg concentration in silicate glasses on CO_2 solubility and solution mechanism: Implication for natural magmatic systems. *Geochimica et Cosmochimica Acta* **198**, 115-130.

Morizet, Y., Vuilleumier, R. and Paris, M. (2015) A NMR and molecular dynamics study of CO_2-bearing basaltic melts and glasses. *Chemical Geology* **418**.

Mysen, B.O., Arculus, R.J. and Eggler, D.H. (1975) Solubility of carbon-dioxide in melts of andesite, tholeiite, and olivine nephelinite composition to 30 kbar pressure. *Contributions to Mineralogy and Petrology* **53**, 227-239.

Mysen, B.O., Eggler, D.H., Seitz, M.G. and Holloway, J.R. (1976) Carbon dioxide in silicate melts and crystals. Part I. Solubiltiy measurements. *American Journal of Science* **276**, 455-479.

Mysen, B.O., Fogel, M.L., Morrill, P.L. and Cody, G.D. (2009) Solution behavior of reduced C-O-H volatiles in silicate melts at high pressure and temperature. *Geochimica et Cosmochimica Acta* **73**, 1696-1710.

Mysen, B.O., Kumamoto, K., Cody, G.D. and Fogel, M.L. (2011) Solubility and solution mechanisms of C–O–H volatiles in silicate melt with variable redox conditions and melt composition at upper mantle temperatures and pressures. *Geochimica et Cosmochimica Acta* **75**, 6183-6199.

Mysen, B.O. and Richet, P. (2005) Volatiles I. The system C-O-H-S, In *Silicate Glasses and Melts*. Elsevier.

Neuville, D.R., Cormier, L., Montouillout, V., Florian, P., Millot, F., Rifflet, J.-C. and Massiot, D. (2008) Structure of Mg-and Mg/Ca aluminosilicate glasses: ^{27}Al NMR and Raman spectroscopy investigations. *American Mineralogist* **93**, 1721-1731.

Ni, H.W. and Keppler, H. (2013) Carbon in silicate melts, In *Reviews in Mineralogy and Geochemistry*, (Eds. Hazen, R.M., Jones, A.P., Baross, J.A.). Mineralogical Society of America, Virginia, pp. 251-287.

Pan, V., Holloway, J.R. and Hervig, R.L. (1991) The pressure and temperature dependence of carbon dioxide solubility in tholeiitic basalt melts. *Geochimica et Cosmochimica Acta* **55**, 1587-1595.

Panich, A.M. (2017) Nuclear magnetic resonance studies of nanodiamond surface modification. *Diamond and Related Materials* **79**, 21-31.

Papenguth, H.W., Kirkpatrick, R.J., Montez, B. and Sandberg, P.A. (1989) ^{13}C MAS NMR spectroscopy of inorganic and biogenic carbonates. *American Mineralogist* **74**, 1152-1158.

Park, S.Y. and Lee, S.K. (2012) Structure and disorder in basaltic glasses and melts: Insights from high-resolution solid-state NMR study of glasses in

diopside–Ca-tschermakite join and diopside–anorthite eutectic composition. *Geochimica et Cosmochimica Acta* **80**, 125-142.

Perraki, M., Proyer, A., Mposkos, E., Kaindl, R. and Hoinkes, G. (2006) Raman micro-spectroscopy on diamond, graphite and other carbon polymorphs from the ultrahigh-pressure metamorphic Kimi Complex of the Rhodope Metamorphic Province, NE Greece. *Earth and Planetary Science Letters* **241**, 672-685.

Prawer, S., Nugent, K.W., Jamieson, D.N., Orwa, J.O., Bursill, L.A. and Peng, J.L. (2000) The Raman spectrum of nanocrystalline diamond. *Chemical Physics Letters* **332**, 93-97.

Prencipe, M., Maschio, L., Kirtman, B., Salustro, S., Erba, A. and Dovesi, R. (2014) Raman spectrum of $NaAlSi_2O_6$ jadeite. A quantum mechanical simulation. *Journal of Raman Spectroscopy* **45**, 703-709.

Revenaugh, J. and Sipkin, S.A. (1994) Seismic evidence for silicate melts atop the 410-km mantle discontinuity. *Nature* **369**, 474-476.

Ruhl, M. and Kürschner, W.M. (2011) Multiple phases of carbon cycle disturbance from large igneous province formation at the Triassic-Jurassic transition. *Geology* **39**, 431-434.

Schindler, T.L. and Vohra, Y.K. (1995) A micro-Raman investigation of high-pressure quenched graphite. *Journal of Physics: Condensed Matter* **7**, L637.

Shames, A.I., et al. (2002) Defects and impurities in nanodiamonds: EPR, NMR and TEM study. *Journal of Physics and Chemistry of Solids* **63**, 1993-2001.

Shcheka, S.S., Wiedenbeck, M., Frost, D.J. and Keppler, H. (2006) Carbon solubility in mantle minerals. *Earth and Planetary Science Letters* **245**, 730-742.

Sherriff, B.L., Grundy, H.D. and Hartman, J.S. (1987) Occupancy of T sites in the scapolite series; a multinuclear NMR study using magic-angle spinning. *Canadian Mineralogist* **25**, 717-730.

Skibsted, J., Hjorth, J. and Jakobsen, H.J. (1990) Correlation between ^{29}Si NMR chemical shifts and mean Si-O bond lengths for calcium silicates. *Chemical Physics Letters* **172**, 279-283.

Smith, K.A., Kirkpatrick, R.J., Oldfield, E. and Henderson, D.M. (1983) High-resolution silicon-29 nuclear magnetic resonance spectroscopic study of rock-forming silicates. *Am. Mineral.* **68**, 1206-1215.

Stagno, V. and Frost, D.J. (2010) Carbon speciation in the asthenosphere: Experimental measurements of the redox conditions at which carbonate-bearing melts coexist with graphite or diamond in peridotite assemblages. *Earth and Planetary Science Letters* **300**, 72-84.

Stagno, V., Ojwang, D.O., McCammon, C.A. and Frost, D.J. (2013) The oxidation state of the mantle and the extraction of carbon from Earth's interior. *Nature* **493**, 84-88.

Stebbins, J.F. (1995) Nuclear magnetic resonance spectroscopy of silicates and oxides in geochemistry and geophysics, In *Mineral Physics & Crystallography: A Handbook of Physical Constants*. American Geophysical Union, pp. 303-331.

Stebbins, J.F. (2017) "Free" oxide ions in silicate melts: Thermodynamic considerations and probable effects of temperature. *Chemical Geology* **461**, 2-12.

Stolper, E., Fine, G., Johnson, T. and Newman, S. (1987) Solubility of carbon dioxide in albitic melt. *American Mineralogist* **72**, 1071-1085.

Sumiya, H. (2004) Microstructure features of polycrystalline diamond synthesized directly from graphite under statid high pressure. *J Mater Sci* **39**, 445-450.

Sverjensky, D.A., Stagno, V. and Huang, F. (2014) Important role for organic carbon in subduction-zone fluids in the deep carbon cycle. *Nature Geosci* **7**, 909-913.

Tao, R., Zhang, L., Stagno, V., Chu, X. and Liu, X. (2017) High-pressure experimental verification of rutile-ilmenite oxybarometer: Implications for the redox state of the subduction zone. *Science China Earth Sciences* **60**, 1817-1825.

Toplis, M.J., Kohn, S.C., Smith, M.E. and Poplett, I.J. (2000) Letter. Fivefold-coordinated aluminum in tectosilicate glasses observed by triple quantum MAS NMR. *American Mineralogist* **85**, 1556-1560.

Tossell, J.A. (1995) Calculation of the C-13 NMR shieldings of the CO_2 complexes of aluminosilicates. *Geochimica et Cosmochimica Acta* **59**, 1299-1305.

Vidano, R. and Fischbach, D.B. (1978) New lines in the Raman spectra of carbons and graphite. *Journal of the American Ceramic Society* **61**, 13-17.

Xu, R., Liu, Y., Wang, X., Zong, K., Hu, Z., Chen, H. and Zhou, L. (2017) Crust recycling induced compositional-temporal-spatial variations of Cenozoic basalts in the Trans-North China Orogen. *Lithos* **274-275**, 383-396.

Xue, X.Y., Stebbins, J.F., Kanzaki, M., McMillan, P.F. and Poe, B. (1991) Pressure-induced silicon coordination and tetrahedral structural-changes in alkali oxide-silica melts up to 12 GPa - NMR, Raman, and infrared-spectroscopy. *American Mineralogist* **76**, 8-26.

Yarger, J.L., Smith, K.H., Nieman, R.A., Diefenbacher, J., Wolf, G.H., Poe, B.T. and McMillan, P.F. (1995) Al coordination changes in high-pressure aluminosilicate liquids. *Science* **270**, 1964-1967.

Appendix.

A1. Abstract Published in Korean Journal

Pressure-load calibration of multi-anvil press and the thermal gradient within the sample chamber

Eun Jeong Kim and Sung Keun Lee

Published in Journal of Mineralogical Society of Korea, 31, 161-172 (2018)

Multi-anvil press (MAP) is one of the high pressure apparatuses and often generates the pressure-conditions ranging from 5 to 25 GPa and temperature-conditions up to 2300 °C. The MAP is, therefore, suitable to explore the pressure-induced structural changes in diverse earth materials from Earth's mantle and the bottom of the mantle transition zone (~660 km). In this study, we present the experimental results for pressure-load calibration of the 1100-ton multi-anvil press equipped in the authors' laboratory. The pressure-load calibration experiments were performed for the 14/8 step, 14/8 G2, 14/8 HT, and 18/12 assembly sets. The high pressure experiments using α-quartz, wollastonite-structure of $CaGeO_3$, and forsterite as starting materials were analyzed by powder X-ray diffraction spectroscopy. The phase transition of each mineral indicates the specific pressure that is loaded to a sample at 1200 °C: a transition of α-quartz to coesite at 3.1 GPa, that of garnet-structure of $CaGeO_3$ to perovskite-structure at 5.9 GPa, that of coesite to stishovite at 9.2 GPa, and that of forsterite to wadsleyite at 13.6 GPa. While the estimated pressure-load calibration curve is generally consistent with those obtained in other laboratories, the

deviation up to 50 tons is observed at high pressure above 10 GPa. This is partly because of the loss of oil pressure at high pressure resulting from the differences in a sample chamber, and the frictional force between pressure medium and second anvil. We also report the ~200 °C/mm of thermal gradient in the vertical direction of the sample chamber of 14/8 HT assembly. The pressure-load calibration curve and the observed thermal gradient within the sample chamber can be applied to explain the structural changes and the relevant macroscopic properties of diverse crystalline and amorphous earth materials in the mantle.

A2. Publication list

Journal Articles

International Journals

Kim, E. J., Fei, Y., and Lee, S. K., Effect of pressure on the short-range structure and speciation of carbon in alkali silicate and aluminosilicate glasses and melts at high pressure up to 8 GPa: ^{13}C, ^{27}Al, ^{17}O and ^{29}Si solid-state NMR study, *Geochimica et Cosmochimica Acta*, **224** 3270-343 (2018).

Lee, S. K., Han, R., **Kim, E. J.**, Jeong, G.Y., Khim H., and Hirose, T., Quasi-equilibrium melting of quartzite upon extreme friction, *Nature Geoscience*, **10** 436-441 (2017).

Ryu, Y.-J, Yoo, C.-S., Kim, M., Yong, X., Tse, J., Lee, S. K., **Kim, E. J.**, Hydrogen-doped polymeric carbon monoxide at high pressure, *The Journal of Physical Chemistry C*, **121** 11078-11086 (2017)

Kim, E. J., Fei, Y., and Lee, S. K. Probing carbon-bearing species and CO_2 inclusions in amorphous carbon-$MgSiO_3$ enstatite reaction products at 1.5 GPa: Insights from ^{13}C high-resolution solid-state NMR. *American Mineralogist,* **101** 1113-1124 (2016**)**

Lee, S. K., Kim, H. –I., **Kim, E. J.**, Mun, K. Y., and Ryu, S. B., Extent of disorder in magnesium aluminosilicate glasses: Insights from ^{27}Al and ^{17}O NMR, *Journal of Physical Chemistry C,* **120** 737-749 (2016)

Lee, S. K. and **Kim, E. J.**, Probing metal-bridging oxygen and configurational disorder in amorphous lead silicates: Insights from ^{17}O solid-state nuclear magnetic resonance, *Journal of Physical Chemistry C*, **119** 748-756 (2015)

Lee, S. K., Kim, H. N., Lee, B. H., Kim, H. I., **Kim, E. J.** Nature of chemical and topological disorder in borogermanate glasses: Insights from B-11 and O-17 solid-state NMR and quantum chemical calculations. *Journal of Physical Chemistry B* **114** 412-420 (2010)

Domestic Journals (Korean)

Kim, E. J. and Lee, S. K. Pressure-load calibration of multi-anvil press and the thermal gradient within the sample chamber. *Journal of Mineralogical Society of Korea* **31**(3) 161-172 (2018)

Kim, E. J. and Lee, S. K. Atomic structure of dissolved carbon in enstatite: Raman spectroscopy and quantum chemical calculations of NMR chemical shift. *Journal of Mineralogical Society of Korea* **24** 289-300 (2011)

In Preparation

Kim, E. J. and Lee, S. K., (*in preparation*) Pressure-induced speciation of carbon in carbon-bearing silicate glasses quenched from melts at high pressure up to 14 GPa: Implications for deep carbon cycle near upper mantle-transition zone boundaries

Kim, E. J., Kim, Y. H., and Lee, S. K., (*in preparation*) Effect of chemical disorder on structural changes in Na-Li silicate glasses quenched from melts at high pressure

Conference Abstracts

International Conferences

Kim, E. J., Fei, Y., and Lee, S. K. Effect of pressure on the speciation of carbon in silicate melts and crystals at high pressure up to 8 GPa:

Insights from multi-nuclear solid-state NMR. Deep Carbon Observatory Early Career Scientist Workshop, Catania, August 28-September 2, 2017. (Oral and poster)

Kim, E. J., Fei, Y., and Lee, S. K. Effect of pressure on the structural changes of silicate network of fluid-bearing silicate melts: Insights from multi-anvil press and multi-nuclear solid-state NMR. 2016 IUCr High-Pressure Workshop, Pohang, September 20-24, 2016. (Poster)

Kim, E. J., Fei, Y., and Lee, S. K. Effect of pressure on the carbon speciation in silicate glasses and melts: Insights from multi-nuclear solid-state NMR. 2015 American Geophysical Union Fall Meeting, San Francisco, December 14-18, 2015. (Poster)

Kim, E. J., Lee, S. K., and Fei, Y., Effect of pressure on the speciation of carbon in silicate glasses: A view from multi-nuclear high resolution solid-state NMR. The 7th Asian Conference on High Pressure Research, Bangkok, January 16-18, 2015. (Poster)

Kim, E. J. and Lee, S. K., Pressure-induced speciation and relaxation of carbon in silicate glasses: Insights from ^{13}C solid-state NMR. International Symposium on Non-Oxide and New Optical Glasses, Jeju, August 24-28, 2014. (Oral)

Kim, E. J., Fei, Y., Tschauner, O. D., Mosenfelder, J. L., Asimow, P. D., and Lee, S. K., Effects of pressure on short-range structure and carbon speciation in silicate melts: Insights from multi-nuclear NMR and X-ray Raman scattering. 2013 American Geophysical Union Fall Meeting, San Francisco, December 9-13, 2013. (Poster)

Domestic Conferences

Kim, E. J. and Lee, S. K., Speciation of carbon in aluminosilicate melts and crystals at the lower part of upper mantle using Raman spectroscopy. Fall Meeting of the Geological Society of Korea, Gyeongju, October 24-27, 2018. (Poster)

Kim, E. J. and Lee, S. K., Carbon-induced structural changes in silicate melts at 9 GPa using solid-state NMR. Annual Joint Conference of Petrological Society of Korea and Mineralogical Society of Korea, Cheongju, May 28-29, 2018. (Poster)

Kim, E. J., Kim Y. H., and Lee, S. K., Effect of pressure on the distribution of cations in Na-Li trisilicate glasses: Insights from solid-state NMR. Annual Joint Conference of Petrological Society of Korea and Mineralogical Society of Korea, Daegu, May 28-29, 2017. (Poster)

Kim, E. J. and Lee, S. K., Structural changes in Na-Li silicate glasses with varying pressure and composition using multi-anvil press. Fall Meeting of the Geological Society of Korea, Pyeongchang, October 26-29, 2016. (Oral)

Kim, E. J. and Lee, S. K., Structural changes of Na-Li silicate glasses with varying pressure: Insights from solid-state NMR and Raman spectroscopy. Annual Joint Conference of Petrological Society of Korea and Mineralogical Society of Korea, Busan, May 26-27, 2016. (Oral)

Kim, E. J. and Lee, S. K., Pressure-load calibration of multi-anvil press for high pressure experiments up to the upper mantle-transition zone boundary. Fall Meeting of the Geological Society of Korea, Jeju, October 28-29, 2015. (Poster)

Kim, E. J. and Lee, S. K., Preliminary studies for high pressure experiments using mutli-anvil press: Pressure-load calibration using mineral phase

transition. Annual Joint Conference of Petrological Society of Korea and Mineralogical Society of Korea, Andong, May 28-29, 2015. (Oral)

Kim, E. J. and Lee, S. K., Effect of pressure on speciation of carbon in silicate melts using ^{13}C solid-state NMR. Annual Joint Conference of Petrological Society of Korea and Mineralogical Society of Korea, Busan, May 29-30, 2014. (Oral)

Kim, E. J. and Lee, S. K., Solubility and speciation of carbon in enstatite and silicate glasses at high pressure: Distribution of carbon in the Earth interior. Fall Meeting of the Geological Society of Korea, Jeju, October 23-27, 2013. (Oral)

Kim, E. J., Lee, S. K., and Fei, Y., Solubility and speciation of carbon in crystalline and amorphous silicates at high pressure using ^{13}C MAS NMR. 2013 Summer Meeting for the Korean Magnetic Resonance Society, Muchangpo, July 1-3, 2013. (Poster)

Kim, E. J., Lee, S. K., and Fei, Y., Speciation of carbon in albite glass at high pressure using solid-state C-13 NMR. Annual Joint Conference of Petrological Society of Korea and Mineralogical Society of Korea, Daejeon, May 23-24, 2013. (Oral)

Kim, E. J. and Lee, S. K., Quantum calculations of equilibrium silicon isotope fractionation factor for silicates with varying degree of polymerization: Implications for Si isotope composition in precambrian chert. Fall Meeting of the Geological Society of Korea, Jeongseon, October 24-27, 2012. (Oral)

Kim, E. J., Lee, S. K., and Fei, Y., Atomistic origins of carbon solubility into crystalline enstatite at 1.5 GPa. Fall Meeting of the Geological Society of Korea, Jinju, May 26-27, 2011. (Oral)

요약 (국문초록)

맨틀은 지구상에서 가장 큰 탄소 저장고로 맨틀 내에서의 탄소의 화학종 변화는 규산염 용융체의 지구물리 및 지구화학적 성질 변화, 맨틀 내의 산소 퓨가시티 조절, 그리고 맨틀 내의 탄소 분포에 중요한 역할을 한다. 이러한 중요성으로, 규산염 용융체 내에 용해된 탄소 화학종에 대한 연구는 4 GPa 까지의 압력 조건에서 활발히 수행되었다. 그러나 시료 합성에서의 어려움으로, 상부 맨틀에 해당하는 4–14 GPa 의 압력 조건에서 규산염 용융체 내의 탄소 화학종 변화와 그에 따른 규산염 물질의 구조 변화에 대한 연구는 아직까지 진행되지 않았다.

본 학위논문에서는 결정질 및 비정질 규산염 물질 내에 존재하는 탄소에 대해 압력에 의한 화학종 변화를 체계적으로 확인하고자 다핵종 (^{13}C, ^{27}Al, ^{29}Si, ^{17}O, and ^{7}Li) 고상 핵자기공명 분광분석 (NMR)과 라만 분광분석을 이용했다. 논문의 주 목적은 결정질 및 비정질 규산염 물질 내에 존재하는 탄소 화학종을 분석하고 정량화하는 것이다. 압력에 의한 알칼리 규산염 용융체의 구조 변화도 함께 수행되었다.

우선 ^{13}C 로 부화된 비정질 탄소와의 반응으로 생성된 엔스테타이트 (enstatite) 결정을 1.5 GPa 에서 합성하고, 시료 내에 존재하는 탄소 화학종을 함유한 유체 포획물 및 탄소 화학종에 대한 체계적인 분석 방법을 수립했다. 라만 스펙트럼에서는 유체 포획물 내에서 CO_2 및 CO, CH_4, H_2O, H_2와 같은 다양한 화학종이 불균질하게 분포하고 있음을 확인하였으나, ^{13}C MAS NMR 스펙트럼에서는 CO_2, CO 와 더불어 라만에서 확인되지 않았던 CO_3^{2-}가 확인되었다. 라만 스펙트럼에서 확인되지 않았던 화학종이 결정질 규산염 내부에 용해된 화학종인지를 확인하기 위해 ^{13}C MAS NMR 스펙트럼에서의 피크 세기와 시료 내의 ^{13}C 함량에 대한 관계식을 세웠다. 관계식으로부터 CO_3^{2-}는 28–45 ppm 존재하는

것으로 확인되었으며, 이것은 엔스테타이트 결정 내의 탄소 용해도(0.05–4.7 ppm)보다 훨씬 높으므로 CO_3^{2-}는 분리된 상으로 존재할 것으로 생각된다. 본 연구에서 엔스테타이트 내의 탄소 화학종을 동정하기 위해 사용된 라만 및 NMR 방법론을 이용하여 앞으로 규산염 결정 내에 존재하는 탄소 화학종을 정량적으로 분석할 수 있을 것으로 생각된다.

8 GPa 까지의 압력에서 이성분계 Na-규산염 용융체와 삼성분계 Na-알루미노규산염 용융체 내에 존재하는 탄소의 압력에 따른 화학종 변화와 그에 따른 규산염 용융체의 구조 변화에 대해 이해하고자 다핵종(^{13}C, ^{27}Al, ^{29}Si, ^{17}O) 고상 NMR 을 이용한 연구가 수행되었다. 이성분계 Na-규산염 용융체에서는 규산염 용융체 내에 용해된 탄산염 이온만이 관찰되었으며, 6 GPa 이상의 압력에서는 규산염 사면체와 연결된 연결탄산염의 형성이 확인되었다. 그에 반해 삼성분계 Na-알루미노규산염 용융체에서는 CO_2, CO, CO_3^{2-}가 확인되었으며, 6 GPa 까지 압력이 증가함에 따라 탄산염 이온의 분율이 증가했다. 네 종류의 탄산염 화학종 중, $Al(CO_3)Si$ 의 분율이 압력의 증가에 따라 가장 많이 증가했으며 이것은 ^{27}Al 3QMAS NMR 스펙트럼에서 보이는 Al 의 위상학적 무질서도의 증가와 관련이 있는 것으로 생각된다. ^{13}C MAS NMR 에서의 피크 세기와 CO_2의 스핀-격자 완화 시간으로부터 계산했을 때, Na-알루미노규산염 용융체 내에 존재하는 탄소의 총함량은 1.5 GPa 에서는 ~1 wt%, 6 GPa 에서 ~4 wt%로 유추된다. 4 GPa 이상의 압력에서 규산염 용융체 내의 탄소 화학종 변화에 대한 본 연구 결과는 상부 맨틀 내에 존재하는 규산염 용융체 내에서의 탄소 화학종 및 함량에 대한 이해를 도울 것으로 생각된다.

탄소가 없는 규산염 용융체에서의 압력에 따른 구조 변화를 이해하고 혼합 양이온 효과를 확인하기 위해서 8 GPa 까지의 고압 환경에서 Na-Li 규산염 용융체의 구조 변화에 대해 NMR 분광분석을

통해 연구했다. ^{29}Si MAS NMR 스펙트럼은 리튬 함량(X_{Li})과 관계없이 압력이 증가함에 따라 고배위수의 Si 함량이 대체적으로 비슷하게 나타남을 보였다. ^{7}Li MAS NMR 스펙트럼에서는 압력 및 X_{Li} 이 증가함에 따라 피크 위치와 폭이 점진적으로 변하는 양상을 보였다. Na-Li 규산염 용융체 내의 ^{7}Li 의 스핀-스핀 완화 시간으로부터, Na 과 Li 의 양이온 무질서도는 1 기압에서는 무작위 분포였다가 고압으로 갈수록 보다 화학적 질서를 이룬다.

14 GPa 까지의 고압 환경에서 탄소를 함유하고 있는 비정질 규산염 내에서 압력에 따른 탄소 화학종 변화를 라만 분광분석과 NMR 을 이용해 분석했다. 탄소를 함유한 Na-알루미노규산염 용융체에서는 CO_2와 CO_3^{2-} 가 존재함을 확인했고, 9.2 GPa 까지 압력이 증가할 때 연결 탄산염의 분율이 증가하며, 이러한 경향성은 이전의 계산 결과와 일치한다. 14 GPa 에서 합성된 탄소를 함유한 Na-알루미노규산염 결정에서는 나노다이아몬드가 확인되었고, ^{13}C MAS NMR 에서는 나노다이아몬드와 탄산염 광물의 존재가 확인됐다. 탄소를 포함한 이성분계 Na-규산염 용융체에서는 14 GPa 까지 압력이 증가함에 따라 연결탄산염의 분율이 60%까지 증가함을 확인했다. 이러한 압력에 따른 연결 탄산염의 증가는 고압 환경에서 탄소를 포함한 비정질 용융체의 중합화과정에 대한 구조적 프록시로 사용될 수 있으며 탄산암 용융체와 규산염 용융체 사이의 불응 분리에 관한 미시적 정보를 제공할 것으로 생각된다.

주요어: 탄소 화학종, 규산염 용융체, 고압 환경, 고상 핵자기공명
분광분석, 라만 분광분석